
Junta de Castilla y León
Consejería de Educación


Universidad de Valladolid

Escuela Técnica Superior de Ingenieros de Telecomunicación

Dpto. de Teoría de la Señal y Comunicaciones e Ing. Telemática

Programa de Doctorado en Tecnologías de la Información y las Telecomunicaciones

TESIS DOCTORAL

On Motion in Dynamic Magnetic Resonance Imaging: Applications in Cardiac Function and Abdominal Diffusion

Presentada por **Santiago Sanz Estébanez** para optar al grado de doctor por la Universidad de Valladolid

Dirigida por los doctores
Carlos Alberola López y Santiago Aja Fernández

13 de septiembre de 2019
Valladolid, España

Título: *Title:*	On Motion in Dynamic Magnetic Resonance Imaging: Applications in Cardiac Function and Abdominal Diffusion
Autor: *Author:*	Santiago Sanz Estébanez
Directores: *Advisors:*	Carlos Alberola López y Santiago Aja Fernández
Departamento: *Department:*	Teoría de la Señal y Comunicaciones e Ing. Telemática

TRIBUNAL / *Committee*

Presidente: *President:*	Dr. Manuel Desco Menéndez
Vocal: *Vocal:*	Dra. Rita G. Nunes
Secretario: *Secreatry:*	Dr. Juan Pablo Casaseca de la Higuera

acuerda otorgarle la calificación de

En Valladolid, a

Acknowledgements

I would like to thank all the people who have contributed this Thesis one way or another. It is not easy to express in a few words all the gratitude deserved to the people that have helped me during this hard process. First of all, I would like to express my gratitude to my advisors, Carlos Alberola and Santiago Aja, for their guidance and kindness.

I also appreciate the founding by the European Social Fund, Operational Program of Castilla y León, and the Junta de Castilla y León, through the Ministry of Education.

I must thank all the staff at the LPI for all the hours of work together and technical support and his valuable help in the comprehension of a large part of the techniques and applications of this Thesis. In turn, I would like to thank the entire group, starting with Fede, Susana, Pablo, Rosa and Álvaro for their companionship and for the human experience we shared. Lastly, I would like to thank Elisa, Elena, Óscar and 13 for sharing their spare-time with contention.

I would like to thank Dr. Lucilio Cordero Grande for his outstanding collaboration during my stay at London. There I had the opportunity to get familiar with true MRI raw data and with image reconstruction techniques. I am also in debt with Dr. Javier Royuela del Val, former member of the LPI, for his help in the development and improvement of the groupwise motion estimation technique.

Finally, I want to express my endless gratitude to my parents and my brother Samuel for supporting me all this years and also for their love and patience. I am also grateful to my friends that supported me through ups and downs, specially Óscar, Manu, Alba, Raúl and Jorge.

Thank you so much all of you and to the others, as well.

Abstract

MRI is a well-established medical imaging technique with excellent tissue contrast and high spatial resolution, without the need for ionizing radiation. However, quantification and compensation of physiological motion during acquisition represent a major issue that must be considered for the development of robust biomarkers. This thesis focuses on the estimation and correction of motion in different MRI modalities, to provide robustness in the assessment of functionality and tissue composition of abdominal organs. The parameters we are seeking to provide should be robust, reproducible, with reduced intra- and inter-observer variability and easy to visualize for a better radiological interpretation.

Specifically, this Thesis focuses on two main tasks: (1) the characterization of the mechanical properties and possible misfunctionalities of the myocardium and (2) the robust estimation of the apparent diffusion coefficient in the liver. For the former, we propose a methodology for the robust estimation of motion and strain, as well as a procedure for identifying the presence of fibrotic tissue and classifying the different aetiologies behind hypertrophic cardiomyopathy. For the sake of comprehensiveness, we have also introduced a thorough description of the harmonic phase techniques and an extensive analysis of the different strategies for robust motion and strain estimation in cardiac tagged magnetic resonance. In addition, a review of the most relevant features in cardiomyopathy screening and classification is carried out.

About the latter, we propose a joint registration and estimation procedure for abdominal diffusion weighted imaging. This approach provides a reproducible apparent diffusion coefficient estimation, which is less sensitive to noise and physiological motion during acquisition, two of the main issues in clinical imaging. The main contribution in this second application is twofold: first, the inclusion of a groupwise registration methodology aimed at minimizing the residuals in the estimation; second, the proposal of filtering stages to alleviate the influence of noise in diffusion parameter estimation, which may lead to spuriously biased estimates, especially in low signal-to-noise-ratio scenarios. The proposed study also evaluates the decrease in accuracy when the noise model is not properly accounted for.

Keywords: Motion Correction, Strain Tensor Estimation, Apparent Diffusion Coefficient, Cardiac Tagged Magnetic Resonance, Diffusion Weighted Images.

LIST OF ACRONYMS

1D	One-Dimensional
2D	Two-Dimensional
3D	Three-Dimensional
4D	Four-Dimensional
ADC	Apparent Diffusion Coefficient
ANOVA	Analysis Of Variance
AP	Anterior-Posterior
AUC	Area Under the Curve
B-SSFP	Balanced Steady State Free Precession
BH	Breath-Hold
BW	Backward
C-SPAMM	Complementary Spatial Modulation of Magnetization
CDF	Cumulative Distribution Function
CG	Conjugate Gradient
CNN	Convolutional Neural Network
CVD	Cardiovascular Diseases
DC	Direct Current
DENSE	Displacement Encoded
DFT	Discrete Fourier Transform
DICOM	Digital Imaging and Communication in Medicine
DKI	Diffusion Kurtosis Imaging
DW	Diffusion Weighted
DW-MRI	Diffusion Weighted Magnetic Resonance Imaging
DWI	Diffusion Weighted Imaging
ECG	Electrocardiogram
ED	End Diastolic
EDI	Entropy of the Distribution of Intensities
EDLVV	End Diastolic Left Ventricular Volume
EF	Ejection Fraction
EPI	Echo Planar Imaging

ES	End Systolic
ESLVV	End Systolic Left Ventricular Volume
FB	Free-Breathing
FCM	Fuzzy C-Means
FFD	Free-Form Deformations
FH	Foot-Head
FND	Frobenius Norm Difference
FOV	Field-Of-View
FT	Fourier Transform
FW	Forward
GD	Gradient Descent
GPU	Graphics Processing Unit
GT	Ground Truth
GW	Groupwise
GWT	Gabor Wavelet Transform
HARP	Harmonic Phase
HCM	Hypertrophic Cardiomiopathy
IFT	Inverse Fourier Transform
IRLS	Iterative Reweighted Least Squares
IVIM	Intravoxel Incoherent Motion
IWFT	Inverse Windowed Fourier Transform
JE	Joint Entropy
LA	Long Axis
LAD	Least Absolute Deviation
LMMSE	Linear Minimum Mean Squared Error
LR	Left-Right
LS	Least Squares
LV	Left Ventricle
MC	Motion Compensation
ME	Motion Estimation
MI	Mutual Information

MIND Modality Independent Neighbourhood Descriptor
ML Maximum Likelihood
MO Multi-Orientation
MP Multi-Peak
MR Magnetic Resonance
MR-C Magnetic Resonance Cine
MR-T Magnetic Resonance Tagging
MRF Markov Random fields
MRI Magnetic Resonance Imaging
MSE Mean Squared Error

NCC Normalized Cross Correlation
NLLS Non Linear Least Squares
NMI Normalized Mutual Information
NMR Nuclear Magnetic Resonance

PCA Principal Component Analysis
PDF Probability Density Function
PGSE Pulse Gradient Spin Echo
PI Parallel Imaging
PW Pairwise

RA Rotation Axis
RF Radio-Frequency
ROI Region Of Interest
RSS Residual Sum of Squares

SA Short Axis
SE Spin Echo
SENSE Sensitivity Encoding
SinMod Sine-wave Modeling
SLVH Secondary forms of Left Ventricular Hypertrophy
SNR Signal-to-Noise-Ratio
SPAMM Spatial Modulation of Magnetization
SSD Sum of Squared Differences
SSFP Steady State Free Precession
ST Strain Tensor
STD Standard Deviation

SVM	Support Vector Machines
SVMg	Gaussian Kernel Support Vector Machines
SVMq	Quadratic Kernel Support Vector Machines
T2W	T2 Weighted
TFE	Turbo Field Echo
TSE	Turbo Spin Echo
TV	Total Variation
UNLM	Unbiased Non-Local Means
US	Ultrasound
VLE	Variance of the Local Entropy
VST	Variance-Stabilizing Transformation
WFT	Windowed Fourier Transform
WHARP	Windowed Harmonic Phase
WLS	Weighted Least Squares
WT	Wall Thickening
XCAT	Extended Cardiac-Torso

TABLE OF CONTENTS

Chapter 1
Introduction

1.1 Motivation

Magnetic Resonance Imaging (MRI) is a relatively new discipline in the realm of applied sciences. An important thrust in the clinical field has come from the imaging of soft tissues in the human body and inner processes therein, such that it has become the gold standard for imaging a broad range of body tissues due to its high spatial resolution and contrast. One of the original reasons for the excitement about MRI was, and continues to be, its relative safety. The non-invasive nature of the magnetic fields makes it possible to diagnose conditions of people of almost any age.

Magnetic Resonance (MR) stems from the application of Nuclear Magnetic Resonance (NMR) to radiological imaging. It is well known that the intrinsic spin of a hydrogen nucleus in a magnetic field precesses around that field at the Larmor frequency which, in turn, linearly depends on the magnitude of the field itself. If a spatially varying magnetic field is introduced across the object, the Larmor frequencies also vary spatially. This spatial encoding represents a key point which opened the door to MRI. Now, the different frequency components of the signal could be separated to provide spatial information about the physical object to be reconstructed. Therefore, we can establish the back and forth mapping between the measured signal space and the image position space by means of the Fourier Transform (FT). By introducing more gradient coils, data reconstruction can be performed by an Inverse Fourier Transform (IFT) for Two-Dimensional (2D) and Three-Dimensional (3D) imaging. In order to better understand how an MR image is created, the signal detection and the underlying image formation theories are also briefly reviewed. In Section 1.3 we aim to provide the basic principles of MRI from a signal processing point of view. For more elaborate information on MRI, we refer the reader to the following excellent references: Kuperman (2000); Liang and Lauterbur (2000); Tofts (2004); Bernstein et al. (2004).

MRI represents a powerful imaging tool for the understanding of the human body, both its anatomy and its function, due to its flexibility and sensitivity to a wide range of tissue properties. Therefore, it can be used to observe different physical phenomena occurring in the human body just by combining different types of pulses in the acquisition sequence, which leads to different modalities with distinct clinical and biological

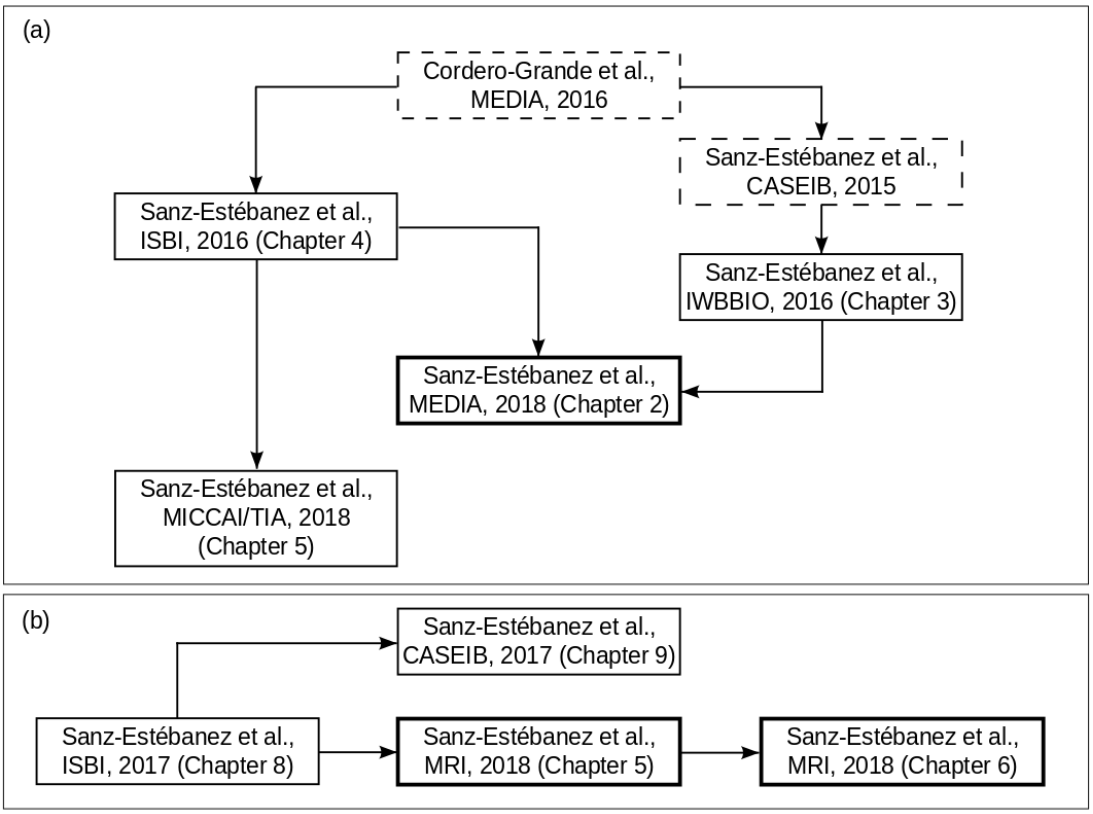

Figure 1.1: Graphical outline of the Thesis context in the fields of (a) myocardial motion and rotation estimation in MR-T and (b) motion robust Apparent Diffusion Coefficient (ADC) estimation in the liver from DW-MRI. Core papers are represented in darker boxes. Relevant contributions which provided an important basis for this work –not included in this Thesis– are also represented with dashed lines. Arrows indicate the order in which the ideas for the publications were conceived.

applications. Two of those modalities are the target application of this Thesis, namely, Magnetic Resonance Tagging (MR-T) and Diffusion Weighted Magnetic Resonance Imaging (DW-MRI), from which the two fundamental parts of this Thesis arise, as shown in Figure 1.1. For a more comprehensive approach to these techniques, we have also provided an introduction to their underlying physical processes.

However, MR data is known to be affected by several sources of quality deterioration due to limitations in the hardware, pulse sequence design, noise or movement of patients. Derived artifacts in MRI may be confused with a pathology or reduce the precision of the diagnosis. Therefore, knowledge of the artifacts and their sources is extremely important in order both to avoid false diagnoses and to learn how to eliminate them.

Besides, MR acquisition is a slow process; this limitation leads to a practical trade-off between scan time, resolution and Field-Of-View (FOV) (Lima da Cruz, 2016; Royuela-del Val, 2017). Therefore, the presence of motion and, specially, physiological motion as it may be in the same order or even faster than the acquisition process itself, represents one of the major obstacles for clinically feasible MRI. Motion of the structures under

study will not only degrade the final images quality but also bother the patient with longer acquisition times (Zaitsev et al., 2015). Consequently, motion occurring during an MR experiment is likely to compromise its diagnostic value. For this reason, patients are typically instructed to remain still. However, some types of motion are unavoidable, such as respiratory, cardiac motion or peristalsis, even when holding the breath, since two Breath-Hold (BH) states are never identical. Abdominal imaging is particularly challenging due to the presence of this type of unavoidable physiological motion. Consequently, Motion Compensation (MC) techniques have been thoroughly studied, specially for low Signal-to-Noise-Ratio (SNR) scenarios such as diffusion imaging or small-lesion imaging.

Despite blurring and other degradations in the final images, the presence of physiological motion during acquisition may also be helpful in clinical diagnosis; MR biomarkers are not only limited to static imaging. Motion biomarkers are also an essential part in various medical applications, being specially useful in the identification and characterization of early stages of pulmonary and Cardiovascular Diseases (CVD). However, reproducible and precise motion biomarkers calculation still are important in clinical research. For the development of clinical biomarkers, a motion robust estimation methodology is mandatory (Padhani et al., 2009). Clinical biomarkers have to fulfill the following characteristics: measurable, accurate (not biased and with low estimation variance), robust (to acquisition protocol parameters), reproducible (inter and intra-subject) and with a clear clinical meaning. Therefore, significant efforts have been made both for robust Motion Estimation (ME) and compensation in the MR field (McLeish et al., 2002).

This Thesis focuses on the influence of physiological motion, specifically, cardiac and respiratory motion, in these two different modalities of body MRI and the development of robust procedures for ME and MC for a reproducible and precise MR biomarker extraction. Particularly, we have faced two problems of interest on which robust ME is a key fact, namely, the calculation of the Strain Tensor (ST) in cardiac MR-T images and the ADC estimation from Diffusion Weighted Imaging (DWI) acquired in the liver. In both cases, robust and reproducible methodologies towards motion artifacts are mandatory. For the former, in order to control the multiple artifacts arising from the different stages of the processing pipeline which will induce a great number of outliers in the strain maps; for the latter, so as to provide a robust parameter estimation methodology suitable for multiparametric Free-Breathing (FB) acquisitions capable of dealing not only with the inherent intensity changes in the sequence but also accurately performing in low SNR scenarios in which the Gaussian assumption no longer holds.

Robustness issues are specially relevant in motion biomarker extraction. In this work, we have focused on the monitorization of motion of a human heart, which is a sensitive indicator of heart disease. Over the last years, MR-T has emerged as the gold standard for representing the detailed motion of a beating heart. However, MR-T processing may be tricky, since a great number of parameters have to be tuned during the different stages in order to avoid outliers arising in final estimates. Therefore, each of the stages has to be cautiously implemented in post-processing to ensure robust and reliable strain estimates. An important family of MR-T processing methods is the Harmonic Phase (HARP) fa-

mily, based on extracting the phase of the complex image (Osman et al., 2000, 1999). This class of methods performs ME by phase-based optical flow, in which the constant pixel brightness assumption is replaced by the potentially more reliable constant pixel phase assumption. This methodology not only allows the reconstruction of small displacements but also directly outputs the deformation gradient tensor without imposing any condition on the deformation field. Nevertheless, without a proper reconstruction scheme, it is prone to be corrupted by intra-voxel phase dispersion, noise, and spectral interferences, further accentuated for the estimation of the ST, as it involves the application of a gradient operator over the complex phase. To alleviate this, we hypothesize that resolving the corrupted areas (especially at the myocardial boundaries) of the estimated tensor using additional data is more beneficial in improving the strain estimation than complex post-processing techniques or outliers suppression methods. This idea has been developed in Chapter 2, which represents the core contribution of the first part of this Thesis (see Figure 1.1).

We have also tried to address some of the problems that appear in diffusion-MRI, adopting a mathematical perspective. Indeed, while inaccurate physical modeling is often designated as the main cause of lack of accuracy and reproducibility, little effort has been made on designing image processing algorithms capable of dealing with these inaccuracies. An important part of the errors that end up in unacceptable diffusion biomarkers can be attributed to the use of naive signal processing algorithms and suboptimal registration methodologies. As previously stated, patient motion is the most important source of artifacts in MRI, specially for abdominal and cardiac applications. This kind of motion artifacts in Diffusion Weighted (DW) images are difficult to avoid, specially in pathological patients unable to hold their breath. Therefore, in order to thoroughly validate the obtained parameters as biomarkers, we have performed experiments under FB conditions, paying special attention to noise and characteristic artifacts along the whole processing pipeline. The implemented MC algorithm has been thoroughly described in Chapters 3 and 4, the most important contributions of the second part of the Thesis, as highlighted in Figure 1.1.

1.2 Objectives

The main objective of this Thesis is to provide the necessary tools for the robust estimation of functional parameters in two dynamic scenarios: the robust calculation of strain- and rotation-related cardiac parameters from MR-T data and the reconstruction of high-resolution ADC maps from multiparametric FB DWI acquisitions in the liver. For the sake of specificity, the detailed objectives can be stated as follows:

1. To propose an automatic processing pipeline for robust cardiac strain imaging and MR motion biomarker extraction that incorporates multiple waveforms (stripes) in the different cardiac axes for artifact-free 3D motion reconstruction. In particular, we have focused on dynamic MR-T sequences to study the deformation of the heart

along the cardiac cycle, specially at End Systolic (ES) phase. To this end, we define the following sub-objectives:

- To propose a methodology for direct estimation of the cardiac ST and related tensorial magnitudes by extending the HARP reconstruction method with the purpose of obtaining more precise and robust measurements. Robust reconstruction of the local phase of the image is grounded on the application of the Windowed Fourier Transform (WFT) and the acquisition of an overdetermined set of stripe orientations. With such a design, we intend to diminish both phase interferences from structures outside the myocardium and instabilities arising from the application of the gradient operator.
- To develop an adaptive procedure to better accommodate the local stripe properties both in the spatial and the spectral domains, using an angled-steered analysis window prior to the WFT and an angle adaptive bandpass filter. Both of them are completely automatic based either on the information available at the DICOM [1] headers or in additional information directly obtained from the data.
- To implement a cardiomyopathy classification tool using tensorial features capable of distinguishing between the heterogeneous groups of Hypertrophic Cardiomiopathy (HCM) and screening for healthy patients. We have designed a two-stage classification scheme using well-known machine learning methods capable of working with different MR modalities. The developed tool has shown to be helpful in the screening and diagnosis of a variety of cardiomyopathy states and aetiologies.
- To design an alternative stripe pattern based on the use of multiple peaks, as opposed to multiple orientations, intended for a single acquisition. For this purpose, we have developed a framework capable of simulating different tag patterns for the sake of finding optimal tag orientations and spacings of the stripes in terms of tensor estimation accuracy.

2. To devise a methodology capable of achieving motion robust ADC estimation for the whole liver, as well as for other abdominal organs, from multiparametric DWI acquisitions. Special attention has been paid to high *b-value* images in which the presence of noise (low SNR) makes the estimation particularly sensitive. This objective has been divided in the following sub-objectives:

   - To develop a framework for the elastic registration of DWI sequences under different paradigms, either Pairwise (PW) or Groupwise (GW), using different likelihood metrics and regularization terms in order to perform an accurate ADC analysis. Due to the non-rigid nature of the proposed approach, not only

[1] Digital Imaging and Communication in Medicine

respiratory and cardiac motion can be compensated for but also Echo Planar Imaging (EPI) geometric distortion is greatly diminished.

- To formulate a joint method capable of simultaneously solving the non-rigid registration and the ADC estimation problems in abdominal applications. The implemented likelihood metric consists of the ADC estimation residuals, which have been inversely weighted according to the signal content in each DW image. Appropriate regularization terms have been introduced in both problems so as to avoid non-reliable transformations and undesirable noise amplification.
- To extend the aforementioned joint methodology to account also for Rician statistics in the data. The original joint algorithm has been improved by introducing a number of filtering stages which are devised for the correction of the biases that arise from the registration and interpolation on non-Gaussian data.

1.3 Background

1.3.1 Magnetic Resonance Physics

As stated in Section 1.1, MRI is grounded on the phenomenon known as NMR, first described in Bloch (1946) and Purcell and Torrey (1946). NMR is concerned with the behavior of the atomic nuclei in the presence of an external magnetic field. Under the influence of a sufficiently strong magnetic field, atomic nuclei with unpaired protons rotate at a given frequency which depends on the field intensity. Therefore, once the Radio-Frequency (RF) pulse has ceased, the excited atomic nuclei will emit this electromagnetic energy back at that same frequency, also known as resonance frequency.

However, to obtain an image of a given tissue or anatomical regions, we have to be able to spatially localize the source of the electromagnetic energy emitted, i.e., the spin density. A spin density can be defined as a pool (concentration) of nuclei precessing at the resonance frequency in a given region.

Furthermore, NMR–derived effects may be used in other MRI modalities, apart from anatomical imaging, which will be discussed in more detail in further sections. The focus of this dissertation is on very different techniques such as MR-T and DW-MRI, although both modalities share several common principles that will be discussed later on.

1.3.1.1 Spin Relaxation Times

Protons, neutrons and electrons show an angular moment known as spin, which may take the following values: $\pm\frac{1}{2}, \pm1, \pm\frac{3}{2}, \pm2, \pm\frac{5}{2}, \pm3 \ldots$. When these particles are paired, their spins are paired as well, so they cancel each other. This is the reason why NMR is only feasible with unpaired protons. In MRI, the particles considered are hydrogen nuclei

associated to water molecules. In this case, there are only two possible values for the spin: $\pm\frac{1}{2}$. However, in MRI, spins cannot be individually analyzed, so the macroscopic behavior of spin systems may be described with classic magnetic field theory. In the absence of an external magnetic field, spins are randomly distributed, so the macroscopic magnetization is null. When an external magnetic field $\mathbf{B}_0$ is applied, the spins will align with the direction of the $\mathbf{B}_0$ field (by convention, it is assumed to be the z axis). Once aligned, spins will adopt one of two possible energy states inducing opposite microscopic magnetizations. The lowest energy state has a slightly greater probability, so an overall magnetization $\mathbf{M}$ appears aligned with $\mathbf{B}_0$. At the same time, the magnetization vector of each of the spins is also subject to a precession movement around $\mathbf{M}$. This precession frequency ω_0 is known as the Larmor frequency (the resonance frequency mentioned before) and may be written as:

$$\omega_0 = \gamma||\mathbf{B}_0|| = \gamma B_0, \tag{1.1}$$

with γ being the gyromagnetic ratio. As previously stated, the Larmor frequency is proportional to the strength of the $\mathbf{B}_0$ field and to the properties of the tissue through γ.

The phase of the precession movement for each spin is random, so the net magnetization $\mathbf{M}$ in the transverse (xy) plane is null, whereas there is a net longitudinal component in the z direction. Once the spins are aligned with the $\mathbf{B}_0$ field and are precessing at the Larmor frequency, they are able to absorb energy from a RF pulse $\mathbf{B}_1(t)$. This pulse may be seen as a circularly polarized magnetic field rotating at the Larmor frequency in the xy plane, so it is coherent with the precession movement. This coherence in the rotation of the spins will induce a rotating component in the xy plane. Besides, as the particle is absorbing energy; the net effect is that an effective magnetic field $\mathbf{B}_{\text{eff}}$ appears aligned either with x or y axis. The spin precession will follow this direction so the magnetization drifts a given angle α from the direction of $\mathbf{B}_0$. We can control the final value of α by setting the area under the pulse $\mathbf{B}_1(t)$; in practice, typical angles are $\alpha = 90°$ and $\alpha = 180°$. Once the pulse $\mathbf{B}_1$ is removed, the spins will emit back the previously absorbed energy, returning to their initial state ($\mathbf{B}_0$ field alignment). During this process, the so-called relaxation, a RF signal is released, which can be read by an antenna, i.e., by the receiving coils located at the MRI scanner.

The relaxation of the spins comprises two different physical processes. Both processes occur at the same time but are completely independent. Besides, these two processes are associated with their corresponding relaxation times, namely T_1 and T_2, being the latter, in general, much shorter.

T_1 (spin–lattice relaxation) represents the time for the longitudinal component of $\mathbf{M}$ to return to its original state, associated with the emission of energy at the Larmor frequency. T_2 represents the time for the transverse component to return to its original state, which is related to thermal equilibrium between spins. By applying the pulse $\mathbf{B}_1(t)$, the spins rotate in a coherent fashion, yielding a net transverse magnetization. This component tends to disappear when the pulse is removed, what is called the spin–spin relaxation.

1.3.1.2 Image Formation

Measuring both relaxation times, we can infer the anatomical properties of the excited volume since these constants are unique for each tissue.

Since the Larmor frequency is proportional to the strength of the external magnetic field ($\mathbf{B}_0$), we can design a spatial gradient of the magnetic field so that different locations can be associated with different magnetic field strengths, and thus to different resonance frequencies. Therefore, by listening to the received signal at different frequencies we can study the different locations of the region excited by the magnetic field. This principle was used for the first time in Lauterbur (1973) to obtain a 2D image. This discovery, together with the Fourier relationship between spin densities and the NMR signal intensity (Mansfield and Grannel, 1973) constitutes the basis for modern MR scanners.

Therefore, by this property, if we apply a spatial gradient in the z direction (during $\mathbf{B}_1(t)$ pulse), the Larmor frequency will vary for each plane z_p in the z direction, so only one of the planes will be excited by the RF pulse, being the only absorbing electromagnetic energy. This principle is used in MRI to select an image slice:

$$\omega_0(z_p) = \gamma B_0 + \gamma G_z z_p, \tag{1.2}$$

where G_z is the modulus of the gradient applied in the slice direction.

The spatial encoding for the xy plane is more complex and a combination of gradients in the x and y directions is needed. A phase/frequency encoding strategy is used in practice. With this strategy, once the slice z_p has been selected with G_z, we can define a plane given by the two gradients G_x and G_y:

$$\omega_0(x, y, z_p) = \gamma B_0 + \gamma G_z z_p + \gamma G_x x + \gamma G_y y, \tag{1.3}$$

in which the lines oriented with an angle $\tan^{-1}(Gx/Gy)$ present the same Larmor frequency. The collected signals will be the superposition of the spins along the lines that compose the plane. Varying the ratio G_x/G_y, we obtain a projected image. However, we still have to infer the spatial information from projections, as is the case of tomography.

For example, if we have chosen the y axis to be the phase encode direction (x axis can also be chosen either way), a pulsed gradient G_y is applied, so the Larmor frequency will differ for each point along that direction. If the length and amplitude of G_y pulse are properly chosen, when G_y is removed the points along y have linearly spaced phases. Consequently, when their Larmor frequencies return to their original value, their spins have different phases. Then, a pulsed gradient in the other direction (G_x in this case) is applied, varying the Larmor frequency along x. The RF signal is measured while G_x is still active. Then, the x direction is encoded within the frequency of the emitted signal, while the y direction is encoded within its phase. Unfortunately, this scheme is prone to ambiguities in the phase encoding: the superposition of several signals with different phases has a phase which is a function not only of the phases of the original signals but also of their amplitudes. In practice, this means that the acquisition has to be repeated several

times with slightly different G_y pulses. The resolution in the y direction will be given by the number of repetitions employed in the acquisition process, while the resolution along x direction will depend only on the number of samples taken. With such an encoding scheme, it is proven (King and Moran, 1984) that the frequency/phase plane is, in fact, the 2D IFT transform of the spatial information.

Without entering into unnecessary details, note that for each phase encoding, the RF signal is the superposition of all the harmonics $\omega_0(x, y_j, z_p) = \omega(x)$ (with y_j the current location of the phase encoding) weighted by the current value of the energy emitted at the location x with Larmor frequency $\omega(x)$. The relation with the FT in the direction of the y axis is not so trivial, but in general the received RF signal s may be modeled as:

$$s(\mathbf{k}) = \int_V W(\mathbf{x})\rho(\mathbf{x}) \exp(j2\pi\mathbf{k}^T\mathbf{x})d\mathbf{x}, \tag{1.4}$$

where $\rho(\mathbf{x})$ is the spin density at the spatial location $\mathbf{x}$ within the FOV of the scanner. V represents the whole spatial domain to be imaged and $W(\mathbf{x})$ is a weighting that accounts for the sensitivity of the receiving coil. Eq. (1.4) is obviously the (weighted) inverse 2D FT of $\rho(\mathbf{x})$ in the dual variable $\mathbf{k}$ for each slice z_p. Following this notation, the signal acquired by the receiving coils is said to be in the k–space, while the signal of interest, i.e. the spin density, is defined on the image domain, also referred to as x–space.

MR scanners usually map the k–space line–by–line; for each repetition of the phase encoding, a pulsed G_x is applied. The frequency encoded RF signal is sampled to achieve a whole line of the 2D IFT of $\rho(\mathbf{x})$. Then, a 2D Discrete Fourier Transform (DFT) is used to recover the image from the sampled k–space for each slice z_p. It is very common in practice to acquire multiple samples of each point in the k–space and then, average all these measurements (Larkman and Nunes, 2007). This serves to the purpose of denoising the final image, thus improving the quality of the data.

1.3.2 Magnetic Resonance Tagging

In this section, we lay the foundation on MR-T. Tagged images can be understood as a combination of two components: the anatomical component (described in Section 1.3.1) and the tagging component that is overlayed on the anatomy.

MR-T basically encodes tissue displacement; this approach conveys motion information, which can be easily identified as measurements of mechanical strain. Strain measures represent a core indicator of cardiac function widely used in clinical practice for the diagnosis and assessment of multiple CVD. In MR-T, magnetization is spatially modulated in a periodic fashion, usually just before the heart tissue begins to contract, at End Diastolic (ED) phase. This modulation appears as tag lines in the image. These tag lines will move and deform themselves along with the tissue, as shown in Fig. 1.2.

Spatial Modulation of Magnetization (SPAMM) tagging is the most common and extended procedure used to produce these tag lines. Details of other methodologies for tagging generation can be found in Axel et al. (2005); Moser and Smith (1990); Zerhouni

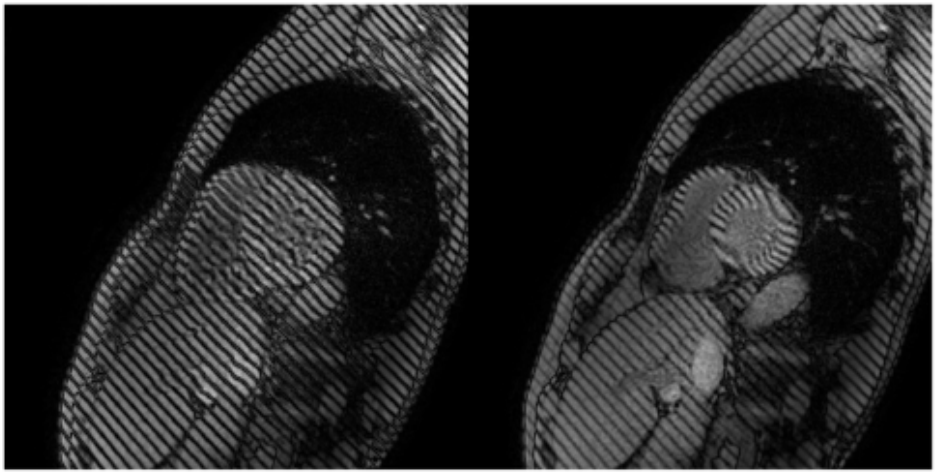

Figure 1.2: Examples of MR-T images of the heart at different cardiac phases: with no deformation at ED phase (left) and a maximal deformation at ES phase (right).

et al. (1988). A very relevant aspect of SPAMM is that it yields a sinusoidal tag pattern, which is ideally suited for HARP-MRI (Osman et al., 2000). The SPAMM sequence is often triggered at ED phase; the point at which the heart is full of blood and undergoes the least amount of motion (McCulloch and Mazhari, 2001). For this purpose, the Electrocardiogram (ECG) signal is usually the one employed to release the trigger.

1.3.2.1 Tagging Pulse Sequence

The application of tags (for simplicity we stick to the 1-1 SPAMM case) consists of four time-varying magnetic fields called pulses. There are two RF pulses, separated by a linear gradient pulse, followed by a spoiler gradient pulse as shown in Fig. 1.3.

A linear gradient pulse is a special type of MR instruction that creates a spatially linearly varying magnetic field. Due to this gradient, each magnetization vector experiences a different external field according to its spatial position and hence precesses at a different frequency. Once the pulse is removed, they will present different phases that yield a small, yet useful, incoherence in the magnetization. In this state of incoherence, a second 90° RF pulse is applied in the same direction as the first RF pulse, so that only the vectors located at the transversal plane will still be precessing. Finally, a spoiler gradient is applied, which makes all precessing vectors out-of-phase with each other, thereby killing the transverse magnetization. Consequently, at the end of the whole process, the magnetization information is stored only in the longitudinal component of magnetization. In other words, the second RF pulse selects the components of $\mathbf{M}_{xy}$ that are orthogonal to the linear gradient, which precisely becomes the cosine of the phase dispersion $\gamma G_x x \tau$.

Basically, a tagging pulse sequence modulates the magnetization in a sinusoidal manner. The final magnetization M_z will look like $M(p,t)\cos(\gamma G_x \tau x)$. As the gradient vector

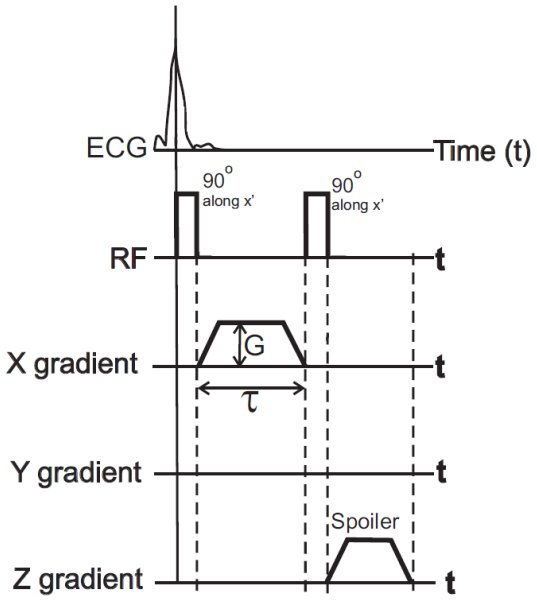

Figure 1.3: 1-1 SPAMM tagging pulse sequence. In this particular example, we use an x-gradient of magnitude $G(t)$ active during a time τ.

$\mathbf{G}$ can be in any direction, the final longitudinal magnetization may be written as:

$$M_z(\mathbf{p}, t) = \mathbf{M}(\mathbf{p}, t) \cos\left(\gamma \int_0^\tau \mathbf{G}^T \mathbf{p} dt\right). \tag{1.5}$$

We have described the case with $\mathbf{G} = [G_x, 0, 0]$ (with M_z modulated along the x axis). This type of tag pattern is called a One-Dimensional (1D) tag. An orthogonal direction of tag can be formed using $\mathbf{G} = [0, G_y, 0]$, modulating M_z along y. If these pulses are applied sequentially in the same tagging pulse sequence, both sinusoidal modulations multiply each other to produce the so-called grid tag patterns.

Improvements for this tagging pulse sequence have been proposed; one of the most common is the well-known Complementary Spatial Modulation of Magnetization (C-SPAMM) (Fischer et al., 1993) which consists of two separate SPAMM acquisitions. The two sinusoidal modulations are dephased π radians, respectively, so the contrast of the resultant sinusoidal modulation is twice as compared to the original 1D tagging pulse sequence. Furthermore, if the Direct Current (DC) component gets subtracted, the tags become zero mean sinusoids. These two properties (zero mean and twice amplitude) are highly desirable for an easier visualization and better clinical inspection.

MR-T has evolved to become the gold standard in diagnosis and characterization of CVD (Edvardsen et al., 2006; McVeigh et al., 1998). However, in comparison to Ultrasound (US) echocardiography, the use of tagging has been very limited in the clinical routine (Budinger et al., 1998). One of its main drawbacks has been the long imaging times and even longer post-processing. MR-T processing and related imaging techniques to tackle this limitation will be thoroughly described in Sections 1.4.1 and 1.4.1.3.

1.3.3 MR Tagging: HARP Imaging

Respiratory motion artifacts and blurring are present in cardiac MRI (Bogaert et al., 2012). In clinical practice, the cardiac cycle (lasting 1 second approx.) is divided into a number of cardiac phases and an image is obtained for each of them. Moreover, to avoid respiratory motion, several breath holdings are required during the acquisition, usually one per slice. In pathologic patients, often with diminished breathing capacity, this approach may not be feasible, resulting in substantially compromised image quality (Chandarana et al., 2011). In opposition, the development of more complex motion robust techniques has been of great help in cardiac function assessment and for the subsequent diagnosis.

Imaging techniques provide essential information for the study and identification of CVD; several modalities have been proposed as an effort to measure advanced cardiac mechanics in the Left Ventricle (LV): speckle tracking echocardiography (Helle-Valle et al., 2005; Bansala and Kasliwalb, 2013), Cine Displacement Encoded (DENSE) MRI (Zhong et al., 2010) or traditional Steady State Free Precession (SSFP), combined with feature tracking techniques (Heermann et al., 2014). Nevertheless, myocardial tissue tagging with cardiovascular MR is currently the gold standard for assessing regional myocardial function (Shehata et al., 2009) and measuring regional contractility (Jeung et al., 2012). If it is not more extended in the daily practice is mainly because it is time consuming, but up to date, it is still the most accurate method to measure cardiac function. Novel techniques, such as HARP imaging, have changed this situation (Osman et al., 1999, 2000). HARP is a tagged image analysis method in near real-time which can be seen as a potential candidate to make MR-T clinically viable (Parthasarathy, 2006).

As mentioned in Section 1.3.2, MR-T allows us to track material points through time, so deformation of the tissue can be calculated from them. Excellent examples of such techniques are: Kerwin et al. (2000); Guttman et al. (1994); Radeva et al. (1997); Kerwin and Prince (2002); Ozturk and McVeigh (2000); Denney and McVeigh (1997).

This is specially relevant, for instance, for the analysis of myocardial motion, whose anomalies are directly related to impaired cardiac function. Hence, local functional indicators extracted from this analysis, such as the ST or the material deformation gradient tensor, may provide additional value to typical global cardiac parameters such as the Ejection Fraction (EF) or the ventricular volumes (Simpson et al., 2013).

Regarding the analysis of MR-T images (Axel et al., 2005), we can differentiate two main families of methods, image-based and k-space-based techniques. Image-based techniques are devised to directly process and analyze the tagged images by identifying the tag lines and tracking their deformation between frames. Examples of such techniques are optical flow (Gupta et al., 1997) or deformable models (Young and Axel, 1992) methodologies, such as Sine-wave Modeling (SinMod) (Arts et al., 2010), which is based on modeling the intensity distribution in the surrounding of each pixel as a summation of sine wavefronts. Alternatively, the k-space-based techniques focus on the FT of the tagged images. These techniques have proven to be much faster and less prone to artifacts (Ibrahim et al., 2016). Most notable methodologies in this category are the HARP tech-

niques (Osman et al., 2000). Recent studies have reported that, although both techniques are consistent in motion estimates, an exaggeration in measurements is often observed for SinMod (Ibrahim et al., 2016), leading to larger biases. For this reason, we have focused on the study of HARP-based methods. A more detailed review of MR-T and related processing techniques can be found in Axel et al. (2005).

HARP methods perform ME by phase-based optical flow, assuming a constant pixel phase assumption. The seminal work presented in Osman et al. (2000) shows that this HARP methodology allows reconstructing the deformation gradient tensor without imposing any condition on the deformation field. However, despite its potential, it is prone to multiple outliers from different sources, as stated in Section 1.1. Not coincidentally, the work by Swoboda et al. (2014) has reported a somewhat poor inter and intra-study reproducibility of strain measurements using the HARP method.

In Parthasarathy (2006), a characterization of the main artifacts observed in HARP reconstructed images is carried out. The author describes the causes involved in the presence of a so-called zebra artifact (crossing tag lines in the local phase images) as well as the multiple reasons why the strain estimation using the conventional HARP method is usually highly inaccurate. Limitations in estimating strain have also been reported for other methods (Tobon-Gomez et al., 2013). However, the proposed strategy for the improvement of strain estimation is based on post-processing the strain maps in order to diminish the influence of corrupted estimations (see also Abd-Elmoniem et al. (2006)).

On the other hand, in Cordero-Grande et al. (2011), it is proposed a technique to demodulate the local phase which balances the spatio-spectral concentration in HARP analysis by using the WFT. This Windowed Harmonic Phase (WHARP) technique turned out to be effective in improving the accuracy in the reconstruction of the complex phase, thus avoiding artifacts in local phase images. Subsequently, the method has been refined in Fu et al. (2013) by tuning the widths of the windows on the basis of the instantaneous spatial frequencies as given by a Gabor Wavelet Transform (GWT) analysis. Other methodologies for improving the strain reconstruction try to resolve the corrupted areas of the estimated tensor using additional data rather than post-processing, such as using C-SPAMM (Rutz et al., 2008) or TruHARP (Agarwal et al., 2010).

1.3.4 Hypertrophic Cardiomyopathy

CVD are a class of diseases that involve the heart or blood vessels and are the leading cause of death globally. From them, cardiomyopathies are the ones associated with structural defects in the heart muscle, particularly in the LV.

From the multiple forms of cardiomyopathies we will focus on HCM since it is one of the most prevalent and studied (Maron et al., 2006). HCM is a condition in which a portion of the heart becomes thickened (asymmetrical wall thickness distribution), which results in the heart being less able to pump blood effectively (Maron et al., 1992). HCM affects about one in 500 people, although dilated cardiomyopathy (enlarged heart cavities and reduced cardiac output) is also a widespread one. Furthermore, it may present

different forms, which may obstacle its tracing and diagnosis. MR is widespread in clinical practice to help diagnose cardiomyopathies, although the protocol may vary with the suspected causes. Therefore, this particular cardiomyopathy is specially useful for testing the ability of the motion-derived features not only for fibrotic tissue detection but also for the classification of the different stages of the disease.

HCM is a relatively common heart muscle disease with a heterogeneous phenotypic expression that occasionally overlaps with other pathologies that also present LV hypertrophy (Maron et al., 2014). The identification of the underlying etiology of the ventricular hypertrophy is a very frequent clinical problem with relevant implications since each etiology needs an specific management and presents a different prognosis. The main features of an HCM heart can be summarized in increased LV mass and thickened walls, especially in the interventricular septum (Urbano-Moral et al., 2014) (see Fig. 1.4).

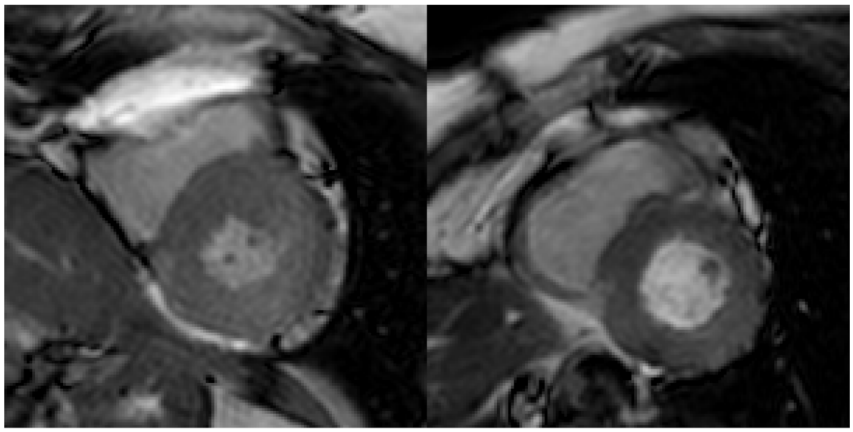

Figure 1.4: Magnetic Resonance Cine (MR-C) images of the heart at ES phase acquired in both an HCM patient (left) and a healthy volunteer (right) depicting morphological change in the LV due to this pathology.

HCM occurs in the presence of myocyte hypertrophy and interstitial and replacement fibrosis which lead to altered forces that are highly correlated to the components of the strain, especially the diagonal ones (Saltijeral et al., 2010). Previous studies have shown that regional LV dysfunctions predate over the morphologic changes related with the phenotypic expression of hypertrophy and obstruction (Dhillon et al., 2014).

Global indices, such as the global longitudinal strain (Shimon et al., 2000), have been employed for CVD identification, reporting noticeable prognostic value. However, local measures could provide more insight into the behavior of fibrotic tissue (Piella et al., 2010).

As stated in Section 1.3.3, the material deformation gradient tensor and the ST obtained with HARP-based or other methodologies may help reveal structural defects in the myocardium. Therefore, descriptors obtained from these tensorial magnitudes have been proposed for cardiomyopathy detection since they have shown high correlation with the presence of fibrosis in some regions of the heart.

In addition to thickening and shortening, the myocardium also undergoes a wringing motion during systolic phases due to the obliquely oriented subendocardial and subepicardial myofibers. In this direction, it has been hypothesized that the presence of greater myocardial torsion may be an indicator of the future presence of myocardial fibrosis (Young and Cowan, 2012).

It is well known that the LV apex globally rotates anticlockwise at a relatively constant rate throughout systole. On the contrary, the base, that initially rotates counterclockwise, reverses direction providing a net clockwise rotation at ES phase. The resulting difference between these two motions is defined as twist. Most LV rotation measures are grounded on this parameter; however, for its calculation a well-defined Rotation Axis (RA) and regular myocardial radii over the whole heart are mandatory. Most of the rotation parameters described in the literature implicitly require an accurate description of an axis of rotation. The center of mass given by myocardial boundaries is widely used as such; however, the heart can translate during the cardiac cycle, which commonly results in misalignments of the center along with subsequent frames, incurring estimation errors.

On the other hand, tensorial analysis provides a more localized characterization of the cardiac deformation. Most of these measures are related to the strain. As stated in Fung (1965), the 3D strain state at any point can be fully represented by three diagonal and three shearing strains. Other significant tensorial magnitudes can also be obtained, such as the Cauchy's ST or the material deformation gradient tensor. Many rotation descriptors can be obtained from these tensorial components either by operating in polar coordinates or just by applying the curl operator. Therefore, these local descriptors can be used to improve cardiac analytics and evaluate the effects of the different CVD on the tissue.

1.3.5 Diffusion Magnetic Resonance Imaging

In what follows, we will focus the discussion on Diffusion-MRI. This modality goes beyond anatomical characterization albeit it was originally proposed to describe the fiber connectivity in the white matter of the brain (Le Bihan, 2014; Jonasson, 2005).

Diffusion-MRI is carried out by taking advantage of the diffusion property of water molecules. Without restrictions, water molecules follow a random walking movement known as Brownian motion. If a particle is at position $\mathbf{x}$ at time t, at time $t + \Delta t$, the Brownian motion pushes it to another random position $\mathbf{x}'$. Its new location is Gaussian distributed with mean x and (isotropic) variance proportional to Δt. This is the principle used by DWI to infer macroscopic tissular permeability (Johansen-Berg and Behrens, 2009; Jones, 2010). In other words, DWI measures the macroscopic diffusion of water molecules. However, this displacement is not always isotropic since existing microstructures within the tissue will not allow water diffusion trough them (or, at least, hinder it). Hence, the water diffusion process may be preferentially produced along some directions or present lower diffusivity depending on the inspected tissue.

In Hanh (1950), it is demonstrated that in the presence of a magnetic field inhomogeneity, thermal motion of the spins leads to the attenuation of its echoes. This basic

principle was used in Stejskal and Tanner (1965) to explicitly measure the diffusion in the Pulse Gradient Spin Echo (PGSE) experiment, schematically described in Fig. 1.5.

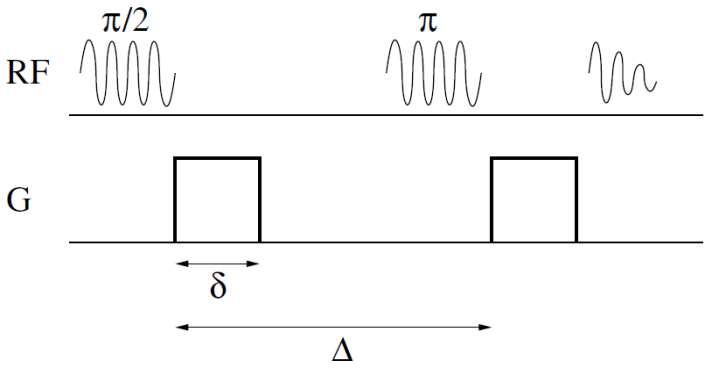

Figure 1.5: Magnetic field gradients for the PGSE experiment. After the RF pulse is applied, the first pulsed diffusion gradient is activated, which induces a phase-shift in the precession of the spins. The next RF pulse inverts the phase of the precession before a second pulsed diffusion gradient is applied.

From Eq. (1.1), we can state the Larmor frequency is proportional to the strength of the magnetic field. When the first gradient pulse is applied, a spatial-dependent variation in the precession frequency of the spins is induced. After a time δ, the pulsed gradient is removed, so the frequency for all spins is again the Larmor frequency ω_0. Since spins have been rotating with different frequencies, their phases will also be different:

$$\phi(\mathbf{x}) = \delta\omega_0 + \varphi(\mathbf{x}) = \delta\omega_0 + \gamma\delta\mathbf{G}^T\mathbf{x}. \tag{1.6}$$

The 180° RF pulse is used to invert the phase of the spins:

$$\varphi'(\mathbf{x}) = -\gamma\delta\mathbf{G}^T\mathbf{x}. \tag{1.7}$$

The second gradient pulse is applied a time Δ after the first one. It is assumed $\Delta \gg \delta$, so the motion of particles during the pulses is negligible compared to the motion during the time between pulses (narrow pulse condition).

After Δ, the particle has moved to a random position $\mathbf{x}'$ described by the conditional (self-diffusion) probability $P_s(\mathbf{x}'|\mathbf{x}, t)$. Consequently, it is affected by a different deviation in the Larmor frequency and also a different phase deviation. From Eq. (1.6), assuming the particle is now at position $\mathbf{x}'$ and an additional phase deviation of 180°, the total phase deviation with respect to the measured signal for which no gradients are applied is:

$$\varphi(\mathbf{x}) = \gamma\delta\mathbf{G}^T(\mathbf{x}' - \mathbf{x}). \tag{1.8}$$

Therefore, according to Eq. (1.8), the obtained signal will be:

$$s(\mathbf{G})/s(0) = \exp(j\gamma\delta\mathbf{G}^T(\mathbf{x}' - \mathbf{x})), \tag{1.9}$$

where $s(0)$ represents the original T_2 signal with no gradients applied and s the acquired signal. Obviously, Eq. (1.9) holds for each particle; however, as MRI scanners cannot model the behavior of each water molecule, but the macroscopic one, or ensemble-average, of all the spins in a spin density $\rho(\mathbf{x})$, the measured signal will be the superposition of phase–shifted spins for all the molecules in the voxel.

The expectation operator can be computed in terms of the diffusion propagator, so the probability density of the ensemble average will be:

$$P(\mathbf{x}'|t) = \int_{\Omega} \rho(\mathbf{x}) P_s(\mathbf{x}'|\mathbf{x}, t) d\mathbf{x}, \tag{1.10}$$

where Ω is the physical space of a voxel and $P_s(\mathbf{x}' \mid \mathbf{x}, t)$ is the conditional Probability Density Function (PDF) for each spin, the so–called self–diffusion probability, which may be modeled as stated in Soderman and Jonsson (1995).

Indeed, the expectation has to be calculated for the joint PDF in both $\mathbf{x}$ and $\mathbf{x}'$ to account for the macroscopic effect inside the voxel, i.e., for all possible initial positions $\mathbf{x}$, and final positions $\mathbf{x}'$. After marginalization (Tristán-Vega, 2009) the joint PDF will be:

$$s(\mathbf{G})/s(0) = \int\int \rho(\mathbf{x}) P_s(\mathbf{x}+\mathbf{R}|\mathbf{x}, \Delta) d\mathbf{x} \exp(j\gamma\delta\mathbf{G}^T\mathbf{R}') d\mathbf{R} = \exp(-4\pi(\Delta - \delta/3)\mathbf{q}^T\mathcal{D}\mathbf{q}), \tag{1.11}$$

where $\mathbf{R} = \mathbf{x}' - \mathbf{x}$ and $\mathbf{q} = \gamma\delta\mathbf{G}/2\pi$ (q-space). This is the well–known Stejskal–Tanner equation (Stejskal and Tanner, 1965) for a given diffusion tensor $\mathcal{D}$ (Basser and Pierpaoli, 1996). Eq. 1.11 is usually rewritten in terms of the *b-value*, typically used in DWI:

$$b = 4\pi||\mathbf{q}||^2(\Delta - \delta/3) = \gamma^2\delta^2||\mathbf{G}||^2(\Delta - \delta/3)/\pi. \tag{1.12}$$

Examples of a DWI acquisition are shown in Fig.1.6.

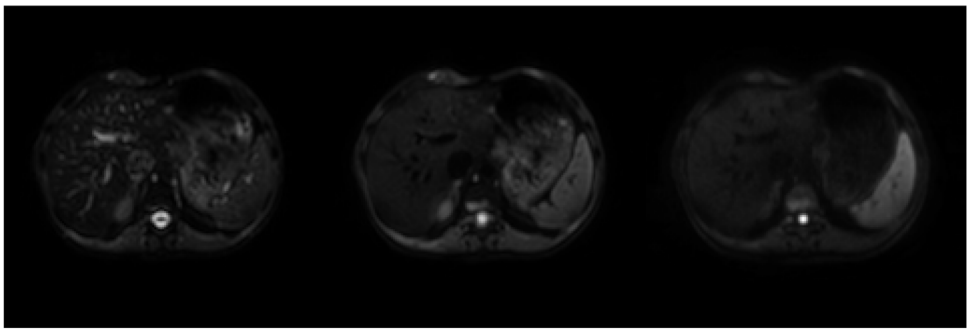

Figure 1.6: DW images of the liver acquired in a healthy volunteer with *b-values* of 0, 100 and 1000 s/mm^2 (from left to right). Figures have been normalized for a better visualization.

In body applications, as isotropic diffusion is generally assumed (Luna et al., 2012; Sandrasegaran et al., 2009), the tensor model can be simplified as follows::

$$s(b)/s(0) = \exp(-b \cdot \mathrm{ADC}), \tag{1.13}$$

where $\mathcal{D}$ has been replaced by a scalar parameter referred to as the ADC, widely used in clinical practice (Padhani et al., 2009; Huisman, 2003; Thoeny and Ross, 2010).

1.3.6 Diffusion Simulation

As stated in Section 1.3.5, diffusion is described as the thermally induced behavior of molecules moving in a microscopic random pattern. This Brownian motion can be modeled as a stochastic process (Lewis et al., 2014) with a Gaussian probability distribution as:

$$P(r,t) \propto \exp\left(\frac{-r^2}{4Dt}\right), \tag{1.14}$$

where D is the diffusion coefficient of the tissue and r is the distance traveled by the molecule during a given time t. This distribution refers to free diffusion; on the other hand, for restricted diffusion, where motion is constrained by hard microstructures, it presents a non-Gaussian distribution with lower D.

For the sake of validation, a series of experiments have been carried out. Synthetic data were used to evaluate accuracy of ADC estimates. DW data have been simulated according to the monoexponential model described in Le Bihan and Breton (1985).

The synthesis of the DW image has been subdivided in two parts. First, the simulation of the b_0 image (T_2), for which the well-known Spin Echo (SE) sequence has been implemented Bernstein et al. (2004):

$$s(0) \propto \rho(1 - e^{T_R/T_1})e^{T_E/T_2}. \tag{1.15}$$

Second, we have simulated the diffusion process by a random walk using the Monte-Carlo method according to Fieremans (2008). The trajectory of a spin is generated by randomly moving the corresponding particle a given number of walks (Wang et al., 2012).

According to the basic theory of diffusion (Johansen-Berg and Behrens, 2009), the displacement of a particle i will induce a proportional phase shift Φ_i^k at each walk k: $\Phi_i^k = 2\pi\gamma G\delta\Delta\vec{d}_i^k$. The final diffusion signal, derived from the bulk phase shift of the N simulated particles in the voxel, can be numerically approximated (Du et al., 2016) as:

$$E = \frac{s(0)}{N}\sqrt{(\sum_{i=1}^{N}\cos(\Phi_i^k))^2 + (\sum_{i=1}^{N}\sin(\Phi_i^k))^2}, \tag{1.16}$$

with $s(0)$ the value of the b_0 image at the given voxel.

The resultant simulated images are shown in Fig. 1.7.

1.3.7 Motion Invariant ADC Calculation

In abdominal organs such as the liver, kidney, or spleen, possible movement of the organ across the different *b-value* scans could result in image misalignment (Abhinav et al., 2016; Stephen et al., 2015). Consequently, the calculation of the ADC map on a pixel-by-pixel basis is error prone and highly likely to incur a boundary smearing (Theilmann et al., 2004).

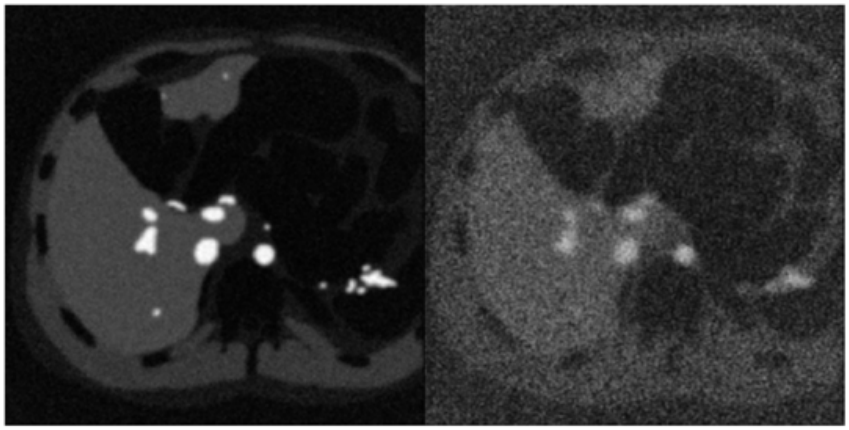

Figure 1.7: Simulated DW images of the liver for b_0 (left) and a *b-value* of 500 s/mm^2. Figures have been normalized for a better visualization.

1.3.7.1 Body Kinematics

For a better comprehension of cardiac and respiratory motion we face, a quantitative mechanics description is provided below. Regarding the heart functionalities, it is known it undergoes a cyclical motion as part of its pumping function. This cardiac cycle can be broadly divided into a systolic (compression) phase lasting approximately 400 ms and a diastolic (relaxation) phase that takes typically between 200 and 800 ms (Weissler et al., 1968). Several studies on the cardiac motion have been performed (Petersen et al., 2006; Petitjean et al., 2005; Jung et al., 2006), particularly focused on the compression of the LV. Results have shown a strong longitudinal component (up to 13 mm near the base), accompanied by significant scaling (approximately 5 mm average) and rotation, up to 10° both in the apex and base, although usually higher in the apex.

Coronary motion has also been studied under BH conditions (Al-Kwifi et al., 2006), revealing predominant Anterior-Posterior (AP) motion (approximately 11.4 mm average), as well as Foot-Head (FH) motion (approximately 9.2 mm average) and Left-Right (LR) motion (approximately 9.1 mm average). Cardiac-induced motion is commonly resolved by means of techniques called cardiac gating or triggering with the aid of an ECG that records the electrical activity of the heart requiring additional hardware and software. However, with such techniques, the whole cardiac cycle may not be used for imaging purposes and, besides, residual cardiac motion may remain.

Regarding respiratory motion, it has been studied for many years, being determined to be, at least, twice in magnitude than heart motion (Bogren et al., 1977), with diaphragmatic motion within the 10 to 20 mm range. These results were complemented suggesting that the FH heart motion is 0.6 times of the FH diaphragm motion (Wang et al., 1995).

The consequences of these types of motion during the acquisition are often reflected in the reconstructed images as ghosting and blurring artifacts. In general, a motion corrupted image can be understood as the superposition of subsampled images in different motion

states, with motion occurring mostly between phase encoding steps. This implies the appearance of multiple replicas within the image unless motion is properly accounted for. Over the last years, multiple motion robust techniques have been developed not relying on new hardware developments, but in advanced signal processing techniques that allow compensating for motion in the acquisition; most of them as post-processing techniques.

Besides, an additional degrading factor stems from the fact that the ultrafast sequence typically used for diffusion studies, i.e. EPI (Kim et al., 1999), suffers from geometric distortions as well as from local signal dropouts caused by static magnetic field inhomogeneities (Bernstein et al., 2004). The resultant geometric distortions are commonly seen near tissue interfaces, where magnetic susceptibility changes rapidly.

A possible solution to reduce the misalignment-related inaccuracies consists in individually delineate the Region Of Interest (ROI) in the different *b-values* images and subsequently extract the mean signal intensity at this region for the different *b-values* and only then, compute the ADC. However, this methodology does not explicitly account for tissue heterogeneity, thus leading to biased ADC estimates.

BH acquisitions are also a popular way of avoiding respiratory motion artifacts with fast scan times. However, when different *b-values* images have been acquired at different BH states and, subsequently, used for ADC estimation, considerable image artifacts can arise stemming from the fact that two apneas are never identical (McLeish et al., 2002).

1.3.7.2 Registration

Image registration algorithms are commonly resorted to correct for image misalignments either on intra- or inter-subject studies. The use of MC techniques is limited by the type and amount of motion that can be compensated for (Aster et al., 2012). With regards to image transformation, it can be either linear or nonlinear. Affine transformations are the most common examples of linear parametric models. Such global models offer a compromise between computational complexity and accuracy in the estimation of the deformations. However, although motion in abdominal organs presents an important rigid bulk motion component, elastic deformations cannot be neglected (Lima da Cruz, 2016). Therefore, rigid and affine approaches may be inaccurate in body applications.

Elastic registration techniques are widespread; for example, the B-spline model has been widely used for diffeomorphic elastic registration (Rueckert et al., 2006, 1999) since provides a good a flexible, robust and smooth fit to the deformation fields.Due to the complexity of nonrigid transformations, manual elastic registration may be helpless and excruciating; therefore, registration methodologies make use of the information present in the images to perform the alignment without user interaction. Most common methods use a reduced subset of points placed over the image, either defined as landmarks or in a grid of control points. Segmentation-based methodologies have also proven to be useful, although, at the price of a careful delineation of the ROI made by qualified staff.

Most approaches pose the registration problem from a PW standpoint (Wachinger and Navab, 2013) by aligning the whole dataset, image by image, with an ideally undis-

torted reference, such as the well-known Demons (Vercauteren et al., 2009) registration algorithm. This procedure, however, is prone to an undesired bias towards the a priori chosen template (Royuela-del-Val et al., 2017), which, depending on its quality, may give rise to multiple outliers in the MC. On the contrary, GW approaches are based on the information obtained from the whole image set, so the bias mentioned above vanishes, showing great performance (Sanz-Estébanez et al., 2018) for DWI registration.

As such, DWI registration is much more challenging than traditional anatomical image registration since additional geometric distortions are present. This problem has been addressed in the literature, stressing the importance of a robust analysis for multiparametric acquisitions, especially in FB conditions. However, most of them are restricted by the diffusion model, which makes it difficult to fit the registered data to a different model.

Methodologies for multiparametric registration towards robust ADC estimation have been designed both for distortion correction (Hong et al., 2015) and MC (Guyader et al., 2015), but from a PW standpoint. GW approaches have been addressed in Veeranghavan et al. (2015) using prior structure segmentations, although the intensity changes due to the diffusion process are not considered. GW approaches that use a Markov Random fields (MRF) have also been described in Kornapoulos et al. (2016). Recently, spatially-constrained approaches have been proposed for liver DWI nonrigid registration (see Kurugol et al. (2017b); Taimouri et al. (2015)) grounded on MRF. With such a design, an increase in the robustness of diffusion parameter estimation is observed by enforcing boundary consistency. However, these approaches are devised for the tracking of small structures, which requires a higher degree of regularization. Besides, despite their elegant formulation, computational needs associated to MRF approaches may be prohibitive.

In Kornapoulos et al. (2016); Kurugol et al. (2017a), it is hypothesized that registration metrics that explicitly take into account the diffusion model and, consequently, the parameters to be estimated will not only make the ulterior ADC analysis more robust but will also alleviate the effects of the additional confounding factors. Different approaches have been described in the literature focused on the improvement of the estimation accuracy of diffusion parameters, for example, Kalman filters (Poupon et al., 2008) or the Linear Minimum Mean Squared Error (LMMSE) framework (Aja-Fernández et al., 2008). Recently, model-free approaches have also been proposed for liver DWI nonrigid registration (see Huizinga et al. (2016)) grounded on Principal Component Analysis (PCA) eigenvalues. However, the absence of a model makes it challenging to choose proper regularization terms that enforce data consistency (fidelity).

The cost function is also a key issue since it has to be able to identify spatial correspondence between anatomical structures. When registration is performed within the same modality, it is plausible to assume a pixel will maintain its intensity along time; therefore, a simple Sum of Squared Differences (SSD) metric can suffice to provide accurate displacement fields for the alignment. On the contrary, when different modalities have to be aligned or great intensity and contrast variation are present in the sequence, as in perfusion or diffusion sequences, it is compulsory resorting to multimodal metrics.

Extensive research has been performed in multimodal alignment. Mutual Information

(MI), first introduced for rigid registration of multimodal scans in Maes et al. (1997), has been widely used as metric for medical image registration. It is based on the assumption that a lower entropy on the joint intensity distribution corresponds to a better alignment. Nevertheless, in practical applications, multiple additional constraints must be introduced due to several weaknesses of MI for nonrigid registration (Haber and Modersitzki, 2007). A non-local shape descriptor (Heinrich et al., 2011), based on denoising schemes, has also been proposed for image registration purposes aiming at extracting anatomically meaningful geometric shapes. However, validation has not been performed over images with relative low SNR, which may be the case in DWI.

The aforementioned approaches are posed in a sequential manner since they focus on a previous registration devised to increase robustness in a later parameter estimation step. However, we hypothesize that introducing accurate and robust motion information in the parameter estimation problem under the same formulation would increase the reproducibility of the representation and, therefore, the quality of the recovered images. One of the main objectives of this Thesis is to develop joint solutions rather than split the problem into different subproblems and resolve them in isolation with different metrics.

On the other hand, restoration schemes, such as the Total Variation (TV) approach (Becker et al., 2011), are also useful in order to obtain high SNR parameter mapping. The presence of noise in the data is precisely a major issue in DW-MRI, since it greatly affects accurate parameter evaluation (Dikaios et al., 2014). It becomes specially relevant at higher *b-values* where the SNR critically decreases. Specifically, it has been shown that insufficient SNR can lead to spuriously low ADC values (Walker-Samuel et al., 2009). Noise-related issues have been thoroughly discussed in Chapter 4.

Recently, deep Convolutional Neural Network (CNN) have been deployed for registration purposes. Registration is posed as a function that maps an input image pair to a deformation field that aligns them. This function is parameterized via a CNN, so given a new pair of images, the alignment is automatically obtained by evaluating this function. Examples of such approaches are: (Schneider et al., 2017; Balakrishnan et al., 2019; Miao et al., 2016; Yang et al., 2017; Che et al., 2019), in which accuracy in deformation estimation is comparable to numerical optimization approaches while operating orders of magnitude faster. However, for these approaches, it is mandatory to train the model to minimize an objective function with a massive amount of images, which may not be available for such specific purposes as DW-MRI registration.

1.3.8 Estimation Theory

The model described in Section 1.3.6 for diffusion simulation is a mathematical entity that relates the intensity of the voxels of the DW images to the underlying diffusion parameters. As such, the task of estimating these parameters is always prone to errors. As mentioned before, MR images are always polluted with noise, and should, therefore, be considered as a set of random variables. These random errors cannot be fixed by improving the diffusion models, they are unavoidable. The theory that deals with the estimation of

parameters from random variables is called statistical parameter estimation theory.

In the statistical parameter estimation theory (Kay, 1993) many estimators have been developed to account for the random nature of the problem in order to accurately retrieve parameters under these circumstances. Below, we explain in more detail the most common parameter estimation methodologies, namely, Least Squares (LS), Weighted Least Squares (WLS) and Maximum Likelihood (ML) approaches.

Let us suppose that the expectation of the random variables X_n depends on $\boldsymbol{\theta}$ as:

$$\mathbb{E}\{X_n\} = \psi_n(\boldsymbol{\theta}), \tag{1.17}$$

where $\psi_n(\boldsymbol{\theta})$ is a deterministic model.

With the LS approach, we seek to minimize the squared differences between the realizations x_n and the model (Eq. (1.17)). Such a difference is often called residual (R). Formally, an LS estimate $\hat{\boldsymbol{\theta}}_{\text{LS}}$ of $\boldsymbol{\theta}$ is defined as:

$$\hat{\boldsymbol{\theta}}_{\text{LS}} = \arg\min_{\boldsymbol{\theta}} \sum_{n=1}^{N} (x_n - \psi_n(\boldsymbol{\theta}))^2. \tag{1.18}$$

In other words, the LS estimate is the value of $\boldsymbol{\theta}$ that yields the least sum of residuals (L_2 norm minimization). Other different statistical optimality criteria can be arranged; the method that minimizes the sum of absolute errors or Least Absolute Deviation (LAD) is also widely spread (L_1 norm minimization). Eq. (1.19) shows the minimization problem to emphasize the differences between LAD and LS:

$$\hat{\boldsymbol{\theta}}_{\text{LAD}} = \arg\min_{\boldsymbol{\theta}} \sum_{n=1}^{N} |x_n - \psi_n(\boldsymbol{\theta})|. \tag{1.19}$$

This may be helpful in studies with a considerable presence of outliers since it will provide equal emphasis to all observations. If it is important to give greater weight to outliers, the method of LS is indeed a better choice. On the contrary, LAD may yield unstable solutions and it does not have an analytical solving method. However, as the problem is linear, any of the many linear programming techniques can still be applied.

If ψ_n is a nonlinear function of $\boldsymbol{\theta}$, the corresponding random vector $\hat{\boldsymbol{\theta}}_{\text{LS}}(\mathbf{x})$ is the Non Linear Least Squares (NLLS) estimator. Sometimes, the squared differences in Eq. (1.18) are multiplied by deterministic values w_n in order to weight the contribution of every residual. In that case, the term weighted is added as prefix.

On the other hand, another important branch of estimators are the so-called ML estimators, which are based on the ML principle. According to the ML principle, given a PDF $p_{\mathbf{x}}(\mathbf{x}|\boldsymbol{\theta})$, it is reasonable to choose as estimate the value of $\boldsymbol{\theta}$ that most likely caused the observations. For fixed $\mathbf{x}$, such a value is the maximum point of the likelihood function, $L(\boldsymbol{\theta}|\mathbf{x})$, which represents the joint probability distribution of the random sample evaluated at the given observations. Such a value is the so-called ML estimate for $\boldsymbol{\theta}$:

$$\hat{\boldsymbol{\theta}}_{\text{ML}} = \arg\max_{\boldsymbol{\theta}} \; L(\boldsymbol{\theta}|\mathbf{x}) \tag{1.20}$$

or by using instead the negative log-likelihood function $\mathcal{L}(\boldsymbol{\theta}|\mathbf{x}) = -\log L(\boldsymbol{\theta}|\mathbf{x})$.

The corresponding random vector $\hat{\boldsymbol{\theta}}_{\mathrm{ML}}(\mathbf{x})$ is called the ML estimator of $\boldsymbol{\theta}$. In the literature, it is very common finding the following expression for $\hat{\boldsymbol{\theta}}_{\mathrm{ML}}$:

$$\hat{\boldsymbol{\theta}}_{\mathrm{ML}} = \arg\min_{\boldsymbol{\theta}} \sum_{n=1}^{N} \mathcal{L}_n(\boldsymbol{\theta}|x_n) \tag{1.21}$$

where $\mathcal{L}_n(\boldsymbol{\theta}|x_n)$ is the negative log-likelihood function of the random variable X_n. This particular expression arises when the elements of $\mathbf{x}$ are independent. Then, the joint PDF, $p_{\mathbf{X}}(\mathbf{x}|\boldsymbol{\theta})$, is the product of the PDF of each of the random variables.

ML estimators and NLLS estimators, both weighted and ordinary (unweighted), share the invariance property (McFadden, 2000). Nevertheless, we cannot make any claim about the optimal properties of the NLLS estimator, unless statistical information about the observations is given. On the other hand, ML estimators have excellent asymptotic properties and can be applied to a wide range of problems; however, it is required we know the formal expression for $p_{\mathbf{X}}(\mathbf{x}|\boldsymbol{\theta})$, which is not always the case. Furthermore, wrong assumptions about the underlying model will induce an important bias. Hence, it is more useful not assuming any model rather than introducing a misleading model in the estimation methodology.

1.4 Methodology

In this section, the methodology applied throughout the Thesis is described in detail and the contributions presented in the subsequent chapters are related to each other.

1.4.1 Cardiac Motion Features Extraction

As indicated in Section 1.2, one of the main contributions of this Thesis is a new and robust methodology for myocardial ME which enables the extraction of local rotation and strain descriptors. This approach intends to provide better comprehension about fibrotic tissue and its mechanical properties.

Motion is measured from MR-T images by means of a WHARP-based methodology using an adaptive windowing technique (see Section 1.3.3), which provides a fast pixel-wise recovery of the deformation information. This Thesis investigates the ability of this method in providing significant diagnostic information. However, an important number of artifacts may obscure the detection of useful features and reduce the clinical utility of the motion biomarkers. Besides, ME is also susceptible to changes in operating and analysis parameters.

We have inspected the performance of the method both in spatial and spectral domains in order to reduce artifact influence and we have redesigned the protocols with

the aim to reduce the number of parameters involved. Furthermore, the obtained cardiac features have been evaluated by a sequential cardiomyopathy classification procedure (Sanz-Estébanez et al., 2016b); we have tested both its ability to discriminate between pathological and healthy patients as well as its discrimination capacity between heterogeneous groups of cardiomyopathies with different genotypes. The goal of this dissertation is to translate this qualitative clinical question into quantifiable engineering problems and to solve them robustly.

1.4.1.1 Materials

For the validation of the proposed approach, our study is designed as a retrospective analysis using a patient database which consists of 56 individuals affected by either primary HCM or Secondary forms of Left Ventricular Hypertrophy (SLVH) (hypertensive heart disease, aortic stenosis or athlete heart disease) and 22 healthy volunteers. All the individuals comprised in the database underwent the ordinary clinical protocol according to their symptoms. Regarding the healthy volunteers, 22 were included in the study with ages between 16 and 84; these subjects underwent the MRI protocol because of a previous suspicion of cardiac pathology but all of them turned out to be healthy. From the pathological cases, 39 of them, with ages from 30 to 86, were diagnosed as primary HCM. These patients showed hypertrophy, predominantly in the LV septum. Following the same protocol, 17 patients were diagnosed of SLVH according to chronic pressure overload. The differential diagnosis between primary HCM and SLVH was based on previous echocardiographic studies and clinical and familiar records. More details about demographic data of controls and both types of pathological cases are provided in Table 2.1.

We have acquired Short Axis (SA) and Long Axis (LA) MR-T datasets for each patient, from apex to base, using a MR C-SPAMM Sensitivity Encoding (SENSE) Turbo Spin Echo (TSE) sequence on a Philips Achieva 3T scanner. Regarding the tagging parameters, we have validated the method for a fixed tag spacing of $k_i = 1/\lambda$, with $\lambda = 7$ mm using two orientations ($\theta = [\pi/4; 3\pi/4]$) in the grid pattern for all patients.

Additionally, we have acquired a Balanced Steady State Free Precession (B-SSFP) SA MR-C sequence at the same location for each patient. The myocardium has been segmented in the ED phase of the MR-C sequence by two cardiologists. These segmentations have been propagated along the cardiac cycle by means of nonrigid GW registration. Cine images at ES phase are also aligned to the tagging orientations so as to translate the information to a common reference system compensated for patient motion. Segmentations are also used to define a ROI in which to compute meaningful measurements.

1.4.1.2 MR Tagging Processing Methodology

In order to get relevant biomarkers, it is mandatory to design a robust methodology for the MR-T processing and the subsequent tensor calculation. We have made use of

the previously mentioned WHARP method to extract the phase images. In addition, we have extended this methodology for the computation of the 3D deformation gradient tensor using SA and LA images on the intersection of the different slices (for points on which LA images were not available, 2D motion has been reconstructed).

This processing pipeline for MR-T was first proposed in Cordero-Grande et al. (2011) so as to obtain locally smooth estimates of the image phase. Subsequently, the tensor estimates have been refined using the LAD method rather the common LS approach, less robust towards outliers and artifacts. In Cordero-Grande et al. (2016) this method has been extended to allow the introduction of an overdetermined set of tagged images (with different stripe orientations), so that artifact presence in the HARP images is greatly diminished. The method has been compared to its non-windowed counterpart in the estimation of the ST, showing great improvement in terms of accuracy and reproducibility both with and without multiple orientations. However, the processing pipeline requires a fine tuning in some stages, especially for the window and filter designs. We have extended the WHARP procedure so as to become completely automatic and adaptive both in the spatial and the spectral domains. We have resorted to an angled-steered analysis window, whereas the band-pass filter has been designed to narrow in the modulation direction and to widen in the orthogonal direction. No parameters are manually set since their values are partially based on the information available at the Digital Imaging and Communication in Medicine (DICOM) headers and in additional information directly estimated from the data. Window and filter designs have been thoroughly described and analyzed in Chapter 5. All the updates have been merged in the proposed pipeline, which we explain in detail in Section 1.4.1.3.

On the other side, we have also checked the ability of the methodology to provide motion descriptors with clinical utility. First, we have proposed an image processing methodology to distinguish fibrotic tissue by assessing the local mechanical properties of the myocardium. The analysis of the local deformation patterns has been carried out with the purpose of finding an agreement between hyperenhanced zones in late enhancement images and areas in the myocardium with abnormal tensor values. The agreement is measured taking as Ground Truth (GT) the manual scar segmentation carried out by two cardiologists in the late enhancement images (Sanz-Estébanez et al., 2015).

We have also made use of the statistical learning theory for the diagnosis of a variety of cardiomyopathies states using MRI-derived features. We have proposed a (sequential) two-stage classification scheme capable of distinguishing between heterogeneous groups of HCM and healthy volunteers. Results have shown that well-established classifying methodologies can be arranged to accommodate the study of HCM with acceptable performance using the aforementioned tensorial measurements, even for reduced and unbalanced sample sets. The sequential classification methodology and the design of each of its inner stages have been described in more detail in Chapter 6.

Although strain measurements have proven useful for cardiomyopathy screening, they cannot tell apart the different genotypes behind these diseases. Therefore, the prognosis in the appearance of fibrotic tissue cannot be achieved with these descriptors. For these

purposes, rotation measures have implemented so as to provide additional information on myocardial mechanics as a complement of standard pump function indices. However, most of the rotation parameters described in the literature assume a cylindrical geometry for the LV, which implicitly requires a fixed RA. Therefore, as stated in Section 1.3.4 any misalignment will induce estimation errors and thus will greatly hinder the subsequent diagnosis and classification. To alleviate this, we have introduced a novel local rotation descriptor based on robust tensorial measurements that relates the presence of increased vorticity values with the fibrotic tissue in the heart. Rotation is estimated by means of the curl operator without any influence of global myocardial parameters, such as RA or cavity radius. With such a design, we can carry out a regional comparative study in patients with different forms of LV hypertrophy coming from different etiologies, namely, HCM and secondary forms of LV hypertrophy, as well as healthy subjects.

In Chapter 2, which constitutes the first core paper of this Thesis, we have included this study which relates the presence of fibrosis with local vortices in myocardial tissue. To the best of our knowledge, this is the first work that makes use of the curl operator for the prognosis of fibrotic tissue.

Furthermore, we have also inspected the design of more appropriate tag patterns, within a single acquisition scenario, by exploring the use of multiple peaks in the k-space, as opposed to multiple orientations. We have assessed, by means of a computational phantom, optimal tag orientations and spacings of the stripe pattern by minimizing the Frobenius Norm Difference (FND) between the GT tensor and the estimated material deformation gradient tensor. In addition, we have measured performance loss with respect to multiple orientations in a real setting. Results indicate that, for a single acquisition, multiple peaks, as opposed to multiple orientations, are indeed preferable. Chapter 7 will explain in more detail these ideas.

1.4.1.3 Strain Estimation in Cardiac Tagged MRI

In this Section, we aim at describing the proposed processing pipeline for robust strain calculation – together with other related magnitudes – in cardiac MR-T.

We will focus on 2D MR HARP images, as 3D acquisitions are rarely used in clinical practice; however the extension of this methodology for 3D strain estimation is straightforward. As stated in Osman et al. (2000), 2D motion reconstruction using the SPAMM technique requires a minimum of 2 linearly independent wave vectors. However, HARP-based methodologies can be extended by allowing the application of more than 2 wave vectors for a more robust estimation. The reconstruction pipeline for robust strain estimation can be decomposed in the following steps:

- Calculation of the local phase of the image.
- Estimation of the material deformation gradient tensor.
- Calculation of the Green–Lagrange ST.

1.4.1.3.1 Local Phase

Let $\mathbf{k}_i^T = k_i \mathbf{u}_i$, with $1 \leq i \leq I$ be the set of acquired wave vectors. For a given cardiac phase, we denote the image corresponding to one of the acquired wave vectors as $I_i[\mathbf{n}]$, with $1 \leq n_j \leq N_j$ $(j = \{1, 2\})$, being N_j is the number of pixels along direction j. By periodically extending this image with period $\mathbf{N}$, we can define its 2D discrete WFT as:

$$S_i[\mathbf{m}, \mathbf{q}] = \frac{1}{Q_1 Q_2} \sum_{\mathbf{n}=-\infty}^{\infty} I_i[\mathbf{n}] w[\mathbf{n} - \mathbf{m}] e^{-j2\pi \sum_{j=1}^{2} \frac{q_j n_j}{Q_j}}, \tag{1.22}$$

with $1 \leq m_j \leq N_j$ and $\mathbf{q} = [q_1, q_2]$ with $1 \leq q_j \leq Q_j$, being $\mathbf{Q}$ the size of the analysis window w. The anisotropic windowing technique performs the extraction of the local phase of the stripe pattern by applying a WFT along the stripe direction combined with a full FT on the direction perpendicular to the stripe over the image at ES phase. Specifically, it is well known (Jain, 1988) that the equation of the straight line that is orthogonal to the unity vector $\hat{\mathbf{u}} = (\cos(\theta), \sin(\theta))$ and for which the distance to a given point $\mathbf{p} = (p_1, p_2)$ is s, turns out to be:

$$(n_1 - p_1)\cos(\theta) + (n_2 - p_2)\sin(\theta) = \hat{\mathbf{u}} \cdot (\mathbf{n} - \mathbf{p}) = s. \tag{1.23}$$

Therefore, if the analysis window is designed as:

$$w(\mathbf{n}) \propto e^{-\frac{s^2}{2\sigma^2}}, \tag{1.24}$$

where $\hat{\mathbf{u}}$ is the tag unity vector read from the DICOM headers and $\mathbf{p}$ the point at which the local FT is calculated. The window will have a rapid tapering, controlled by parameter σ, in the modulation direction but will suffer no attenuation in the orthogonal direction, thus obtaining the aforementioned anisotropic windowing. For the window design, σ has been set equal to the nominal tag spacing, as read from the DICOM headers.

This windowing technique provides a representation of the image spectrum in the surroundings of each pixel of the original image, so HARP bandpass filtering techniques can be directly applied on the spatially localized spectrum of the image. The assumption of anisotropy is still a key fact, considering that the spectrum will suffer a significant stretching orthogonal to the modulation direction caused by the anisotropic window. With such a design, spectral interferences will be mitigated. Then, for each pixel $\mathbf{m}$, we build a filter H_i parameterized spatially by $\boldsymbol{\lambda}$, $H_i^{\boldsymbol{\lambda}}[\mathbf{m}, \mathbf{q}] = H_i^{\boldsymbol{\lambda}[\mathbf{m}]}[\mathbf{q}]$ to filter the WFT:

$$\hat{S}_i[\mathbf{m}, \mathbf{q}] = H_i^{\boldsymbol{\lambda}}[\mathbf{m}, \mathbf{q}] S_i[\mathbf{m}, \mathbf{q}] \tag{1.25}$$

To adequately retrieve the shape of the spectral peak, we have resorted again to an anisotropic filter composed by a Gaussian bandpass filter along the modulation direction and an allpass filter along the orthogonal direction. This is done by means of an spectral mask as defined in Eq. (1.24) where, as before, $\hat{\mathbf{u}}$ is the tag unity vector read from the

DICOM headers and $\mathbf{p}$ is the location of the maximum of the spectrum inside a region in the surroundings of the reference spatial frequency of the tags $\mathbf{k}_i$, defined by $\{\mathbf{k} : \frac{k_i}{2} \leq k \leq 2k_i \wedge |\theta - \angle\mathbf{k}| \leq \frac{\pi}{6}\}$. Hence, we can write the filter parameters as $\boldsymbol{\lambda}[\mathbf{m}] = (\mathbf{p}, \hat{\mathbf{u}}, \sigma)$.

However, this approach, as such, is only suitable for 1D stripe patterns, since, in grid acquisitions, higher order spectral peaks arising from intermodulations may fall within the filter bandwidth (especially in the allpass direction). To alleviate this, an additional constraint (by cropping the filter) has been imposed by $\{\mathbf{k} : |\theta - \angle\mathbf{k}| \leq \frac{\pi}{4}\}$, so that its bandwidth is limited to a region in the surroundings of the peak of interest.

For the filtering stage, σ has been estimated as stated in Otsu et al. (1979), i.e., using a spectral threshold that is calculated minimizing the bimodal intraclass variance. To this end, we have defined a rectangular region in the surroundings of the spectral peak $\mathbf{p}$ according to $\{\mathbf{k} : |s| \leq \frac{k_i}{2}\}$; once the threshold is calculated from the information within that area, a foreground region is obtained. As it is only necessary to estimate the width of the Gaussian filter in the modulation direction, the foreground points are projected over that direction, the sample Standard Deviation (STD) is calculated and σ is set as four times that measure. This way we assure that approximately 99 % of these points fall within an amplitude $\sqrt{2}/2$ times the maximum of the filter.

Finally, the WHARP image can be reconstructed in the spatial domain by using an Inverse Windowed Fourier Transform (IWFT)

$$\hat{I}_i[\mathbf{n}] = \sum_{\mathbf{m}=-\infty}^{\infty} \sum_{q_1=1}^{Q_1} \sum_{q_2=1}^{Q_2} \hat{S}_i[\mathbf{m}, \mathbf{q}] w[\mathbf{n} - \mathbf{m}] e^{j2\pi \sum_{j=1}^{2} \frac{q_j n_j}{Q_j}} \tag{1.26}$$

from which the phase can be easily extracted:

$$\phi_i[\mathbf{n}] = \angle \hat{I}_i[\mathbf{n}]. \tag{1.27}$$

1.4.1.3.2 Material Deformation Gradient Tensor

Once the phase is obtained, we, first, have to compute its gradient since the spatial deformation gradient tensor

$$\mathbf{f}(\mathbf{x}) = \frac{\partial \mathbf{X}}{\partial \mathbf{x}^T}(\mathbf{x}) \tag{1.28}$$

is related with the gradient of the image $\phi_i(\mathbf{x})$ by Osman et al. (2000):

$$\mathbf{k}_i^T \mathbf{f}(\mathbf{x}) = \frac{\partial^* \phi_i}{\partial \mathbf{x}^T}(\mathbf{x}) = \min \left\{ \frac{\partial \phi_i}{\partial \mathbf{x}^T}(\mathbf{x}), \frac{\partial \mathcal{W}(\phi_i + \pi)}{\partial \mathbf{x}^T}(\mathbf{x}) \right\}, \tag{1.29}$$

with $\mathcal{W}(\cdot)$ the wrapping operator, which maps its argument in the interval $[-\pi, \pi)$. The discretization of the gradient operator is achieved by first applying Forward (FW) and Backward (BW) finite differences both for the original phase and the π-shifted one. Then, we take the minimum of each pair as indicated in Eq. 1.29, and finally, average them to construct the centered finite differences.

Then, we arrange the set of wave vectors $\mathbf{k}_i$ in matrix form by:

$$\mathbf{K} = (\mathbf{k}_1, \mathbf{k}_2, \cdots, \mathbf{k}_I)^T, \tag{1.30}$$

so that $\text{rank}(\mathbf{K}) = 2$ (linear independence condition). The same goes with the gradient of the phase images:

$$\mathbf{Y}(\mathbf{x}) = \left(\frac{\partial^* \phi_1}{\partial \mathbf{x}}(\mathbf{x}), \frac{\partial^* \phi_2}{\partial \mathbf{x}}(\mathbf{x}), \cdots, \frac{\partial^* \phi_I}{\partial \mathbf{x}}(\mathbf{x}) \right)^T, \tag{1.31}$$

so we get the following expression (in discrete form):

$$\mathbf{Y}[\mathbf{n}] = \mathbf{K}\mathbf{f}[\mathbf{n}]. \tag{1.32}$$

Alternatively, the material deformation gradient tensor $\mathbf{F}[\mathbf{n}] = \mathbf{f}^{-1}[\mathbf{n}]$ can be described by:

$$\mathbf{K} = \mathbf{Y}[\mathbf{n}]\mathbf{F}[\mathbf{n}]. \tag{1.33}$$

In order to solve the previous equation (estimate $\mathbf{F}[\mathbf{n}]$), one could resort to the LS method:

$$\mathbf{F}[\mathbf{n}] = (\mathbf{Y}^T[\mathbf{n}]\mathbf{Y}[\mathbf{n}])^{-1}\mathbf{Y}^T[\mathbf{n}]\mathbf{K}. \tag{1.34}$$

However, considering the fact that the introduction of an overdetermined set of stripes pursues the minimization of phase interferences, which introduce outliers when performing the HARP image gradient computation, our proposal is to resort to the LAD method, due to its robustness. LAD gives equal emphasis to all observations, in contrast to LS which, by squaring the residuals, gives more weight to large residuals, that is, outliers in which predicted values are far from actual observations. In the LAD case, we seek unknown parameters that minimize the sum of the absolute values of the residuals. Hence, the reconstruction is performed iteratively by:

$$\mathbf{F}_{l+1}[\mathbf{n}] = (\mathbf{Y}^T[\mathbf{n}]\mathbf{W}_l[\mathbf{n}]\mathbf{Y}[\mathbf{n}])^{-1}\mathbf{Y}^T[\mathbf{n}]\mathbf{W}_l[\mathbf{n}]\mathbf{K}, \tag{1.35}$$

with $\mathbf{W}_l[\mathbf{n}]$ a diagonal weight matrix obtained by:

$$W_l^{jj}[\mathbf{n}] = \frac{1}{\sqrt{\sum_{h=1}^{2} \left(K^{jh} - \sum_{g=1}^{2} Y^{jg}[\mathbf{n}] F_l^{gh}[\mathbf{n}] \right)^2}} \tag{1.36}$$

and establishing $\mathbf{F}_0[\mathbf{n}] = \mathbf{I}$, with $\mathbf{I}$ the identity matrix. An analogous set of equations could be used to estimate $\mathbf{f}[\mathbf{n}]$.

1.4.1.3.3 Green–Lagrange Strain Tensor

The target for standard myocardial motion analysis is to estimate the Green-Lagrange ST $\mathbf{E}$, which is defined by:

$$\mathbf{E}[\mathbf{n}] = \frac{1}{2}(\mathbf{F}^T[\mathbf{n}]\mathbf{F}[\mathbf{n}] - \mathbf{I}), \tag{1.37}$$

Once $\mathbf{E}[\mathbf{n}]$ is estimated, we can compute its radial, circumferential and shearing components (longitudinal component will not vary given that $\mathbf{L}^T = [0, 0, 1]$) by contraction:

$$\begin{aligned} E_{\mathbf{RR}}[\mathbf{n}] =& \mathbf{R}^T[\mathbf{n}]\mathbf{E}[\mathbf{n}]\mathbf{R}[\mathbf{n}] \\ E_{\mathbf{CC}}[\mathbf{n}] =& \mathbf{C}^T[\mathbf{n}]\mathbf{E}[\mathbf{n}]\mathbf{C}[\mathbf{n}] \\ E_{\mathbf{RC}}[\mathbf{n}] =& \mathbf{R}^T[\mathbf{n}]\mathbf{E}[\mathbf{n}]\mathbf{C}[\mathbf{n}] \\ E_{\mathbf{RL}}[\mathbf{n}] =& \mathbf{R}^T[\mathbf{n}]\mathbf{E}[\mathbf{n}]\mathbf{L}[\mathbf{n}] \\ E_{\mathbf{LC}}[\mathbf{n}] =& \mathbf{L}^T[\mathbf{n}]\mathbf{E}[\mathbf{n}]\mathbf{C}[\mathbf{n}], \end{aligned} \tag{1.38}$$

using the material polar coordinate system $(\mathbf{R}, \mathbf{C}, \mathbf{L})$ centered at the center of mass of the epicardium and scaled to the resolution of the MR-T space. The $\mathbf{R}[\mathbf{n}]$ and $\mathbf{C}[\mathbf{n}]$ vectors represents the radial and circumferential direction coordinate vectors which map Cartesian coordinates into polar coordinates in the MR-T space.

Usually, one is interested in the so-called Green-Lagrange ejection strain which is the one that relates the maximum deformation at ES phase with the reference configuration at ED phase. Thus, for calculating the aforementioned descriptor, the above procedure should be applied to the ES phase.

These ideas have been introduced in Cordero-Grande et al. (2016) for the strain reconstruction of SA views of the heart in BH MR-T. The reconstruction method here described provides better quality (both qualitative and quantitatively) than other state-of-the-art related methods, including those which make use of adaptive approaches. More details about the nature of the analysis window and the bandpass filter are given in Chapter 5.

1.4.1.3.4 Vortical Features

Tensorial analysis focuses on the properties of the tissue that provide localized characterization of the motion. From these measurements, an important group of rotation descriptors can also be obtained using differential operators.

Our work elaborates on vortical patterns widely employed for the identification of abnormal flow patterns. In this Thesis, the term vortex will be used in the solid mechanics context as a local abnormally increased rotation component. In order to find evidence of perturbations within the myocardial tissue, material vortical patterns can then be associated with increased values of a dynamic rotation parameter extracted from the deformation gradient tensor.

We hypothesize that a local increase of the vorticity (in modulus) arises within myocardial segments with fibrosis-related perturbations. Nonetheless, high vorticity values, irrespective of the fibrosis degree, are prone to appear in myocardial boundaries, giving rise to multiple outliers in rotation estimation.

Chapter 2 which, as previously stated, constitutes the first core paper, focuses on the development of cardiac rotation features derived from strain and stress tensors, with special attention to the analysis of vortical patterns present in cardiac deformation. Both rotation and strain features have been thoroughly developed and tested using a cardiomyopathy classification tool in order to prove the appropriateness of these features towards the assessment of the different states in HCM.

1.4.1.3.5 Myocardial Segmentation Propagation

As stated in Section 1.4.1.1, the myocardium has been segmented on the ED phase of the MR-C sequence by two cardiologists. However, motion descriptors involve multiple cardiac phases in their definition. Therefore, it is necessary to accurately propagate this manual delineations along the different phases of the cardiac cycle.

We have tackled the problem by introducing a monomodal GW non-rigid registration step as a robust ME procedure for cardiac MR-C images. This methodology was first proposed by Cordero-Grande et al. (2013a) for misalignment correction in first-pass cardiac perfusion imaging and has been adapted to the segmentation propagation problem.

The local transformation is represented as a combination of B-spline Free-Form Deformations (FFD) (Rueckert et al., 2006). A Gradient Descent (GD) optimization scheme is used, where the step size is updated according to the variation in the registration metric. The SSD of the image intensity has been chosen as such. To constrain the spline-based FFD transformation to be smooth, we introduce a penalty term which regularizes the transformation; this term is composed by first and second order spatial and temporal derivatives. Trade-off parameters of the optimizer are set empirically. Linear interpolation is used to obtain the intensity of the deformed MR-C images on a rectilinear grid. More details on the B-spline transformation and the interpolation are given in Appendix B.

However, the propagation of the segmentations along the cardiac cycle may not suffice. An additional registration step is necessary since MR-T and MR-C sequences may not be aligned. To alleviate this, we have resorted to a rigid registration methodology capable of dealing with the tagging pattern.

We have processed the MR-T images to improve the myocardium-blood contrast. The strategy adopted consists in removing the tagging pattern (in the frequency domain) using an optimized detagging technique (Makram et al., 2015), followed by myocardium-blood contrast enhancement (Makram et al., 2016). The method is based on the application of band-stop filters to remove the harmonic peaks, which are responsible for creating the tagging pattern, in the image's k-space. Once the image has been detagged and normalized, common PW rigid alignment procedures can be applied. Mean Squared Error (MSE) is the metric that evaluates the image similarity during the registration. On the other hand,

the chosen optimizer is a regular step GD, where the step size is constant until the gradient abruptly changes direction. At this point, the step size is halved. This step has only been performed at ES phase to perform a regional analysis of the ST at that phase since it is the one where the maximum deformation with the reference configuration can be observed. More details on the segmentation propagation and alignment are given in Chapter 6.

1.4.2 Joint ADC Estimation and Registration

In this Thesis we also seek to address some of the open challenges of image registration by proposing fast and robust methods based on the well-established registration framework of B-spline FFD. This non-rigid framework is specially useful when imaging abdominal organs such as the liver, kidney, and spleen, where elastic motion may not be resolved using classical rigid approaches.

We have focused on multimodal image registration, particularly in diffusion-MRI, in which the anatomical features in the images might have different intensities. This makes naive intensity based registration methods unsuitable, although multimodal registration also represents a great challenge due to the multiple sources of error. However, inaccurate physical modeling has been reported as the main cause of the lack of accuracy and reproducibility in the estimates. Therefore, an increasing number of contributions focusing on more complex diffusion models have been proposed, rather than trying to minimize these inaccuracies in simpler models.

Our contribution is a novel methodology, adopting a mathematical perspective within the monoexponential model, for the motion-robust ADC estimation in the whole liver, as well as for other abdominal organs in multiparametric DWI acquisitions.

1.4.2.1 Materials

The validation experiments have been carried out using different sources of data. We have developed a synthetic diffusion phantom using a simulation environment based on the Four-Dimensional (4D) Extended Cardiac-Torso (XCAT) phantom (Segars et al., 2010) focused on the liver. The phantom is built from a whole body model that contains highly detailed anatomical labels which feed a high resolution synthetic image. The 4D XCAT phantom incorporates state-of-the-art respiratory and cardiac mechanics which provide sufficient flexibility to simulate effects of cardiac and respiratory nonrigid motion from a user-defined parameter set. Respiratory motion is defined by a motion vector field derived from two time curves, one controlling the expansion and compression of the diaphragm and the other controlling the amount of AP chest expansion. Therefore, the phantom will provide us not only with the images themselves, but also with GT deformation fields and a synthetic reference ADC map. Although we assume BH acquisitions, different BH states have been simulated for the different *b-values*.

Additionally, the images were synthetically distorted according to Weis and Budinsky (1990) so as to simulate geometric distortions typically observed in EPI acquisitions. Transformation parameters have been set so that distortion amplitude increases with the *b-value*, although physiological motion always remains predominant. SNR has been set to 10 dB for the b_0 image and decreases along with the *b-value*. Complex Gaussian noise has been added during the acquisition simulation resulting in Rician noise for the magnitude images (Aja-Fernández and Vegas-Sánchez-Ferrero, 2016).

Furthermore, we have performed an MRI acquisition on a phantom consisting of a bottle filled with a watery solution. Finally, we have performed MRI acquisitions over a sample of four healthy volunteers. We have acquired both an axial SENSE DWI and a T2 Weighted (T2W) TSE sequence on a Philips Achieva 3T scanner in each case of study. The latter will be used to manually delineate the whole liver as ROI χ on which meaningful measurements will be obtained. All the subjects signed the ordinary informed consent for the MR session and agreed in writing to share the resulting images for research purposes. Personal data were treated according to current legislation.

Acquisition and resolution details for all the sequences (both real and synthetic) employed in the ADC estimation related experiments are shown in Table 8.1.

1.4.2.2 Diffusion Weighted Imaging Registration

We have first tackled the problem of motion insensitive ADC estimation by introducing GW nonrigid registration techniques as a preprocessing MC step previous to the ADC estimation. In Sanz-Estébanez et al. (2017) we presented an study intended to assess the adequateness of GW and PW paradigms within an elastic transformation model for the alignment of DW sequences, focusing on the liver. The suitability of different well-known multimodal voxel-based metrics, such as Entropy of the Distribution of Intensities (EDI), Variance of the Local Entropy (VLE), Modality Independent Neighbourhood Descriptor (MIND) and Normalized Cross Correlation (NCC) was also tested. An elastic multimodal alignment procedure was designed not only for breathing-derived misalignment correction but also accounting for geometric distortions. ADC estimation reproducibility was measured by means of a residual analysis due to the absence of GT. More details about the framework are provided in Chapter 8.

However, the resolution of the motion corrupted ADC estimation in a sequential manner yields a suboptimal solution due to the non-convex nature of the elastic registration procedure. Besides, registration and estimation problems have often been posed with different formulations (cost functions); therefore, the solution for both problems is likely to fall within local minima with such a sequential resolution. To alleviate this, a joint registration and estimation procedure is introduced, in which a common formulation is posed. The joint cost function incorporates weighting parameters that balance the influence of the different images according to the DW signal content. The resulting joint methodology provides better quality (considering both qualitative and quantitative criteria) than sequential methods, including those making use of alternative GW registration methods.

The described method incorporates in the optimization function two regularization terms that account for smoothness in both deformation fields and ADC maps. Chapter 3, which constitutes the second core paper of this Thesis, explains in detail the joint formulation.

Although this scheme has shown to be able to successfully cope with the movement of the patient, it has not taken into account any model for the noise. As a consequence, some steps of the procedure may introduce a bias. This bias may significantly affect ADC estimation in low SNR scenarios since the Gaussian assumption may not hold. Therefore, in order to cope with both the presence of noise and physiological motion simultaneously, we have incorporated within the original pipeline proper methods which correct the interpolation bias, and which, accordingly, improve the ADC estimation. We have shown that the complete algorithm yields higher quality ADC maps as compared to the original formulation, especially when higher *b-values* have been acquired in the sequence. Those biases introduced by the presence of noise have been thoroughly described and analyzed in Chapter 4, which constitutes the third core paper of the Thesis.

We have also had the chance to make use of this methodology in a more complex environment, specifically in a cardiac DWI acquisition. The joint methodology has proven to be reliable for misalignment correction and robustness in the estimation of diffusion parameters, thus providing denoised ADC maps of the heart. A more comprehensive description of this approach has been included in Chapter 9.

1.4.2.3 Motion and Noise Models: Description

In this Section, we aim at describing the models we have assumed for the estimation of both motion and noise variance. In both cases, we are facing complex problems on which some simplifications/transformations over the data are mandatory to address them.

For the former, we have resorted to B-spline curves to obtain a smooth representation of the displacement field. This approach allows us to reduce the dimensionality of the problem by mapping a pixelwise-defined deformation field to a set of control points displacements. Besides, due to the smooth character of spline curves, it is easier to define a regularization term capable of dealing with possible foldings or crossings in the deformation fields. On the other hand, for the latter, we have used a Variance-Stabilizing Transformation (VST) to simplify the analysis of the data. In our case, the VST will represent a function that maps spatially variant Rice data to (independent) Gaussian distributed data. Once the noise variance is obtained by conventional methodologies, we can recover the spatially variant nature of the noise using a homomorphic filter.

1.4.2.3.1 Elastic Motion Modeling

In every application in which motion is accounted for, the model plays a crucial role in the success of the registration. In brain applications, for example, affine transformations are often the best option due to its simplicity, i.e., only translations, rotations and shea-

rings are accounted for. Besides, they provide a quite good approximation to the optimal solution since elastic components are considerably small.

Nonrigid registration focuses on modeling local stretching and compression of the tissue rather than on bulk deformations. Nonrigid transformations are more suitable for abdominal applications due to the elastic nature of the tissue. A popular approach to model non-rigid deformations is to use spline-based transformations (Kybic and Unser, 2003; Rueckert et al., 2006). Using this approach, the deformation can be represented as a FFD based on B-splines which represents a powerful tool and can be written as the product of the familiar 1D B-splines.

The underlying concept behind FFD is to enclose the image within a control point mesh or another hull object and transform the image within the mesh as the control points are displaced over the image. This mesh will be defined from the control points $\mathbf{P} = \{\mathbf{p_u}\} = \{\mathbf{p}_{u_1}, \ldots, \mathbf{p}_{u_L}\}$ with $C_{1,l} \leq u_l \leq C_{2,l}$, whose coordinates in the coordinate system of the image will be:

$$\mathbf{p_u} = \mathbf{c} + \boldsymbol{\Delta}^{\mathbf{p}} \circ \mathbf{u}, \tag{1.39}$$

where $\boldsymbol{\Delta}^{\mathbf{p}} = (\Delta_1^{\mathbf{p}}, \Delta_2^{\mathbf{p}}, \Delta_3^{\mathbf{p}})$[2] is the control point mesh resolution and $\mathbf{c}$ represents the center of our ROI. With such a design, the transformation that maps the coordinate system of the image to the coordinate system of the control point mesh will be:

$$v(\mathbf{x}) = \mathbf{x} \circ (\boldsymbol{\Delta}^{\mathbf{p}})^{-1}, \tag{1.40}$$

being $(\boldsymbol{\Delta}^{\mathbf{p}})^{-1} = [1/\Delta_1^{\mathbf{p}}, 1/\Delta_2^{\mathbf{p}}, 1/\Delta_3^{\mathbf{p}}]$.

As mentioned before, the spline-based transformation can be represented by the product of 1D B-splines, as follows:

$$\mathbf{x}' = \mathbf{x} + \sum_{u_1=C_{1,1}}^{C_{2,1}} \sum_{u_2=C_{1,2}}^{C_{2,2}} \sum_{u_3=C_{1,3}}^{C_{2,3}} \left(\prod_{l=1}^{3} B_E(v_l(x_l - p_{u_l})) \right) \boldsymbol{\theta}_{\mathbf{u}}, \tag{1.41}$$

where $\boldsymbol{\theta}_{\mathbf{u}}$ represents the set of control points displacements and B_E the E-th order B-spline function obtained through the Cox-de Boor recursion formula as defined in De Boor (1978).

The deforming control point mesh has local properties, i.e., displacement of a control point will only influence its local vicinity in the image. Therefore, the performance of the registration method is limited by the resolution of the control point mesh, which is linearly related to the computational complexity. More global and intrinsically smooth deformations can only be modeled using a coarse control point spacing, whereas more localized and intrinsically less smooth deformations require a finer spacing.

Despite the smooth nature of B-spline FFD, it is not guaranteed that the resulting deformation will be neither smooth nor invertible in some regions of the image, especially in denser meshes, which may give rise to multiple artifacts in the registered images. To

[2]Operator $\circ$ denotes the Hadamard product.

avoid this, the optimal transformation $\mathbf{T}_{\boldsymbol{\theta}}$ is found by minimizing a cost function H which comprises two competing goals: the first one represents the cost associated with the similarity measure (i.e., the residuals), while the second term corresponds to a regularization term which constrains the transformation to be smooth (Rueckert et al., 1999). Therefore, the registration problem can be posed as finding an optimal parameter set ($\boldsymbol{\theta}$ in Eq. (1.41)) which defines a transformation $\mathbf{T}_{\boldsymbol{\theta}}$ so that:

$$\mathbf{T}^* = \arg\min_{\mathbf{T}} \; H(\mathbf{T}) \equiv \arg\min_{\boldsymbol{\theta}} \; H(\boldsymbol{\theta}). \tag{1.42}$$

As stated in Section 1.1, we have resorted to GW registration methodologies due to their benefits with respect to PW approaches. Accordingly, the transformation $\mathbf{T}_{\boldsymbol{\theta}}$ will not provide a direct mapping between the images themselves, but to a reference common framework built from the whole image set as represented in Fig. 1.8.

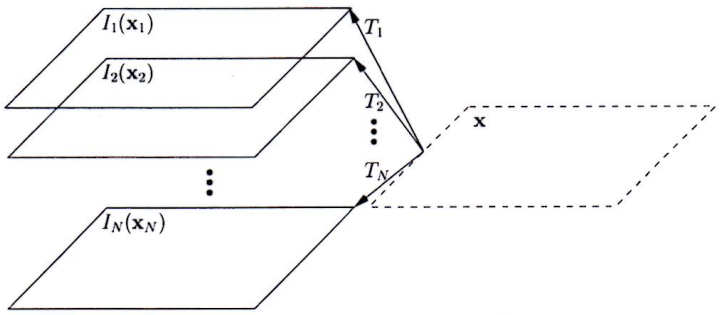

Figure 1.8: GW registration graphical representation

To constrain the transformation to be smooth, we have resorted to a thin-plate penalty term composed by the first and second order spatial derivatives of the transformation displacements. Eq. (1.43) poses the formulation to be solved for the GW DWI registration:

$$\mathbf{T} = \arg\min_{\mathbf{T}} \int_{\chi} \left(V(\mathbf{x}, \mathbf{T}) + \sum_{b=0}^{N_b} \sum_{l=1}^{L} \lambda_1 \left(\sum_{l'=1}^{L} \left(\frac{\partial T_l(\mathbf{x}, b)}{\partial x_{l'}} \right)^2 \right) + \lambda_2 \left(\sum_{l'=1}^{L} \sum_{l''=1}^{L} \left(\frac{\partial^2 T_l(\mathbf{x}, b)}{\partial x_{l'} \partial x_{l''}} \right)^2 \right) \right) d\mathbf{x}, \tag{1.43}$$

with L the dimensionality of the problem (2D or 3D). In our case, DWI registration, derivatives have been approximated by finite differences both in the spatial dimension $\mathbf{x}$ and in the *b-value* coordinate (b).

Basically, the solution for $\boldsymbol{\theta}$ is found by seeking the minimum of the function H in the LS sense. The minimum of H is found by setting its derivative to zero:

$$\nabla H(\boldsymbol{\theta}) = 0 \tag{1.44}$$

The solutions to this problem are usually achieved by iterative methods. A simple fast iterative solution is the GD where each step is taken as follows:

$$\boldsymbol{\theta}^{j+1} = \boldsymbol{\theta}^{j} - \frac{\mathbf{W}}{|\chi|}\nabla H(\boldsymbol{\theta}^{j}) \tag{1.45}$$

The gradient of the likelihood term $V(\mathbf{x})$ with respect to each of the control points $\theta_{k,n}$ (n indexes the number of image) can be obtained as:

$$\frac{\partial V(\mathbf{x})}{\partial \theta_{k,n}} = \frac{\partial V}{\partial I_n}\sum_{l=1}^{L}\frac{\partial I_n}{\partial x_{n,l}}\frac{\partial x_{n,l}}{\partial \theta_{k,n}}(\mathbf{x}) = 2R(\mathbf{x})J(\mathbf{x}) \tag{1.46}$$

where each term after the first equality corresponds, respectively, to the derivative of the metric with respect to the n-th image, the gradient of the image and the derivative of the transformation (given by Eq. (1.41)) with respect to the control point displacements. The gradient term can also be seen as the product of the residuals (R) by the jacobian (J).

In a similar fashion, we can obtain derivatives with respect to the regularization terms to obtain the gradient of the final cost function. More details are given in Appendix C.

To ensure convergence of the procedure, two conditions have to be met simultaneously: $\frac{1}{KN}||\boldsymbol{\theta}^{j-1} - \boldsymbol{\theta}^{j}|| < \epsilon_T$ & $\frac{1}{|\chi|}(H^{j-1} - H^{j}) < \epsilon_H$, related to the variation in the estimated transformation and the cost function, respectively.

B-spline transformation has been applied over the bounding box of a previously delineated ROI (χ) covering the whole liver in order to diminish computational costs. To avoid possible border discontinuities, a final iteration is performed in which the control point mesh is designed to cover the whole image.

Apart from GD, which is prone to fall into local minima, many optimization algorithms have been proposed in literature, such as the Conjugate Gradient (CG) (Hestenes and Stiefel, 1952), which is a more efficient and commonly used approach. The advantage of CG is that each step in the space of the operator is taken in an orthogonal direction to all previous search directions. This means that convergence is much faster, as no redundant steps are performed. Then, the search directions will comprise an orthonormal basis built on the so-called Krylov subspace. The first direction corresponds to the GD direction, whereas for subsequent iterations the search direction is updated by $J^H J$.

Each iteration of the CG updates the solution along decreasing eigenvalues of $(J^H J)^j$ (Hansen, 2010). Late iterations are associated with smaller eigenvalues (high frequency information) which are more likely to produce amplified noise. For this reason, the number of iterations in CG is commonly set to be small in order to regularize the solution.

1.4.2.3.2 Noise Variance Estimation

Another major issue to be considered in the proposed pipeline is a robust noise estimation since the filtering stages of our method requires the noise variance σ^2 to be known or at least (smoothly) estimated both from the background and the foreground regions.

Noise estimation procedure is also a sensitive step in the pipeline since incorrect noise variance estimates may introduce greater biases than the ones we intend to correct. Widely employed methodologies to estimate stationary σ^2 can be found in Aja-Fernández and Vegas-Sánchez-Ferrero (2016).

The principal source of noise in MR data is the heat source, i.e., the subject or object to be scanned (what is commonly referred to as thermal noise), followed by electronic noise in the receiver chain (Weisskoff et al., 1993; Aja-Fernández and Vegas-Sánchez-Ferrero, 2016), produced by the stochastic motion of free electrons in the coils and by eddy current losses in the patient. There are in general two ways to deal with noise in estimation: first, to include the noise model into the estimation formulation and second, to remove or reduce the noise with some filtering or denoising methodologies. Many authors have precisely introduced Rician statistics in the estimation of diffusion models (Walker-Samuel et al., 2009; Jha and Rodríguez, 2012; Landman et al., 2007) to accurately retrieve ADC estimates, although at the price of significantly increasing computational complexity. On the other hand, denoising techniques (Aja-Fernández et al., 2008; Manjón, José V and Coupé, Pierrick and Concha, Luis and Buades, Antonio and Collins, D Louis and Robles, Montserrat, 2013; Tristán-Vega et al., 2012; Reischauer and Gutzeit, 2017) have also been developed as preprocessing steps with the purpose of removing the noise-induced bias from the data for the sake of a robust estimation in subsequent stages. For the latter, the most accepted model is to consider that MR magnitude images are corrupted by Rician noise (Sijbers et al., 1998; Aja-Fernández and Vegas-Sánchez-Ferrero, 2016). This is a common assumption in MRI, mostly valid for single-coil acquisitions and multi-coil imaging, like SENSE (Pruessmann et al., 1999), for instance. In the former, noise depends on a single scalar parameter σ while on the later, noise can become non-stationary, i.e., the variance of noise will depend on the position $\sigma(\mathbf{x})$. Nonetheless, many data processing techniques still assume stationary distributions as a model.

It is usually argued that these noise-induced biases do not seriously affect MR images and an identically distributed signal-independent Gaussian model is commonly assumed. However, this may not be suitable when performed over images with relative low SNR, which is the case in DW-MRI in higher *b-values* (Thunberg and Zetterberg, 2007), since it may lead to the introduction of a noise-induced bias which will alter subsequent estimations. Therefore, for the non-stationary Rician case, a more complex noise estimation step is needed due to the spatially variant nature of the noise variance $\sigma^2(\mathbf{x})$. We have resorted to a method proposed in Pieciak et al. (2017); Aja-Fernández et al. (2014), that uses a VST which transforms the magnitude data from a signal-dependent noise to an independent one. Afterwards, the spatial variability of noise has been retrieved by a homomorphic filtering. This procedure is able to estimate the spatially variant noise maps using only a single image at fixed *b-value*, which is the case considered here.

The main goal of a VST is to compensate for the change of the variance with respect to the change of the mean value (whenever this relationship is known) in order to provide a constant variance (Bartlett, 1947). In the case of MRI, this methodology has mainly focused on signal-dependent noise estimation and removal procedures (Maggioni et al., 2013;

Foi, 2011). Concerning our problem, we seek a function that maps non-stationary Rice data to its stationary Gaussian distributed counterpart. Then, by performing a suitable homomorphic filtering, we can retrieve the original non-stationary noise map.

Let M denote a Rician random variable ($M \geq 0$) with non-centrality parameter A and scale parameter σ (i.e., $M \propto \text{Rice}(A, \sigma)$, whose PDF is defined as:

$$p(M|A,\sigma) = \frac{M}{\sigma^2} \exp\left(-\frac{M^2+A^2}{2\sigma^2}\right) I_0\left(\frac{MA}{\sigma^2}\right) \tag{1.47}$$

where I_0 is the modified Bessel function of the first kind and zeroth order.

We propose the parameterization of the stabilization transformation as:

$$f_{\text{stab}}(M|\sigma,\boldsymbol{\theta}) = \sqrt{\max\left\{\theta_1^2 \frac{M^2}{\sigma^2} - \theta_2, 0\right\}}, \tag{1.48}$$

with $\boldsymbol{\theta} = (\theta_1, \theta_2)$ a parameter vector whose coefficients are to be estimated so that the result of this VST is a normal random variable with unitary variance; specifically, this can be efficiently achieved by using numerical optimization procedures (Nelder and Mead, 1965) for the minimization of a cost function defined as follows:

$$\begin{aligned} G(f_{\text{stab}}(M|\sigma,\boldsymbol{\theta})) = \lambda_1(1 - \text{Var}\{f_{\text{stab}}(M|\sigma,\boldsymbol{\theta})\})^2 + \lambda_2(\text{Skewness}\{f_{\text{stab}}(M|\sigma,\boldsymbol{\theta})\})^2 + \\ + \lambda_3(\text{Kurtosis}\{f_{\text{stab}}(M|\sigma,\boldsymbol{\theta})\} - 3)^2, \end{aligned} \tag{1.49}$$

where the variance, skewness and kurtosis are substituted by the sampling moments obtained from observations of the transformation. Then, the aforementioned parametric VST is applied to the noisy magnitude MR image $I(\mathbf{x})$:

$$I_{\text{stab}}(\mathbf{x}) = \widehat{\sigma_0(\mathbf{x})} \cdot f_{\text{stab}}(I(\mathbf{x})|\widehat{\sigma_0(\mathbf{x})}, \boldsymbol{\theta}_{\text{opt}}(\mathbf{x})), \tag{1.50}$$

where $\widehat{\sigma_0(\mathbf{x})}$ is a prior noise map.

Once the data is stabilized, we can use a non-stationary Gaussian noise variance estimator. In this work, we will make use of the Gaussian homomorphic approach proposed in Aja-Fernández et al. (2014), since it has proved its accuracy and robustness. We assume the image to be a noise-free component $A(\mathbf{x})$ corrupted with additive Gaussian distributed noise $N(\mathbf{x}; 0, \sigma^2(\mathbf{x}))$ with zero mean and spatially variable variance $\sigma^2(\mathbf{x})$.

$$I_{\text{stab}}(\mathbf{x}) \approx A(\mathbf{x}) + \sigma(\mathbf{x}) N(\mathbf{x}; 0, 1). \tag{1.51}$$

Now, we have adopted the homomorphic approach to separate the low-frequency noise map $\sigma(\mathbf{x})$ in Eq 1.51. First, the mean is removed from the magnitude of variance-stabilized MR image $I_{\text{stab}}(\mathbf{x})$ by means of a bilateral filter (Tomasi and Manduchi, 1998). Then, if we apply the logarithm over the data:

$$\log|I_C(\mathbf{x})| = \log|I_{\text{stab}}(\mathbf{x}) - \mathbb{E}(I_{\text{stab}}(\mathbf{x}))| = \log\sigma(\mathbf{x}) + \log|N(\mathbf{x}; 0, 1)|, \tag{1.52}$$

we can separate the low-frequency component with a simple lowpass filter due to the multiplicative character of the noise. Therefore, if we assume $|N(\mathbf{x}; 0, 1)|$ follows a half-Gaussian distribution, we can consider the lowpass filtering a good approximation to the mean:

$$\mathrm{LPF}\{\log |I_C(\mathbf{x})|\} \approx \log \sigma(\mathbf{x}) + \log \sqrt{2} - \frac{\gamma_e}{2}, \tag{1.53}$$

where LPF is a low-pass filter and γ_e the Euler-Mascheroni constant. Finally, Eq. 1.53 leads to a spatially variant noise estimator defined as follows:

$$\widehat{\sigma(\mathbf{x})} \approx \frac{1}{\sqrt{2}} \exp\left(\mathrm{LPF}\{\log |I_C(\mathbf{x})|\} + \frac{\gamma_e}{2}\right). \tag{1.54}$$

We have restricted the proposed spatially variant noise estimator to operate only over a predefined ROI over the liver since adjacent organs may also affect noise estimation.

1.5 Thesis Overview

The following list of publications, also sketched in Figure 1.1, summarizes the scientific production of the Thesis. The main contributions and limitations of the described approaches and future research lines are presented in Chapter 10.

1.5.1 List of Publications

Core publications

- **Chapter 2 :** Sanz-Estébanez, S., Cordero-Grande, L., Sevilla, T., Revilla-Orodea, A., de-Luis-García, R., Martín-Fernández, M. and Alberola-López, C. (2018). Vortical features for myocardial rotation assessment in hypertrophic cardiomyopathy using cardiac tagged magnetic resonance. *Medical Image Analysis*, 47:191-202.
- **Chapter 3:** Sanz-Estébanez, S., Rabanillo, I., Royuela-del-Val, J., Aja-Fernández, S. and Alberola-López, C. (2018). Joint groupwise registration and ADC estimation in the liver using a b-value weighted metric. *Magnetic Resonance Imaging*, 46:1-9.
- **Chapter 4:** Sanz-Estébanez, S., Pieciak, T., Alberola-López, C. and Aja-Fernández, S. (2018). Robust estimation of the apparent diffusion coefficient invariant to acquisition noise and physiological motion. *Magnetic Resonance Imaging*, 53:123-133.

Conference/Workshops papers

- **Chapter 5:** Sanz-Estébanez, S., Cordero-Grande, L., Aja-Fernández, S., Martín-Fernández, M. and Alberola-López, C. (2016). Spatial and spectral anisotropy in HARP images: an automated approach. In *Proceedings of the 13th IEEE International Symposium on Biomedical Imaging: From Nano to Macro*, pp:1105-1108, Prague, Czech Republic.

- **Chapter 6:** Sanz-Estébanez, S., Royuela-del-Val, J., Merino-Caviedes, S., Revilla-Orodea, A., Sevilla, T., Cordero-Grande, L., Martín-Fernández, M. and Alberola-López, C. (2016). An automated tensorial classification procedure for left ventricular hypertrophic cardiomyopathy. In *Proceedings of the 4th International Conference on Bioinformatics and Biomedical Engineering*, vol:9656, pp:184-195, Granada, Spain.

- **Chapter 7:** Sanz-Estébanez, S., Cordero-Grande, L., Martín-Fernández, M. and Alberola-López, C. (2018). Robust windowed harmonic phase analysis with a single acquisition. In *Proceedings of the 21st International Conference on Medical Image Computing & Computer Assisted Intervention. 1st International Workshop on Thoracic Image Analysis (MICCAI/TIA 2018)*, vol:11040, pp:135-146, Granada, Spain.

- **Chapter 8:** Sanz-Estébanez, S., Peña-Nogales, Ó., de-Luis-García, R., Aja-Fernández, S. and Alberola-López, C. Groupwise non-rigid registration on multiparametric abdominal DWI acquisitions for robust ADC estimation: comparison with pairwise approaches and different multimodal metrics. In *Proceedings of the 14th IEEE International Symposium on Biomedical Imaging: From Nano to Macro*, pp:1156-1159, Melbourne, Australia.

- **Chapter 9:** Sanz-Estébanez, S., Royuela-del-Val, J., Broncano-Cabrero, J., Aja-Fernández, S. and Alberola-López, C. ADC-weighted joint registration-estimation for cardiac diffusion magnetic resonance imaging. In *Proceedings of the XXXV Annual Congress of the Spanish Society of Biomedical Engineering (CASEIB 2017)*, pp:41-44, Bilbao, Spain.

Additional publications not included in this Thesis

- Sanz-Estébanez, S., Merino-Caviedes, S., Sevilla, T., Revilla-Orodea, A., Martín-Fernández, M. and Alberola-López, C. Cardiac strain assessment for fibrotic myocardial tissue detection in left ventricular hypertrophic cardiomyopathy. In *Proceedings of the XXXIII Annual Congress of the Society of Biomedical Engineering (CASEIB 2015)*, pp:5-8, Madrid, Spain.

- Cordero-Grande, L., Royuela-del-Val, J., Sanz-Estébanez, S., Martín-Fernández, M. and Alberola-López, C. (2016). Multi-oriented windowed harmonic phase reconstruction for robust cardiac strain imaging. *Medical Image Analysis*, 29:1-11.

- Sanz-Estébanez, S., Royuela-del-Val, J., Sevilla, T., Revilla-Orodea, A., Aja-Fernández, S. and Alberola-López, C. Harmonic auto-regularization for non rigid groupwise registration in cardiac magnetic resonance imaging. In *Proceedings of the XXXIV Annual Congress of the Spanish Society of Biomedical Engineering (CASEIB 2016)*, pp:10-13, Valencia, Spain.

- Royuela-del-Val, J., Godino-Moya, A., Menchón-Lara, RM., Sanz-Estébanez, S., Simmross-Wattenberg, F., Martín-Fernández, M. and Alberola-López, C. (2018).

Joint non-rigid motion and image MRI SENSE reconstruction. In *Proceedings of the 26th Annual Meeting of the International Society of Magnetic Resonance in Medicine*, p:4107, Paris, France.

- Rabanillo, I., Sanz-Estébanez, S., Aja-Fernández, S. Hajnal, J., Alberola-López, C. and Cordero-Grande, L.,(2018). Joint image reconstruction and phase corruption maps estimation in multi-shot echo planar imaging. In *Proceedings of the 21st International Conference on Medical Image Computing & Computer Assisted Intervention. 1st Workshop on Computational Diffusion MRI (MICCAI/CDMRI 2018)*, Granada, Spain.

- Sanz-Estébanez, S., Moya-Sáez, E., Royuela-del-Val, J. and Alberola-López, C. On the construction of non linear adjoint operators: application to L1-penalty dynamic image reconstruction. In *Proceedings of the XXXVI Annual Congress of the Spanish Society of Biomedical Engineering (CASEIB 2018)*, pp:3-6, Ciudad Real, Spain.

Chapter 2

Vortical Features for Myocardial Rotation Assessment in Hypertrophic Cardiomyopathy using Cardiac Tagged Magnetic Resonance

Published as:

Sanz-Estébanez, S.[1], Cordero-Grande, L.[2], Sevilla, T.[3], Revilla-Orodea, A.[3], de-Luis-García, R.[1], Martín-Fernández, M.[1] and Alberola-López, C.[1] (2018). Vortical features for myocardial rotation assessment in hypertrophic cardiomyopathy using cardiac tagged magnetic resonance. *Medical Image Analysis*, 47:191-202.

[1] Laboratorio de Procesado de Imagen, Department of Teoría de la Señal y Comunicaciones e Ingeniería Telemática, ETSIT, Universidad de Valladolid, Campus Miguel Delibes s.n., 47011, Valladolid, Spain.

[2] Centre for the Developing Brain and Department of Biomedical Engineering, Division of Imaging Science and Biomedical Engineering, King's College London, St Thomas' Hospital, SE1 7EH, London, U.K.

[3] Unidad de Imagen Cardiaca , Hospital Clínico Universitario de Valladolid, CIBER de enfermedades cardiovasculares (CIBERCV), 47005, Valladolid, Spain.

Left ventricular rotational motion is a feature of normal and diseased cardiac function. However, classical torsion and twist measures rely on the definition of a rotational axis which may not exist. This paper reviews global and local rotation descriptors of myocardial motion and introduces new curl-based (vortical) features built from tensorial magnitudes, intended to provide better comprehension about fibrotic tissue characteristics mechanical properties. Fifty-six cardiomyopathy patients and twenty-two healthy volunteers have been studied using tagged magnetic resonance by means of harmonic phase analysis. Rotation descriptors are built, with no assumption about a regular geometrical model, from different approaches. The extracted vortical features have been tested by means of a sequential cardiomyopathy classification procedure; they have proven useful for the regional characterization of the left ventricular function by showing great separability not only between pathological and healthy patients but also, and specifically, between heterogeneous phenotypes within cardiomyopathies.

Keywords: Myocardial Rotation; Tagged Magnetic Resonance; Vortical Features; Hypertrophic Cardiomyopathy

2.1 Introduction

HCM (Maron et al., 2014) is a relatively common heart muscle disease with a heterogeneous phenotypic expression that occasionally overlaps with other pathologies that also present LV hypertrophy. Differentiating the underlying etiology of the ventricular hypertrophy is a frequent clinical problem with relevant implications since each etiology needs a specific management and presents a different prognosis. HCM is characterized by a hypertrophied and nondilated LV (Baron, 2008), often with an asymmetrical wall thickness distribution. HCM occurs in the presence of myocyte hypertrophy and interstitial and replacement fibrosis, which cause the walls of the ventricles to thicken (Maron et al., 1992) and a reduction on the cavity volume is usually observed. This thickening may block blood flow out of the ventricle. Therefore, the main features of a HCM heart summarize in increased LV mass and thickened walls, especially in the interventricular septum (Urbano-Moral et al., 2014). These abnormalities lead to altered forces revealing a significant reduction in the diagonal components of the strain (Saltijeral et al., 2010). Previous studies have shown that regional LV dysfunctions predate over the morphologic changes related with the phenotypic expression of hypertrophy and obstruction (Dhillon et al., 2014).

As previously stated, etiological factors are of great importance in the CVD detection (Maron et al., 2006). Global indices, such as the global longitudinal strain (Shimon et al., 2000), have been employed for CVD identification, reporting noticeable prognostic value; however, local measurements could provide more insight to the behavior of fibrotic tissue (Piella et al., 2010). In this direction, it has been hypothesized that the presence of greater myocardial twist may be associated with a greater degree of myocardial fibrosis in HCM patients. Consequently, assessment of LV rotation mechanics as a characteristic of cardiac function may help differentiate the presence of fibrosis (Young and Cowan, 2012). Consistently with these studies, we adhere to the appropriateness of local analyses and their clinical value on the basis that most heart diseases typically affect localized regions of the myocardium. In addition, local studies can be used to improve cardiac analytics, which may help predict the effects of specific CVD on the tissue.

Rotation parameters have recently gained increasing attention due to their simplicity and ease of quantification; they constitute interesting measures of cardiac performance which provide additional information on myocardial mechanics as a complement of standard pump function indices (Rüssel et al., 2009a). However, most of the rotation parameters described in the literature implicitly require an accurate description of a RA. The center of mass given by myocardial boundaries is widely used as such; however, the heart can translate during the cardiac cycle, which commonly results in misalignments of the center along subsequent frames, incurring in estimation errors. Hence, non biased calculation methods, which compensate centroid motion, are mandatory for the use of LV torsion as a measure of myocardial dysfunction quantification (Sengupta et al., 2008). Still, additional drawbacks have been reported; Young et al. (1994) state that, for HCM, the RA is shifted from the LV center of mass towards the inferoseptal region. In addition,

for HCM patients, due to their characteristic asymmetrical wall thickness distribution, accurate centroid estimation could become a extremely challenging task.

Imaging techniques provide essential information for the study of these pathologies; several modalities have been proposed in an effort to measure advanced cardiac mechanics in the LV: speckle tracking echocardiography (Helle-Valle et al., 2005; Bansala and Kasliwalb, 2013), DENSE MRI (Zhong et al., 2010) or traditional cine SSFP MRI, combined with feature tracking techniques,(Heermann et al., 2014), to mention a few. Nevertheless, myocardial tissue tagging with cardiovascular magnetic resonance is currently the gold standard for assessing regional myocardial function (Shehata et al., 2009). If it is not widely used in the daily practice is because it is time consuming, but to date is an accurate method to measure regional contractility (Jeung et al., 2012). MR-T (Ibrahim et al., 2016) is usually performed by spatial magnetization modulation SPAMM (Axel and Dougherty, 1989) or a variant of this technique. SPAMM is grounded on the ability of altering the magnetization of the tissue (within the limitations of relaxation times in MR) even in the presence of motion. The tagging procedure is based on the superposition of a spatial modulation over the applied gradients which may be subsequently tracked throughout the cardiac cycle, from which the cardiac function can be assessed.

HARP based methods (Osman et al., 2000) are widely used as a ME technique in MR-T. These methods are capable of reconstructing displacement fields accurately, grounded on the assumption of constant local phase, which turns out to be more reliable than the constant pixel brightness assumption. This approach is based on the use of SPAMM tag patterns, which modulate the underlying image, producing a set of spectral peaks in the Fourier domain. Each of these spectral peaks carry information about a particular component of tissue motion, and this information can be extracted using phase demodulation methods, obtaining tensorial descriptors of deformation and, for our case, rotation estimations.

Curl is a differential operator that describes the infinitesimal rotation of a vector field. Its direction determines the RA while its magnitude shows the amount of rotation. The term vortex is commonly associated to a localized increased value on the magnitude of the given curl vector (this property will be hereafter referred to as vorticity). The local rotation measured by the curl operator should not be confused with the bulk angular velocity vector observed within the myocardial tissue with respect to a fixed cardiac axis.

Numerous 4D phase-contrast MRI (Köhler et al., 2013) studies have made use of the curl operator. Flow vortical patterns in the heart chambers, the aorta, the carotid sinus and pulmonary circulation are physiological, but can also be related to certain pathologies including aortic aneurysms, pulmonary hypertension and congenital heart defects. Vortical patterns often occur because of morphological alterations, vessel widening or after stenosis (von Spiczak et al., 2015). These structures may alter the pressure and shear forces on the walls and trigger processes leading to cell death.

It is our understanding that curl can also quantify the local rotation within the muscle. Consequently, in this paper we introduce a novel local rotation descriptor based on robust tensorial measurements that relates the presence of increased vorticity values with the

hypertrophic tissue in the heart. Rotation is estimated without influence of global myocardial parameters, such as axis of rotation or cavity radius, allowing a regional comparative study in patients with LV hypertrophy of different etiologies; HCM and Secondary forms of LV Hypertrophy SLVH, as well as healthy subjects. To the best of our knowledge, this is the first study that relates local vortices in myocardial tissue with the presence of fibrosis.

2.2 Materials and Methods

2.2.1 Materials

For the validation of the proposed approach, our study is a retrospective analysis based on a database of patients who underwent the ordinary clinical protocol according to their symptoms; the database consisted in 78 individuals who were affected by either primary HCM or SLVH (hypertensive heart disease, aortic stenosis or athlete heart disease) or were healthy volunteers. The number of pathologic patients was 56; 39 of them, with ages from 30 to 86, were diagnosed as primary HCM. These patients showed hypertrophy, predominantly in the septal region of the LV. Following the same protocol, 17 patients were diagnosed of SLVH according to chronic pressure overload. The differential diagnosis between primary HCM and SLVH was based on previous echocardiopraphic studies and clinical and familial records. About the healthy volunteers, 22 were included in the study with ages between 16 and 84; these subjects underwent the MRI protocol because of a previous suspicion of cardiac pathology but all of them turned out to be healthy.

All subjects signed the ordinary informed consent for the MR session and agreed in writing to share the resulting images for research purposes. Personal data were treated according to current legislation. Demographic data of both controls and cases, the latter indexed by pathology type, are given in Table 2.1.

Table 2.1: Demographic data of the pathologic and healthy patients in the study (mean ± std).

Patients	HCM	SLVH	Healthy Vol.
Number of cases	39	17	22
Age	58 ± 16.3	69.8 ± 10.5	49.2 ± 21.8
Sex (M/F)	27/12	12/5	14/8
Ejection Fraction (%)	70.4 ± 5.4	69.7 ± 6.1	63.6 ± 6.5
Diastolic LV volume (ml)	140.6 ± 22.8	131 ± 50.3	150.3 ± 31.5
Systolic LV volume (ml)	42 ± 9	41.8 ± 22.4	53.8 ± 13.9
Wall thickening (%)	78.4 ± 20.1	79.8 ± 18.6	89.6 ± 16.9

We have acquired SA and LA MR-T datasets for each patient, from apex to ba-

se, using a MR C-SPAMM SENSE TSE sequence on a Philips Achieva 3T scanner. Regarding the tagging parameters, we validate the method for a fixed tag spacing of $k_i = 1/\lambda$, with $\lambda = 7$ mm using two different orientations $\mathbf{U_i} = (cos(\theta_i); sin(\theta_i))$ with $\theta = [\pi/4; 3\pi/4]$ for the stripe directions.

Additionally, we have also acquired a B-SSFP SA MR-C sequence at the same spatial location for each patient; snapshots of the acquired sequences are shown in Fig. 2.1. The myocardium has been segmented in the ED phase of the MR-C sequence by two cardiologists. Cine segmentations are used to align the tagging orientations to a common reference system to correct for patient motion. The ED segmentation is used to define a ROI in which to compute meaningful measurements. Resolution details about these sequences are included in Table 2.2.

Table 2.2: Details on the sequences of MR images used in the paper. Δ_p: Reconstructed Pixel Resolution (mm). Δ_s: Slice Thickness (mm). N_p: Number of pixels for dimension. N_t: Number of Temporal Phases. N_s: Number of slices. T_R: Repetition Time (ms). T_E: Echo Time (ms). α: Flip Angle (degrees).

Parameters	Δ_p	Δ_s	N_p	N_t	N_s	T_R	T_E	α
MR-T SA	1.21-1.32	10	256-432	16-25	10-15	2.798-6.154	1.046-3.575	7-25
MR-C SA	0.96-1.18	8-10	240-320	30	10-15	2.902-3.918	1.454-2.222	45
MR-T LA	1.21-1.34	10	240-340	15-27	1-3	2.903-4.507	1.097-2.897	10-45
MR-C LA	0.98-1.25	8-10	256-448	30	1-3	2.858-3.529	1.251-2.132	45

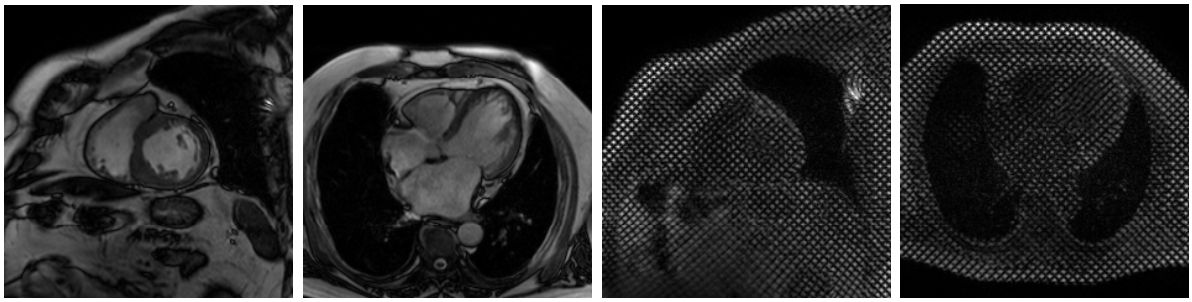

Figure 2.1: Example images of the sequences acquired for the study. MR-C SA, MR-C LA, MR-T SA and MR-T LA, from left to right.

2.2.2 Methods

2.2.2.1 Preprocessing

We have implemented a preprocessing pipeline in order to (a) propagate the ROI in MR-C from ED to the ES phase —in which subsequent calculations will be carried out— and (b) align the MR-C and MR-T sequences at ES. These two steps are:

- Registration

  The MR-C sequence is processed by means of a GW elastic registration procedure (Cordero-Grande et al., 2013a) in order to propagate the ED segmentations towards ES phase. The transformation is achieved by B-spline based FFD (Rueckert et al., 2006). A GD optimization scheme is performed where the SSD of image intensities is used as registration metric. A smoothness penalty term has also been introduced to constrain the spline-based FFD transformation to be smooth.

- Alignment

  An affine registration method is performed to align MR-T and MR-C images at ES phase. The MR-T sequence has been detagged by means of a homomorphic filtering procedure (Makram et al., 2015) prior to the alignment process.

2.2.2.2 Motion estimation

3D HARP motion reconstruction using the C-SPAMM technique requires a minimum of 3 linearly independent wave vectors (Osman et al., 2000). We have extended the aforementioned HARP methodology for the computation of the deformation gradient tensor using SA and LA images on the intersection of the slices as shown in Fig. 2.2. For points on which LA images were not available, 2D motion has been reconstructed.

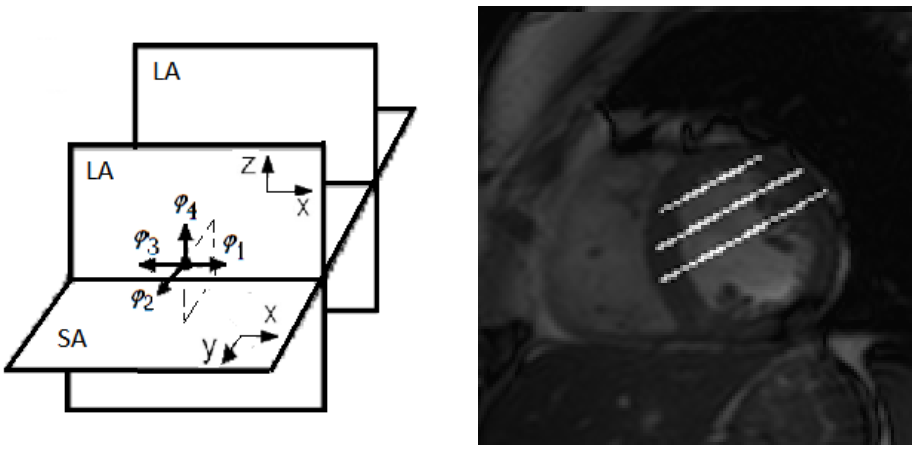

Figure 2.2: The figure on the left sketches the proposed 3D HARP motion reconstruction scheme for the intersected points between SA and LA planes, which are shown in the figure on the right over the SA.

The ME technique is based on the extraction of the local phase of the grid pattern according to the method presented in Cordero-Grande et al. (2011, 2016). A WFT is applied to the image at ES phase. The WFT provides a representation of the image spectrum in the surroundings of each pixel of the original image, so HARP band pass filtering techniques can be directly applied on the spatially localized spectrum of the image. To

adequately retrieve the shape of the spectral peaks, we have resorted to an anisotropic filtering approach combining Gaussian band-pass and all-pass filters as proposed in Sanz-Estébanez et al. (2017). Finally, each of the image phase $\varphi_i(\mathbf{x})$ (two for each plane) can be extracted in the spatial domain from the IWFT of the aforementioned filtered spectrum.

As mentioned before, we have extended the HARP methodology by allowing the estimation of motion under the application of a set of four wave vectors. Therefore, 3D deformation gradient tensor can be robustly recovered at the intersection points of both axes, by applying the methodology presented in Cordero-Grande et al. (2016). The material deformation gradient tensor $\mathbf{F}(\mathbf{x})$ can be estimated from the gradient of the phase image as stated in Osman et al. (2000) as:

$$\mathbf{K} = \frac{\partial \varphi}{\partial \mathbf{x}}(\mathbf{x})\mathbf{F}(\mathbf{x}) = \mathbf{Y}(\mathbf{x})\mathbf{F}(\mathbf{x}), \tag{2.1}$$

where $\mathbf{K}$ represents the two stripe orientations of four given wave vectors corresponding to each tagged image. Robust estimation of $\mathbf{F}(\mathbf{x})$ is achieved through LAD procedure. The reconstruction is performed via Iterative Reweighted Least Squares (IRLS):

$$\mathbf{F}_{l+1}(\mathbf{x}) = (\mathbf{Y}^T(\mathbf{x})\mathbf{W}_l(\mathbf{x})\mathbf{Y}(\mathbf{x}))^{-1}\mathbf{Y}^T(\mathbf{x})\mathbf{W}_l(\mathbf{x})\mathbf{K}, \tag{2.2}$$

with $\mathbf{W}_l(\mathbf{x})$ a diagonal weighting matrix, which is updated at each iteration by considering fitting residuals (Cordero-Grande et al., 2016).

From this estimated tensor, the main cardiac function characteristics can be obtained through the Lagrangian ST, defined as:

$$\mathbf{E}(\mathbf{x}) = \frac{1}{2}(\mathbf{F}(\mathbf{x})^T\mathbf{F}(\mathbf{x}) - \mathbf{I}). \tag{2.3}$$

The spatial resolution of the reconstructed tensors depends on the width of the HARP band pass filter (Parthasarathy and Prince, 2003, 2004); the HARP method is upper limited by half of the tag spacing (small deformation assumption). However, WHARP methods (Sanz-Estébanez et al., 2017; Cordero-Grande et al., 2016) try to accommodate the band pass filter to the the local frequency of the signal in order to approach to the maximum achievable resolution. Therefore, effective HARP resolution will vary dynamically, allowing large deformations, as those observed at ES, being captured at a maximal scale of 1.5 times half the tag spacing.

These tensors have been calculated at ES, where the greatest deformation along the cardiac cycle takes place.

2.2.2.3 Rotation parameters

In addition to thickening and shortening, the myocardium also undergoes a wringing motion during systolic phases due to the obliquely oriented subendocardial and subepicardial myofibers. Many descriptors have been proposed to measure this motion that rely on either global information derived from simplified anatomical models or on tensorial strain and deformation magnitudes built from local motion estimates.

Measures based on global information

It is well known that the LV apex globally rotates anticlockwise at a relatively constant rate throughout systole. On the contrary, the base, initially rotating anticlockwise, reverses direction providing a net clockwise rotation at ES phase. The resulting difference of these two motions is defined as twist, defined to be positive by convention (Young and Cowan, 2012).

There is currently a lack of standardization for methods used to characterize the global LV twisting motion. These descriptors rely on geometrical models of the heart for torsion and twist calculation. Consequently, both a well-defined fixed RA and regular myocardial radii over the whole heart are mandatory. For example, torsion has been traditionally calculated as relative rotation in degrees (Lorenz et al., 2000), rotation per length in degrees/mm, torsional shear angle, also in degrees (Buchalter et al., 1990), and longitudinal-circumferential shear strain (dimensionless) (Fung, 1965). Traditional rotation indices are obtained by vectorial product between position vectors at ES $\mathbf{u}_{\vec{ES}}$ and ED $\mathbf{u}_{\vec{ED}}$ phases as:

$$sin(\beta) = \frac{|\mathbf{u}_{\vec{ED}} \times \mathbf{u}_{\vec{ES}}|}{|\mathbf{u}_{\vec{ED}}||\mathbf{u}_{\vec{ES}}|}. \tag{2.4}$$

As stated above, twist computation depends on the exact locations of the apical and basal slices and requires accurate MC, specially for centroid motion correction. Twist per unit length is also widespread, since torsion is relatively constant in the longitudinal direction (Young and Cowan, 2012). Nonetheless, this measure does not scale appropriately between hearts of different sizes and we have not observed a significant complementary value with respect to the twist.

The torsional shear angle is a measure of the change in angle between line segments which are initially aligned with the anatomical axes of the LV. Many studies have used the formula given by Aelen et al. (1997). However, it has been demonstrated that it usually overestimates deformation (Rüssel et al., 2009b), so we have resorted to an unbiased alternative formula based on circumferential displacements:

$$T = \frac{(\beta_{apex} r_{apex} - \beta_{base} r_{base})}{D}, \tag{2.5}$$

where D is the distance between selected segments.[1] However, HCM characteristic endocardial irregularities may hinder the accurate estimation of both the myocardial radius and the axis, which are crucial in this formulation.

[1]Rotation parameter β has been pixelwise estimated; therefore, rotation measures expressed on (2.5) are referred to the median of the rotation distribution on basal and apical segments.

Tensorial descriptors

Another important group of rotation descriptors focus on the properties of the tissue that provide localized characterization of the motion by tensorial analysis. As stated in solid mechanics (Fung, 1965), the 3D strain state at any point in a body can be fully represented by three diagonal strains and three shear strains. From them, the longitudinal-circumferential shear (E_{lc}) is a useful measure closely related to torsion. According to this analysis, local torsion measures can be defined, i.e., the 3D local torsion shear can be given by:

$$sin(\theta_{lc}) = \frac{2E_{lc}}{\sqrt{1+2E_{cc}}\sqrt{1+2E_{ll}}}, \tag{2.6}$$

where E_{cc} and E_{ll} represent the circumferential and longitudinal strains, respectively; these components can be obtained by straightforward operations on the Cartesian components in (2.3). Nevertheless, shear strains are several magnitudes lower than diagonal strains, so factors other than inotropic state may greatly affect its estimation (Petitjean et al., 2005).

Angular variation between two states of stress in the plane in Cartesian coordinates can be expressed by a single angle ϕ as stated in Fung (1965):

$$tan(2\phi) = \frac{2\varepsilon_{xy}}{\varepsilon_{xx} - \varepsilon_{yy}}, \tag{2.7}$$

where ε represents the Cauchy's ST ($\boldsymbol{\varepsilon}$) directly related with the stress tensor by the Lamé parameters (Fung, 1965). Particular values of ϕ show angular variation of stress principal directions between both states (ES and ED phases).

Additionally, in Cordero-Grande et al. (2013b) a novel rotation parameter has been proposed built from the (longitudinal) transformation that suffers a local coordinate at ED through time in the **LR** plane as given by the material deformation gradient tensor **F**.

$$\alpha^{LRl} = arctan(-F_{lr}/F_{ll}). \tag{2.8}$$

Our work ellaborates on vortical patterns widely employed for the identification of abnormal flow patterns. Nonetheless, the term vortex bears different interpretations as defined in the literature. For most flow studies performed in clinical practice, the term vortex denotes rotating motion, where stream or pathlines tend to curl back on themselves (Markl et al., 2011). In fluid dynamics, a vortex is a region in a fluid in which the flow is rotating around an axis line, which may be straight or curved. More explanatory notes on the theoretical definition of the term vortex can be found in Stalder et al. (2010). In this paper, the term vortex will be used in the solid mechanics context as a local abnormally increased rotation component. In order to find evidence of perturbations within the myocardial tissue, material vortical patterns can then be associated to increased values of an dynamic rotation parameter extracted from the deformation gradient tensor.

The curl of a given deformation field $\mathbf{u}$ describes local spinning vectors (see Fig. 2.3) and can be calculated as:

$$\vec{\omega}(t) = \begin{pmatrix} \omega_x(t) \\ \omega_y(t) \\ \omega_z(t) \end{pmatrix} = \frac{1}{2}\nabla \times \vec{\mathbf{u}}(t) = \frac{1}{2}\begin{pmatrix} \frac{\partial u_z}{\partial y} - \frac{\partial u_y}{\partial z} \\ \frac{\partial u_x}{\partial z} - \frac{\partial u_z}{\partial x} \\ \frac{\partial u_y}{\partial x} - \frac{\partial u_x}{\partial y} \end{pmatrix} = \frac{1}{2}\begin{pmatrix} F_{zy} - F_{yz} \\ F_{xz} - F_{zx} \\ F_{yx} - F_{xy} \end{pmatrix}, \tag{2.9}$$

where F_{ab} represents a component of the material deformation gradient tensor in Cartesian coordinates. Hereinafter, vortical parameters will be expressed in Cartesian coordinates as opposed to the cylindrical coordinates from the ST used in (2.6).

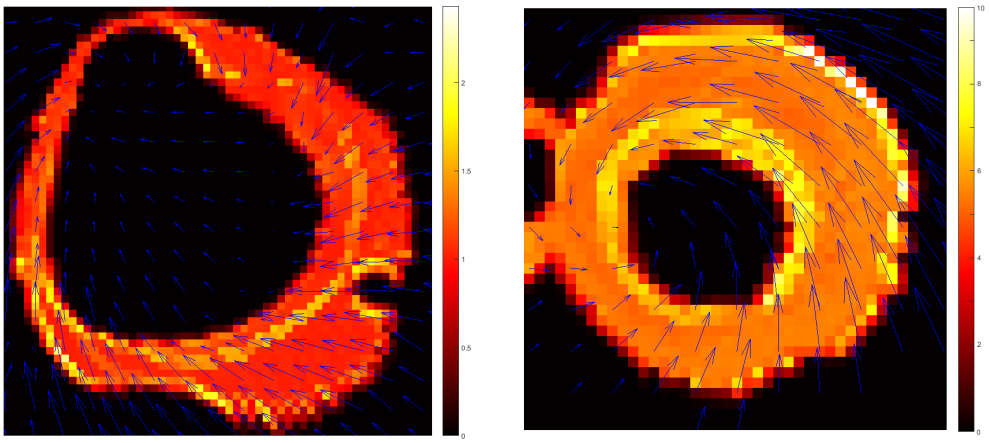

Figure 2.3: Examples of vorticity vector modulus at ES from (2.9) in basal and apical slices, left and right respectively. The arrows show the extracted cardiac displacement field while the colour represents the intensity of vorticity (unitless). Some outliers are observed near the boundaries due to the difficulty of HARP methods in tracking material points in the presence of great intensity changes. Scales are set to best accomodate the range of values on the given cardiac plane, since myocardial rotation varies in modulus and direction along the cardiac axis.

In this paper we hypothesize that local increasing of vorticity values (in modulus) arises within myocardial segments with fibrosis-related perturbations. Nonetheless, high vorticity values, irrespective of the fibrosis degree, are prone to appear in myocardial boundaries, giving rise to multiple outliers in rotation estimation.

These vorticity measures are insensitive to the definition of the rotation axis, although 3D deformations are needed for its proper reconstruction. When LA information is not available, only the longitudinal component (ω_z) of the vorticity vector can be estimated. In addition, if the cardiac axis is not planned properly, vorticity parameters will be estimated with a systematic error related to the angular error of the axis. However, as it is common in clinical practice, we will assume that the main axis of rotation will lie on the LA planes (i.e., will be normal to the SA image planes). Hence, the ω_z component of the vorticity vector provides clinical compliance as it is aligned with the wringing motion of myocardial

fibers. Thus, a phase increment due to the aforementioned local rotation can be extracted by integration:

$$\int_{t_{ED}}^{t_{ES}} \omega_z(t)\mathrm{d}t = \vartheta(t_{ES}) - \vartheta(t_{ED}) = \vartheta(t_{ES}) \approx \frac{\omega_z(t_{ES})}{2}(t_{ES} - t_{ED}). \tag{2.10}$$

This parameter will be referred to as local rotation ϑ. Therefore, twist motion will be approximated as

$$\text{Twist } \vartheta = |\vartheta_{\text{base}} - \vartheta_{\text{apex}}|. \tag{2.11}$$

For comparative purposes, we will also estimate ϑ and β rotation distributions with two other different methodologies. First, we will analyse the capabilities of the elastic registration algorithm described in Section 2.2.2.1 applied to MR-C to detect rotation from the estimated deformation fields. Second, we have employed an atlas-based approach that consists of a spheroidal model (Young and Axel, 1992) fitted at ED and that deforms due to the forces exerted from a stripe tracking procedure (Young et al., 1995) on the MR-T sequence throughout the cardiac cycle. Deformations are formulated from continuous parameter functions which, in addition, include parameterized twisting and rotation axis deformation as given in Park et al. (1996) and, therefore, can be applied to any shape.

2.2.2.4 Classification

We have resorted to a classification method (Sanz-Estébanez et al., 2016b) to assess the discriminating ability of the rotation features previously described. The procedure, sketched in Fig. 2.4, consists in an automated processing pipeline to classify heterogeneous groups of ventricular hypertrophy (and controls) from myocardial functional descriptors. The proposed classification method is grounded on the idea that populations overlap strongly irrespective of the specific features selected for classification if the problem is addressed through a single stage. Our purpose is to classify a sample into one of three classes, namely, control, primary HCM and SLVH. Since secondary hypertrophy patients have subtle differences with respect to the other two classes, we have resorted to a two-stage classification procedure. Thus, we have divided the classification process in three stages and performed a feature selection step for each stage independently, following a sequential methodology that adapts to the characteristics of the population at every stage. Different machine learning methods (both supervised and unsupervised) have been implemented for each stage and all their possible combinations have been tested.

Mechanical descriptors extracted from the aforementioned tensors are an essential part of the classification procedure. We have considered different groups of features. First, the components of the ST in the cylindrical coordinate system $\{\mathbf{R}, \mathbf{C}, \mathbf{L}\}$ are accounted for. We also use twist and torsion features (see Table 2.3) built from the aforementioned rotation parameters as extracted from the MR-T and MR-C sequences, as well as using

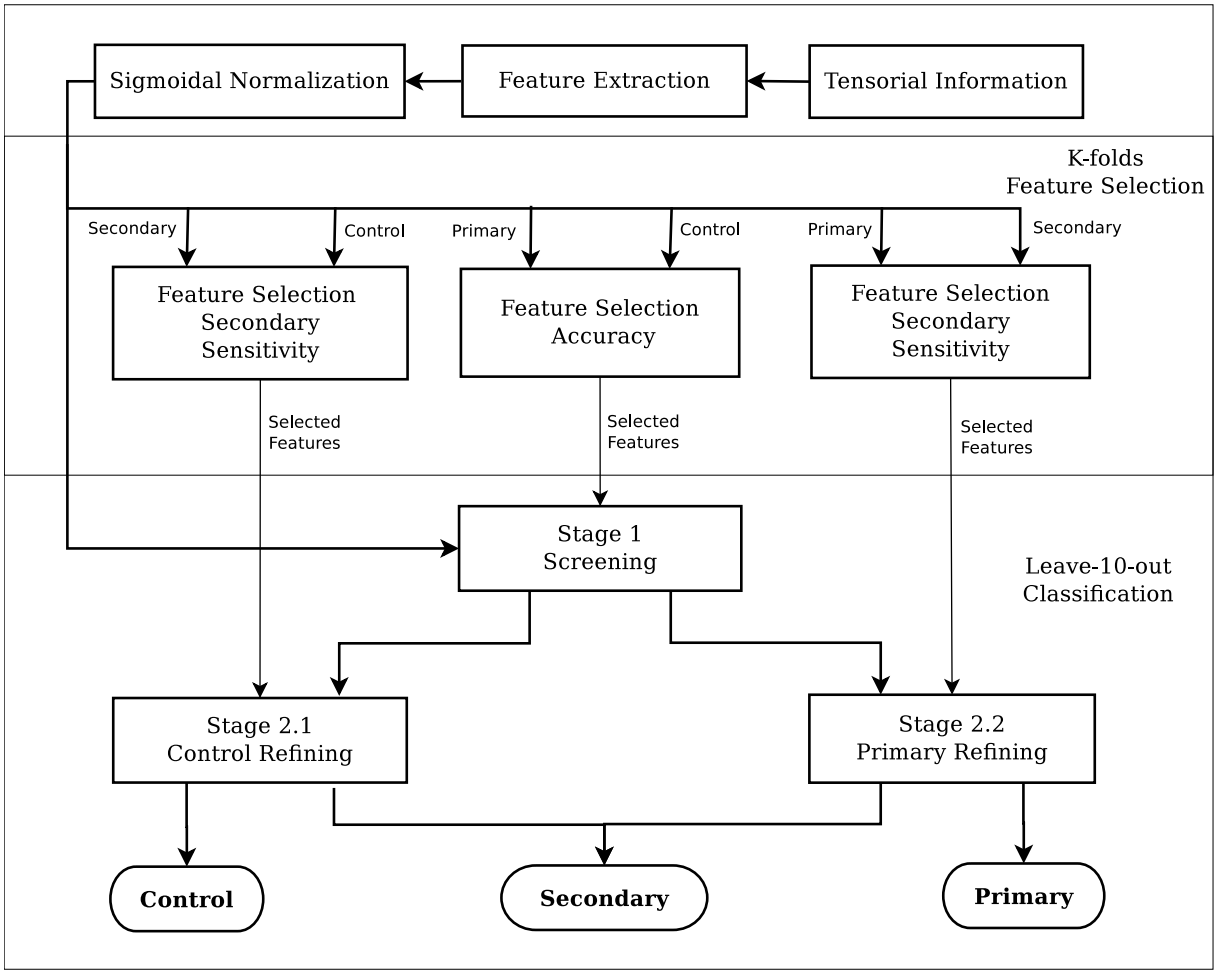

Figure 2.4: Pipeline for the feature selection and classification stages.

the spheroidal model we have previously referred to. Additionally, since some rotation-related components have opposite directions in apex and base, we consider the location of the zero crossing for these components as well.

For the feature extraction step, we have previously selected for each feature the most representative cardiac segments (Cerqueira, 2002) within clinical practice. For twist and torsion descriptors, we have considered septal segments, whereas for tensorial parameters, mid-ventricular or basal segments have been chosen. In Table 2.3 we show the segments involved in the calculation of each of the features; then the overall feature is, for robustness purposes, the median of the distribution within those segments, which will be the input to the classifier. For the twist parameters the feature extracted is the difference between medians on apical and basal septal segments. On the other hand, for the zero crossing parameter, the feature represents the height of the cardiac axis at which the given rotation parameter, estimated slice by slice, changes its sign. Notice that the feature extraction step is grounded on clinical knowledge, i.e., it is not data-driven.

Table 2.3: Cardiac segments involved during the feature extraction stage for each one of the motion descriptors employed in the classification procedure. For each row, only one feature will be extracted, summarizing all the segments indicated below. The extracted features will be the input to the feature selection step, from which the final (survivor) feature vector (from 2 to 5 components) will arise. The number within braces indicates the equation that defines the parameter.

Segment	1	2	3	4	5	6	7	8	9	10	11	12	13	14	15	16	17
E_{rr} (2.3)							✓	✓	✓	✓	✓	✓					
E_{cc} (2.3)							✓	✓	✓	✓	✓	✓					
E_{ll} (2.3)	✓	✓	✓	✓	✓	✓											
E_{lc} (2.3)							✓	✓	✓	✓	✓	✓					
$\|\|\omega\|\|$ (2.9)	✓	✓	✓	✓	✓	✓	✓	✓	✓	✓	✓	✓					
Twist ϑ (2.11)		✓	✓											✓			
Twist β (2.4)		✓	✓											✓			
Twist ϕ (2.7)		✓	✓											✓			
T (2.5)	✓	✓	✓	✓	✓	✓							✓	✓	✓	✓	
α^{LRl} (2.8)		✓	✓					✓	✓					✓			
θ_{lc} (2.6)		✓	✓					✓	✓								
ω_z zero cross. (2.9)	✓	✓	✓	✓	✓	✓	✓	✓	✓	✓	✓	✓	✓	✓	✓	✓	
β zero cross. (2.4)	✓	✓	✓	✓	✓	✓	✓	✓	✓	✓	✓	✓	✓	✓	✓	✓	

As reflected in Fig. 2.4, after feature extraction we carry out a normalization stage in order to diminish the influence of possible outliers. A sigmoidal function, with its scale factor set according to Theodoridis and Koutroumbas (1999), is used to this end. Data are mapped on the interval $(0, 1)$ by imposing a generalized logistic function; outliers will tend to appear at either of the two extremes, while maintaining a linear relation for the rest of the data. Then, normalized features are arranged in vectors with different number of components (2 through 5). All possible combinations of features indicated in Table 2.3 have been tested.

Feature selection and classification performance assessment has been carried out in a similar but sequential manner. For both, data samples have been randomized and a *Leave-10-out* method has been applied; the proportions of control/primary/secondary have been kept unaltered along trials. Specifically, for feature selection in the first classification stage, we classify the samples in controls and primaries and calculate the accuracy; the feature set with the highest figure is selected for this stage. In parallel, and for the second stage, controls and secondaries are classified on one branch (left branch) and primaries and secondaries on the other branch. In this case, features are selected with the criterion of maximizing the sensitivity to secondaries so as to avoid bias towards the groups with larger sample size, specially between HCM and SLVH. This procedure has been labeled in Fig. 2.4 as *K-fold Feature Selection*. As for finding classification performance, a similar cross validation procedure has been carried out (labeled in Fig. 2.4 as *Leave-10-out Classification*) on new randomizations. The classifiers tested have been Fuzzy C-Means (FCM) (Bezdec, 1981) and Support Vector Machines (SVM) (Cortes and Vapnik, 1995) both Quadratic Kernel Support Vector Machines (SVMQ) and Gaussian Kernel Support

Vector Machines (SVMG) (Vert et al., 2004).

In order to assess the performance of a given feature in the classification procedure we have measured its surviving percent rate. This parameter shows the membership probability of the given feature to the feature vector extracted from the feature selection step; in other words, it is the frequency that the feature is employed within any of the stages of the classification along trials.

2.3 Results

2.3.1 Rotation analysis

Torsion is known to be dependent on LV shape, with reduced twist in more spherically shaped hearts and increased torsion with concentric hypertrophy due to an increased lever arm for myocardial fibers. In HCM, torsion has been reported to increase despite reduced circumferential and longitudinal shortening (Young and Cowan, 2012). These findings, together with others described in Section 2.1, can be observed in the results included in Table 2.4, where the mean and STD of the twist and torsion distributions derived from the aforementioned rotation features are shown.

Table 2.4: Twist and torsion parameters extracted from the MR-T sequence (mean ± std) for segments in Table 2.3 for each population. The number within braces indicates the equation that defines the parameter.

Populations	HCM	SLVH	Control
Twist ϑ (2.11)	10.46±2.11	9.23±2.28	7.33±2.08
Twist β (2.4)	13.53±2.50	13.80±3.37	9.87±2.81
Twist ϕ (2.7)	2.73±0.53	2.71±0.64	1.25±0.072
T (2.5)	7.26±1.14	6.85±1.90	4.63±1.68
E_{lc} (2.3)	0.02±0.003	0.022±0.01	0.011±0.006
θ_{lc} (2.6)	7.94±1.66	7.22±1.81	3.18±0.39
α^{LRl} (2.8)	1.83±1.57	2.08±1.98	2.82±1.79

In Fig. 2.5 we show snapshots of mid-ventricular slices of the local rotation extracted by means of the vortical approach as described in (2.10) for a HCM and a SLVH case as well as for a healthy volunteer. In general, septal segments for HCM have shown higher vorticity, specially when compared to lateral segments, whereas for secondary cases this behavior can be observed in any of the cardiac segments. In healthy volunteers the extracted values are lower compared to HCM patients independently of the cardiac segment.

In Fig. 2.6, we show color codes of the mean ± STD (respectively, inner and outer rings within each segment) of the rotation parameters over the 17-segment model (Cerqueira,

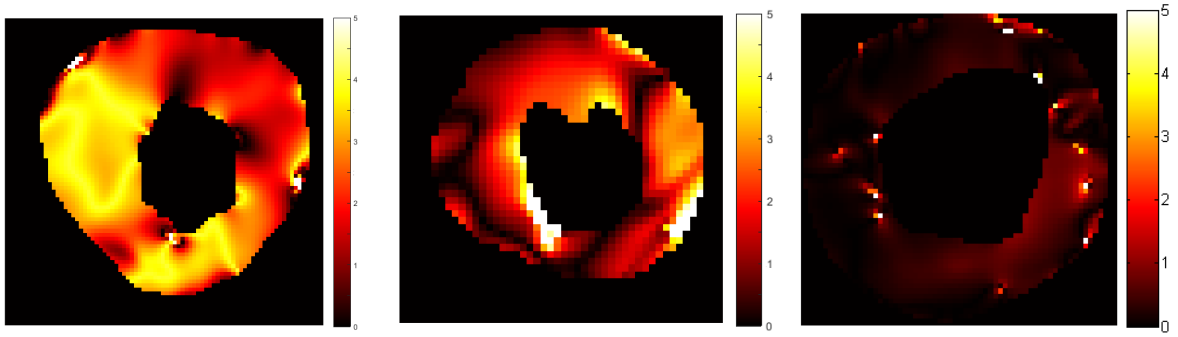

Figure 2.5: Snapshots on vortical-based rotation measurement ω_z from (2.9) for HCM, SLVH and a healthy volunteer over mid-ventricular slices (from left to right).

2002), estimated from both the vortical approach given in (2.10) and the traditional approach by (2.4) for the resulting distribution of the deformation vector field. Additionally, and for the sake of comparison, rotation parameters extracted with the elastic registration procedure over MR-C and from the deformable model have been included as well in the second and third rows, respectively.

Student t-tests[2] have been performed to highlight differences on the mean of the vorticity modulus and the aforementioned rotation distributions on each of the 17 cardiac segments. Each population of the study has been compared with the other two, separately for each rotation parameter; the numerical results are shown in Table 2.5 and graphically in Fig. 2.7 bull's eye display. It is noticeable that the vortical approach seems to show larger differences between populations compared to the traditional approach. Septal segments seem to bear higher discriminating capability, specially when twist is measured by the vortical approach. Additionally, we have performed (two-way) Analysis Of Variance (ANOVA) tests over the ϑ distributions extracted from MR-C and MR-T sequences as well as using the deformable model (over MR-T) for each population and cardiac segment. Significant differences ($p < 10^{-3}$) have been found in the vast majority of the comparisons. ϑ and β distributions were not compared since the measured parameters do not represent the same component of the physiological rotation motion.

2.3.2 Classification analysis

We have assessed the survival rate of the feature selection stage of the classifier (recall Fig. 2.4). Results are shown in Table 2.6 for the features described in Table 2.3; features obtained from both the MR-C elastic registration as well as from the spheroidal deformable model have also been included. Additionally, we have also included conventional indices of cardiac motion used in clinical practice, such as Wall Thickening (WT) over mid-ventricular slices (see Dong et al. (1994); Prasad et al. (2010) for more details), EF

[2]Similar conclusions have been obtained when performing U-Tests over these same distributions.

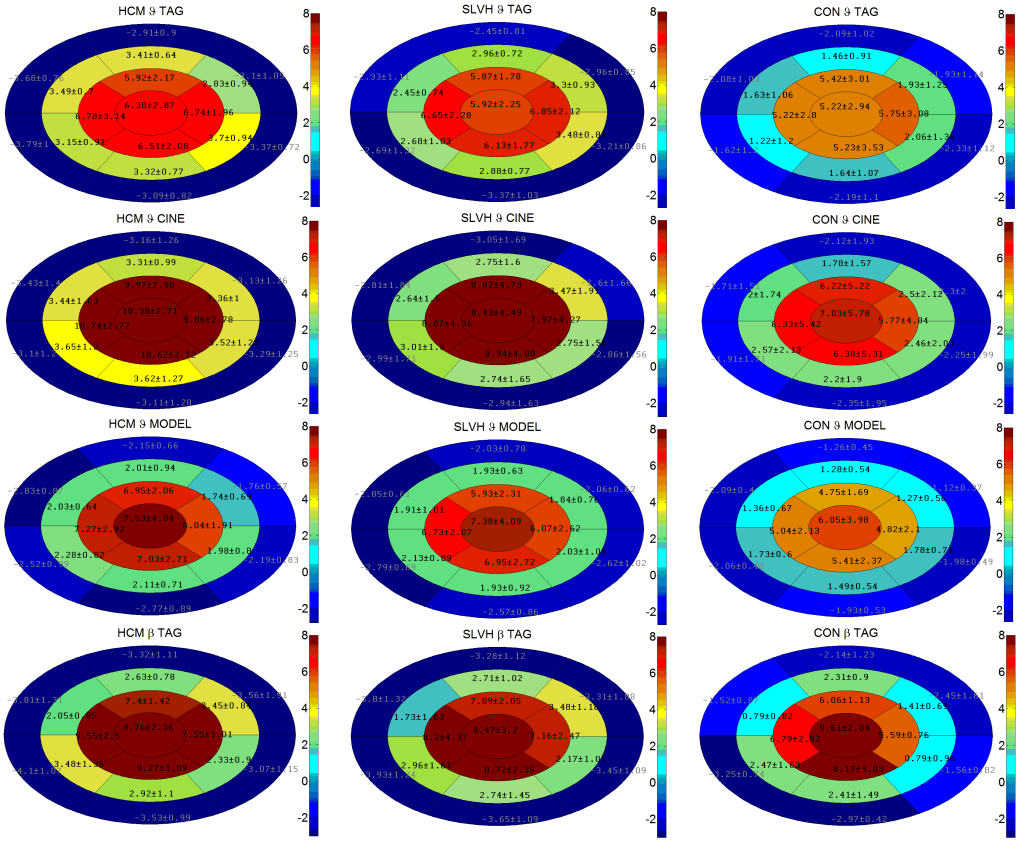

Figure 2.6: Regional study of the aforementioned vortical rotation parameters obtained from the MR-C and MR-T sequences, as well as using the deformable model over the latter, for the different populations. Traditional rotation is also depicted in the last row. For each cardiac segment two colors are depicted, the inner showing mean + std and the outer for mean − std.

and LV volume, End Diastolic Left Ventricular Volume (EDLVV) and End Systolic Left Ventricular Volume (ESLVV).

The most repeated configuration of the classifier consisted of FCM for stages 1 and 2.2 and SVMG for stage 2.1. The best accuracy figures were obtained when using diagonal ST components on stage 1, whereas for stages 2.1 and 2.2, the best feature vectors turned out to be $[E_{ll}, \text{Twist}\vartheta_{TAG}, \text{Twist}\phi]$ and $[E_{ll}, E_{cc}, \text{Twist}\vartheta_{TAG}, ||\vec{\omega}||]$, respectively. If we take into account not only the best classifier but we also rank performance and analyze the first, say, ten results, the composition of the selected feature vectors shows some degree of variability which seems very much in accordance with the results in Table 2.6.

In terms of end-to-end performance, the obtained accuracy (86 %) seems comparable in classification figures with other procedures (see Gopalakrishnan et al. (2014); Puyol-Antón et al. (2017)) although, in these cases, no SLVH are analyzed, so comparisons have to be made cautiously. In disaggregated terms, the sequential classifier has obtained sensitivity figures higher than 70 % for each group (specifically, 81 % for control, 72 % for secondary hypertrophy patients and 95 % for primary HCM patients). It is worth

Table 2.5: p-values for the comparisons between distributions (H, S and C stand for HCM, SLVH cases and controls, respectively) of the given rotation parameters indexed by number of segment. When unspecified, MR-T is the image source. Significance level after Bonferroni correction is 0.017.

	Differences on ϑ distributions			Differences on β distributions			Differences on $\vartheta CINE$ distributions			Differences on $\vartheta MODEL$ distributions		
Seg.	H. vs S.	C. vs S.	H. vs C.	H. vs S.	C. vs S.	H. vs C.	H. vs S.	C. vs S.	H. vs C.	H. vs S.	C. vs S.	H. vs C.
1	0.078	0.001	$\leq 10^{-6}$	0.91	0.01	0.001	0.20	0.008	$\leq 10^{-6}$	0.19	0.033	$\leq 10^{-6}$
2	0.022	$\leq 10^{-6}$	$\leq 10^{-6}$	0.97	$2.49 \cdot 10^{-6}$	$\leq 10^{-6}$	0.47	$\leq 10^{-6}$	$\leq 10^{-6}$	0.12	$\leq 10^{-6}$	$\leq 10^{-6}$
3	0.065	$\leq 10^{-6}$	$\leq 10^{-6}$	0.65	$5.82 \cdot 10^{-5}$	$\leq 10^{-6}$	0.10	0.002	$\leq 10^{-6}$	0.24	$\leq 10^{-6}$	$\leq 10^{-6}$
4	0.33	$\leq 10^{-6}$	$\leq 10^{-6}$	0.71	$1.77 \cdot 10^{-6}$	$\leq 10^{-6}$	0.66	$\leq 10^{-6}$	$\leq 10^{-6}$	0.093	$8.23 \cdot 10^{-5}$	$\leq 10^{-6}$
5	0.52	$\leq 10^{-6}$	$\leq 10^{-6}$	0.31	$5.48 \cdot 10^{-6}$	$\leq 10^{-6}$	0.090	0.002	$\leq 10^{-6}$	0.073	$6.88 \cdot 10^{-5}$	$\leq 10^{-6}$
6	0.092	$\leq 10^{-6}$	$\leq 10^{-6}$	0.23	$8.04 \cdot 10^{-5}$	$3.05 \cdot 10^{-5}$	0.057	$1.17 \cdot 10^{-4}$	$\leq 10^{-6}$	0.55	0.0095	$\leq 10^{-6}$
7	0.64	0.002	$3.12 \cdot 10^{-5}$	0.78	0.26	0.21	0.18	0.022	$3.29 \cdot 10^{-5}$	0.055	0.0037	$\leq 10^{-6}$
8	0.011	$7.32 \cdot 10^{-5}$	$\leq 10^{-6}$	0.16	0.008	$3.03 \cdot 10^{-6}$	0.042	0.098	$6.34 \cdot 10^{-5}$	0.038	0.002	$\leq 10^{-6}$
9	0.049	0.17	0.002	0.27	0.41	0.028	0.09	0.010	$4.29 \cdot 10^{-4}$	0.013	0.051	$6.81 \cdot 10^{-5}$
10	0.12	0.27	0.044	0.29	0.89	0.20	0.53	0.016	$3.52 \cdot 10^{-5}$	0.34	0.046	$2.25 \cdot 10^{-4}$
11	0.018	$6.88 \cdot 10^{-6}$	$\leq 10^{-6}$	0.58	$5.79 \cdot 10^{-4}$	$1.37 \cdot 10^{-6}$	0.25	0.037	$1.98 \cdot 10^{-5}$	0.091	0.047	0.12
12	0.006	$8.21 \cdot 10^{-6}$	$\leq 10^{-6}$	0.94	0.004	$6.94 \cdot 10^{-5}$	0.26	0.18	$1.34 \cdot 10^{-4}$	0.65	0.059	0.064
13	0.10	0.092	0.002	0.57	0.085	0.002	0.040	0.092	$2.69 \cdot 10^{-4}$	0.021	0.0068	$\leq 10^{-6}$
14	0.79	0.068	$5.38 \cdot 10^{-5}$	0.54	0.017	0.001	0.055	0.003	$\leq 10^{-6}$	0.032	0.0082	$\leq 10^{-6}$
15	0.18	0.061	0.003	0.56	0.58	0.24	0.018	0.019	$\leq 10^{-6}$	0.76	0.019	$2.16 \cdot 10^{-5}$
16	0.46	0.045	$\leq 10^{-6}$	0.25	0.019	0.001	0.18	0.38	0.018	0.083	0.025	$\leq 10^{-6}$
17	0.87	0.86	0.22	0.73	0.88	0.82	0.14	0.17	0.27	0.81	0.17	$3.76 \cdot 10^{-4}$

mentioning that no primary is classified as control and viceversa; therefore, the pipeline proposed seems a proper screening tool. Secondary patients performance is clearly lower as compared with both controls and primary HCM patients, possibly due to a smaller sample size as well as the subtle differences they show.

Finally, in order to assess the relative strength of the different measures in classification performance, we have run the classification pipeline with different features subsets. In particular, in Table 2.7 we have compared confusion matrices obtained with the full feature set (MR-T + MR-C + Deformable model + Conventional clinical indices) and with MR-T features only. From the latter, we have also shown classification performance obtained discarding traditional and vortical rotation features, respectively.

2.4 Discussion

The relationship between myocardial fibrosis and local mechanics is important for the diagnosis and treatment of cardiomyopathies (Karamitsos and Neubauer, 2011). This paper shows that LV rotation is essential for proper myocardial function. In our case, most of the measurements shown in Table 2.4 indicate that LV rotation can be considered as a marker for cardiac disease identification and might be helpful for cardiomyopathy understanding, thus providing complementary information to standard pump function indices.

The diagonal components of the ST (E_{cc}, E_{ll} and E_{rr}), defined in (2.3), have provided the highest separability between pathologic and healthy groups (cardiomyopathy screening) as shown in Table 2.6; our results are in accordance with this finding (Saltijeral et al., 2010). Twist parameters seem to be also valuable in this step, showing higher survival rate than shear strains and torsion parameters. For the refinement step for controls/SLVH (stage 2.1 in Fig. 2.4) the E_{cc} component in mid-ventricular areas is the most

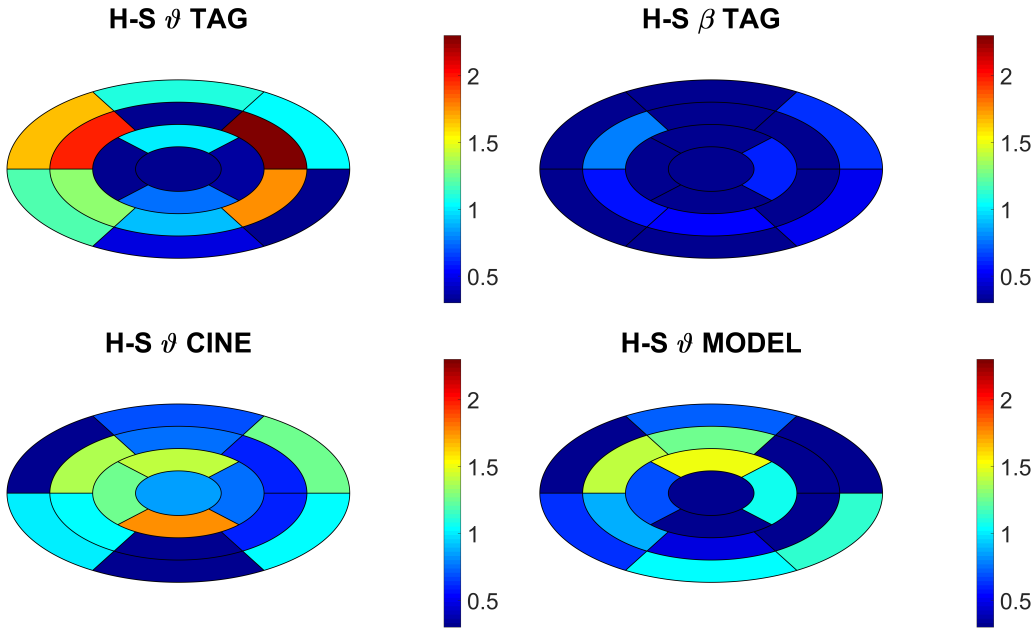

Figure 2.7: p-value bull's-eye plots from intra-segment comparisons between primary HCM and SLVH patients for ϑ distributions obtained with different methodologies, as well as traditional rotation β distribution. Scale is defined as $-log_{10}$(p-value).

discriminative. Amongst the rotation-based parameters, vorticity modulus $||\vec{\omega}||$ and twist ϑ_{TAG} remain the most discriminative features.

In parallel, for the classifier stage 2.2, lower figures on the global performance are obtained. Besides, the selected feature vector presented one more component and two curl-derived entries; it consisted of a combination of two diagonal strain parameters, the vorticity modulus (2.9) and the twist extracted from the vortical approach (2.10). Extending the analysis to more (than one) high-ranked features vectors, we observe a greater degree of heterogeneity as well as the frequent presence of ω_z (2.9). Consequently, the proposed curl-derived parameters (2.9)-(2.11) have turned out to be particularly useful for the discrimination of primary and secondary cases as reflected by sensitivity figures extracted from Table 2.7.

To the best of our knowledge, this is the first study in HCM patients that relates vorticity in cardiac deformation fields with local myocardial mechanics and its abnormalities; our results suggest that vorticity may help deepen on the underlying characteristics behind primary and secondary cases of LV hypertrophy. For these parameters, neither the length nor the center of the heart are needed, so no bias is introduced in their estimation; as we have described above, vorticity is directly related to the deformation gradient tensor and, consequently, it can be estimated from the same information used in the ST (2.3) analysis. In addition, they show higher survival rates than techniques that use fixed LV axis and center representations, giving rise to a more reliable parameter.

Table 2.6: Surviving percent rate of the features employed in the classification procedure (see notation in Fig. 2.4). Stage 2.2 is devised to SLVH-to-HCM sensitivity, while stage 2.1 refers to SLVH-to-Control sensitivity.

Features	Stage 2.2	Stage 2.1	Stage 1
E_{rr}	7	38	35
E_{cc}	54	24	60
E_{ll}	49	50	37
E_{lc}	22	11	6
$\|\|\vec{\omega}\|\|$	43	25	19
Twist ϑ TAG	42	32	27
Twist ϑ CINE	7	2	13
Twist ϑ MODEL	15	8	7
Twist β TAG	19	16	16
Twist β CINE	8	5	4
Twist β MODEL	12	3	0
Twist ϕ	18	20	24
T	8	13	18
θ_{lc}	3	0	1
α^{LRl}	7	9	10
ω_z zero cross. TAG	21	13	4
ω_z zero cross. CINE	2	5	2
ω_z zero cross. MODEL	12	3	0
β zero cross. TAG	14	1	3
β zero cross. CINE	0	2	1
β zero cross. MODEL	3	1	0
WT	0	8	10
EF	0	6	3
EDLVV	0	0	1
ESLVV	0	2	0

The color-coded results shown in Fig. 2.6 reveal that patients with both forms of ventricular hypertrophy present greater rotation distributions as compared with controls over most segments both for vortical (2.10) and traditional (2.4) rotations. As for primary HCM patients, there is a clear increased rotation (in modulus) for all segments, but high vorticity areas are mainly located on septal segments. SLVH patients showed a somewhat different pattern in mid-ventricular and basal regions of the heart, presenting higher values than controls; those values are not focused on septal segments but a slight bias to lateral segments may exist. Other regional analyses have also been performed by means of automatic LV segmentation (Bai et al., 2016; Liang et al., 2015). However, the presence of hypertrophic tissue and other pathologies may bias the final parcellation of the cardiac segments. For this reason, we have made use of the 17-segment model as a consistent and well-established model for motion analysis (Smiseth et al., 2016). The

Table 2.7: Confusion matrices for classification performance with different feature subsets. Matrices have been normalized with respect to the total number of patients. Each column represents the instances in a predicted class while rows represent the instances in an actual class.

	Full Feature Set			MR-T only			Vortical only			Traditional only		
	C	S	H	C	S	H	C	S	H	C	S	H
C	0.236	0.064	0	0.243	0.057	0	0.24	0.06	0	0.234	0.066	0
S	0.023	0.145	0.032	0.038	0.144	0.018	0.021	0.141	0.038	0.038	0.127	0.035
H	0	0.017	0.483	0	0.025	0.475	0	0.022	0.478	0	0.023	0.477

usefulness of the vortical parameters has also been reflected by the improvement shown in Table 2.7 with respect to traditional rotation parameters and the minor degradation with respect to the full-feature option when curl-derived parameters are used in isolation.

Our results also indicate a higher performance of MR-T for ME with respect to MR-C; however, it is well-known that HARP procedures have some difficulties in correctly estimating the phase in the vicinity of boundaries. In those areas, elastic registration procedures over MR-C is usually more robust. For this reason, a coordinated procedure that weighs both information sources according to position may potentially provide better figures.

Additionally, vortical measures were compared when extracted both from the HARP method and by deforming a spheroidal model previously fit. Similar vorticity values were obtained although the extracted vortical patterns from the spheroidal model showed higher spatial smoothness due to the regularized functions used to define the deformation, thereby reducing its usefulness for classification (see Table 2.6).

Finally, conventional global indices in HCM diagnosis (see Table 2.1) have also been tested in the classifier. Neither of them presented a very representative survival rate (even in stage 1), hence, their influence on final performance does not seem relevant.

2.5 Conclusions and future lines

In this paper we have related anomalies on local vortical patterns with the presence of fibrotic tissue by means of an image processing pipeline and a two-stage sequential classification method. Local rotation parameters are estimated by means of a robust motion and tensor analysis so that potential biases of global analyses are avoided.

Local rotation was significantly increased in primary HCM patients, specially in the septum, compared to controls and secondary cases; in the latter, vortical abnormalities may show a slight trend to lateral segments and with values less pronounced than primaries. These findings may provide important information in hypertrophic diseases to establish a differential diagnostic between these two classes.

Classification figures, although collateral in the paper, are promising; clearly, discrimination between primary HCM and secondary cases is more challenging than between HCM and controls. Therefore, figures related to the former problem have been lower than

those related to the latter. A larger cohort may let us increase this number in the near future. Classification of SLVH cases has proven to be a challenging task but figures, despite not being remarkable, are likely to improve when equalizing the number of subjects in the study or by introducing features that take into account the position of vortical peaks.

Acknowledgments

This work was partially supported by the Spanish Ministerio de Ciencia e Innovación under Research Grant TEC2013-44194-P, the European Regional Development Fund (ERDF-FEDER) under Research Grant TEC2014-57428-R, the Spanish Junta de Castilla y León under Grant VA069U16 and the European Social Fund (ESF-FSE).

Chapter 3

Joint Groupwise Registration and ADC Estimation in the Liver using a b-Value Weighted Metric

Published as:

Sanz-Estébanez, S.[1], Rabanillo-Viloria, I.[1], Royuela-del-Val, J.[1], Aja-Fernández, S.[1] and Alberola-López, C.[1] (2018). Joint groupwise registration and ADC estimation in the liver using a b-value weighted metric. *Magnetic Resonance Imaging*, 46:1-9.

[1] Laboratorio de Procesado de Imagen, Department of Teoría de la Señal y Comunicaciones e Ingeniería Telemática, ETSIT, Universidad de Valladolid, Campus Miguel Delibes s.n., 47011, Valladolid, Spain.

The purpose of this work is to develop a groupwise elastic multimodal registration algorithm for robust ADC estimation in the liver on multiple breath hold diffusion weighted images.
Methods: We introduce a joint formulation to simultaneously solve both the registration and the estimation problems. In order to avoid non-reliable transformations and undesirable noise amplification, we have included appropriate smoothness constraints for both problems. Our metric incorporates the ADC estimation residuals, which are inversely weighted according to the signal content in each diffusion weighted image.
Results: Results show that the joint formulation provides a statistically significant improvement in the accuracy of the ADC estimates. Reproducibility has also been measured on real data in terms of the distribution of ADC differences obtained from different *b-values* subsets.
Conclusions: The proposed algorithm is able to effectively deal with both the presence of motion and the geometric distortions, increasing accuracy and reproducibility in diffusion parameters estimation.

Keywords: Diffusion Weighted Imaging; Joint Optimization; Groupwise Registration; ADC Estimation; Residual Minimization Metric

3.1 Introduction

DWI is a MRI technique sensitive to molecular displacement that assesses cell membrane density and tortuosity of the extracellular space based upon differences in water proton mobility in tissues. DWI is increasingly employed for tissue evaluation as it is a relatively quick non-contrast technique that provides characteristic quantitative parameters of the tissue, such as the well-known ADC. ADC has been shown to be a positive indicator of tumor response (Kim et al., 1999) due to its ability to measure displacement of water molecules, giving evidence about cellular organization and cell permeability of micro-structures (Le Bihan, 2014).

Nonetheless, in order to thoroughly validate the ADC as a biomarker, a robust parameter estimation methodology suitable for multiparametric acquisitions is mandatory. However, this is not an easy task since a number of factors degrade the quality of this sort of acquisitions. The most evident factor is the signal intensity dropout observed for increasing *b-values* (defined in section 3.2), leading to images with very different SNR.

A confounding factor that greatly affects image quality is motion, mainly physiological motion. BH acquisitions are a popular way of avoiding respiratory motion with fast scan times. This technique is satisfactory for relatively fit patients but large volumes or high resolution scans can hardly be covered during the BH. Moreover, when images with different *b-values* are acquired at different BHs and, later, used for ADC estimation, considerable image artifacts can arise (McLeish et al., 2002) that stem from the fact that two BH states are never identical. Respiratory gating has been proposed to alleviate this problem, but this solution is also approximate.

An additional degrading factor stems from the fact that the ultrafast sequence typically used for diffusion studies, i.e. EPI, suffers from geometric distortions as well as from local signal dropouts caused by static magnetic field inhomogeneities (Bernstein et al., 2004). The resultant distortions are commonly seen near tissue interfaces, where magnetic susceptibility changes rapidly.

Besides, the presence of noise (Aja-Fernández and Vegas-Sánchez-Ferrero, 2016) in the images is also a major issue, becoming specially critical at higher *b-values*.

These problems have been addressed in the literature, as we now summarize.

Extensive research has been carried out on motion-robust sequences and motion correction techniques in MRI (Zaitsev et al., 2015); however, the use of MC techniques is commonly limited by the type and amount of motion that can be compensated for (Pipe, 1999).

Image transformations can be either linear or nonlinear. Rigid and affine transformations are the most common examples of linear parametric models used for image registration. Such global models offer a compromise between computational complexity and accuracy in the estimation of the deformations. On the other hand, nonlinear transformations are used to deal with the nonrigid motion of the human anatomy, such as elastic deformations of anatomical structures (Glocker et al., 2011) or sliding motion between organs.

Most approaches pose the registration problem from a PW standpoint (Wu et al., 2008) using an –ideally– undistorted image as reference. This procedure, however, is prone to an undesired bias towards the a priori chosen template (Wachinger and Navab, 2013), which, depending on its quality, may give rise to multiple outliers in the registration. On the other hand, GW approaches are based on an image reference that is built out of the whole image set to be registered, so the bias mentioned above disappears. We have resorted to the latter type of registration, due to its reported benefits in different fields (Royuela-del-Val et al., 2017).

The implemented metric for DWI registration has to be able to identify spatial correspondence between anatomical structures despite the great intensity and contrast variations along the different *b-value* images. To this end, we have resorted to multimodal metrics.

MI, first introduced for rigid registration of multimodal scans in Maes et al. (1997), has been widely used as metric for medical image registration. It is based on the assumption that a lower entropy on the joint intensity distribution corresponds to a better registration. Nevertheless, in several practical applications, multiple additional constraints must be introduced due to the several weaknesses of MI for nonrigid registration (Haber and Modersitzki, 2007). A non-local shape descriptor (Heinrich et al., 2011), based on denoising schemes, has also been proposed for image registration purposes aiming at extracting anatomically meaningful geometric shapes. However, validation has not been performed over images with relative low SNR, which is the case in DWI for higher *b-values*.

Methodologies for multiparametric registration towards robust ADC estimation have been designed both for distortion correction (Hong et al., 2015) and MC (Guyader et al., 2015), but from a PW standpoint. GW approaches have been addressed in Veeranghavan et al. (2015) using prior structure segmentations, although the intrinsic intensity changes due to the diffusion process are not considered. Hence, we hypothesize that a registration metric that explicitly takes into account the parameters to be estimated, as proposed in Kornapoulos et al. (2016); Kurugol et al. (2017a), will not only make the ulterior ADC analysis more robust but will also alleviate the effects of the different confounding factors.

Recently, model-free approaches have also been proposed for liver DWI nonrigid registration (see Huizinga et al. (2016)) grounded on PCA eigenvalues. However, the absence of a model makes difficult to choose proper regularization terms that enforces data consistency (fidelity). Besides, although a very promising approach, proposed linear weightings for the metric may not be the best option for this eminently non-linear problem.

In this paper we propose the joint formulation for the estimation-GW registration problem. We aim at finding the optimal transformation of multiparametric DWI datasets that lead to optimal ADC estimates, imposing a TV constraint on the ADC maps, as well as a smoothness penalty term on the transformation. We incorporate within the registration metric some weighting parameters that balance the influence of the different images according to the DW signal content. We will show that our proposed algorithm solves the estimation-registration optimization problem yielding higher quality ADC maps as compared to other previously reported approaches.

3.2 Theory

3.2.1 Diffusion Basis

Diffusion is described as the thermally induced behaviour of molecules moving in a microscopic random pattern, often referred to as Brownian motion. The resulting motion can be modeled as a stochastic process with a Gaussian probability distribution (Lewis et al., 2014) described as:

$$P(r,t) \propto \exp\left(\frac{-r^2}{4Dt}\right), \tag{3.1}$$

where D is the diffusion coefficient and r is the distance traveled by the molecule during a given time t. This distribution refers to free diffusion; however, for restricted diffusion, where motion is constrained by hard microstructures, as in tissues, it presents a non-Gaussian distribution with lower apparent D, or ADC.

DWI is sensitive to this microscopic motion. Common approaches to estimate this motion assume a monoexponential decay in the DW signal (Le Bihan and Breton, 1985) described as follows:

$$S = S_0 e^{-b \cdot \mathrm{ADC}}, \tag{3.2}$$

where S_0 denotes the signal intensity obtained with a null diffusion gradient and b, the so-called *b-value* (Stejskal and Tanner, 1965), is a function of the applied gradient that determines the strength of the diffusion weighting:

$$b = (\gamma G \delta)^2 \left(\Delta - \frac{\delta}{3}\right), \tag{3.3}$$

with γ the spin gyromagnetic ratio, G and δ the gradient strength and length and Δ the time between consecutive gradients.

For the sake of conciseness, we have focused on the monoexponential diffusion model. However, the methodology here proposed could be easily extended towards more complex diffusion models, such as Intravoxel Incoherent Motion (IVIM) (Le Bihan et al., 1988; Kurugol et al., 2017a) or Diffusion Kurtosis Imaging (DKI) (Steven et al., 2014).

3.2.2 Joint ADC Estimation-Registration Algorithm

As previously stated, we intend to jointly register axial abdominal DW images acquired in different BH as well as to estimate the ADC maps; we pose the problem as the following joint registration-estimation scheme:

$$[\mathrm{ADC}, \tau] = \underset{\mathrm{ADC},\tau}{\arg\min} \int_{\chi} \left[H(\mathbf{S}, \mathrm{ADC}(\mathbf{x}), \tau(\mathbf{x})) + \beta ||\mathrm{ADC}(\mathbf{x})||_{TV} + \lambda \mathrm{Reg}(\tau(\mathbf{x}))\right] d\mathbf{x}, \tag{3.4}$$

where $\mathrm{Reg}(\tau(\mathbf{x}))$ is a penalty term which favors the transformation τ to be smooth. Local transformation $\mathbf{T}(\tau)$ is defined as a combination of B-spline (Rueckert et al., 2006) FFDs

where τ represents each of the displacements of the control points. On the other hand, $||\text{ADC}(\mathbf{x})||_{\text{TV}}$ represents the spatial TV regularization term, defined as:

$$||\text{ADC}(\mathbf{x})||_{\text{TV}} = ||\nabla_{\mathbf{x}}\text{ADC}(\mathbf{x})||_{l_1}. \tag{3.5}$$

The influence of these two regularization terms is balanced by trade-off parameters λ and β, respectively.

The spatial TV regularization term is introduced so that it contributes to noise artifact removal in the estimated ADC map dealing with the inhomogeneities derived from the inherent low SNR of each *b-value* image. A previous ADC estimation performed by means of NLLS method has also been introduced in the estimation problem as ADC initialization.

As for the metric H, our proposal aims at directly minimizing the residuals in the ADC estimation, so it is defined as:

$$H(\mathbf{S}, \text{ADC}, \tau) = \sum_{j=0}^{N_b} W_j^i (S_j(T_j(\tau^{i-1}(\mathbf{x}))) - \widehat{S}_j(\text{ADC}^i(\mathbf{x})))^2, \tag{3.6}$$

where S_j represents the acquired image and $\widehat{S}_j$ is the estimated intensity value from the current (i-th) ADC estimate obtained by applying Eq. (3.2) ($\widehat{S}_j = S_0 \exp(-b_j \text{ADC}^i)$) for a given *b-value* j out of a total of N_b.

The proposed metric extends the one presented in Kornapoulos et al. (2016) by adding proper weighting parameters related to the underlying noise distribution of the magnitude images. Those weights, initially unitary, are redefined through iterations along with the predicted DW signals from ADC estimates as:

$$\mathbf{W}^i = \exp(-2\mathbf{b}Q(\text{ADC}^i)), \tag{3.7}$$

where Q represents the median of the distribution in the ROI χ, previously defined. Those weights are a redefinition of the ones proposed by Veraart et al. (2013) for linearized WLS estimation.

Overall, the first and second terms are intended to reconstruct a high SNR ADC map, while the third, jointly with the first term, intends to register the images to provide the data a better fit to the monoexponential model.

We solve Eq. (3.4) by sequentially solving the estimation and registration problems separately, leaving outer parameters fixed, via *ceteris-paribus* analysis. Hence, we iteratively alternate between estimating model parameters and the optimal transformation until convergence both on transformation norm and metric updates is reached.

First, the diffusion parameters are estimated by means of the NESTA algorithm as described in Becker et al. (2011), applied to the following optimization problem:

$$\text{ADC} = \arg\min_{\text{ADC}} \int_{\chi} [H(\mathbf{S}, \text{ADC}, \tau) + \beta||\text{ADC}(\mathbf{x})||_{TV}]\, d\mathbf{x}. \tag{3.8}$$

Then, we perform the GW registration by means of the previously introduced metric. To constraint the transformation to be smooth, we have resorted to a thin-plate penalty term composed by the first and second derivatives of the transformation displacements along the spatial dimension. Eq. (3.9) poses the registration problem to be solved in this step:

$$\tau = \arg\min_{\tau} \int_{\chi} \left(H(\mathbf{S}, \mathrm{ADC}, \tau) + \sum_{b=0}^{N_b} \sum_{l=1}^{L} \lambda_1 \left(\sum_{l'=1}^{L} \left(\frac{\partial \tau_l(\mathbf{x}, b)}{\partial x_{l'}} \right)^2 \right) + \lambda_2 \left(\sum_{l'=1}^{L} \sum_{l''=1}^{L} \left(\frac{\partial^2 \tau_l(\mathbf{x}, b)}{\partial x_{l'} x_{l''}} \right)^2 \right) \right) d\mathbf{x}, \tag{3.9}$$

where τ_l represents each of the displacement components of the transformation (with $L = 2$ for the 2D case). Derivatives are approximated by finite differences both in the spatial dimension $\mathbf{x}$ and in the *b-value* coordinate b.

A GD optimization scheme is used (Sanz-Estébanez et al., 2017), where the step size ω^i is updated along iterations according to the variation in the registration metric as:

$$\omega^{i+1} = \begin{cases} 2\omega^i & \text{if } H^{i+1} < H^i \\ \omega^i / 1.2 & \text{otherwise.} \end{cases} \tag{3.10}$$

Linear interpolation is used to obtain the intensity of the deformed images on a rectilinear grid. Trade-off parameters of both optimizers have been set empirically; as for the volunteers, one of them was used for parameter setting and those parameters were used for the rest of the cohort. Notice that the transformation model does not account for sliding motion. However, there are some extensions (Delmon et al., 2013) designed to deal with that issue.

The steps of the optimization problem are summarized in Table 3.1.

3.3 Materials

3.3.1 Diffusion Simulation

DWI image synthesis is subdivided in two parts. First, the b_0 image is simulated; in this work we use the well-known SE sequence, for the intensity values in the image are given by Bernstein et al. (2004):

$$S_0 = M_z^0 (1 - e^{-T_R/T_1}) e^{-T_E/T_2} = K_s \rho (1 - e^{-T_R/T_1}) e^{-T_E/T_2}, \tag{3.11}$$

where ρ, T_1, T_2 stand for the proton density and longitudinal and transverse relaxation times assigned for each simulated tissue in the volume, respectively. K_s is a proportionality constant (unitary set) which depends on the sensitivity in signal detection.

Table 3.1: Steps in the registration-estimation algorithm.

	Registration-estimation optimization problem
Input:	**S** measured DW signals at different *b-values*.
Output:	$\widehat{\text{ADC}} \leftarrow \text{ADC}^i$ Estimated ADC map after i iterations.
	$\widehat{\tau} \leftarrow \tau^i$ Final transformation after i iterations.
Initialize:	ADC^0, S_0 Initial diffusion parameters estimation by NLLS.
	$\mathbf{W}^0$ Initial weights for the estimation metric.
Step 1:	Estimate denoised ADC^i map by solving Eq. (3.8) with fixed τ.
Step 2:	Update weights $\mathbf{W}^i$ from ADC estimates according to Eq. (3.7)
Step 3:	Estimate τ^i by solving Eq. (3.9) with fixed ADC.
Step 4:	Compute variation in metric and transformation norm.
	Go back to Step 1 until convergence is reached:
	$(\|\|\tau^{i-1} - \tau^i\|\| < \epsilon_T \;\; \& \;\; (H^{i-1} - H^i) < \epsilon_H \;)$.

Second, we simulate isotropic diffusion by a random walk process using the Monte-Carlo method according to the methodology presented in Fieremans (2008). Particles were initially randomly spread (uniformly distributed) in the voxel and the trajectory of a spin was generated by randomly moving the particle i during each walk.

According to the basic theory of diffusion (Johansen-Berg and Behrens, 2009), this particle displacement will induce a proportional phase shift Φ_i^k at each walk k as: $\Phi_i^k = 2\pi\gamma G\delta\Delta\vec{d}_i^{\,k}$. The final diffusion signal, derived from the bulk phase shift of the N simulated particles, can be numerically approximated (Du et al., 2016) by:

$$E = \frac{S_0}{N}\sqrt{(\sum_{i=1}^{N}\cos(\Phi_i^k))^2 + (\sum_{i=1}^{N}\sin(\Phi_i^k))^2}, \tag{3.12}$$

where S_0 represents the b_0 image intensity from Eq. (3.11).

3.3.2 Synthetic Data

For validation, we have developed a synthetic diffusion phantom using a simulation environment based on the 4D XCAT phantom (Segars et al., 2010) focusing on the liver. The phantom is built from a whole body model that contains high level detailed anatomical labels, which feed a high resolution image synthesis procedure. The 4D XCAT phantom incorporates state-of-the-art respiratory and cardiac mechanics, which provide sufficient flexibility to simulate effects of cardiac and respiratory nonrigid motion on the liver from a user-defined parameter set. Respiratory motion is defined by a motion vector field derived from two time curves, one controlling the change in diaphragm height and along the respiratory cycle and the other controlling the amount of anterior-posterior expansion of the chest. Although we assume BH acquisitions, different BHs have been

simulated for the different *b-values*. Residual cardiac artifacts have been neglected. Therefore, the phantom will provide us not only with the images themselves, but also with ground-truth deformation fields and a synthetic reference ADC map.

Additionally, the images were synthetically distorted according to Weis and Budinsky (1990) so as to simulate geometric distortions typically observed in EPI acquisitions. Transformation parameters have been set so that distortion amplitude increases with the *b-value*, although physiological motion always remains predominant. The resultant simulated images are shown in Fig. 3.1, from which the global influence of the simulated geometric distortion and the different BH on each image can be observed, as well as the simulated decreasing SNR (set to 10 dB for b_0 image). Complex Gaussian noise has been added in the coils resulting in Rician noise for the magnitude images (Aja-Fernández and Vegas-Sánchez-Ferrero, 2016).

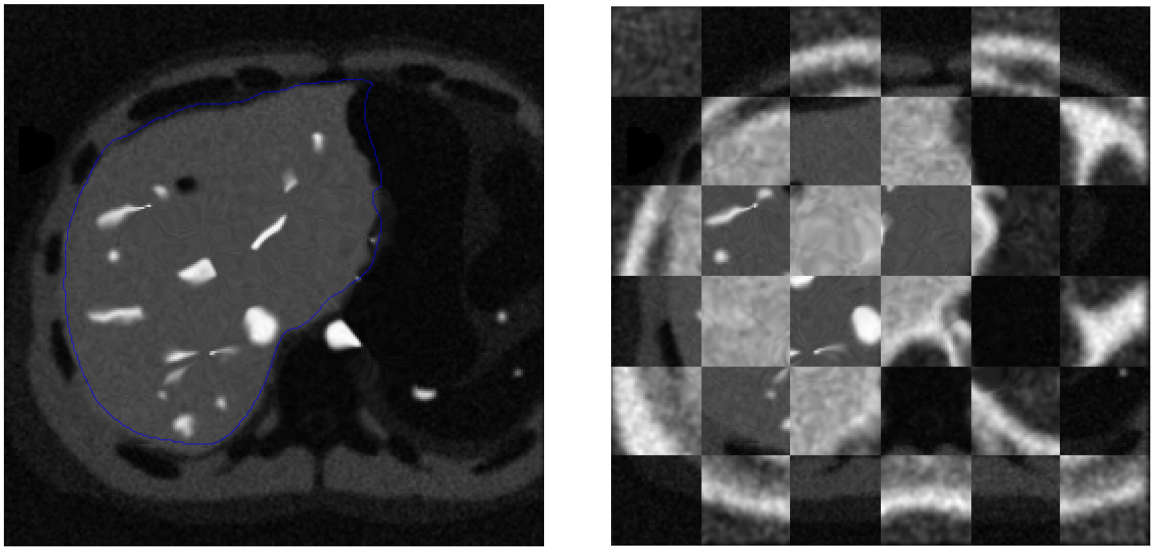

Figure 3.1: Axial slices of the simulated diffusion sequence. The figure on the left shows the image corresponding to the *b-value* of 10 s/mm^2, as well as the ROI (χ) boundary in blue (extracted from the b_0 image), while the figure on the right is a checkerboard with *b-values* of 100 and 1000 s/mm^2.

3.3.3 Real Data

Additionally, we have performed MRI acquisitions over a sample of four healthy volunteers. Axial SENSE DWI and T2W TSE sequences have been acquired on a Philips Achieva 3T scanner in each case of study. The latter will be used to manually delineate the whole liver as ROI χ on which meaningful measurements will be obtained. All the subjects signed the ordinary informed consent for the MR session and agreed in writing to share the resulting images for research purposes. Personal data were treated according to current legislation.

Acquisition and resolution details for real and synthetic sequences are shown in Table 3.2.

Table 3.2: Details on the image sequences used in the paper. Δ_p : Spatial Resolution (mm). Δ_l : Slice Thickness (mm). N_p: Number of pixels along each direction. N_b: Number of *b-values*. N_s: Number of slices. T_E: Echo Time (ms). N_g: Number of diffusion gradients. Card.: Cardiac Period (s). Resp.: Respiratory Period (s).

Params.	XCAT	DWI volunt.
Δ_p	1	1.23-1.85
Δ_l	10	5.5
N_p	268	224-320
N_b	10	10
N_s	21	20-40
T_E	93	65.65-72.1
N_g	1	3
Card.	1	$\sim$ 1
Resp.	4	Free

Sampling of *b-values* is finer for lower *b-values* according to Luna et al. (2012). Ten *b-values* are common for every sequence.
Those are $b \in \{0, 10, 20, 50, 100, 200, 500, 1000, 1500, 2000\} s/mm^2$.

3.4 Methods

3.4.1 Reference Metrics

All datasets, both real and synthetic, have been processed with different GW multimodal metrics (Sanz-Estébanez et al., 2017) as well as different registration methodologies. As for the former, apart from the one here proposed (bWei, from b-Weighted), we have tried EDI (Learned-Miller, 2006), MIND (Heinrich et al., 2011) and the one proposed in Kornapoulos et al. (2016) based on non-weighted ADC residuals (ADC). Many more metrics have been proposed to tackle this problem (see Glocker et al. (2011)); however, from our point of view, the ones here proposed compose a sufficiently representative sample. Details on the implemented metrics are shown in Table 3.3.

As for the latter, the Demons (Vercauteren et al., 2009) registration algorithm (DEM) has been implemented using a MI based metric; the solution based on multiresolution MRF (Komodakis et al., 2007) has been also tested with different metrics, namely, SSD, Joint Entropy (JE), NCC and Normalized Mutual Information (NMI). These registration algorithms have been implemented under the PW paradigm, in which the b_0 image has been taken as the image template for all of them.

Table 3.3: Metric equations for the methods used in the paper. Notation: MI and $\mathcal{E}$ stand for the MI between two images and the entropy of a given image, respectively. For the NCC metric, μ comes to represent the intensity mean in the given region χ. p represents a Parzen window estimation (Wells III et al., 1996) of the intensity distribution for EDI metric, while in the JE approach this distribution is extracted by histogramming. D_p and V in MIND metric are within-patch distances and variance estimates on a neighborhood given by r. Afterwards, simple monomodal measures built from MIND differences will be used as pixel-wise metric.

Metric	**H Equation**	**Reg. method**
DEM	$\mathrm{MI}(I_1, I_2 \circ \tau)$	PW Demons
NCC	$-\frac{\sum_{\mathbf{x}\in\chi}(I_1(\mathbf{x})-\mu_1)(I_2(\tau(\mathbf{x}))-\mu_2)}{\sqrt{\sum_{\mathbf{x}\in\chi}(I_1(\mathbf{x})-\mu_1)^2 \sum_{\mathbf{x}\in\chi}(I_2(\tau(\mathbf{x}))-\mu_2)^2}}$	PW MRF
JE	$-\sum_{\mathbf{x}\in\chi} p(I_1(\mathbf{x}), I_2(\tau(\mathbf{x}))) \log(p(I_1(\mathbf{x}), I_2(\tau(\mathbf{x}))))$	PW MRF
NMI	$-\frac{MI(I_1, I_2\circ\tau)}{\mathcal{E}(I_1)+\mathcal{E}(I_2\circ\tau)}$	PW MRF
SSD	$\sum_{\mathbf{x}\in\chi}(I_1(\mathbf{x}) - I_2(\tau(\mathbf{x})))^2$	PW MRF
EDI	$\frac{-1}{N_b}\sum_{j=1}^{N_b} \log(p(S_j(\tau(\mathbf{x}))))$	GW
MIND	$\mathrm{MIND}(I, \mathbf{x}, r) \propto \exp\left(\frac{D_p(I,\mathbf{x},\mathbf{x}+r)}{V(I,\mathbf{x})}\right)$	GW
ADC	$\sum_{j=0}^{N_b}(S_j(\tau(\mathbf{x})) - \widehat{S}_j(\mathbf{x}))^2$	GW
bWei	$\sum_{j=0}^{N_b} W_j(S_j(\tau(\mathbf{x})) - \widehat{S}_j(\mathbf{x}))^2$	Joint GW

The aforementioned methodologies have been built as sequential approaches (except for our proposal) as they focus on registration only. Therefore, ADC has to be estimated once registered the DWI dataset. For this purpose, we have resorted to the NLLS method described in Section 3.2.2. For the PW framework, the b_0 image have been chosen to be the reference.

3.4.2 Evaluation for synthetic data

We have first carried out synthetic experiments with the data provided by the XCAT computational phantom on which different BHs were simulated for each image on each slice. Therefore, we can measure the error in the estimation of the simulated deformation field, as well as the accuracy in ADC estimation for all methodologies in Section 3.4.1.

We have considered two different scenarios for this synthetic experiment. For the first, we have made use of the simulated dataset as described in Section 3.3. While, for the second we have convolved the GT ADC map with a Gaussian blurring kernel ($\sigma = 5$) so as to generate non-smooth simulated datasets, i.e. with higher TV.

We have also tested, on the smooth ADC scenario, the added benefits of our method with respect to each of its constituents; specifically, we compare the results obtained from solving the joint problem, as posed in Eq (3.4) with respect to solving, on one hand, Eq. (3.8) setting $\mathbf{T}$ as the null transformation —i.e., a smoothed estimation-only solution— and, on the other hand, solving Eq. (3.9) —i.e., the non-smoothed joint solution ("Only Reg"). Additionally, the joint problem has been solved once more, but with unitary invariant weights in order to asses the influence of the weights in the estimation ("Non-weighted").

Finally, on the smooth ADC scenario again, we have also studied the effects of the aforementioned simulated artifacts in a disaggregated manner and the ability of the proposed joint formulation to deal with them in terms of error. To that end, we have redesigned the XCAT computational phantom in order to develop three additional datasets, each of them affected only by a unique artifact: respiratory motion (different BH), exponentially decreased SNR and geometric distortions. These error measures have also been calculated within a set of 10 *b-values*. Complementary, we have repeated the same procedure with a subset of 6 *b-values*, particularly $b \in \{0, 20, 100, 500, 1000, 1500\} s/mm^2$, in order to assess the influence of the simulated artifacts when a smaller dataset is available.

3.4.3 Evaluation on real data

For the real data, due to the absence of a ground-truth, validation has to be performed by indirect measures and qualitative visual assessment.

We, therefore, propose an indirect validation procedure based on the estimates of the ADC obtained with different subgroups of *b-values*, with lengths of $N_b = [3, 6, 8]$, out of the total number of *b-values* available (as indicated in Section 3.3 this number is $N = 10$

for all patients). Basically, we perform $K = \binom{N}{N_b}$ ADC estimations of each slice for each patient, changing only the combination of the *b-values* (and its corresponding images) that enter the optimization problem.

Ideally, for a fixed N_b, in the absence of noise, distortions and misalignments, all the K ADC estimations should be pixelwise equal. Therefore, a natural measure of the reproducibility of the estimation method for a predefined value of N_b is the similarity between these ADC estimates from the different *b-value* combinations. Accordingly, we have calculated the absolute differences between each possible pair out of the K ADC estimates, giving rise to $K(K-1)/2$ comparisons for each pixel in the liver.

3.5 Results

3.5.1 Results on Synthetic Data

In this section, we test the ability of the proposed methodology for MC, distortion correction and robust ADC estimation. We used the simulated XCAT dataset to measure the relative error (over the previously defined ROI χ) on the ADC estimates for the methodologies described in Section 3.4.1.

In Fig. 3.2 we show the boxplot diagrams of the relative error distributions from ADC estimation as a measure of accuracy in MC and distortion correction. Besides, we have also measured the error module for the estimation of the deformation fields for both scenarios described in Section 3.4.2, the originally simulated ADC and the blurred one. The variance of the estimations is greatly diminished when performing previous registration, with the exception of the SSD metric which, as monomodal metric, presents much worse figures.

Mann-Whitney U-tests have also been performed for each pair of ADC error distributions (for the original scenario), showing significant differences for most cases. The results are shown in Table 3.4. For all the tests we describe, data are taken 10 pixels apart (images were decimated by a factor of ten before selecting the samples) to diminish correlation in the datasets. Significant differences have always been found when comparing our proposal (bWei) with different methodologies and metrics ($p < 10^{-6}$ for most of them).

Fig. 3.3 shows the boxplot diagrams of the error distributions in ADC estimation for the problems described in Section 3.4.2. Namely, the joint formulation (both weighted and non-weighted), as well as the only-registration and only-estimation problems.

Significant differences have been found when performing Mann-Whitney U-Tests on the relative error distributions between the estimation obtained from the joint formulation with respect to the other solutions, $p < 10^{-6}$ for estimation-only and unitary weighted joint formulations and $p = 0.00051$ for the non-smoothed solution ("Only Reg").

Finally, in Fig. 3.4 we show the boxplot diagrams of the error distributions in ADC estimation for the datasets described in Section 3.4.2 affected only by a unique artifact. Namely, respiratory motion, geometrical distortion and noise. As the figure indicates, for

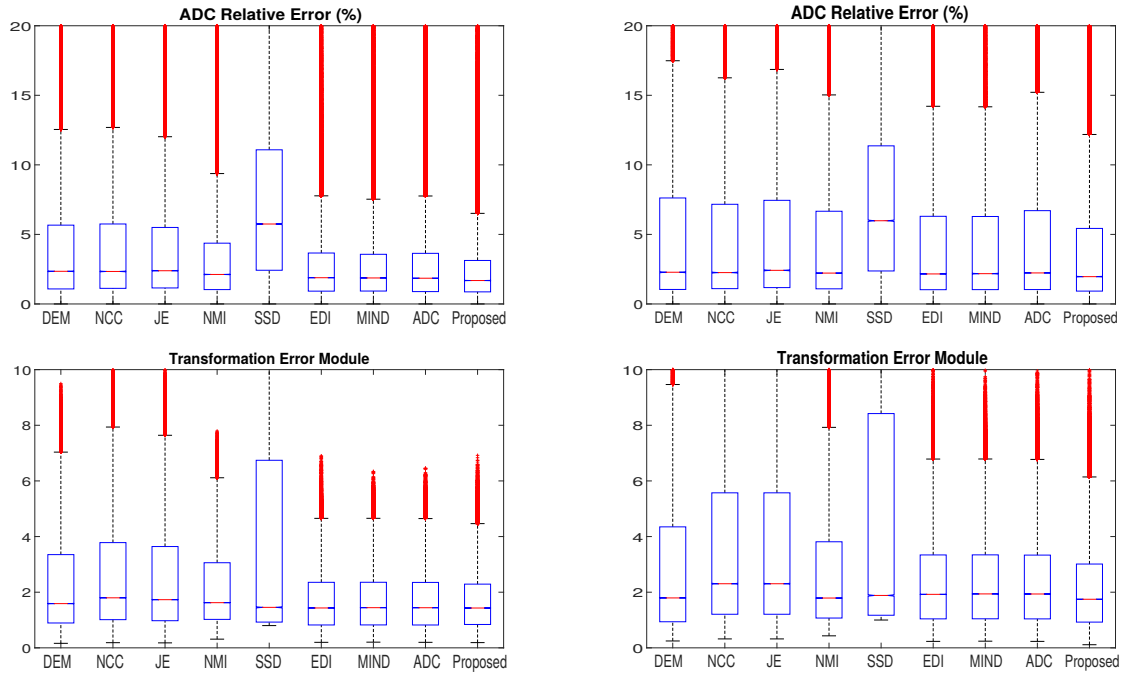

FIGURE 3.2: Relative error on ADC estimation and module error (mm) for the deformation field obtained with the different methodologies. Figures on the left show the results for the originally simulated scenario, while the ones on the right are taken from the high TV scenario.

TABLE 3.4: Mann Whitney U-tests on the ADC error distributions among different implemented metric under PW and GW paradigms for the originally simulated scenario (low TV).

Methods	NCC	JE	NMI	SSD	EDI	MIND	ADC	bWei
DEM	0.4902	0.1537	5.73×10^{-5}	$< 10^{-9}$	$< 10^{-6}$	$< 10^{-6}$	$< 10^{-6}$	$< 10^{-6}$
NCC	-	0.4465	2.69×10^{-6}	$< 10^{-9}$	$< 10^{-6}$	$< 10^{-6}$	$< 10^{-6}$	$< 10^{-6}$
JE	-	-	$< 10^{-6}$	$< 10^{-9}$	$< 10^{-6}$	$< 10^{-6}$	$< 10^{-6}$	$< 10^{-6}$
NMI	-	-	-	$< 10^{-9}$	6.01×10^{-6}	$< 10^{-6}$	$< 10^{-6}$	$< 10^{-6}$
SSD	-	-	-	-	$< 10^{-9}$	$< 10^{-9}$	$< 10^{-9}$	$< 10^{-9}$
EDI	-	-	-	-	-	0.424	0.1636	6.19×10^{-6}
MIND	-	-	-	-	-	-	0.5604	0.00102
ADC	-	-	-	-	-	-	-	0.00323

the 6 *b-values* case, noise has a higher influence on the outcome whilst distortion seems to lead in the 10 *b-values* case.

Mann-Whitney U-tests were performed between each error distribution and its counterpart in the 6 *b-values* subset ($p < 10^{-6}$ for all these cases). Significant differences were also found between each pair of error distributions within the same dataset, obtaining $p < 10^{-3}$ for all cases regardless of the number of *b-values*.

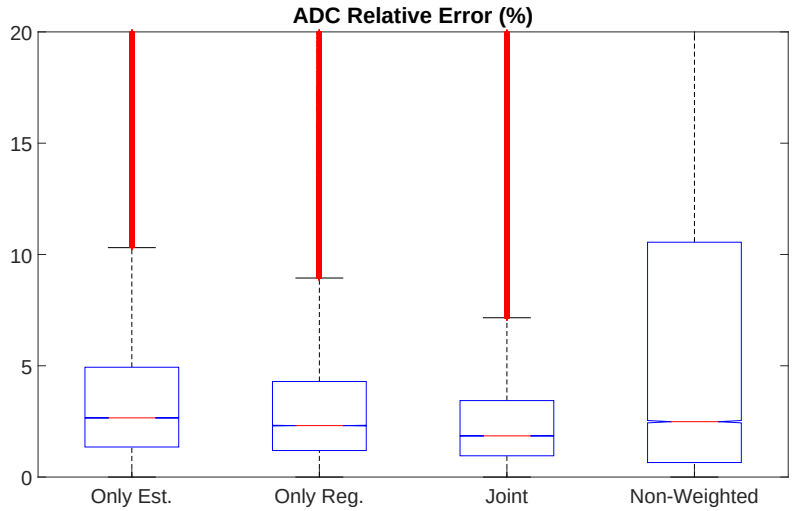

Figure 3.3: Relative error on ADC estimates for the different problems solved.

3.5.2 Results on Real Data

Evaluation on real data will be performed according to the scheme described in Section 3.4.3. As sketched in Fig. 3.5, we have used the cumulative distribution of the absolute differences on the ADC estimates obtained for each metric and registration procedure listed in Table 3.3 to show the reproducibility of the different methodologies for different number of acquired *b-values*.

Additionally, in Table 3.5 we show the normalized area Area Under the Curve (AUC) for the cumulative distributions sketched in Fig. 3.5. Notice that, if perfect estimations were obtained, the cumulative distribution would draw a unitary step function (AUC = 1), so that these parameters well reflect reproducibility of the methods.

Table 3.5: Normalized AUC for the cumulative distribution of ADC absolute differences among the different implemented metrics with different number of *b-values*.

Methods	DEM	JE	NCC	NMI	SSD	EDI	MIND	ADC	bWei
N_b= 8	0.8623	0.8518	0.8517	0.8385	0.7779	0.9075	0.9065	0.8360	0.9087
N_b= 6	0.8414	0.8381	0.8396	0.8394	0.7524	0.8791	0.8788	0.7849	0.8887
N_b= 3	0.8220	0.8333	0.8372	0.8337	0.7280	0.8754	0.8166	0.7417	0.8819

Finally, in Fig. 3.6 we show some snapshots on the resultant estimated ADC to visually notice the topology preserving capability of the proposed methodology, when compared to the one obtained with the unregistered sequence.

Final execution time will mostly depends on the computation time per iteration (maximum iterations set to 20 for all methods) that will be dominated by the time required for

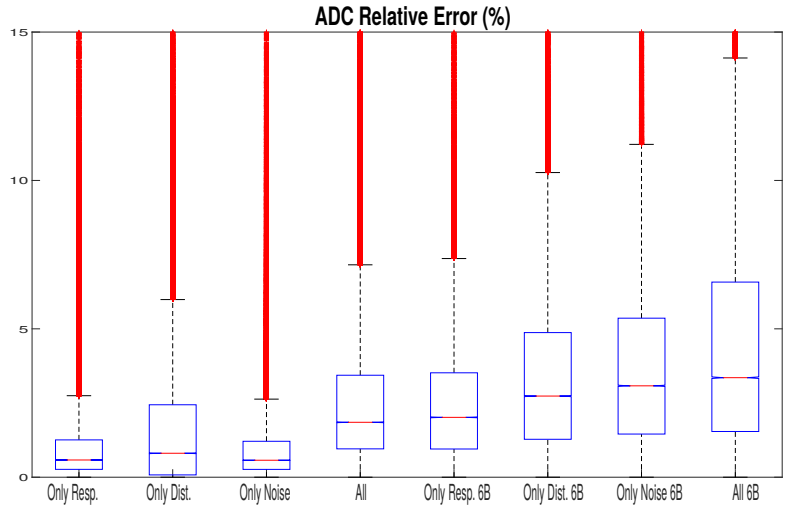

Figure 3.4: Relative error on ADC estimates in presence of different artifacts with different number of *b-values*.

calculating the metric and its derivative. The proposed algorithm has been implemented using MATLAB 2016a without any specific code optimization. All experiments have been run on a Intel Core i5-4210M processor with 8GB RAM and 2 cores (2 threads/core). Our algorithm requires approximately 40s to complete the whole process for a given slice of the images described in Table 8.1. However, processing times would be significantly decreased (less than 3s) when using GPU.

3.6 Discussion

Most common multimodal registration approaches on DWI data use general purpose registration similarity metrics, the minimization of which bring forth maximizing unspecific structural similarities between the images; therefore, the estimation problem is a byproduct but not the specific target. Nonetheless, the methodology here proposed makes use of a metric that is directly related to the specific problem to be solved. Thus, we can establish a direct correspondence between the performance of the registration procedure and the goodness-of-fit to the data model for the estimation stage.

From the results observed in Fig. 3.2, we can see that the methodology here presented is effective at improving robustness when obtaining direct ADC estimates and provides accurate deformation measures from DWI sequences as compared to other state-of-the-art techniques in both considered scenarios. Notice that, the proposed methodology is able to accurate recover deformation fields without introducing any bias in estimation, although robustness of both measures is greatly diminished in the second scenario. Hence, the introduced spatial TV term plays an important role, specially in very noisy environments,

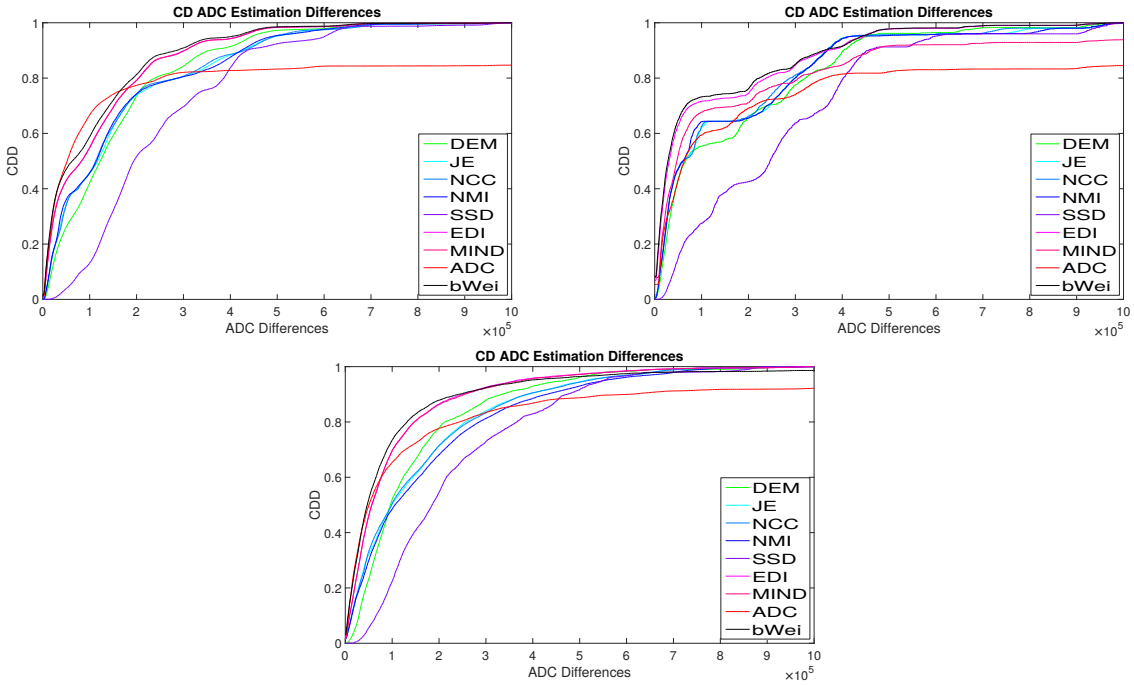

Figure 3.5: Cumulative distribution of absolute differences on ADC estimates for the different methods with a fixed number of *b-values*: $N_b = 3$ (left), $N_b = 6$ (right) and $N_b = 8$ (down).

since succeeds in preserving the local structure of the liver while getting rid of the residual noise present in the images. On the other hand, the introduction of the GW registration scheme leads to a robust registration of the different *b-value* images, avoiding the implicit bias that stems from the selection of an image template, which is mandatory in PW registration. These terms seem to have a higher impact than the weighting defined in Eq. (3.7) since our GW methodology used with metrics EDI, MIND and ADC is closer to bWei than other methods defined at the upper part of Table 3.3.

Fig. 3.3, conclusively supports the hypothesis that the joint formulation is a better option than letting the methods run in isolation and the introduction of weighting parameters in the metric significantly improves the robustness in the estimation. Nevertheless, we should stress that the parameters involved in the estimation problem, particularly the ones related to the spatial TV term in Eq. (3.8), may greatly influence performance in this step. A fine tuning of these parameters is needed in order to prevent the TV term from oversmoothing the structural boundaries so that its impact is just a mild denoising. Trade-off parameters within the Reg function in Eq. (3.4) (see Eq. (3.9)) are not so critical in this scenario due to the inherent smoothness of the deformation fields of the phantom. This seems to be the reason why differences in performance between the sequential registration-estimation problem and the joint formulation were not so distant to each other, albeit statistical differences in favor of our method do exist.

Apart from using a metric that is targeted to the specific estimation problem, the

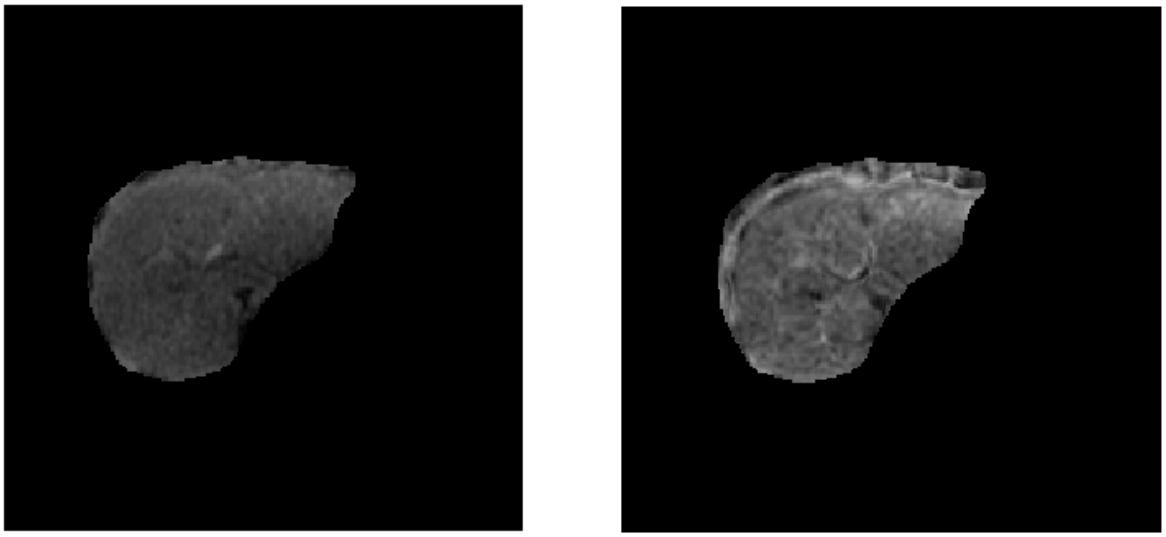

Figure 3.6: Estimated ADC from the original sequence and the registered one (from left to right).

introduction of the weights in our metric has a twofold effect, namely, both to make the metric robust against noise as well as to avoid the effects of geometric distortion. As shown in Fig. 3.4, with our proposed metric, the influence of the artifacts over the whole simulation differs when changing the number of *b-values*. For the experiment with 6 *b-values*, the most prevalent artifact is noise, whereas for the 10 *b-values* experiment, distortion leads. The influence of noise naturally decreases when increasing the number of samples, however, this effect is less noticeable for distortion. This may explain why a formulation which explicitly takes into account both sources of error has overcome other estimation approaches. The introduced weights represent a trade-off between *b-value* images avoiding biases towards low *b-values* in registration, being more preponderant as larger differences in the SNR are found.

Validation on real data (see Fig. 3.5) has been carried out using reproducibility measures based on ADC differences. Reproducibility has been tested using datasets of 3,6 and 8 *b-values*. It can be observed that our method presents the highest figures, specially if compared to its non-weighted counterpart (Kornapoulos et al., 2016). This could be due to ADC-dependent weights preventing from non-reliable transformations present mainly on low SNR images. Differences, as it is expected, diminish as the number of *b-values* increases. We have assumed Rician noise, although for SENSE acquisitions it may not be true, specially for lower *b-values*. This would result in a biased ADC estimation, which may not be assessed by reproducibility measures.

From visual inspection, we conclude that our approach is able to better preserve structure, as it reveals tissues boundaries more clearly (tissue heterogeneity, anatomical structure) in the final reconstructed ADC (see Fig. 3.6) for both lobes of the liver.

3.7 Conclusions

In this paper we have proposed a novel approach to jointly register diffusion weighted images as well as to provide robust ADC estimates; to this end, we have defined a cost function that embeds a data-fidelity term specifically designed for the specific ADC estimation problem, which also incorporates a set of weights that penalize acquisitions with a lower SNR.

Experimental results demonstrate that the GW approach helps to cope with motion artifacts and corrects for geometrical distortions compared to PW approaches, while the joint formulation showed significant improvements in robustness and reproducibilty of ADC estimates with respect to other methods described in the literature.

We are currently exploring how to adapt this estimation method to accelerated acquisition schemes for automatic ADC-maps reconstruction.

Acknowledgments

This work was partially supported by the Spanish Ministerio de Ciencia e Innovación under Research Grant TEC2013-44194-P, the European Regional Development Fund (ERDF-FEDER) under Research Grant TEC2014-57428-R, the Spanish Junta de Castilla y León under Grant VA069U16 and the European Social Fund (ESF-FSE).

Chapter 4

Robust Estimation of the Apparent Diffusion Coefficient Invariant to Acquisition Noise and Physiological Motion

Published as:

Sanz-Estébanez, S.[1], Pieciak, T.[2], Alberola-López, C.[1] and Aja-Fernández, S.[1] (2018). Robust estimation of the apparent diffusion coefficient invariant to acquisition noise and physiological motion. *Magnetic Resonance Imaging*, 53:123-133.

[1] Laboratorio de Procesado de Imagen, Department of Teoría de la Señal y Comunicaciones e Ingeniería Telemática, ETSIT, Universidad de Valladolid, Campus Miguel Delibes s.n., 47011, Valladolid, Spain.

[2] AGH University of Science and Technology, al. Mickiewicza, 30-059, Kraków, Poland.

In this work we have proposed a methodology for the estimation of the apparent diffusion coefficient in the body from multiple breath hold diffusion weighted images, which is robust to two preeminent confounding factors: noise and motion during acquisition.
Methods: We have extended a method for the joint GW multimodal registration and apparent diffusion coefficient estimation, previously proposed by the authors, in order to correct the bias that arises from the non-Gaussianity of the data and the registration procedure.
Results: Results show that the proposed methodology provides a statistically significant improvement both in robustness for displacement fields calculation and in terms of accuracy for the apparent diffusion coefficient estimation as compared with traditional sequential approaches. Reproducibility has also been measured on real data in terms of the distribution of apparent diffusion coefficient differences obtained from different *b-values* subsets.
Conclusions: Our proposal has shown to be able to effectively correct the estimation bias by introducing additional computationally light procedures to the original method, thus providing robust apparent diffusion coefficient maps in the liver and allowing an accurate and reproducible analysis of the tissue.

Keywords: Diffusion Weighted Imaging; Acquisition Noise; Patient Movement Correction; Multimodal Groupwise Registration; Apparent Diffusion Coefficient

4.1 Introduction

DW-MRI is a non-contrast technique sensitive to molecular displacement which provides the capability to non-invasively assess microstructure organization within the tissue and cell membrane density upon differences in water proton mobility (Jones, 2010). DW-MRI is increasingly employed for tissue evaluation as it provides characteristic quantitative parameters of the tissue.

Among the different values that can be derived from the diffusion signal, the ADC is the most commonly used biomarker, which is obtained after applying a monoexponential decay model to the diffusion images of isotropic tissues (Le Bihan et al., 1986). ADC values have shown to be accurate indicators of tumor response to therapy (Kim et al., 1999; Thoeny and Ross, 2010), as well as the severity of liver fibrosis and cirrhosis (Sandrasegaran et al., 2009). However, in order to thoroughly validate the ADC as an imaging biomarker, a robust parameter estimation methodology suitable for multiparametric acquisitions is necessary. Unfortunately, quantitative ADC mapping is affected by multiple artifacts and confounding factors, including motion-related errors (Jha and Rodríguez, 2012), image distortions caused by susceptibility, and noise-related effects (Aja-Fernández et al., 2013). Although most of the proposed estimation techniques in the literature have focused on the reduction of these artifacts, those methods have usually considered ADC estimation and the reduction of the different confounding factors and artifacts as two different problems that are usually treated separately. Nonetheless, even applying the most complex models and estimation techniques over the DWI, the confounding factors may lead to false conclusions and wrong estimation of the ADC.

In abdominal organs such as the liver, kidney, or spleen, possible movement of the organ across the different *b-value* scans could result in image misalignment (Abhinav et al., 2016; Stephen et al., 2015). Consequently, computing the ADC map on a pixel-by-pixel basis is error-prone, highly likely incurring a boundary smearing (Theilmann et al., 2004). In clinical practice, to reduce this misalignment-related inaccuracies, the ROI should be individually segmented in the different *b-value* images to extract the mean signal intensity at this region pixels for the different *b-values* and only then, compute the ADC. However, this methodology does not explicitly account for tissue heterogeneity, thus leading to biased ADC estimates in several clinically relevant scenarios.

BH acquisitions are also a popular way of avoiding respiratory motion artifacts with fast scan times. However, when images with different *b-values* have been acquired at different BHs and, subsequently, used for ADC estimation, considerable image artifacts can arise that stem from the fact that two BH states are never identical (McLeish et al., 2002).

Extensive research has been carried out on motion-robust sequences in MRI (Zaitsev et al., 2015). Most approaches have posed the registration problem from a PW standpoint. This procedure, however, is prone to an undesired bias towards the a priori chosen template (Wachinger and Navab, 2013). On the other hand, GW approaches are based on an image reference built out of the whole image set, so the bias mentioned above vanishes.

Recently, spatially-constrained approaches have also been proposed for liver DWI non-rigid registration (see Kurugol et al. (2017b); Taimouri et al. (2015)) grounded on MRF, showing an increase in robustness of diffusion parameter estimation by enforcing boundary consistency. GW approaches that use a MRF have also been described (Kornapoulos et al., 2016). However, the first two approaches are devised for the tracking of small structures and organs, thus requiring a higher degree of regularization. In addition, despite their elegant formulation, computational needs associated to MRF approaches are high. With respect to the latter, in Sanz-Estébanez et al. (2018), we showed a better performance of our scheme.

In Sanz-Estébanez et al. (2018), we have previously presented a novel light methodology for joint ADC estimation and GW registration of DW images in the liver. However, despite its good performance, the method did not take into account any possible bias introduced by the noise present in the data.

The presence of noise in the data is precisely a major issue in DW-MRI, since it greatly affects accurate evaluation of signal decay parameters (Dikaios et al., 2014), becoming specially critical at higher *b-values*, where the SNR decreases. Specifically, it has been shown that insufficient SNR can lead to spuriously low ADC values and a high variance (low precision) in estimation (Walker-Samuel et al., 2009; Aja-Fernández et al., 2013).

The principal source of noise in MR data is the heat source, i.e., the subject or object to be scanned (what is commonly referred to as thermal noise), followed by electronic noise in the receiver chain (Weisskoff et al., 1993; Aja-Fernández and Vegas-Sánchez-Ferrero, 2016), produced by the stochastic motion of free electrons in the coils and by eddy current losses in the patient, which are inductively coupled to the coils. There are different ways to cope with the noise component in the estimation of diffusion parameters; but, due to its random nature, a probabilistic modeling is a proper and powerful solution. The most accepted model is to consider that MR magnitude images are corrupted by Rician noise (Sijbers et al., 1998; Aja-Fernández and Vegas-Sánchez-Ferrero, 2016). This is a common assumption in MRI, mostly valid for single–coil acquisitions and multi–coil Parallel Imaging (PI) methods reconstructed with a spatial matched filter, like SENSE (Pruessmann et al., 1999), for instance. In the former, noise depends on a single scalar parameter, σ while on the later, noise can become *non–stationary*, i.e., the variance of noise will depend on the position and σ must be replaced by $\sigma(\mathbf{x})$. Nonetheless, many data processing techniques still assume stationary distributions as a model, forgetting about the non-stationarity of the data. This is probably due to the fact that most noise estimators in the literature are based on a single noise variance (σ^2) value for all the pixels in the image.

It is usually argued that these noise-induced biases do not seriously affect MR images and an identically distributed signal-independent Gaussian model is commonly assumed. However, this may not be suitable when performed over images with relative low SNR, which is the case in DW-MRI in higher *b-values* (Thunberg and Zetterberg, 2007), since it may lead to the introduction of a noise-induced bias which greatly affect subsequent estimations.

There are in general two ways to cope with noise in estimation: first, to include the noise model into the estimation pipeline and second, to remove or reduce the noise with some filtering or denoising method. Many authors have precisely introduced Rician statistics in the estimation of diffusion models (Walker-Samuel et al., 2009; Jha and Rodríguez, 2012; Landman et al., 2007) to accurately retrieve ADC estimates, thus significantly increasing computational complexity. On the other hand, denoising techniques (Aja-Fernández et al., 2008; Aja-Fernández et al., 2008; Manjón, José V and Coupé, Pierrick and Concha, Luis and Buades, Antonio and Collins, D Louis and Robles, Montserrat, 2013; Tristán-Vega et al., 2012; Reischauer and Gutzeit, 2017) have also been developed as preprocessing steps with the purpose of removing the noise-induced bias from the data for the sake of robustifying estimation in subsequent stages.

The purpose of this paper is to define a complete framework that allows the ADC estimation from DW-MRI data taking into account two preeminent confounding factors: the motion of the patient and the physiological noise present in the data. To that end, the work is grounded on a methodology for joint ADC estimation and GW registration that we have previously presented in Sanz-Estébanez et al. (2018). Although that scheme has shown to be able to successfully cope with the movement of the patient, it did not take into account any model for the noise. As a consequence, some steps of the procedure may introduce a significant bias. In order to cope with both confounding factors simultaneously, we have incorporated within the original pipeline proper methods which correct for the interpolation bias that arises from the weighting of non-Gaussian (skewed) distributed data, and which, accordingly, improve the ADC estimation. We have shown that the complete algorithm yields higher quality ADC maps when compared to other previously reported approaches.

4.2 Theory

4.2.1 Signal and Noise Modelling

In order to obtain relevant information from a limited amount of acquisitions, it is necessary to assume a diffusion model that allows the estimation of the diffusion measures related to the properties of the different tissues. To that end, many different models have been proposed in the literature (Le Bihan et al., 1986; Le Bihan et al., 1988; Kurugol et al., 2017a), where the simplest is the assumption of a monoexponential model to the DW signal decay (Le Bihan and Breton, 1985). Such model gives a quantitative diffusion value that has proved to successfully characterize different tissues in the body. This model will be adopted in this paper; nonetheless, the methodology here proposed could be easily extended towards more complex diffusion models.

The acquired complex signal in the monoexponential model is defined as:

$$A(\mathbf{x}) = A_0(\mathbf{x})e^{-b\cdot \mathrm{ADC}(\mathbf{x})}, \tag{4.1}$$

where b is the weighting of the diffusion sequence, the so-called *b-value* (Stejskal and Tanner, 1965), which determines the strength of applied diffusion weighting. $A_0(\mathbf{x})$ denotes the complex noiseless signal intensity obtained with a null diffusion gradient. This noise-free DW signal is not available, since the scanner provides a noise corrupted version. For practical purposes, it is usually assumed that the noise in the image domain is a zero-mean, spatially uncorrelated Gaussian process, with equal variance in both the real and imaginary parts (Aja-Fernández and Vegas-Sánchez-Ferrero, 2016):

$$S(\mathbf{x}) = A(\mathbf{x}) + N(\mathbf{x}; 0, \sigma^2), \tag{4.2}$$

with $A(\mathbf{x})$ being a noise-free signal and $N(\mathbf{x}; 0, \sigma^2)$ is a complex Gaussian distributed noise with zero-mean and a constant variance σ^2. In the case that the data is acquired by several receiving coils, the exact same distribution is assumed for all of them.

In clinical and research scenarios, however, it is more usual to work with magnitude data rather than its complex representation. Thereby, in its simplest form, the magnitude information is retrieved by applying the absolute value operator over the complex signal, i.e., $M(\mathbf{x}) = |S(\mathbf{x})|$. Hereinafter, we will work with the magnitude images M. Since the modulus operator is not a linear transformation, the Gaussianity assumption is no longer valid in magnitude data. Hence, the noise becomes signal-dependent and it is modeled according to Rician statistics (Aja-Fernández and Vegas-Sánchez-Ferrero, 2016).

In advanced acquisition techniques that involve PI, interpolation and other reconstruction techniques, different noise models may arise. However, many of them may yield to non-stationary Rician distributions: the noise variance $\sigma^2(\mathbf{x})$ is no longer constant, but it depends on the position $\mathbf{x}$ within the image. Hereinafter, we will consider both variants, i.e., stationary and non-stationary Rician distributed magnitude DW data. The method here proposed can be easily extended to other noise models, such as the nc-χ distribution.

4.2.2 Motion Correction and ADC estimation

To overcome the issues related with the misalignment between the different *b-value* images, we must accurately retrieve the motion compensating displacement fields, so that we can obtain a consistent representation of the organ of study, thus avoiding blurred ADC estimates and motion artifacts. Due to the significant signal intensity dropout observed in the images when increasing the *b-value*, it is mandatory to resort to multimodal methodologies.

Therefore, we have made use of the method we have previously proposed in Sanz-Estébanez et al. (2018), a methodology to jointly estimate the ADC map and register DW-MRI sequences acquired in different BH states. The processing pipeline has been depicted in Fig. 4.1. Briefly stated, the procedure performs an elastic multimodal GW registration step in which the transformation $\boldsymbol{\tau}$ (see Eq. (4.4)) has been defined as a combination of B-spline FFDs (Rueckert et al., 1999). The objective function to be optimized for the registration problem presents the function H in Eq. (4.4) as data fidelity term; this

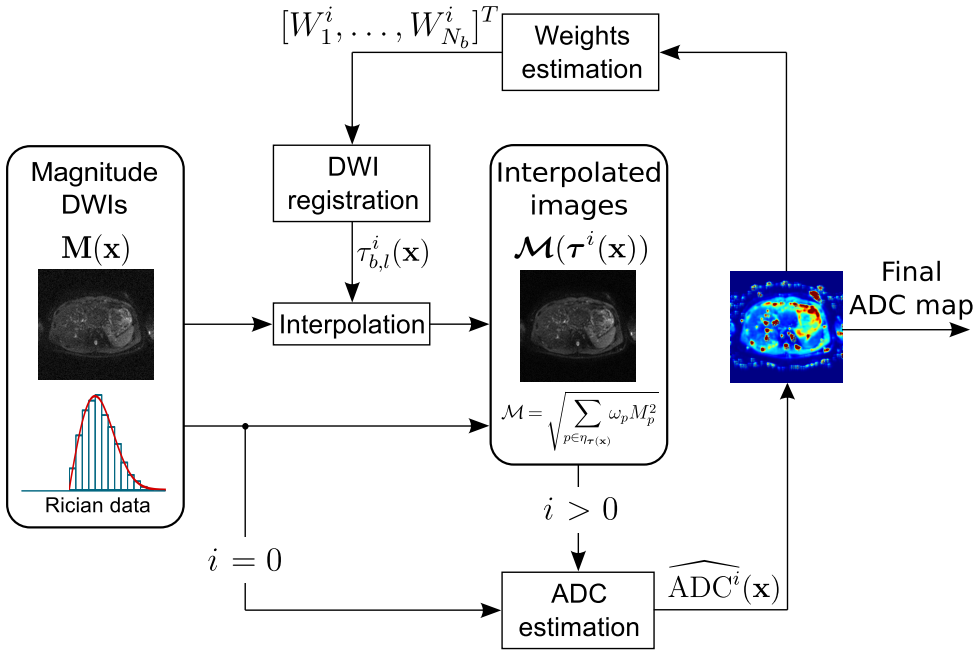

Figure 4.1: Pipeline of joint registration and ADC estimation under Gaussian assumptions. Superscript (i) indicates number of iteration, while subscripts b and l indicate *b-value* of the image and displacement direction, respectively.

function is based on Eq. (4.1) as the FW model, which should match the measured DW magnitude data as defined in Sanz-Estébanez et al. (2018):

$$H(\mathbf{M}, \mathrm{ADC}, \boldsymbol{\tau}) = \sum_{b=1}^{N_b} W_b^i(\mathcal{M}_b(\tau^i(\mathbf{x}))) - \widehat{M}_b(\mathrm{ADC}^i(\mathbf{x})))^2, \tag{4.3}$$

where $\widehat{M}_j$ is the estimated intensity value (in magnitude) from the current (i-th) ADC estimate obtained by applying Eq. (4.1) for a given *b-value* b out of a total of N_b. The proposed metric additionally incorporates a N_b-component vector $\mathbf{W}$ which weighs each component of the data fidelity term according to the expected signal content, i.e., weights are a decreasing function of the *b-value* (Veraart et al., 2013). This weighting vector is initially constant and unitary but their components are updated along the iterations. The transformation $\boldsymbol{\tau}$ has been driven to be smooth by means of a penalty term based on its first and second order derivatives, resulting in the following optimization problem:

$$\boldsymbol{\tau}^i = \arg\min_{\boldsymbol{\tau}} \int_\chi \left(H(\mathbf{M}, \widehat{\mathrm{ADC}^i}, \boldsymbol{\tau}) + \sum_{b=1}^{N_b} \sum_{l=1}^{L} \lambda_1 \left(\sum_{l'=1}^{L} \left(\frac{\partial \tau_{b,l}(\mathbf{x})}{\partial x_{l'}} \right)^2 \right) + \lambda_2 \left(\sum_{l'=1}^{L} \sum_{l''=1}^{L} \left(\frac{\partial^2 \tau_{b,l}(\mathbf{x})}{\partial x_{l'} \partial x_{l''}} \right)^2 \right) \right) d\mathbf{x}, \tag{4.4}$$

where $\mathbf{M}$ are the magnitude images and $\tau_{b,l}$ represents each of the displacement components of the transformation (with $L = 2$ for the 2D case) for each *b-value* image. Derivatives have been approximated by finite differences in the spatial dimension $\mathbf{x}$. The influence of the regularization term has been balanced by λ_1 and λ_2. Quadratic interpolation has been used to obtain the intensity of the deformed images on a rectilinear grid.

For the ADC estimation, the optimization functional comprises the same weighted metric H as used for the registration procedure and an additional TV regularization term on the ADC map to ensure smooth estimates. Specifically:

$$\widehat{\mathrm{ADC}^i} = \arg\min_{\mathrm{ADC}} \int_{\chi} \left[H(\mathbf{M}, \mathrm{ADC}, \boldsymbol{\tau}^{i\text{-}1}) + \beta ||\mathrm{ADC}(\mathbf{x})||_{\mathrm{TV}} \right] d\mathbf{x}, \tag{4.5}$$

with $||\mathrm{ADC}(\mathbf{x})||_{\mathrm{TV}}$ the spatial TV on the ADC which is controlled by a non-negative constant β. We should stress that the parameters involved in the estimation problem, particularly the ones related to the spatial TV term in Eq. (4.5), may greatly influence the performance of this step. A fine tuning of these parameters is needed in order to prevent the TV term from oversmoothing the structure in the ADC map so that its impact is just a mild denoising. However, notice that, by placing the TV ADC estimation at the end of the pipeline, it will not interfere with other stages of the procedure, thus keeping magnitude images untouched and simplifying parameter setting.

In this original formulation, no noise model has been taken into account. That could not be a problem in Gaussian distributed data, but in distributions with certain skewness (like Rician, Rayleigh, nc-χ or Gamma), operations like those carried out in Fig. 4.1 are known to produce certain bias that can seriously affect the output values of the different steps (specially due to the iterative nature of the procedure) and consequently the accuracy of the final ADC estimate. In the following section, those biases introduced by the presence of noise, will be analysed and properly corrected.

4.2.3 Noise-induced Bias Correction

According to the scheme described in Fig. 4.1, the ADC has been estimated from the registered magnitude images, which have been obtained through interpolation using the transformation $\boldsymbol{\tau}$ previously estimated. The interpolated (squared) images $\mathcal{M}^2(\boldsymbol{\tau}(\mathbf{x}))$ have been obtained as:

$$\mathcal{M}^2(\boldsymbol{\tau}(\mathbf{x})) = \sum_{\mathbf{x}_p \in \eta_{\boldsymbol{\tau}(\mathbf{x})}} \omega_p M^2(\mathbf{x}_p), \tag{4.6}$$

with $\eta_{\boldsymbol{\tau}(\mathbf{x})}$ a square neighborhood around the transformed pixel. If the original magnitude data $M(\mathbf{x})$ are assumed to follow a Rician distribution, data after a rigid registration will still remain Rician distributed, since no operation are done on the values of the different pixels, only on the positions. Thus, the squared interpolation can be seen as the weighted sum of squared Rician signals. We have calculated the expected value of the output (for

the sake of simplicity, we drop spatial dependence and denote transformed pixel as j with neighborhood η_j):

$$\begin{aligned}\mathbb{E}\left\{\mathcal{M}_j^2\right\} &= \mathbb{E}\left\{\sum_{p\in\eta_j}\omega_p M_p^2\right\} = \sum_{p\in\eta_j}\omega_p\mathbb{E}\left\{M_p^2\right\} \\ &= \underbrace{\sum_{p\in\eta_j}\omega_p A_p^2}_{\text{original interpolation}} + \underbrace{2\sum_{p\in\eta_j}\omega_p\sigma_p^2}_{\text{bias}}.\end{aligned} \tag{4.7}$$

It can be seen that the last term corresponds to a bias, which should not be neglected in low SNR scenarios. Besides, this bias will be fed back inside the optimization loop, thus increasingly affecting ADC estimates.

In order to remove this bias in Eq. (4.7), we have decided to avoid any filtering of the data. Although filtering techniques have shown proper performance in many estimation problems, we have preferred to keep the original data whenever possible, to avoid any loss of information that overfiltering may produce. In this case, we can easily remove this noise-induced bias by estimating the signal $\sum_{p\in\eta_j}\omega_p A_p^2$. If we know the value of the variance of noise for each pixel in the image σ_p^2, we can simply define the interpolated signal as:

$$\left(\mathcal{M}_j^{\mathrm{C}}\right)^2 = \mathcal{M}_j^2 - 2\sum_{p\in\eta_j}\omega_p\sigma_p^2. \tag{4.8}$$

The non-squared signal will be finally obtained as:

$$\mathcal{M}_j^{\mathrm{C}} = \sqrt{\max\left\{\sum_{p\in\eta_j}\omega_p M_p^2 - 2\sum_{p\in\eta_j}\omega_p\sigma_p^2,\ 0\right\}}. \tag{4.9}$$

The maximum operator has been introduced to avoid any negative term inside the square root. If noise is assumed to be stationary, the variance of noise is the same for all the image and therefore the parameter σ_p^2 simply becomes σ^2.

The ADC estimation pipeline with the inclusion of the interpolation bias correction is shown in Fig. 4.2, where $\mathbf{W}^0$ represents the initial weighting parameter and $\widehat{\sigma}^2(\mathbf{x})$ is an estimate of the noise variance. For the sake of generalization, we have assumed the latter to be spatially dependent.

It is worth pointing out that the suitability of the Rician bias correction procedure will greatly depend on the local SNR; when a high SNR is present, a Gaussian distribution can be assumed, so no bias should appear in the data. On the other hand, when the signal tends to zero, data becomes Rayleigh distributed, so Rician correction may be inaccurate. Therefore, our method will have more clear benefits on tissues with shorter T_2; overall, any acquisition parameter that affects either the signal content (T_E, mono or multi-echo

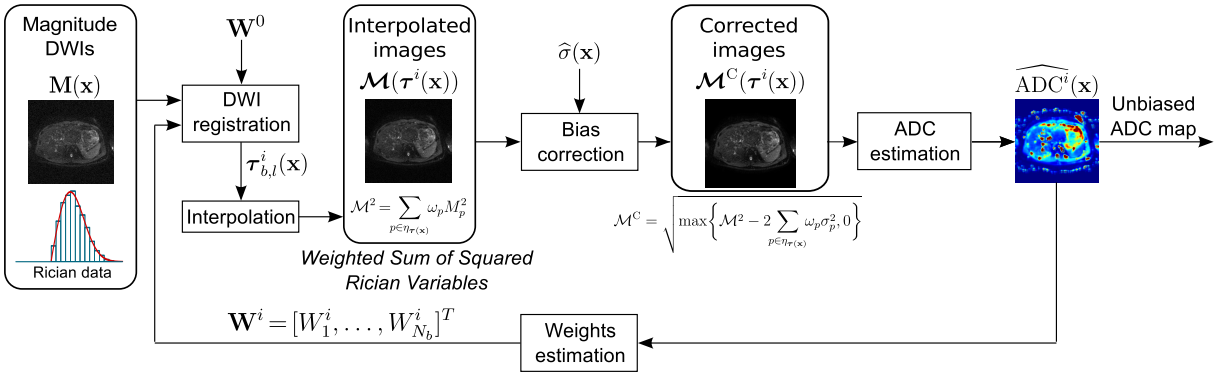

Figure 4.2: ADC estimation procedure with motion compensation and noise-induced bias correction. $\mathbf{W}^0$ is the initial weighting parameter and $\widehat{\sigma}(\mathbf{x})$ is an estimate of the noise variance.

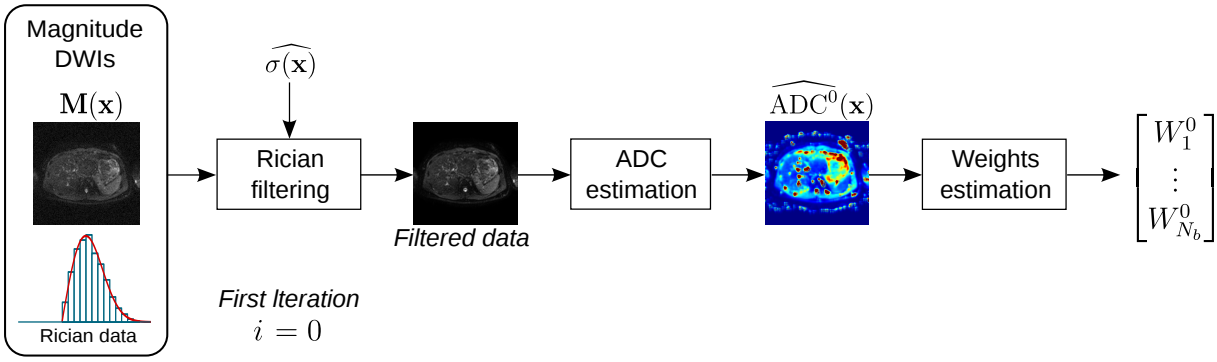

Figure 4.3: First iteration of the ADC estimation procedure: a Rician noise filtering step is introduced prior to the first estimation of the ADC and the registration weights.

sequence, *b-value*) of the noise (receiver bandwidth) will have an impact in the model suitability.

In order to obtain the initial weighting parameter $\mathbf{W}^0$, a previous ADC estimation has to be performed. The original Rician data is used for this estimation, since no prior registration is carried out. As a consequence, the noisy data are directly used in this estimation. In order to reduce the bias and variance of this previous step, we propose to introduce a Rician noise filter. The filtering will only be used in this first step. Once the first set of weights is available, this filter is no longer needed, since the bias can be directly removed without any denoising step. That way, we avoid any possible overfiltering of the images that may distort anatomical details and hinder the subsequent registration. For clarity, Fig. 4.3 sketches the detailed processing in the initial iteration.

One major issue to be also considered in the proposed pipeline is a robust noise estimation. Our method requires the noise variance σ^2 to be known or at least (smoothly) estimated from the data both from the background and the foreground regions. Methodologies widely employed to estimate stationary σ^2 can be found in Aja-Fernández and Vegas-Sánchez-Ferrero (2016).

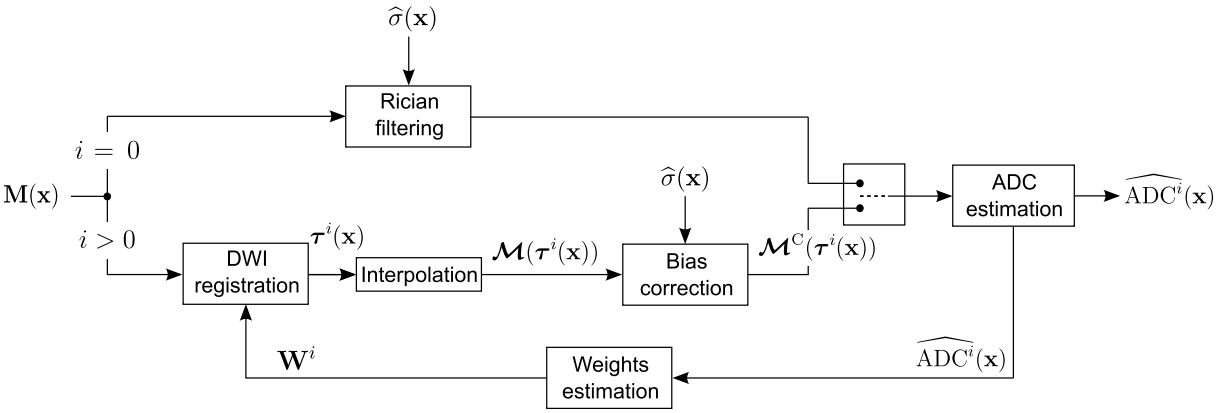

Figure 4.4: Pipeline of the proposed ADC estimation method. The method corrects the motion of the patient through registration while reduce the bias induced by Rician noise. The switch drawing indicates that ADC estimation takes as input images the ones coming from the upper branch only at first iteration whereas taking them from the lower branch in subsequent iterations.

For the non-stationary Rician case, a more complex noise estimation step is needed due to the spatially variant nature of the noise variance $\sigma^2(\mathbf{x})$. Therefore, we have resorted to a method proposed in Pieciak et al. (2017); Aja-Fernández et al. (2014), that uses a VST which transforms the magnitude data from a signal-dependent noise to an independent one. Afterwards, the spatial variability of noise has been retrieved by a homomorphic filtering. We have restricted the spatially variant noise estimators to operate only over a predefined region avoiding outer organs influence. This procedure is able to estimate the spatially variant noise maps using only a single image at fixed *b-value*, which is the case considered here. Noise parameters have been precalculated and then stored for its later use inside the algorithm loop.

Finally, for the sake of completeness, we show in Fig. 4.4 the whole processing pipeline in which the two-tier processing is clearly depicted.

4.3 Materials and Methods

4.3.1 Materials

4.3.1.1 Diffusion Simulation

DW-MRI synthesis has been subdivided in two parts. Firstly, the b_0 image has been simulated; in this work we made use of the well-known SE sequence, for the intensity values in the image are given by Bernstein et al. (2004):

$$A_0 \propto \rho(1 - e^{-T_R/T_1})e^{-T_E/T_2}, \tag{4.10}$$

where ρ, T_1, T_2 stand for the proton density, longitudinal and transverse relaxation times assigned for each simulated tissue in the volume, respectively.

Secondly, we have simulated isotropic diffusion by a random walk process using the Monte-Carlo method according to the methodology presented in Fieremans (2008). Particles were uniformly distributed in the voxel and the trajectory of a spin was generated by randomly moving the particle during each walk. The final diffusion signal, derived from the bulk phase shift Φ_i^k of the K simulated particles, can be numerically approximated (Du et al., 2016; Johansen-Berg and Behrens, 2009) by:

$$A = \frac{A_0}{K}\sqrt{(\sum_{i=1}^{K}\cos(\Phi_i^k))^2 + (\sum_{i=1}^{K}\sin(\Phi_i^k))^2}, \tag{4.11}$$

where A_0 is the noiseless b_0 image intensity from Eq. (4.10). Complex Gaussian noise has been added afterwards according to Eq. (4.2). We have simulated the following *b-values*: $b \in \{0, 10, 20, 50, 100, 200, 500, 1000, 1500, 2000\}$ s/mm^2. Sampling of *b-values* is finer for lower *b-values* according to Luna et al. (2012).

4.3.1.2 Synthetic Data

For validation, we have developed a synthetic diffusion phantom using a simulation environment based on the 4D XCAT phantom (Segars et al., 2010). The phantom is built from a whole body model that contains high level detailed anatomical labels, which feed a high resolution image synthesis procedure. The 4D XCAT phantom incorporates state-of-the-art respiratory and cardiac mechanics, which provide sufficient flexibility to simulate non-rigid motion effects on the liver from a user-defined parameter set. Therefore, the phantom will provide us not only with the images themselves, but also with GT deformation fields and a synthetic reference ADC map. For the ADC simulation, we have covered the whole volume of the liver (both lobes). The parameters of the bulk phase shift simulation have been set so that the GT simulated ADC values present a distribution with $1.6 \pm 0.4 \times 10^{-3}$mm^2/s (mean $\pm$ std).

The resulting simulated images are shown in Fig. 4.5, from which the global influence of the different BH on each image can be observed, as well as the simulated decreasing SNR (Rician stationary noise). Moreover, SENSE acquisitions have also been simulated. Therefore, non-stationary noise has been generated, which presents a spatial pattern that depends on a number of imaging parameters (Aja-Fernández and Vegas-Sánchez-Ferrero, 2016) such as, coils sensitivities, SENSE acceleration factor and correlation between coils. An exemplary synthetic non-stationary noise pattern is presented in Fig. 4.5.

4.3.1.3 Real Data

Additionally, we have performed MRI acquisitions over a sample of four healthy volunteers. Axial SENSE DWI and T2W TSE sequences have been acquired on a Philips

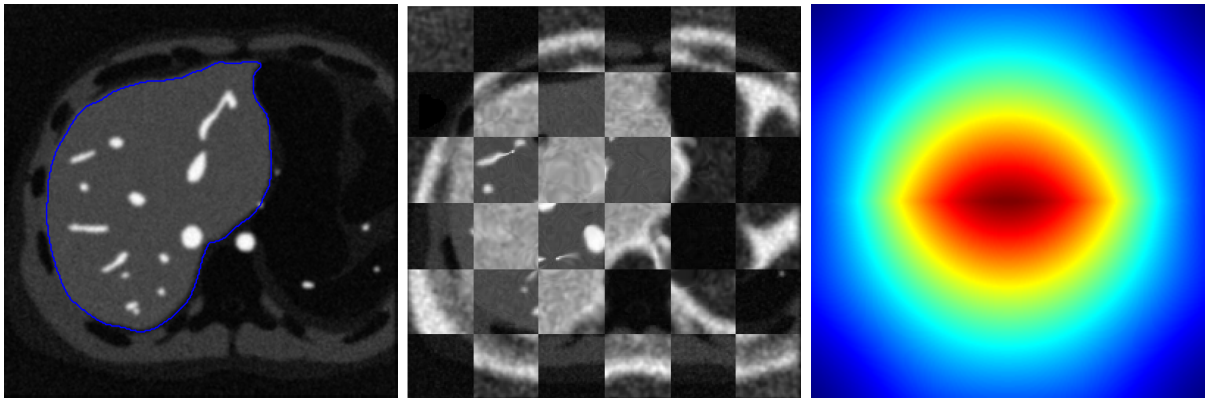

Figure 4.5: Axial slices of the simulated diffusion sequence. The figure on the left shows the image corresponding to the b_0, as well as the ROI (χ) boundary in blue, while the figure on the center is a checkerboard with *b-values* of 100 and 1000 s/mm^2. The figure on the right shows noise map for non-stationary Rician noise simulation with an acceleration factor of 2 and correlations between coils set to 0.1.

Achieva 3T scanner in each case of study. The latter will be used to manually delineate the whole liver as ROI χ on which meaningful measurements will be obtained. All the subjects signed the ordinary informed consent for the MR session and agreed in writing to share the resulting images for research purposes. Personal data were treated according to current legislation. Sequence details for real and synthetic data are shown in Table 4.1.

Ten *b-values* have been chosen to be common for every sequence and volunteer.

4.3.2 Methods

4.3.2.1 Reference Methods

Both real and synthetic datasets have been processed using different GW multimodal metrics (Sanz-Estébanez et al., 2017) as well as PW registration methodologies. As for the former, apart from the pipeline here proposed, we have tried the EDI (Entr.) (Learned-Miller, 2006), MIND (Heinrich et al., 2011) and the joint formulation proposed in Sanz-Estébanez et al. (2018) based on weighted ADC residuals (bWei).

As for the latter, the Demons (Pennec et al., 1999) registration algorithm (DEM) has been implemented using a MI based metric; this registration algorithm has been implemented under the PW paradigm. Therefore b_0 image has been selected as the image template.

These methodologies have been built as sequential approaches (except for the joint procedure) as they focus on registration only. Consequently, ADC estimates are obtained once the DWI dataset is fully registered. We have solved the NLLS problem for ADC estimation using the Levenberg-Marquardt method.

On the other hand, for the Rician noise filter we have implemented different literature filtering approaches to compare its performance inside our proposed pipeline. Namely, we

Table 4.1: Details on the image sequences used in the paper. Δ_p : Spatial Resolution (mm). Δ_l : Slice Thickness (mm). N_p: Number of pixels along each direction. N_b: Number of *b-values*. N_s: Number of slices. T_E: Echo Time (ms). N_g: Number of diffusion gradients. Card.: Cardiac Period (s). Resp.: Respiratory Period (s).

Params.	XCAT	DWI volunt.
Δ_p	1	1.23-1.85
Δ_l	10	5.5
N_p	268	224-320
N_b	10	10
N_s	21	20-40
T_E	93	65.65-72.1
N_g	1	3
Card.	1	~ 1
Resp.	4	Free

have tested a reported LMMSE procedure (Aja-Fernández et al., 2008; Aja-Fernández et al., 2008), a Wiener filter (assuming a Gaussian noise model), an Unbiased Non-Local Means (UNLM) denoising scheme (Aja-Fernández and Krissian, 2008; Buades et al., 2005) and a non local transform-domain filter (BM4D) (Maggioni et al., 2013).

4.3.2.2 Evaluation on synthetic data

We have first carried out a comparison using the data provided by the XCAT computational phantom for the different filtering procedures described in Section 4.3.2.1 under different scenarios in order to assess its suitability. We have also measured the improvement due to the bias correction step, i.e., the pipeline shown in Fig. 4.1 with the Rician filter removed (Interp.). Our original procedure (Sanz-Estébanez et al., 2018) is also shown for reference.

Furthermore, for the synthetic experiment we have simulated different types of noise both stationary ("St.") and non-stationary ("NS") Rician noise, the latter using the noise map represented in Fig. 4.5. Hence, we can measure both the error in the estimation of the simulated deformation field $\boldsymbol{\tau}$ and accuracy in ADC estimation for the methodologies presented in Section 4.3.2.1.

Besides, we have compared our proposal with respect to the approach described in Sanz-Estébanez et al. (2018), in which the joint estimation-registration is performed although under an underlying Gaussian assumption in order to assess robustness towards different SNRs. For this purpose, we have measured the error obtained over the ADC map estimated for stationary and non-stationary noise with different noise variances.

We have always used the GT noise variance $\sigma^2(\mathbf{x})$ in the synthetic experiments so as to avoid possible biases from noise estimation methodologies. Experiments have been performed 100 times with different noise executions.

4.3.2.3 Evaluation on real data

For the real data, due to the absence of a GT, validation has to be performed by indirect measures and qualitative visual assessment. We, therefore, have proposed an indirect validation procedure based on the estimates of the ADC obtained with different subgroups of *b-values*, with lengths of $n_b = [3, 6, 8]$, out of the total number of *b-values* available ($N_b = 10$). Specifically, we have performed $K_b = \binom{N_b}{n_b}$ ADC estimations for each pixel per slice and patient, changing only the combination of the *b-values* (maintaining the same number of *b-values*) that enter the optimization problem. Ideally, for two combinations of n_b values, the ADC estimates should be pixelwise equal. Therefore, a natural measure of the method reproducibility is the similarity between all ADC estimates. Accordingly, we have calculated the absolute differences between each possible pair out of the K_b ADC estimates, giving rise to $K_b(K_b - 1)/2$ possible comparisons for each pixel in the liver, which will conform the distribution of ADC differences. Robustness will be measured in terms of the variability of this pattern, the more variable, the less robust the method.

The value of $\sigma(\mathbf{x})$, needed as an input parameter, has been estimated from the data using the method in Pieciak et al. (2017) over a predefined ROI avoiding the influence of outer organs.

4.4 Results

4.4.1 Results on Synthetic Data

Fig. 4.6 shows boxplot diagrams of the error distributions in ADC estimation for different filtering procedures (as enumerated in Section 4.2.3) with respect to the original bWei approach. We have also included the results without filtering. From the results, we can conclude that the bias correction step itself is beneficial in order to improve ADC estimation. Regarding noise reduction at the first iteration, it is observed that LMMSE filter outperforms other state-of-the-art approaches; the gain is observed not only in precision, as shown in the figure, but also in speed.

Mann-Whitney U-tests were performed for the ADC error distributions on both scenarios. Significant differences were found for each of the different filtering procedures with respect to the non-filtered scheme (greater differences were found with respect to the original bWei approach). Best figures were obtained with the LMMSE filter, $p = 0.0031$ and $p < 10^{-3}$ for scenarios in Fig. 4.6, with $\sigma = 10$ and $\sigma = 35$, respectively ($p < 10^{-6}$ against bWei for both). Therefore, hereinafter, this filtering method will be used.

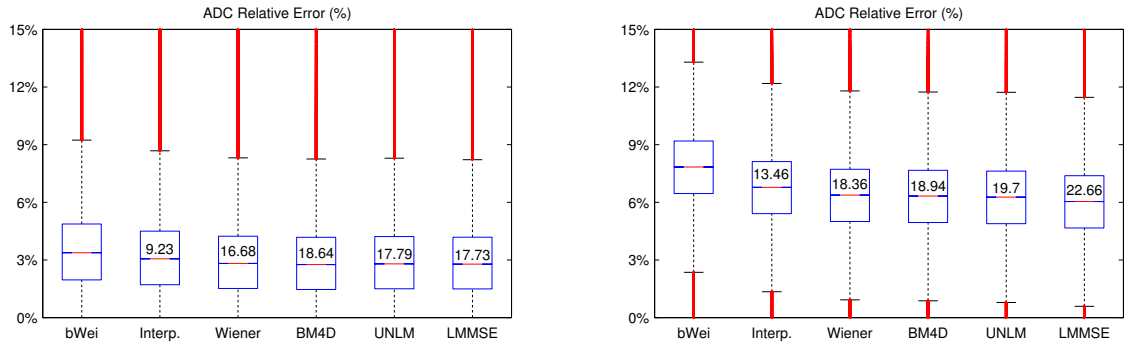

Figure 4.6: Relative error on ADC estimates for the different customized filtering schemes described in Section 4.3.2.2 for stationary noise ($\sigma = [10,35]$, in left and right figures, respectively). Numbers inside the boxes indicate the error reduction (%) with respect to original pipeline.

We now test the ability of the proposed methodology on motion correction and robust ADC estimation. We have measured the relative error (over a predefined ROI χ) on the ADC estimates under the noise scenarios described in Section 4.3.2.2 for the different methodologies enumerated in Section 4.3.2.1 as well as our proposal.

In Fig. 4.7 we show the boxplot diagrams of the relative error distributions from ADC estimation as a measure of estimation accuracy. Besides, we have also measured the error module of the estimated deformation fields with respect to the GT provided by the XCAT phantom.

Mann-Whitney U-tests have also been performed for the ADC error distributions obtained with our method and with the others in the same scenario. Significant differences were found, although greater in the non-stationary scenario ($p < 10^{-3}$) than in the stationary case ($p < 0.05$) for all methods. To diminish correlation effect in these tests, images have been decimated by a factor of ten, i.e., pixels entering the tests are taken 10 pixels apart at the acquired resolution.

From results in Fig. 4.7, we can state that the proposed methodology is effective at improving robustness when obtaining ADC estimates from DW-MRI sequences and, besides, provides accurate deformation measures, specially when compared to other sequential state-of-the-art techniques, in stationary and spatially-variant noise scenarios; results for the second case are, as expected, worse. Fig. 4.8 shows the evolution of the ADC estimation error with respect to the noise level (both stationary and spatially-variant) for the original joint registration-estimation approach (Sanz-Estébanez et al., 2018) and our present proposal.

We can see from Fig. 4.8 that the here proposed methodology can provide accurate estimation under very noisy conditions, with mean error being below 10 % until $\sigma = 25$ and $\sigma = 15$ for the stationary and non-stationary cases, respectively. This is specially relevant when performance is compared with the original bWei approach, which exponentially decreases for $\sigma > 15$. The figure also indicates that at higher SNR differences in estimation between traditional Gaussian procedure and our Rician-based proposal can be neglected,

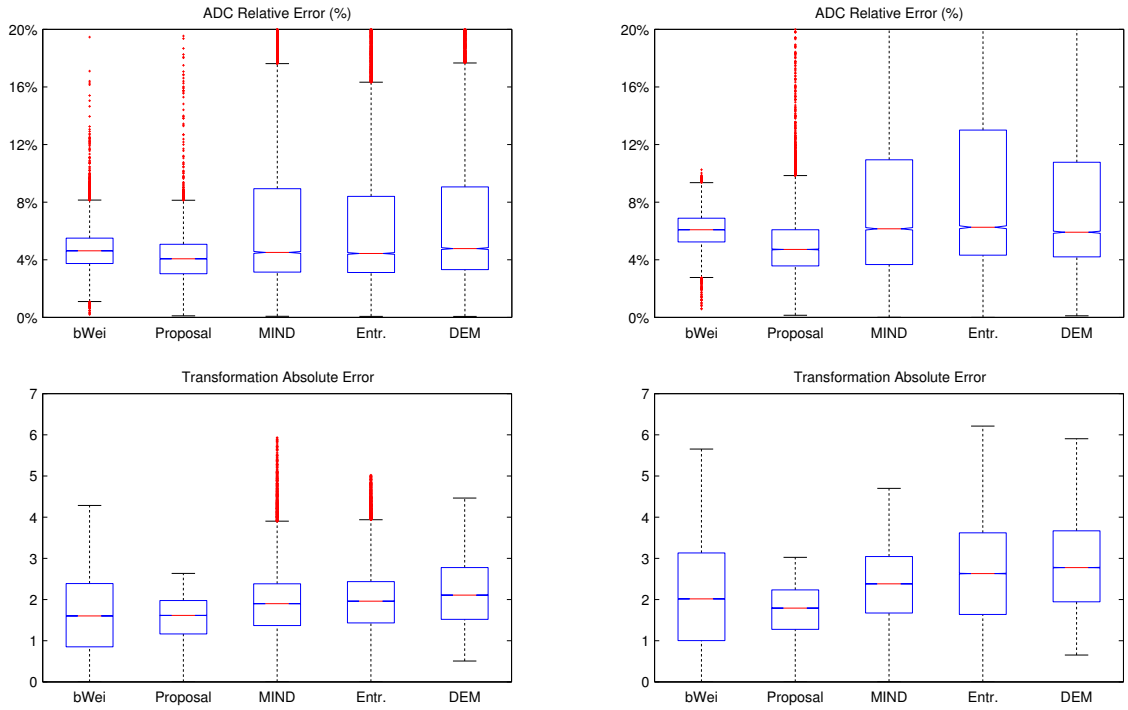

Figure 4.7: Relative error on ADC estimation (first row) and module error (mm) for the deformation field (second row) obtained with the different methods in stationary ($\sigma = 20$) and non-stationary (with $\sigma(\mathbf{x})$ median set to 20) noise contaminated scenarios, shown in the left and right respectively.

as expected.

4.4.2 Results on Real Data

Evaluation on real data has been performed according to the scheme described in Section 4.3.2.3. As sketched in Fig. 4.9, we have used the Cumulative Distribution Function (CDF) of the absolute differences on the ADC estimates obtained so as to show the reproducibility of the different methodologies for different number of acquired *b-values*. Proposal without TV regularization has also been plotted so one can assess the influence of TV step over ADC estimates for the different *b-values* subgroups.

It can be observed in Fig. 4.9 that the proposed method shows the highest figures, specially when a lower number of *b-values* is employed and, besides, the curves show a more "monotonic" behavior, what constitutes a good trend towards the absence of bias in the ADC estimation, both in the boundaries and in the interior of the liver. Nevertheless, notice that, since we are resorting to reproducibility measures in the real data, bias in ADC estimation cannot be represented. Therefore, possible errors in the estimation, either caused by the noise variance estimation method or by the monoexponential model assumption, which does not account for the perfusion component in the data, will not be

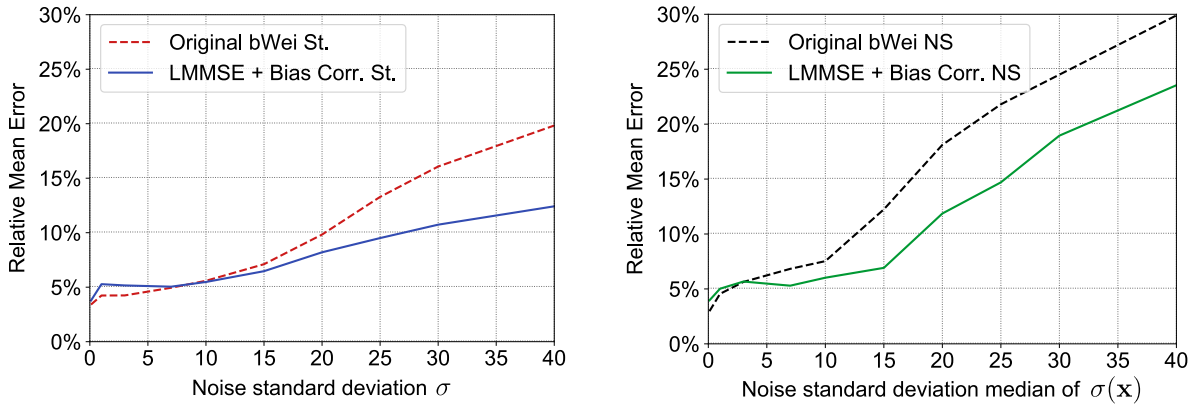

FIGURE 4.8: Mean relative error (%) on ADC estimates in presence of different noise levels σ for both approaches. In the non-stationary noise scenario the x-axis shows the median of $\sigma(\mathbf{x})$.

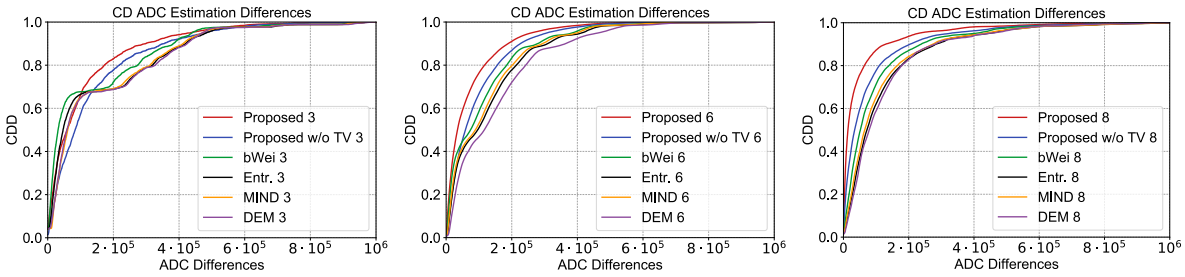

FIGURE 4.9: Cumulative distribution of absolute differences on ADC estimates for the different methods with a fixed number of *b-values*: $n_b = 3$ (left), $n_b = 6$ (center) and $n_b = 8$ (right).

reflected.

Finally, in Fig. 4.10 we show some snapshots on the resulting estimated ADC to visually notice the noise removal ability of the proposed methodology over real data. From visual inspection, we can support that our approach effectively removes the noise in final ADC maps maintaining liver structures integrity. Fig. 4.10 also shows a reduction in the smearing near tissue boundaries, which will allow delineation of structures inside the liver directly over the reconstructed ADC map.

4.5 Discussion

The ADC is known to provide useful information *in vivo* about body tissues, specially in abdominal organs. However, the accuracy of the estimation of this parameter is affected by different external factors, some related to the estimation procedure itself, some to the accuracy of the adopted model and some to the so-called confounding factors. In this work, we have focused on the latter: the reduction of the influence of two preeminent confounding factors in order to improve the accuracy in the estimation of the ADC.

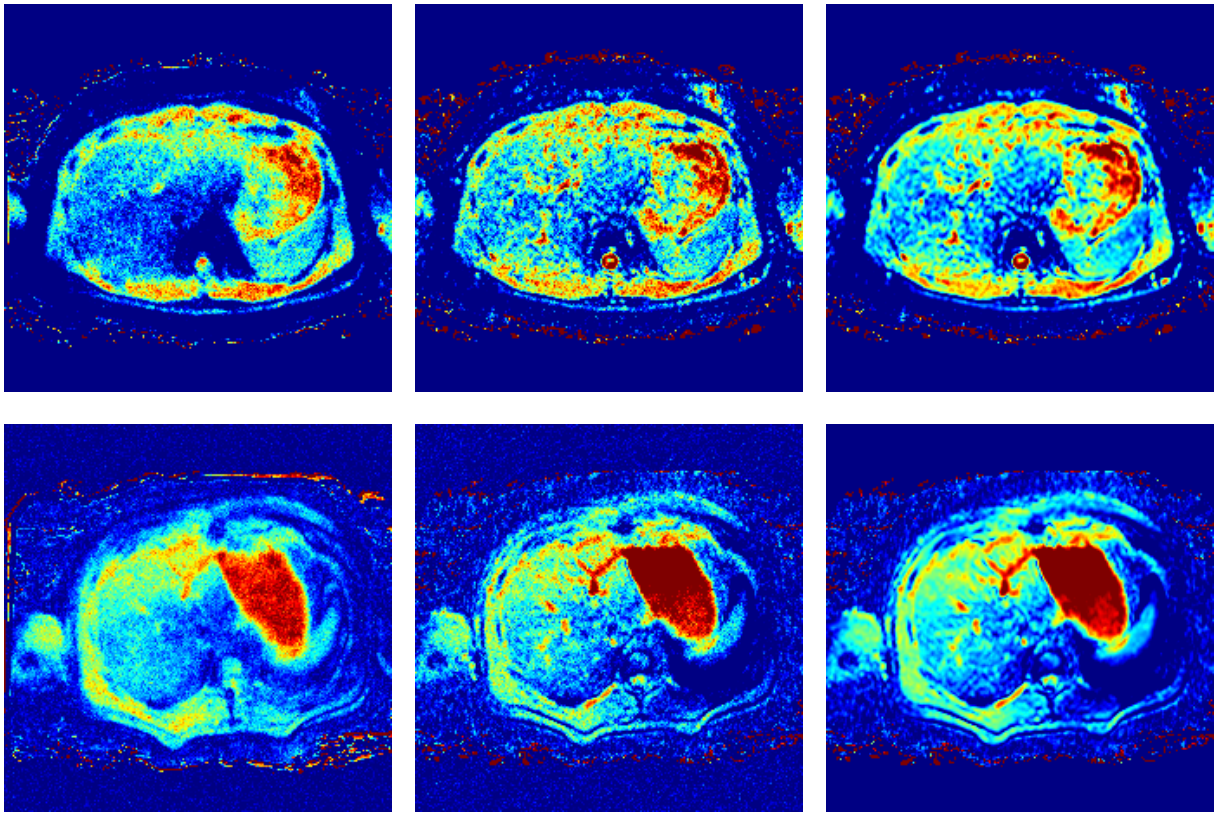

Figure 4.10: Real ADC maps for two different patients estimated directly from the original acquired sequence (left) as well as when using the bWei approach (center) and the here proposed methodology with bias correction (right).

To that end, we have presented a step-by-step approach for simultaneous correction of motion artifacts and removal of noise-induced bias in the ADC estimation from DW-MRI sequences acquired in different BH states.

The proposed methodology has shown to be specially accurate in recovering ADC maps, showing a significant reduction of the estimation bias when compared to previous approaches. The bias correction procedure plays an important role, improving the performance, specially when the Gaussian assumption does not hold, as shown in Fig. 4.8. It is important to point out that the whole scheme is grounded on the assumption of an underlying noise model for the acquisitions. In this work we have chosen the Rician distribution, for being the most accepted model in MRI. However, other models can also be easily adopted, without many changes in the general scheme. The relevant issue is precisely to adopt a model: overlooking the use of a statistical model for signal and noise may lead to implicitly assume non-skewed distributions.

As a design choice we have opted to avoid using any filtering procedure to reduce noise. Instead, we have removed the interpolation bias of the data by a simple subtraction. One may discuss that, this way, we only reduce the *bias* of the estimation, but not the

variance. While this is true, we have taken a conservative approach: we believe that it is more important to avoid any obliteration of the original data by overfiltering than to reduce the estimation variance.

As a matter of fact, a filter was indeed used, but only on the first iteration in order to obtain an initial set of weights. We have tested different methods and we have finally resorted to LMMSE filtering as preprocessing step since it provides the best performance as shown by Fig. 4.6 but also due to its lower computational complexity. From Fig. 4.6, we can also state the relevance of initial iterations in the procedure since the introduction of a filtering stage has significantly improved performance not only with respect to the original proposal (bWei) but also when the first ADC estimation is directly performed over magnitude images.

The proposed pipeline has also proven to be robust towards different types of noise, both stationary and spatially-variant. It has been shown that just by introducing a computationally light stage after interpolation we were able to correct the bias stemming from data weighting without apparently increasing estimates variance, even for low SNR datasets (i.e., variance effects of estimating unknown quantities in Eq. (4.9) do not seem relevant). Hence, the introduction of more complex models in the optimization equations may slightly improve performance but at the price of greatly increasing computational complexity of the algorithm.

With regards to the estimation of the deformation fields, we can see in Fig. 4.7 that the mean absolute error seem has experienced only a slight improvement as compared to the original proposal (bWei); however, robustness has been significantly increased. This robustness gain is mainly caused by improvement of the registration performance nearby tissue interfaces inside the liver due to bias removal. This bias reduction (coming both from the GW registration and Rician correction) allowed a better alignment with the ADC reference, specially at higher *b-values* on which these boundaries are barely distinguishable. For this reason, smearing in the ADC maps obtained from the motion compensated DW-MRI sequences has been greatly reduced, which in turn will also benefit the subsequent registration stage.

Notice that both procedures, noise bias correction and motion compensation, have shown its benefits towards robust ADC estimation separately. However, in this paper we have also demonstrated that its simultaneous use is beneficial for each other when employed inside the iterative procedure, providing additional values with respect to sequential approaches or BH acquisitions. Furthermore, the unified framework has been validated with in vivo human data, suffering from involuntary motion using reproducibility figures. From the improvement observed in Fig. 4.9, we can see that our procedure allows higher flexibility towards the chosen *b-values* as well as to the total number of images acquired. Furthermore, we can observe that the introduced TV term seems beneficial in preventing noise, although a fine tuning is necessary to avoid oversmoothing in ADC estimates. Visual assessment from Fig. 4.10 also reveals the motion compensating capability of the method, producing detailed ADC maps, specially as compared to the ones obtained from the original scanner sequence. Therefore, we can support that the proposed pipeline is

suitable to be embedded into direct ADC reconstruction acquisition protocols, which will not only reduce scan time but also possible variabilities due to *b-value* selection.

4.6 Conclusions

In this paper we have extended the joint registration and ADC estimation procedure for DW-MRI sequences in order to provide unbiased ADC estimates. To this end, we have designed a processing pipeline with smartly located filtering stages capable of dealing with the possible biases generated inside the optimization loop.

Experimental results demonstrate that the proposed approach helps to robustly cope with non-rigid motion artifacts, thus providing an accurate estimation under noisy (also for non-stationary) environments showing higher robustness and reproducibility towards low SNR datasets and *b-value* selection.

Acknowledgments

This work was partially supported by the European Regional Development Fund (ERDF-FEDER) under Research Grants TEC2014-57428-R and TEC2017-82408-R, the Spanish Junta de Castilla y León under Grant VA069U16 and the European Social Fund (ESF-FSE). Tomasz Pieciak acknowledges National Science Centre (2015/19/N/ST7/01204).

Chapter 5

Spatial and Spectral Anisotropy in HARP Images: An Automated Approach

Published as:

Sanz-Estébanez, S.[1], Cordero-Grande, L.[2], Aja-Fernández, S.[1], Martín-Fernández, M.[1] and Alberola-López, C.[1] (2016). Spatial and spectral anisotropy in HARP images: an automated approach. In *Proceedings of the 13th IEEE International Symposium on Biomedical Imaging: From Nano to Macro*, pp:1105-1108, Prague, Czech Republic.

[1] Laboratorio de Procesado de Imagen, Department of Teoría de la Señal y Comunicaciones e Ingeniería Telemática, ETSIT, Universidad de Valladolid, Campus Miguel Delibes s.n., 47011, Valladolid, Spain.

[2] Centre for the Developing Brain and Department of Biomedical Engineering, Division of Imaging Science and Biomedical Engineering, King's College London, St Thomas' Hospital, SE1 7EH, London, U.K.

Strain and related tensors play a major role in cardiac function characterization, so correct estimation of the local phase in tagged images is crucial for quantitative myocardial motion studies. We propose an Harmonic Phase related procedure that is adaptive in the spatial and the spectral domains: as for the former, we use an angled-steered analysis window prior to the Fourier Transform; as for the latter, the bandpass filter is also angle-adaptive. Both of them are narrow in the modulation direction and wide in the orthogonal direction. Moreover, no parameters are manually set since their values are partially based on the information available at the DICOM headers and additional information is estimated from data. The procedure is tested in terms of accuracy (on synthetic data) and reproducibility (on real data) of the deformation gradient tensor, measured by means of the distribution of the Frobenius norm differences between two tensor datasets.

Keywords: Tagged Magnetic Resonance Imaging; Harmonic Phase; Strain Tensor; Anisotropic Gaussian Window; Automatic Band-Pass Filtering; Thresholding

5.1 Introduction

MR-T is based on the generation of a set of saturated magnetization planes on the imaged volume which may be subsequently tracked throughout the cardiac cycle (Shehata et al., 2009). This modality is of special relevance in the analysis of myocardial motion to provide local functional indicators, such as the strain or the strain rate tensor (Axel et al., 2005).

Regarding the analysis of MR-T, an important family of methods are based on the extraction of the complex image phase obtained by bandpass filtering the spectral peaks introduced by the applied modulation; these methods are based on the fact that the HARP is linearly related to a directional component of the true motion (Osman et al., 2000); these methods are capable of reconstructing dense displacement fields accurately grounded on the assumption of constant local phase, which turns out to be more reliable than a constant pixel brightness assumption.

Subsequent works have focused on the nonhomogeneous deformation of the stripe pattern and have made use of the WHARP (Cordero-Grande et al., 2011) to balance the spatial and spectral localization of the image to be filtered by means of a truncated Gaussian window (as an appropriate trade-off between spatial and frequency resolutions); the result of which is a smooth local phase estimation. However, in this approach, Gaussian windows used prior to the WFT are isotropic, which constitutes a limitation on the capability to adapt to the locally changing stripe pattern. This Gaussian window has been made adaptive in Fu et al. (2013), hereafter referred to as AWHARP, to accommodate tag local properties but, with such a design, performance is dependent of the absolute tag orientation of the original stripe pattern, which is a suboptimal design choice as well.

Once the local spectrum is calculated, a HARP bandpass filtering stage should be performed to extract the phase. A circumferential spectral filter centered at the location of the maximum of the spectrum is proposed in Cordero-Grande and Alberola-López (2012) following the assumption of an isotropic estimation procedure. In Osman et al. (2000) a smooth ellipse is chosen for the bandpass region of the filter because it has a simple geometry appropriate for the gross shape of the spectral peaks. This approach implicitly makes use of the concept of anisotropy, but key parameters, such as the bandwidth or the eccentricity of the ellipse, are manually set.

Thresholding methods based on variance (Otsu et al., 1979; Gilles and Heal, 2014) or entropy (Cattaneo et al., 2011) could provide automatic estimates of the appropriate filter parameters. These methods, however, should be complemented with means of producing smooth transfer functions that are capable of dealing with the nonhomogeneities caused by pattern deformations. To the best of our knowledge, the filtering schemes proposed in the HARP literature are not capable of automatically adjusting to these spectral peaks, specially in the case of the aforementioned isotropic windowing procedures where the spectral overlapping caused by the anatomical image could result in an artifacted reconstruction.

In this paper we will show that the assumption of anisotropy along the processing

pipeline (both at windowing prior to the FT and at the filtering stage) is beneficial in order to avoid spectral interferences without losing deformation information. In addition,we also estimate the filter parameters direclty from data, so our procedure leads to a fully automatic ME technique. The method here proposed will be hereafter referred to as automatic anisotropic WHARP, i.e., AA-WHARP.

5.2 Materials and methods

5.2.1 Materials

We have acquired a medial slice of a MR SPAMM SENSE Turbo Field Echo (TFE) sequence on a Philips Achieva 3T scanner. The images have a spatial resolution of (1.333x1.333) mm^2 and a slice thickness of 8 mm. The acquisition parameters are T_E = 3.634 ms, T_R = 6.0182 ms and $\alpha = 10°$. Tag spacing has been set so that k = $1/\lambda$ with λ=7 mm; multiple tag orientations have been obtained that fully span the orientation plane, uniformly from 0 to π with a separation of $\pi/18$ radians.We have also acquired a SENSE balanced TFE cine sequence with spatial resolution of (1.25x1.25) mm^2, a slice thickness of 8 mm, T_E = 1.663 ms, T_R = 3.325 ms and $\alpha = 45°$. The cine sequence is acquired at the same slice location as the tagging sequence. The myocardium is segmented in the ED and ES phases of the cine sequence and in the ED phase of all the acquired orientations of the tagging sequence. The cine segmentation at ED phases is used to align the tagging orientations to a common reference system to correct for patient breathing motion. The ES segmentation is used to define a ROI on which to compute meaningful measures of the ST.

In order to have a deformation GT, heart motion has been estimated from the cine sequence by means of a FFD (Rueckert et al., 2006). Then, an undeformed tagging modulation has been added at ED phase to the original cine sequence and the result has been deformed by the synthetic transformation to give rise to a simulated tagging sequence with motion parameters known beforehand. As it is well-known, FFDs are obtained by manipulating an underlying mesh of control points. Their spacing as well as the B-spline (Lee et al., 1997) order act as parameters of the FFD (Rueckert et al., 2006); in our case, we have used a dense control point mesh as well as a high order B-spline (control points spacing is set to 5 mm and a 3^{rd} order B-spline has been selected) so that our model can accommodate highly local nonrigid deformations. Additive noise with zero mean and tag fading have also been included in the simulation.

5.2.2 Methods

As stated in Section 5.1, the original HARP makes use of a complete FT although the tag pattern in MR-T images suffers local variations, i.e., nonhomogeneities. To alleviate

this limitation, WFT methods have been proposed both with fixed size (Cordero-Grande and Alberola-López, 2012) and adaptive spatial windows (Fu et al., 2013).

The anisotropic windowing technique here proposed is based on the extraction of the local phase of the stripe pattern by applying a WFT along the stripe direction combined with a full FT on the direction perpendicular to the stripe over the image at ES phase. Specifically, it is well known (Jain, 1988) that the equation of the straight line that is orthogonal to the unity vector $\hat{\mathbf{n}} = (\cos(\theta), \sin(\theta))$ and for which the distance to a point $\mathbf{p} = (p_x, p_y)$ is s, turns out to be

$$(x - p_x)\cos(\theta) + (y - p_y)\sin(\theta) = \hat{\mathbf{n}} \cdot (\mathbf{x} - \mathbf{p}) = s. \tag{5.1}$$

Therefore, if the analysis window is designed as:

$$w(\mathbf{x}) \propto e^{-\frac{s^2}{2\sigma^2}}, \tag{5.2}$$

where $\hat{\mathbf{n}}$ is the tag unity vector read from the DICOM headers and $\mathbf{p} = (p_x, p_y)$ the point at which the local FT is calculated, then the window will have a rapid tapering, controlled by parameter σ, in the modulation direction but will suffer no attenuation in the orthogonal direction. For the window design, σ has been set equal to the nominal tag spacing (as read from the DICOM headers). Once the local spectrum is calculated, HARP bandpass filtering techniques can be directly applied on the spatially localized spectrum of the image to extract the phase. The assumption of anisotropy is a key fact, considering that the spectrum will suffer a significant stretching orthogonal to the modulation direction as compared with the isotropic counterpart, caused by the anisotropic window (see Fig. 5.1). In addition, spectral interferences seem mitigated in the anisotropic version.

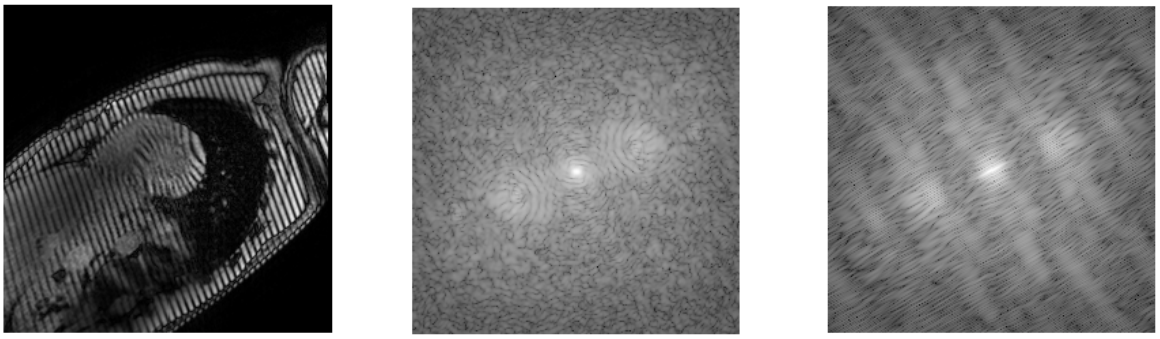

(a) MR-T at ES (b) Isotropic WFT (c) Anisotropic WFT

Figure 5.1: Effects of the WFT design over the image spectrum.

To adequately retrieve the shape of the spectral peak, we have resorted to an anisotropic filter composed by a Gaussian bandpass filter along the modulation direction and an allpass filter along the orthogonal direction. This is done by means of a spectral mask as defined in Eq. 5.2 where, as before, $\hat{\mathbf{n}}$ is the tag unity vector read from

the DICOM headers and $\mathbf{p}$ is the location of the maximum of the spectrum inside a region in the surroundings of the reference spatial frequency of the tags $\mathbf{k}_i$, defined by $\left\{\mathbf{k} : \frac{k_i}{2} \leq k \leq 2k_i \wedge |\theta - \angle\mathbf{k}| \leq \frac{\pi}{6}\right\}$.

For the filtering stage, σ has been estimated by means of the Otsu's method, i.e., by comparing with an spectral threshold that is calculated minimizing the bimodal intraclass variance (Otsu et al., 1979). To this end, we define a rectangular region in the surroundings of the spectral peak $\mathbf{p}$ according to $\left\{\mathbf{k} : |s| < \frac{k_i}{2}\right\}$; once the threshold is calculated from the information within that area, a foreground region is obtained. However, as it is only necessary to estimate the width of the Gaussian filter in the modulation direction, the foreground points are projected over that direction, the sample STD is calculated and σ is set as four times that measure. This way we assure that approximately 99 % of these points fall within an amplitude $\frac{1}{\sqrt{2}}$ times the maximum of the filter.

Finally, the local phase can be extracted in the spatial domain from the inverse anisotropic WFT of the aforementioned filtered spectrum. Once the local phase images are reconstructed, standard procedures are applied to estimate the material deformation gradient tensor $\mathbf{F}$, at ES phase(Osman et al., 2000; Cordero-Grande et al., 2014).

5.2.3 Validation

Validation is carried out in terms of the variability of the material deformation gradient tensor estimate $\mathbf{F}$ at the ES phase; as for accuracy, this variability is calculated between the GT and the tensor estimates obtained from each pair of orthogonal stripes used. As for reproducibility, variability is calculated out of the tensor estimates obtained from two different sets of orthogonal stripes pairs. Ideally, the tensors should be equal for all datasets and estimation procedures. Therefore, a natural measure for our purposes is the FND of the tensors estimates, which is defined as:

$$FND(\mathbf{x}) = \sqrt{\sum_{m=1}^{2}\sum_{n=1}^{2}(\mathbf{F}^1_{mn}(\mathbf{x}) - \mathbf{F}^2_{mn}(\mathbf{x}))^2}. \tag{5.3}$$

where $\mathbf{F}^j_{m,n}(\mathbf{x})$ stands for the (m,n) component of the tensor $\mathbf{F}^j$ at pixel $\mathbf{x}$, calculated from method (or dataset) j ($j = \{1,2\}$).

Recall from section 5.2.1 that 18 stripe directions have been imaged; this gives rise to 9 pairs of orthogonal stripes as well as $\binom{9}{2} = 36$ pairwise comparisons. Therefore, as for the reproducibility experiment on real data, we have stacked together all the FND values for all pixels and all pairwise comparisons. For the experiment on synthetic data, the stack consist of 9 comparisons to the GT tensor in every pixel.

5.3 Results

Figure 5.2 shows the cumulative distribution of FND, as defined in Eq. 5.3; the plots are indexed by the method used for the tensor estimation. For the non-automatic methods under test, the filter bandwidth is normalised with respect to the wave number of the applied modulation using the parameter $\mu = r/k$. This parameter has been set to 0.35 according to Cordero-Grande and Alberola-López (2012) for both experiments. The figures show that both in terms of accuracy and of reproducibility, the proposed method outperforms previous proposals, i.e., the FND distributions are closer to the ideal distributions. Notice that no dependence on the orientation is observed since data from different orientations are stacked together.

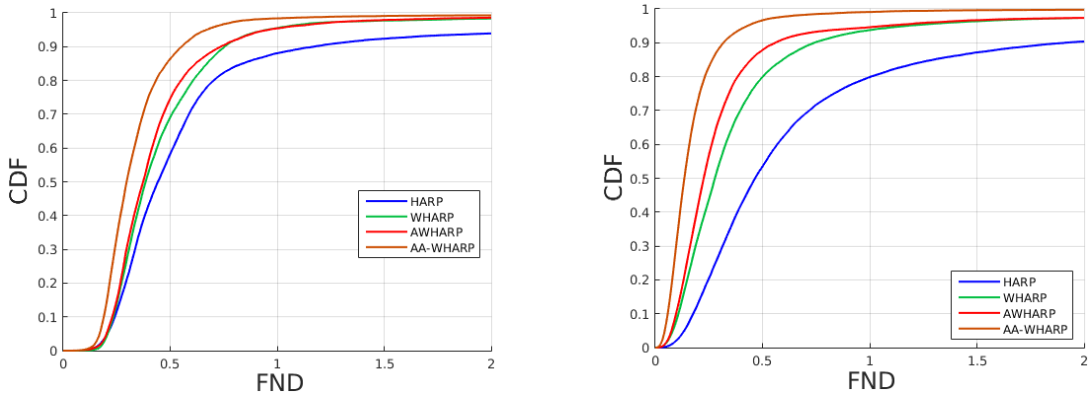

(a) Synthetic Data (b) Volunteer Data

Figure 5.2: CDF of FND for the sets considered in Section 5.2.1.

As for Figure 5.3, we show the median of the FND distributions (hereafter referred to as $\nu(FND)$) for the aforementioned estimation methods as a function of the normalized filter bandwidth. Specifically, we have tried several values of μ in the range [0.2,0.7]. The proposed method is a non-parametric one, so presents a plain response.

Figure 5.4 does show such a dependence. Specifically, for each orientation indicated in the horizontal axis (together with its orthogonal accompanying direction) we have calculated the FND for each of the other 8 orientation pairs; data samples have been stacked together and then the $\nu(FND)$ is calculated. Clearly, the method here proposed shows less orientation sensitiveness than previous proposals.

5.4 Discussion

From the results in Section 5.3 we can see that the methodology here presented is effective in improving both robustness and accuracy when obtaining direct strain measurements from MR-T sequences; as indicated, the distribution of FND is closer to the

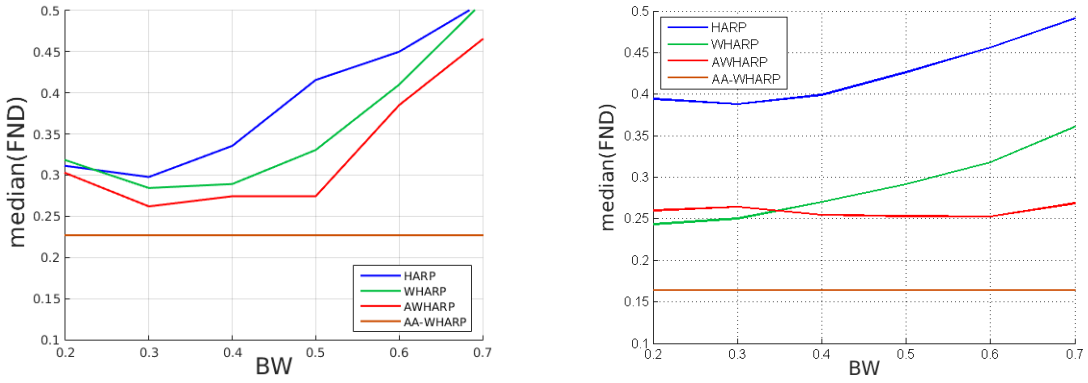

(a) Synthetic Data (b) Volunteer Data

FIGURE 5.3: $\nu(FND)$ for different bandwidths.

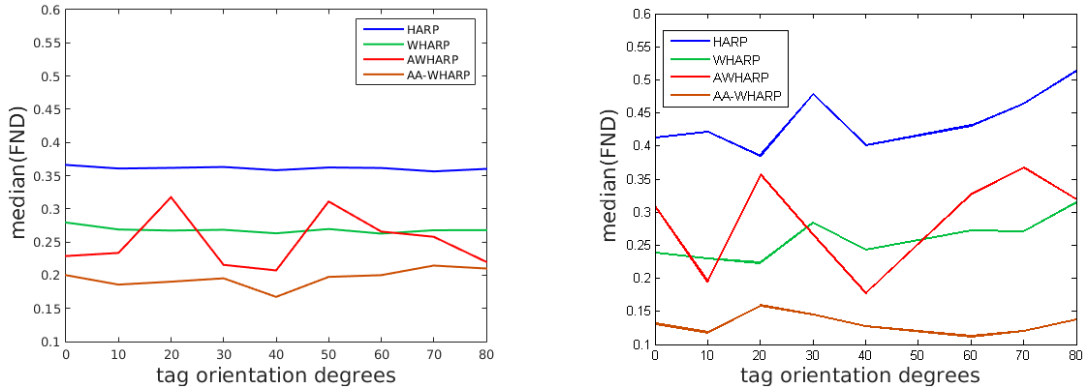

(a) Synthetic Data (b) Volunteer Data

FIGURE 5.4: $\nu(FND)$ for the orthogonal pairs of Section 5.2.1.

ideal pattern and no crossing between curves and our proposal are observed. Interferences, however, so still remain, so further research in this direction should be considered. In any case, the notion of anisotropy both in spectral and spatial domains seems beneficial with respect to other adaptive and/or isotropic approaches.

Figure 5.3 shows a considerable improvement in terms of $\nu(FND)$ of reproducibility and precision for the AA-WHARP method with respect to reported methods for a wide range of μ values, specially with higher bandwidths.

The proposed anisotropic design leads to an automated bandwidth estimation method resulting in a smooth Gaussian filter that outperforms other HARP based methods when reconstructing the tensor with arbitrary orthogonal pairs of orientations.

It is worth noting that, as indicated in Figure 5.4, AWHARP is sensitive to the pattern orientation despite its adaptive condition; the fluctuations in $\nu(FND)$ have considerable higher peaks than those from our AA-WHARP; it should be highlighted that AWHARP shows very similar behaviour to WHARP in the vicinity of 45° since at this (nominal)

orientation the analysis window in AWHARP is close to isotropic. This fact is reflected in both figures. The proposed method, however, remains fairly orientation independent, but for residual interference and interpolation effects.

5.5 Conclusions

A robust and reliable automatic ME technique is achieved thanks to an anisotropic design all along the processing pipeline. The windowing procedure proposed consists in an anisotropic Gaussian window whose shape remains unaltered but it rotates according to the nominal pattern orientation. Since the spectral peaks undergo a significant stretching, we resort to an anisotropic filtering procedure to diminish spectral interference. The proposed spectral design, in addition, lends itself to a full automatic bandwidth estimation method. Results indicate an improving performance with respect to reported methods for a wide range of filter bandwidths.

Chapter 6
An Automated Tensorial Classification Procedure for Left Ventricular Hypertrophic Cardiomyopathy

Published as:
Sanz-Estébanez, S.[1], Royuela-del-Val, J.[1], Merino-Caviedes, S.[1], Revilla-Orodea, A.[3], Sevilla, T.[3], Cordero-Grande, L.[2], Martín-Fernández, M.[1] and Alberola-López, C.[1] (2016).An Automated Tensorial Classification Procedure for Left Ventricular Hypertrophic Cardiomyopathy. In *Proceedings of the 4th International Work-Conference on Bioinformatics and Biomedical Engineering*, vol: 99656, pp:184-195, Granada, Spain.

[1] Laboratorio de Procesado de Imagen, Department of Teoría de la Señal y Comunicaciones e Ingeniería Telemática, ETSIT, Universidad de Valladolid, Campus Miguel Delibes s.n., 47011, Valladolid, Spain.

[2] Centre for the Developing Brain and Department of Biomedical Engineering, Division of Imaging Science and Biomedical Engineering, King's College London, St Thomas' Hospital, SE1 7EH, London, U.K.

[3] Unidad de Imagen Cardiaca , Hospital Clínico Universitario de Valladolid, CIBER de enfermedades cardiovasculares (CIBERCV), 47005, Valladolid, Spain.

Cardiovascular diseases are the leading cause of death globally. Therefore, classification tools play a major role in prevention and treatment of these diseases. Statistical learning theory applied to magnetic resonance imaging has led to the diagnosis of a variety of cardiomyopathies states. We propose a two-stage classification scheme capable of distinguishing between heterogeneous groups of hypertrophic cardiomyopathies and healthy patients. A multimodal processing pipeline is employed to estimate robust tensorial descriptors of myocardial mechanical properties for both short-axis and long-axis magnetic resonance tagged images using the least absolute deviation method. A homomorphic filtering procedure is used to align the cine segmentations to the tagged sequence and provides 3D tensor information in meaningful areas. Results have shown that the proposed pipeline provides tensorial measurements on which classifiers for the study of hypertrophic cardiomyopathies can be built with acceptable performance even for reduced samples sets.

Keywords: Magnetic Resonance Tagging; Fuzzy clustering; Support Vector Machines; Homomorphic Filtering; Harmonic Phase; Hypertrophic Cardiomyopathy; Least Absolute Deviation.

6.1 Introduction

Classifications of heart muscle diseases have proved to be exceedingly complex and in many respects contradictory. Cardiomyopathies are an important and complex group of heart muscle diseases with multiple etiologies and heterogeneous phenotypic expression. Therefore, systematic classifications have traditionally been viewed as useful exercises that promote greater understanding of these diseases (Baron, 2008).

HCM is very common and can affect people of any age. About one out of every 500 people has HCM. Men and women are equally affected. HCM is a common cause of sudden cardiac arrest in young people, including young athletes. Etiological factors are of great importance in CVD detection (Karamitsos and Neubauer, 2011); specifically, genetic studies have been conducted in order to classify cardiomyopathies and to assess patients predisposition to suffer HCM (Richard et al., 2003; Braunwald et al., 2002).

Imaging techniques provide essential descriptors for the study and classification of cardiomyopathies and, from them, cardiac MR is increasingly becoming the standard technique as it provides information to assess the myocardial morphology, function and structure. Its use is especially relevant for quantitative analysis of myocardial motion, the anomalies of which are directly related with impaired cardiac function. From the set of MR acquisition techniques, MR-T has become the reference modality for evaluating strain evolution in the human heart. This modality is based on the generation of a set of saturated magnetization planes on the imaged volume which may be subsequently tracked throughout the cardiac cycle (Jeung et al., 2012), from which the cardiac function can be assessed. HARP based methods (Osman et al., 2000) are capable of reconstructing deformation fields accurately grounded on the assumption of constant local phase, which turns out to be more reliable than a constant pixel brightness assumption.

Global image-derived measures have been reported, such as the global longitudinal strain (Shimon et al., 2000), which turns out to be an interesting tool that correlates with the global presence of fibrosis. A relation between extent of cardiac muscle cell disorganization and LV wall thickness has also been established (Maron et al., 1992); however, imaging studies focused on the characterization and classification of the nature of HCM are relatively scarce.

In order to provide greater understanding about these factors, comparative regional studies have been carried out in Piella et al. (2010) for athletes, controls and HCM patients; the authors reveal a significant reduction in the diagonal components of the strain in HCM patients and athletes, but this reduction was not associated to any particular segment and it was even present in non-fibrotic regions. In Cordero-Grande et al. (2013b) a local analysis is performed fusing the information of MR-C and Late Enhancement MR to provide more insight into the mechanical properties of the fibrotic tissue in HCM. Automated classifiers have been developed in Gopalakrishnan et al. (2014) and Rahman et al. (2015) using global biomarkers derived from MR-C and ECG, respectively. Although the authors report noticeable prognostic values for the identification of different CVD, only global measures were used; however, local measurements may be of additional

Table 6.1: Details on the sequences of MR images used in the paper. Δ_p : Spatial Resolution (mm). Δ_l : Slice Thickness (mm). N_p: Number of pixels along each direction. N_t: Number of Temporal Phases. N_s: Number of slices. T_R : Repetition Time (ms). T_E: Echo Time (ms). α: Flip Angle (°).

	Δ_p	Δ_l	N_p	N_t	N_s	T_R	T_E	α
MR-T SA	1.21-1.32	10	256-432	16-25	10-15	2.798-6.154	1.046-3.575	7-25
MR-C SA	0.96-1.18	8-10	240-320	30	10-15	2.902-3.918	1.454-2.222	45
MR-T LA	1.21-1.34	10	240-340	15-27	1-3	2.903-4.507	1.097-2.897	10-45
MR-C LA	0.98-1.25	8-10	256-448	30	1-3	2.858-3.529	1.251-2.132	45

utility for the characterization of the fibrosis that accompanies primary/secondary HCM.

In this paper we propose an automated processing pipeline to classify heterogeneous groups of HCM from myocardial functional descriptors obtained out of the deformation gradient tensor estimated from MR-T images by means of a robust reconstruction method. We have applied different machine learning methods (supervised and unsupervised) using a sequential methodology that adapts to the characteristics of the subjects at every stage.

6.2 Materials and Methods

6.2.1 Materials

For the validation of the proposed approach on real data, we have performed cardiac studies in a population of 47 subjects, 23 of which are affected by primary HCM, 10 are affected by secondary HCM and the control group consists of 14 healthy volunteers.

A SA MR-T dataset, providing a coverage from apex to base, is acquired for each patient using a MR C-SPAMM SENSE TFE sequence on a Philips Achieva 3T scanner. Additionally, we have also acquired a SENSE balanced-TFE SA MR-C sequence at the same spatial location for each patient, where the myocardium has been manually segmented at the ED phase. Segmentations are also used to define a ROI on which to compute meaningful measures of the strain. LA MR-T datasets and the corresponding MR-C sequence have also been acquired following the aforementioned acquisition protocol in each case. Additional details on these sequences are included in Table 6.1.

6.2.2 Methods

The processing pipeline is divided in the following steps:

6.2.2.1 Alignment

An alignment stage is performed with the purpose of mapping the MR-C segmentations provided by the cardiologist onto the MR-T sequence. First, the temporal correspondence of the MR-T images with the MR-C sequence is established by means of the DICOM timestamps; then, an affine registration method is performed to align MR-T and MR-C images at the correct time instant. To that end, the MR-T sequence is detagged following an homomorphic filtering procedure (Aja-Fernández et al., 2014) to improve registration performance. Similar detagging procedures have been reported in Makram et al. (2015) for global measures estimation. The proposed dettaging method is described below.

Let us assume a simple case in which an image $I(\mathbf{x})$ consists of an anatomical image $I_0(\mathbf{x})$(low-pass) multiplied by a tag pattern $f(\mathbf{x};\mathbf{g})$, where the gradient directions are given by $\mathbf{g} = [g_1, g_2]$. Our purpose is to estimate $I_0(\mathbf{x})$ from the final image $I(\mathbf{x})$. Our method is based on the assumption that the anatomical image shows a low variability, i.e., it can be considered a low pass signal. This principle is not always fulfilled as boundaries present sharp intensity changes. Consequently, we calculate the local mean of the image in order to alleviate the power smearing caused by the abrupt myocardium background transition and next, we separate anatomical and tag signals by applying the logarithm:

$$\log(I_n(\mathbf{x})) = \log(\overline{I}(\mathbf{x})) \approx \log I_0(\mathbf{x}) + \log f(\mathbf{x};\mathbf{g}). \tag{6.1}$$

where $\overline{I}(\mathbf{x})$ denotes the local mean. The tag pattern term $\log f(\mathbf{x};\mathbf{g})$ has its energy localized at specific frequencies, while the term $\log I_0(\mathbf{x})$ is a low frequency signal. We can suppress the residual influence of the tag pattern using a notch filter on $\log(I_n(\mathbf{x}))$. The position of the spectral peaks can be easily estimated from the information obtained from the DICOM headers, so we have resorted to an isotropic Gaussian filter with radius r for every spectral peak detected. The filter bandwidth is normalized with respect to the wave number k of the applied modulation by using the parameter $\mu = r/k = 0.3$ according to Cordero-Grande et al. (2011).

The whole filtering pipeline is depicted in Figure 6.1:

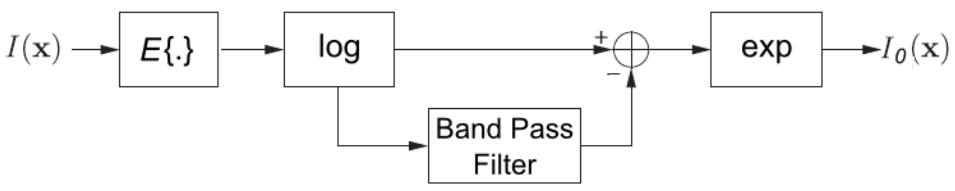

Figure 6.1: Pipeline of homomorphic filtering procedure.

6.2.2.2 Estimation of the Material Deformation Gradient Tensor

The estimation technique is based on the extraction of the local phase of the grid pattern according to the method presented in Cordero-Grande et al. (2011). A WFT is applied to the image at the ES phase. The WFT provides a representation of the image spectrum in the surroundings of each pixel of the original image, so HARP Bandpass filtering techniques can be directly applied on the spatially localized spectrum of the image. The complex image can be reconstructed in the spatial domain by using an IWFT prior to extract the phase.

As stated in Osman et al. (2000), 3D HARP motion reconstruction using the SPAMM technique requires a minimum of 3 linearly independent wave vectors. In this paper we extend the aforementioned HARP methodology by allowing the application of a set of 4 wave vector (performing this estimation technique on C-SPAMM MR-T LA and SA images), so 3D deformations can be robustly recovered, at least at the intersection points of both axes, applying the methodology presented in Cordero-Grande et al. (2016).

We can arrange the set of the four given wave vectors $\mathbf{k}_i^T$ in matrix form by:

$$\mathbf{K} = \left[\mathbf{k}_{1,SA}^T, \mathbf{k}_{2,SA}^T, \mathbf{k}_{1,LA}^T, \mathbf{k}_{2,LA}^T\right]^T. \tag{6.2}$$

The material deformation gradient tensor $\mathbf{F}(\mathbf{x})$ is related to the gradient of the phase image $\phi_i(\mathbf{x})$ as stated in Osman et al. (2000). Rearranging the gradient of the phase images in matrix form as:

$$\mathbf{Y}(\mathbf{x}) = \left[\frac{\partial^* \phi_{1,SA}}{\partial \mathbf{x}^T}(\mathbf{x}), \frac{\partial^* \phi_{2,SA}}{\partial \mathbf{x}^T}(\mathbf{x}), \frac{\partial^* \phi_{1,LA}}{\partial \mathbf{x}^T}(\mathbf{x}), \frac{\partial^* \phi_{2,LA}}{\partial \mathbf{x}^T}(\mathbf{x})\right]^T, \tag{6.3}$$

we obtain the material deformation gradient $\mathbf{F}(\mathbf{x})$ from:

$$\mathbf{K} = \mathbf{Y}(\mathbf{x})\mathbf{F}(\mathbf{x}). \tag{6.4}$$

In order to estimate $\mathbf{F}(\mathbf{x})$, one could resort to the LS method. However, bearing in mind that HARP-like methods suffer phase interferences (especially within the vicinity of boundaries), which give rise to outliers , our proposal is to resort to the LAD method, due to its robustness (Cordero-Grande et al., 2016). Hence, the reconstruction is performed iteratively by:

$$\mathbf{F}_{l+1}(\mathbf{x}) = (\mathbf{Y}^T(\mathbf{x})\mathbf{W}_l(\mathbf{x})\mathbf{Y}(\mathbf{x}))^{-1}\mathbf{Y}^T(\mathbf{x})\mathbf{W}_l(\mathbf{x})\mathbf{K}, \tag{6.5}$$

with $\mathbf{W}_l(\mathbf{x})$ a diagonal weight matrix obtained by:

$$W_l^{jj}(\mathbf{x}) = \frac{1}{\sqrt{\sum_{h=1}^{3}\left(K^{jh} - \sum_{g=1}^{3} Y^{jg}(\mathbf{x})F_l^{gh}(\mathbf{x})\right)^2}} \tag{6.6}$$

and initially establishing $\mathbf{F}_0(\mathbf{x}) = \mathbf{I}$, with $\mathbf{I}$ the identity matrix.

Once $\mathbf{F}(\mathbf{x})$ is reconstructed, the Green-Lagrange ST can be easily obtained as: $\mathbf{E}(\mathbf{x}) = 1/2(\mathbf{F}^T(\mathbf{x})\mathbf{F}(\mathbf{x}) - \mathbf{I})$.

6.2.2.3 Classification

Mechanical descriptors are extracted from the aforementioned tensors. We considered the projected components of the ST on the usual radial-circumferential-longitudinal $\{r, c, l\}$ space. These components will be referred to as E^{ab}, where a and b will be components of this space. In all the cases, all the features will be averaged within three areas in the heart along its LA; specifically, we will consider components at the base, mid-ventricle and apex. On the other hand, we will also calculate the curl of the deformation field as a measure of rotation. We will generically refer to the twist as the unsigned difference between two components that measure rotation (Fung, 1965), one at the base, the second one at the apex. When we refer to the rotation modulus, the specific component will be the unsigned average of the component in the mid-ventricle area. Additionally, since some rotation-related components have opposite directions in apex and base, we will consider the location of the zero crossing for these components.

Once the principal heart motion descriptors have been calculated, a normalization stage (Theodoridis and Koutroumbas, 1999) is applied in order to diminish the influence of possible outliers. A sigmoidal function is used to this end; data are mapped on the interval $(0, 1)$.

Our purpose is to classify a sample into one of three classes, namely, control, primary HCM and secondary HCM. Since secondary HCM patients have subtle differences with respect to the other two classes, we have resorted to a two-stage classification procedure (see Fig. 6.2). At the first stage we grossly pursue to distinguish between controls and primary HCM. Secondary HCM patients will fall on either of the two mentioned partitions. As for the second stage the purpose is to tell apart controls and secondary HCM, on one hand, and primary and secondary HCM, on the other hand. Notice that primary HCM patients incorrectly classified as a control in the first stage (or vice versa) will not be correctly classified; however, as we will describe later, this situation hardly takes place.

Optimal feature selection and classification are intimately related; those features whose classification figures are the highest are considered as the optimal features for that classification stage. To minimize overtraining, despite the reduced sample size, a Leave-10-out cross validation procedure has been used and data samples have been randomized; the proportions of control/primary/secondary have been kept unaltered along trials. For every trial we record the feature set with best performance; after one hundred trials we can identify the feature vector that has been selected the most; this will be the chosen one for the classification stage. As for finding classification performance, the procedure is repeated with a new randomized Leave-10-out procedure using the aforementioned selected feature vector as the input. In all the cases, 3-component feature vectors have been tested. Higher dimensionality has been tried but with no improve in performance.

The procedure described above has been carried out using FCM (Bezdec, 1981) and SVM (Cortes and Vapnik, 1995) both SVMQ and SVMG kernels (Vert et al., 2004). We have also tested a combination of them at different stages. As for the fuzzy clustering, the method requires that a threshold is set for the membership grade of each partition to

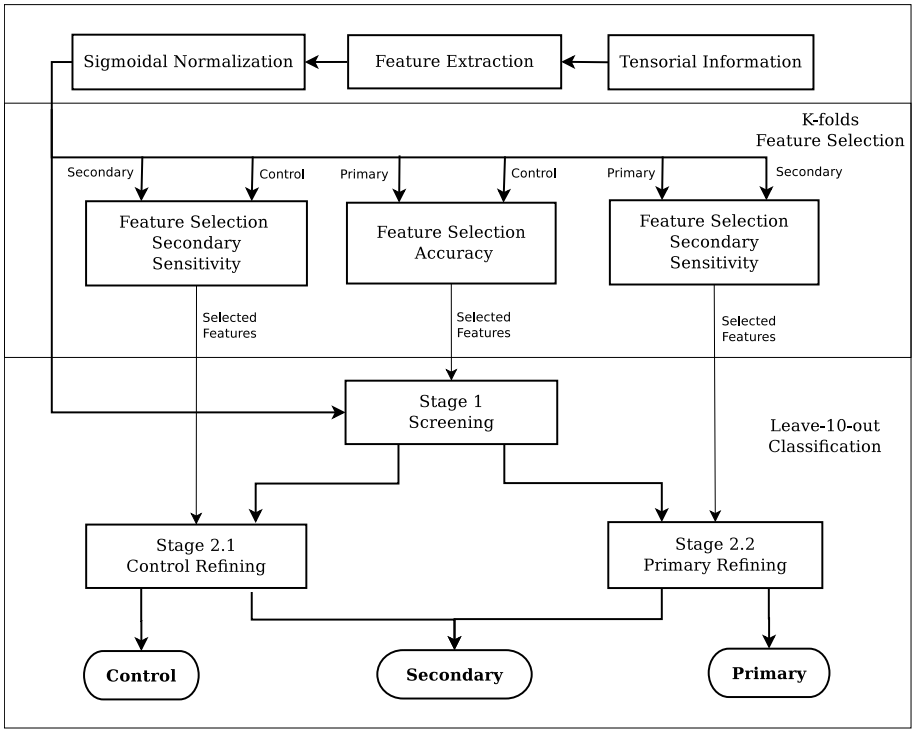

Figure 6.2: Pipeline of the feature selection and classification stages.

carry out a final hard threshold. This value is another parameter that has to be optimized.

As for the first stage, the selected features are the ones that provide the highest accuracy involving only healthy and primary HCM. The modulus of E^{cc} and curl as well as the twist of the curl of the 2D deformation field (Fung, 1965) have proven to provide a good separability between these groups for each one of the tested classification techniques.

Then, for both output partitions of the first stage, another classification is established with the purpose of detecting secondary HCM cases in groups of healthy volunteers and primary HCM, respectively. The objective of this stage is to increase the classifier sensitivity with respect to secondary HCM cases; if several feature vectors share the maximum sensitivity with respect to this group, we select the feature vector with maximum specificity (i.e., with maximum sensitivity with respect to the other class, controls in classifier 2.1 and primaries in classifier 2.2, following the notation in Figure 6.2).

It turns out that the selected feature vector for classifier 2.2 consists of E^{lc} and E^{rc} components in mid-ventricular slices and E^{ll} over basal slices for the FCM analysis; for both SVM analyses, zero crossing of E^{rc} component as well as the curl of the 2D deformation field substitute the components E^{ll} and E^{rc}. On the other hand, for the 2.1 classifier, higher variability was found. Modulus of E^{cc} and E^{rr} components in the mid-ventricular area as well as the twisting obtained from eigenvector shift (Fung, 1965) were used in the SVMG analysis, while for SVMQ the latter was replaced by the twisting given by the principal directions tangent angle (Fung, 1965). As for FCM analysis, E^{cc}

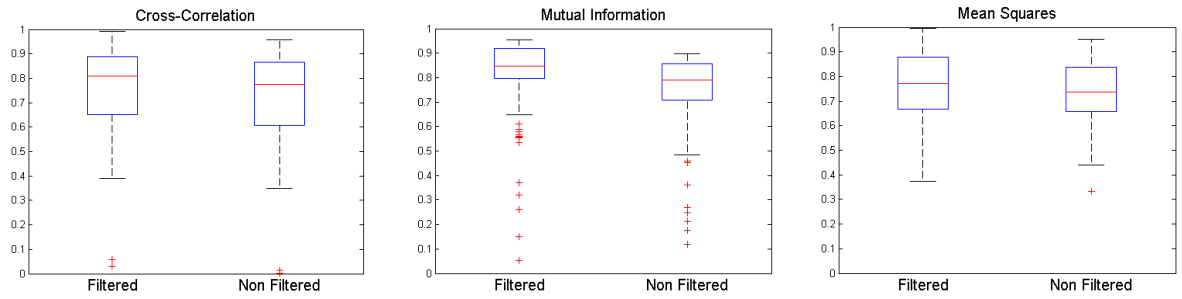

Figure 6.3: Boxplot diagrams of the Dice Coefficient for different registration methods with and without homomorphic filtering.

modulus, curl zero crossing and its modulus have been accounted for.

6.3 Results

6.3.1 Alignment

For the homomorphic filtering procedure, the validation is performed in terms of contour overlapping, measured by means of the Dice Coefficient (Dice, 1945). Different affine registration procedures have been performed in order to align MR-C image at ED phase with its corresponding in the original MR-T and the filtered sequences. The resulting transformation is applied to the MR-T segmentation at ED phase and the Dice coefficient is calculated between the latter and the original MR-C segmentation. Boxplot diagrams of the Dice coefficient distributions obtained with the three similarity metrics compared are displayed in Figure 6.3.

Mann-Whitney U-tests have been used to determine whether significant improvements exist in the medians of the Dice coefficient distributions when carrying out the homomorphic filtering stage; three different metrics have used, the results of which are, p= 0.0154 for NCC (Avants et al., 2008), p=$2.03E-11$ for MI and p= 0.0134 for SSD; consequently, in the three cases significant differences have been observed.

6.3.2 Tensorial Estimation

For each patient described in Section 6.2.1, 3D deformation gradient tensors are obtained from the LS and the LAD methods; the 2D components of these tensors (i.e., excluding the five terms related to the longitudinal component) should ideally be equal to the components of the 2D tensor obtained directly from the MR-T SA images. So, since in the 2D case four parameters are estimated out of two orientations and in 3D nine are estimated out of four, we take the 2D tensor as the reference and measure the quality of the estimator in 3D as the similarity between its 2D components with those

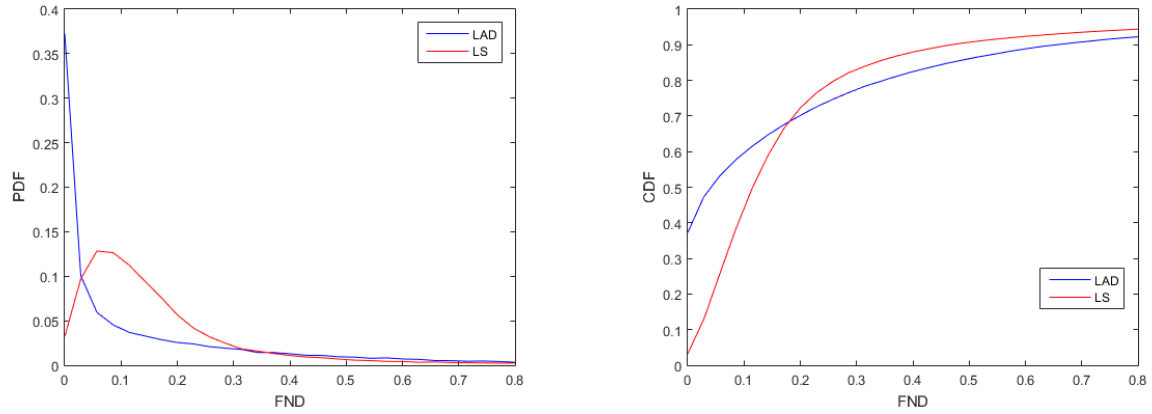

Figure 6.4: FND and CDF of the tensors obtained by either LAD or LS reconstruction method with respect to the 2D tensor reconstructed with minimal wave vectors.

Table 6.2: Confusion matrices for the FCM, SVMQ, SVMG and *mixed* classifers.

	FCM			SVMQ			SVMG			Mixed		
	Con	Sec	Pri	Con	Sec	Pri	Con	Sec	Pri	Con	Sec	Pri
Con	0.245	0.055	0	0.225	0.072	0.003	0.215	0.085	0	0.239	0.061	0
Sec	0.051	0.125	0.024	0.063	0.136	0.001	0.08	0.119	0.001	0.036	0.147	0.017
Pri	0.012	0.016	0.472	0	0.148	0.352	0.004	0.069	0.427	0	0.034	0.466

of the 2D tensor. Similarity is calculated in terms of the FND (Cordero-Grande et al., 2016) between the 2D tensor and its correspondence in the 3D tensor.

Figure 6.4 shows the distribution of the FND indexed for each of the methods used for the 3D tensor estimation (left) as well as the corresponding FND CDF (right). Significant differences have been found between medians of both error distributions by means of the Mann-Whitney U-test (p=$8.94E-22$).

6.3.3 Classification

Finally, we show the performance of the classification algorithm in Table 6.2 by means of normalized confusion matrices. Each column of the matrix represents the instances in the predicted class, while each row represents the instances in the actual class. This allows more detailed analysis than mere proportion of correct guesses (accuracy).

From Table 6.2 global accuracy as well as measures of specificity and sensitivity can be obtained for each group and each classification method. The approach referred to as *mixed* consists of FCM in stages 1 and 2.2 and SVMG in stage 2.1.

6.4 Discussion

In Section 6.3.1 we have described an alignment stage aimed at mapping the MR-C segmentations provided by cardiologist onto the MR-T sequence. The segmentations are used to define a ROI on which to compute meaningful measures of the tensor. This stage could be performed for every cardiac phase as MR-C sequence has been preprocessed by means of a GW elastic registration procedure in order to propagate the ED segmentations along the whole cardiac cycle.

Figure 6.3 shows an increase in the overlapping of the segmentations when the homomorphic filter is applied to the image independently of the metric used in the registration procedure; specifically, the improvement in performance caused by the homomorphic filter is higher than the improvement obtained by switching the registration metric. Therefore, we can conclude that a preprocessing stage is relevant in order to perform precise registration over MR-T images.

Although in this paper the ultimate goal of the alignment stage is the projection of segmentations, this stage can be also applied to other more ambitious objectives, such as a multimodal scheme of material point tracking along the cardiac cycle or finding the association between gadolinium accumulation in late enhancement images and local mechanical abnormalities in the myocardium. We have taken some steps in this latter direction (Cordero-Grande et al., 2013b; Sanz-Estébanez et al., 2015).

As for the tensor estimation technique, a better response in terms of robustness is observed in Figure 6.4 for the LAD estimator with respect to LS. The results conclusively support the hypothesis that the LAD estimator is better suited for this reconstruction problem, where the main source of inconsistencies seems to be the presence of phase interferences as opposed to the presence of noise in the measurements. Specifically, the CDF curve is left skewed although heavier tails are observed, i.e., the majority of the estimations are more accurate than for the LS method, at the expense of the onset of larger errors whenever estimations are inaccurate.

From the results in Section 6.3.3 we can see that the methodology here presented seems effective in classifying HCM patients out of tensorial descriptors obtained from MR-T sequences. Better sensitivity figures are observed for both control and primary HCM patients with respect to the secondary patients, for which performance is clearly lower (specially for SVMQ), possibly due to the small data sample included in the study for this group. A poor sensitivity to primary HCM is observed when using SVMQ, resulting in the lowest global accuracy. A quadratic kernel seems inadequate for this problem, possibly due to the multiple states present in primary HCM. On the other hand, SVMG provides best performance in detecting secondary HCM. Consequently, we have resorted to a *mixed* approach to take advantage of the accuracy in primary HCM detection of FCM analysis and the secondary HCM sensitivity shown by SVMG, obtaining sensitivity figures higher than 70 % for each group (especifically, 80 % for control, 73 %for secondary patients and 93 % for primary patients). It is worth mentioning that no primaries as classified as controls and vice versa; therefore, the pipeline proposed seems a proper screening tool.

6.5 Conclusion

A processing pipeline for the tensorial classification of HCM is presented which builds upon a robust 3D tensor estimation technique from SA and LA MR-T sequences and a novel homomorphic filtering preprocessing step. This filtering method has significantly improved the accuracy of the alignment and it paves the way to construct multimodal processing schemes in which different modalities can be accurately dealt with, as it would be the case for MR-C, MR-T and Late Enhancement MR.

A comparative study in terms of robustness provided by LAD and LS estimators in real datasets has also been carried out, supporting the hypothesis that LAD estimator is worth taking for an overdetermined reconstruction problem in tagging images.

For the classifier itself, we have compared three different classification methods used in machine learning, namely, FCM and SVM with quadratic and Gaussian kernels. We have shown that the fuzzy approach provides better global accuracy results although it is not suitable for small data sets, while SVM do. Consequently, we have resorted to a mixed approach that takes advantage of both techniques obtaining high rates in global accuracy with more balanced sensitivities of each class with respect to those obtained with a unique classifier in the sequential procedure.

Although our classifier is designed for HCM patients, it can be easily tuned for other CVD as long as appropiate biomarkers are available; these biomarkers could be derived from different technologies.

Acknowledgments.

This work was partially supported by the Spanish Ministerio de Ciencia e Innovacion under Research Grant TEC2013-44194-P, the Spanish Ministerio de Ciencia e Innovacion and the European Regional Development Fund (ERDF-FEDER) under Research Grant TEC2014-57428-R, the Spanish Junta de Castilla y Leon under Grant VA136U13 and the European Social Fund (ESF-FSE).

Chapter 7

Robust Windowed Harmonic Phase Analysis with a Single Acquisition

Published as:

Sanz-Estébanez, S.[1], Cordero-Grande, L.[2], Martín-Fernández, M.[1] and Alberola-López, C.[1] (2018). Robust windowed harmonic phase analysis with a single acquisition. In *Proceedings of the 21st International Conference on Medical Image Computing & Computer Assisted Intervention. 1st International Workshop on Thoracic Image Analysis (MICCAI/TIA 2018)*, vol:11040, pp:135-146, Granada, Spain.

[1] Laboratorio de Procesado de Imagen, Department of Teoría de la Señal y Comunicaciones e Ingeniería Telemática, ETSIT, Universidad de Valladolid, Campus Miguel Delibes s.n., 47011, Valladolid, Spain.

[2] Centre for the Developing Brain and Department of Biomedical Engineering, Division of Imaging Science and Biomedical Engineering, King's College London, St Thomas' Hospital, SE1 7EH, London, U.K.

The HARP methodology is a widely extended procedure for cardiac tagged magnetic resonance imaging since it is able to analyse local mechanical behaviour of the heart; extensions and improvements of this method have also been reported since HARP was released. Acquisition of an over-determined set of orientations is one of such alternatives, which has notably increased HARP robustness at the price of increasing examination time. In this paper, we explore an alternative to this method based on the use of multiple peaks, as opposed to multiple orientations, intended for a single acquisition. Performance loss is explored with respect to multiple orientations in a real setting. In addition, we have assessed, by means of a computational phantom, optimal tag orientations and spacings of the stripe pattern by minimizing the Frobenius norm of the difference between the GT and the estimated material deformation gradient tensor. Results indicate that, for a single acquisition, multiple peaks as opposed to multiple orientations, are indeed preferable.

Keywords: Cardiac Tagged Magnetic Resonance Imaging; Harmonic Phase; Multi-Harmonic Analysis; Robust Strain Reconstruction.

7.1 Introduction

Measures of local myocardial deformation are essential for a deeper comprehension of heart functionalities for both normal and pathologic subjects (Jeung et al., 2012). MR-T is a noninvasive method for assessing the displacement of heart tissue over time (Shehata et al., 2009). This modality is based on the generation of a set of saturated magnetization planes on the imaged volume, so that material points may be tracked throughout the cardiac cycle (Ibrahim, 2011) and local functional indicators, such as the ST (Simpson et al., 2013), can be estimated.

Regarding the analysis of MR-T images (Axel et al., 2005), we can differentiate two main families of methods, image-based and k-space-based techniques. The image-based techniques are devised to directly process and analyse the tagged images by identifying the tag lines and tracking their deformation between frames. Examples of such techniques are optical flow (Horn and Schunck, 1981) or deformable models (Young and Axel, 1992) methodologies. Alternatively, the k-space-based techniques focus on the FT of the tagged images. Compared to the image-based, k-space-based techniques have proven to be much faster and less prone to artifacts (Ibrahim et al., 2016). Most notable methodologies in this category are SinMod (Arts et al., 2010) and HARP (Osman et al., 2000) analysis. Recent studies have reported that, although both techniques are consistent in motion estimates, an exaggeration in measurements is often observed for SinMod (Ibrahim et al., 2016), leading to larger biases. Therefore, we have focused on HARP-based methods. These methods are grounded on the extraction of the complex image phase obtained by bandpass filtering the spectral peaks introduced by the applied modulation; they rely on the fact that the extracted harmonic phase is linearly related to a directional component of the true motion (Osman et al., 2000). Hence, dense displacement fields can be recovered on the basis on a constant local phase assumption, which turns out to be more reliable than a constant pixel brightness assumption.

An in-depth study of the HARP method is provided in Parthasarathy (2006); the author uses a communications-based approach to analyze the method in detail, including resolution, dynamic range and noise. Signal processing solutions based on the WFT (Cordero-Grande et al., 2011) have been proposed to balance the spatial and spectral localization of the image, thus obtaining smooth local phase estimations. Adaptive approaches have been subsequently proposed in Fu et al. (2013); Sanz-Estébanez et al. (2016a) in order to accommodate tag local properties both in window and filter designs, respectively. However, slight improvements have been reported with respect to non-adaptive methods, taking into account the considerable computational cost increasing.

Techniques to synthesize more desirable tag patterns have also been proposed using multiple harmonic peaks, both with different tag spacings (Atalar and McVeigh, 1994) and new profiles (Osman and Prince, 2004). Methodologies that make use of multiple orientations (Moser and Smith, 1990; Agarwal et al., 2010; Cordero-Grande et al., 2016) have also been devised to improve the quality of the estimated motion at the prize of increasing acquisition time. Besides, these methodologies require of non-trivial image re-

gistration techniques to align the multiple acquisitions, which itself may also have an important impact on processing conclusions.

In this paper we depart from the reported idea that using an overdetermined set of orientations, Multi-Orientation (MO), significantly increases the quality of the estimated deformation gradient tensor (Cordero-Grande et al., 2016); however, our purpose is to convey information within a single acquisition at the expense of a worse performance with respect to multiple acquisitions. Therefore, we have explored performance of using two peaks with two orthogonal orientations within a single acquisition, as opposed to multiple single-peaked orientations in multiple acquisitions, and we quantify performance loss. Then, we find out through optimization both tag orientation and spacing of two stripes patterns that are set free when another two are set beforehand. Interestingly, our results indicate that the latter approach converges to the former, i.e., two orthogonal orientations with two peaks is the preferable solution when a unique acquisition is pursued.

7.2 Materials

MR-T is usually performed by SPAMM (Axel and Dougherty, 1989), which is grounded on the ability of altering the magnetization of the tissue in presence of motion. This process will generate a modulation with different sinusoidal functions. Each of these sinusoids will be given by its wave vector $\mathbf{k}_i$ with $\mathbf{k}_i = k_i \mathbf{u}_i$, where k_i is the wave number (related to its frequency) and $\mathbf{u}_i$ its orientation vector (corresponding to the orientation of the applied gradient).

We have acquired a medial slice on an adult volunteer using a MR SPAMM SENSE TFE sequence on a Philips Achieva 3T scanner. The image has a spatial resolution of $1.333 \times 1.333\,\mathrm{mm}^2$ and a slice thickness of 8 mm. The acquisition parameters are $T_E = 3.634\,\mathrm{ms}$, $T_R = 6.018\,\mathrm{ms}$ and $\alpha = 10°$. Regarding the tagging parameters, the tag spacing has been set to $\lambda = 7\,\mathrm{mm}$, with its different harmonic peaks at $\mathbf{k} = \{1, 2\}/\lambda$ and different orientations $u_i = (\cos(\theta_i), \sin(\theta_i))$. The specific orientations are $\theta_i = -85° + i \cdot 5°$ with $0 \leq i \leq 35$, therefore with $-85° \leq \theta_i \leq 90°$. Two grid patterns have also been acquired with $45° - 135°$ and $0° - 90°$ orientations.

Simulated SPAMM sequences (Rutz et al., 2008) have also been launched both with one (1D) and two orientations (2D), with different λ values and multiple spectral peaks, some examples of which are shown in Fig 7.1. Harmonic coefficients have been set according to Osman and Prince (2004).

Optimization experiments have been performed on the synthetic data; the computational phantom consists in an annulus centered at the myocardium with $R_i = 28$ and $R_o = 40$ as its inner and its outer radii, respectively. An incompressible radially varying deformation has also been applied according to $r = \sqrt{R^2 - \gamma R_i^2}$, where γ controls the degree of deformation and r and R represent the spatial and material radial coordinates, respectively. Notice that for the simulated SPAMM synthetic data, we have not included noise, tag fading or other undesired effects. We have preferred not to simulate these

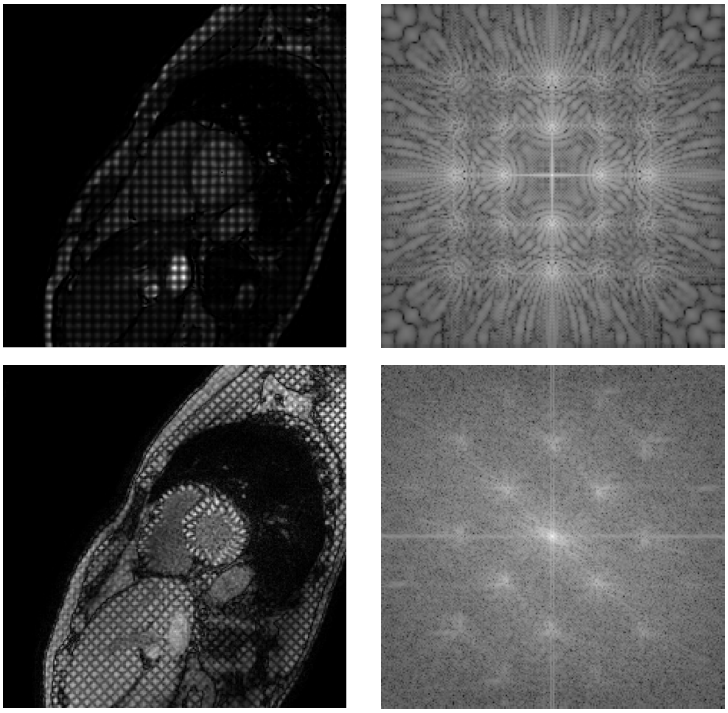

Figure 7.1: The two upper images show synthetic data (2D) while real dataset is sketched below for 2D in a $45° - 135°$ grid. All intermodulations for the 2D case are present.

confounding factors, which are present in real data, in order to remove its influence in the final tag pattern design.

7.3 Method

7.3.1 Reconstruction Pipeline

As stated in Osman et al. (2000), HARP motion reconstruction using SPAMM requires a minimum of 2 linearly independent wave vectors. The proposed approach allows us to accommodate multiple wave vectors stemming from the different orientations and harmonic peaks. Reconstruction pipeline can be summarized in the following steps (see Fig. 7.2):

- **Calculation of the local phase of the image.** For a given cardiac phase, we compute the 2D discrete WFT (Cordero-Grande et al., 2016) to obtain the local spectrum $S[\mathbf{m}]$ for each image $I[\mathbf{x}]$. The window employed at this step is real, even, of unit norm, and monotonically decreasing for positive values of its argument. Hence, the obtained discrete WFT can be seen as a set of discrete FTs applied to the result of windowing an image throughout its support.

Once local spectrum is calculated, a complex bandpass filter is applied to extract the corresponding phase to each wave vector i. Therefore, for each pixel of the image, we have built a circumferential spectral filter, whose radius is linearly related to a previously defined bandwidth, which has been centered at the maximum of the spectra inside a predefined region located in the surroundings of the reference spatial frequency of the tags.

The final WHARP image, for each wave vector, can be reconstructed in the spatial domain by using an IWFT from which its phase is readily extracted, i.e., $\phi_i[\mathbf{x}] = \angle\hat{I}_i[\mathbf{x}]$.

- **Material deformation gradient tensor estimation at end-systolic phase.** The material deformation gradient tensor $\mathbf{F}(\mathbf{x})$ can be estimated from the gradient of the phase image $\mathbf{Y}(\mathbf{x})$ as stated in Osman et al. (2000). Robust estimation of $\mathbf{F}(\mathbf{x})$ is achieved through LAD procedure (Cordero-Grande et al., 2014). Reconstruction is performed via IRLS:

$$\mathbf{F}_{l+1}(\mathbf{x}) = (\mathbf{Y}^T(\mathbf{x})\mathbf{W}_l(\mathbf{x})\mathbf{Y}(\mathbf{x}))^{-1}\mathbf{Y}^T(\mathbf{x})\mathbf{W}_l(\mathbf{x})\mathbf{K}, \tag{7.1}$$

where $\mathbf{K}$ represents the given wave vectors and $\mathbf{W}_l(\mathbf{x})$ a diagonal weighting matrix updated at each iteration by considering the fitting residuals (Cordero-Grande et al., 2016). For illustration purposes, the Green-Lagrange ST is also computed in the polar coordinate system.

7.3.2 Optimal Tag Pattern Search

In order to find the optimal tag pattern, we have carried out an optimization procedure on the synthetic data; the procedure is schematically shown in Fig. 7.2. The upper part shows how the GT data is obtained. First, the stripe patterns, consisting in two sets of two orthogonal directions are generated. Each pattern is then applied to a previously acquired cine sequence. Each pattern is applied in isolation so that no interference arises. Then, the methodology described in Section. 7.3.1 is applied to calculate $\mathbf{F}^{GT}$.

The stripes are oriented as $0°, 45°, 90°, 135°$ with $\lambda = 7.15$ mm and only the DC component and the two symmetric peaks are included in the simulation. The analysis window w of the WFT is defined as stated in Section 7.3.1 and its size has been set to $\mathbf{Q} = [32, 32]$.

The bandpass filter parameters, for each pixel $\mathbf{x}$ and wave vector i, are represented as $\boldsymbol{\beta}_i[\mathbf{x}] = (\hat{\mathbf{k}}_i[\mathbf{x}], \rho)$, where ρ is the radius of the filter, which is centered at $\hat{\mathbf{k}}[\mathbf{x}]$.The filter bandwidth is normalized with respect to the wave number ($\mu = \rho/k$, $k = 2\pi/\lambda$) so that area of all filters remains the same along the pipeline.

As for the lower part of the figure, the tags are multiplied to each other as well as to the cine sequence; intermodulations are therefore present in the problem. Then, the aforementioned reconstruction procedure is performed but for the fact that the WFT is

applied to the image degraded by interference. When the bandpass filter bank is applied, channels are processed in parallel. In this case, two stripes $(0°, 90°)$ remain fixed with its tag spacing at $\lambda_{1,2} = 7.15$ mm. The other two stripes are considered as variables in the optimization problem, both in tag orientation and spacing $(\theta_3, \theta_4, \lambda_3, \lambda_4)$. The objective function to be minimized is defined upon the FND between a GT tensor F^{GT} and the estimated tensor with a specific value of the variable $\mathbf{\Theta}$ (see below); this function is integrated over a predefined ROI χ that encloses the myocardium. Formally:

$$\mathbf{\Theta}^* = \arg\min_{\mathbf{\Theta}} \int_{\chi} FND(\mathbf{x}, \mathbf{\Theta})^2 d\chi = \arg\min_{\mathbf{\Theta}} \int_{\chi} \sum_{m=1}^{2} \sum_{n=1}^{2} (F_{mn}^{GT}(\mathbf{x}) - F_{mn}(\mathbf{x}, \mathbf{\Theta}))^2 d\chi$$

with $\mathbf{\Theta} = \left[\begin{array}{cccc} \theta_3, & \theta_4, & \lambda_3, & \lambda_4 \end{array} \right]$.

The solution has been obtained by means of the Nelder-Mead algorithm (Nelder and Mead, 1965). This algorithm does not require derivatives of the objective function. Simulation has been limited to four stripes to avoid an overwhelming peak interference.

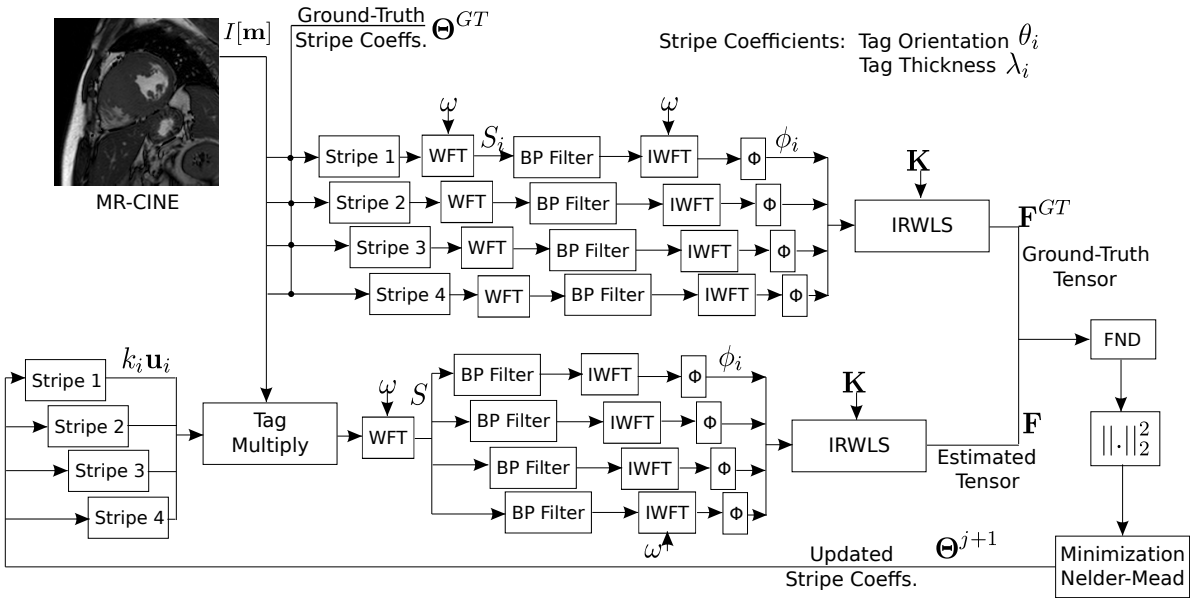

Figure 7.2: Flowchart of the optimization procedure for optimal stripes parameter search. Notice that connections from the Nelder-Mead algorithm to stripes 1 and 2 do not undergo any variation.

7.4 Evaluation and Discussion

The importance of the number of orientations is measured in Fig. 7.3 in terms of reproducibility for the real dataset. Estimated tensors should be equal irrespective of the stripe pattern used; therefore, a useful measure of reproducibility is the FND defined

above but applied in this case to two instances of the reconstructed tensor with two different, albeit comparable, stripe sets. Specifically, given two stripe sets with the same number of orientations and their respective reconstructed tensors, we have calculated the median of the $FND(\mathbf{x})$ with both for $\mathbf{x} \in \chi$.

Fig. 7.3 shows the impact on reproducibility of using either additional orientations or additional harmonic peaks.

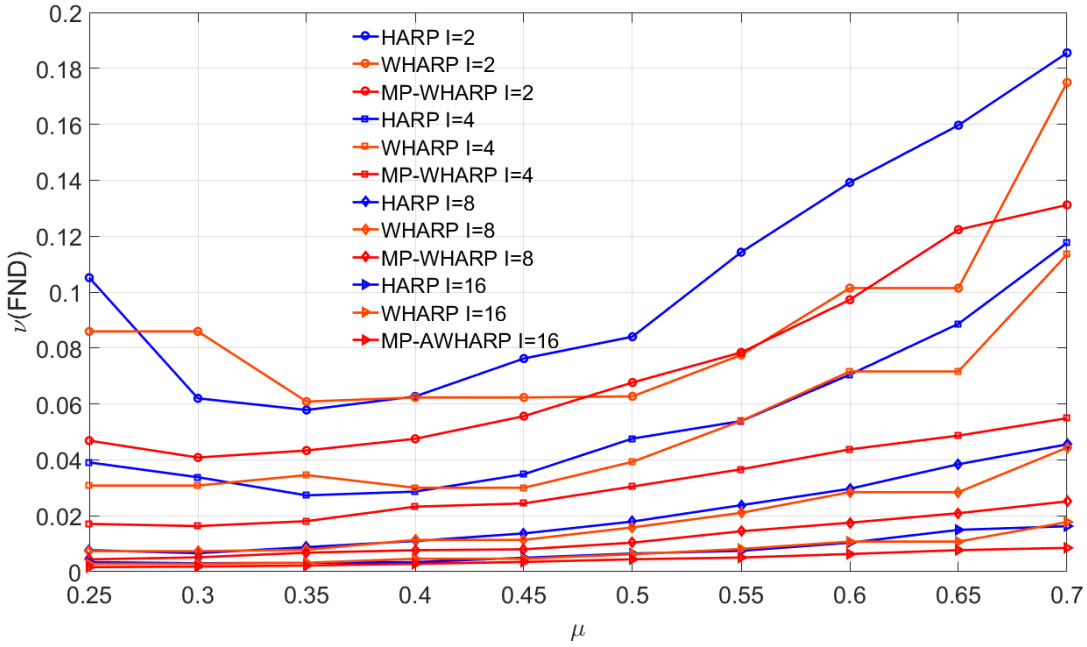

Figure 7.3: Median of the FND $\forall \mathbf{x} \in \chi$ obtained with different number of images as a function of the filter bandwidth μ.

As previously described in Cordero-Grande et al. (2016), an overdetermined set of stripes increases reproducibility at the price of a higher number of acquisitions. For a given number of orientations the Multi-Peak (MP) windowed approach (WHARP) shows additional improvement for moderate bandwidths. HARP analysis has also been added showing lower figures. When bandwidth is excessive, interference from nearby peaks reduces the stability of results. MP-WHARP obtained with I=2 is located halfway between the other results with I=2 and those with I=4. This solution would require a single acquisition while I=4 requires at least two, for a grid pattern.

For the synthetic dataset, Fig. 7.4 shows the MSE of the ST principal components ($\hat{E}^{rr}$) and ($\hat{E}^{cc}$) for different options (windowed, MP, MO) as a function of the degree of deformation γ. In these figures solid lines are obtained with multiple images (I=18) and dashed lines with only two orthogonal directions (I=1); in both, grid patterns have been used. As can be observed, MO and MP play a satisfactory role for moderate values of γ. It is worthy to say that MP approach presents a notable performance, even with a unique grid-like acquisition. On the other side, when severe deformation is applied to the

I=1 cases, non-MP approaches depart dramatically from the GT while LAD algorithm maintains quality fairly unaltered for the MP version (dashed-red line).

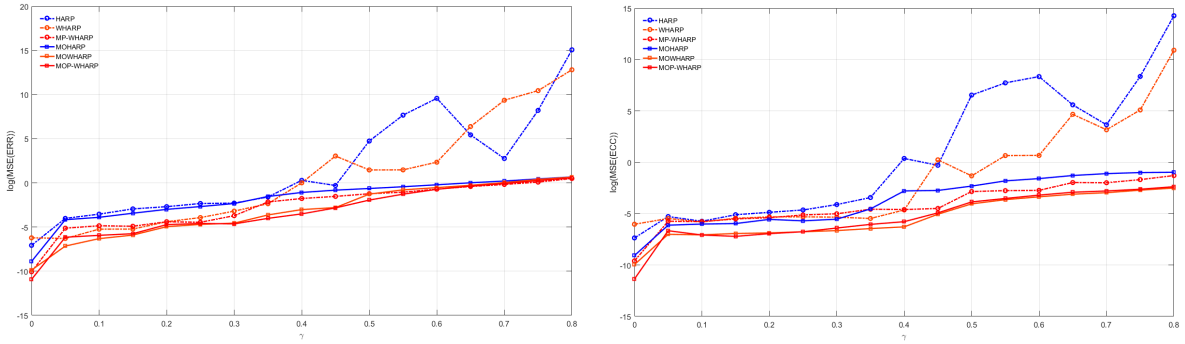

Figure 7.4: Log-MSE of ($\hat{E}^{rr}$) (left) and ($\hat{E}^{cc}$) (right) for $\mu = 0.35$. Solid line denotes reconstruction error with 18 images while dashed dashed lines are obtained with only two.

In Fig. 7.5, we show the output of the optimization procedure described in Section. 7.3.2. According to the figure, the two free orientations turn out to align with the two that remained fixed, although spectral separation is lower than the separation of the steady peaks with respect to the DC component; specifically, the steady peaks are located at $k = 7.15^{-1} = 0.14$ mm^{-1}, while the other two turn out to be located (on average) $k \sim \frac{1.6}{7.15}$ mm^{-1}. This output, however, is not directly available in equipments routinely used in clinical settings.

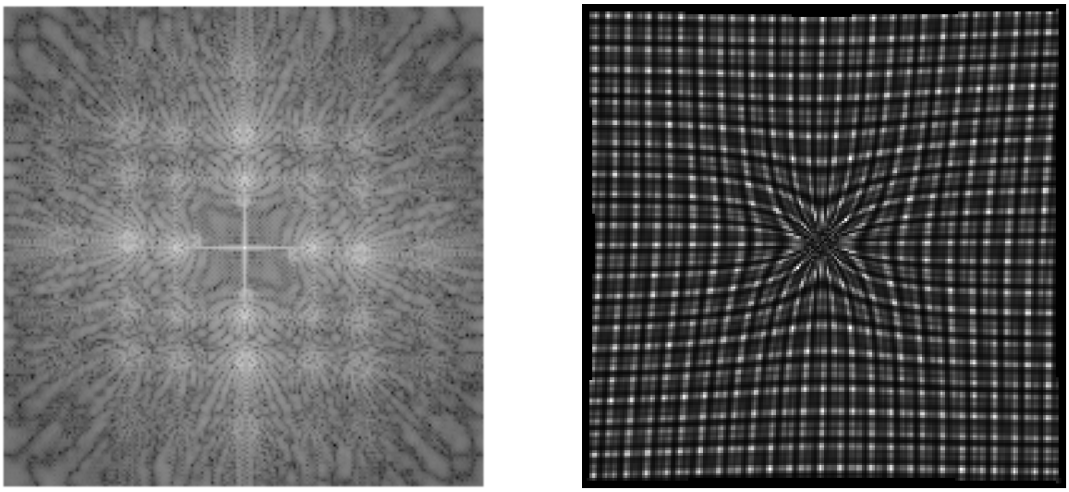

Figure 7.5: Final configuration of the tag pattern obtained with Nelder-Mead algorithm both on k-space (left figure) and spatial domain (centered at right figure) with $\gamma = 0.45$.

Therefore, we have carried out an additional two-fold experiment in order to test relevance of peak separation or, equivalently, tag spacing. For this purpose, we have calculated the MSE in E^{rr} estimation for both 1D and 2D cases; for the former, we have

simulated a pattern with two peaks in the same direction, where the first peak is located at $\lambda_1 = 7.15$ and the second peak is translated, in k-space, along that direction. For the latter, the pattern consists of a multiplication of two such 1D patterns in orthogonal directions. Results, as shown in Fig. 7.6, indicate that optimal separation depends on the degree of deformation γ, with higher sensitivity in the 1D case, whereas, for 2D, sensitivity is much lower for $\gamma \geq 0.3$. In this interval, performance is fairly constant so a $\frac{1}{\lambda_1} = 0.14$ separation, i.e., location of harmonically related peaks, seems an appropriate design choice. This is the case of a grid pattern with second order SPAMM acquisition, which is a commonly available sequence. Presence of noise and tag fading in simulation will presumably increase smearing in k-space, making this space more crowded, so this conclusions tend to reinforce. With this in mind, it may be appealing to include even more peaks in the acquisition. However, growing between-peak-interference may severely affect estimates. For that reason, we have limited our experiments to a maximum of four stripes per acquired image. Further research should be developed in this direction to assess the influence of heavily-peaked acquisitions in the robustness of reconstructions.

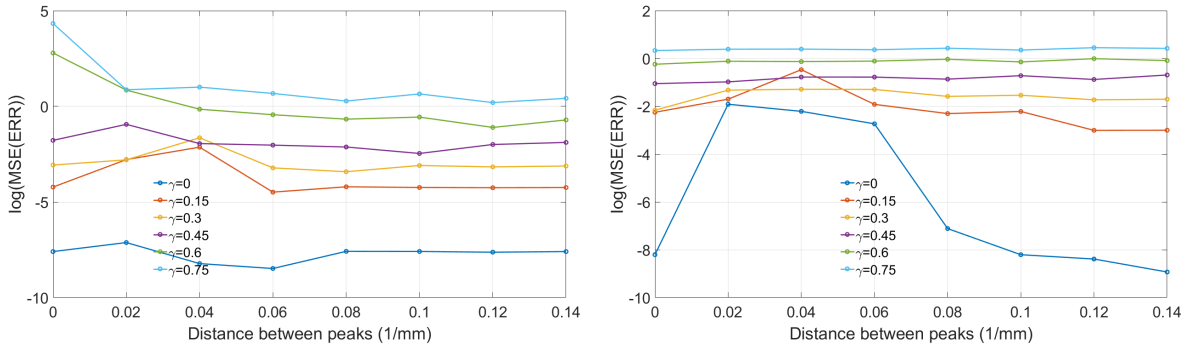

Figure 7.6: Log-mean squared error in E^{rr} estimation as a function of the distance between peaks in presence of different degrees of deformation with a fixed $\mu = 0.35$. 1D and 2D cases have been plotted in left and right figures, respectively

Additionally, in Fig. 7.7 we show the FND obtained on real data with different stripe sets for different bandwidths; we have used as a silver estimate of $\mathbf{F}$ the one obtained with the eight 1D orientations indicated in Section. 7.2. Specifically, we have tried the following subsets: $45° - 135°$ and $0° - 90°$ in a grid (2D) pattern with two peaks per orientation, and $45° - 135°$, $0° - 90°$, $45° - 135° - 0° - 90°$ and $30° - 60° - 120° - 150°$ for line (1D) acquisitions with a unique peak. The figure reveals that harmonic MP solution with a single acquisition overcomes the solution obtained with two orthogonal line acquisitions and it provides a reasonable performance loss with respect to four-orientation reconstructions, i.e., those needing two acquisitions, at least, in commercial equipments. Therefore, we can conclude that our solution shows an appropriate balance between estimation robustness and time consumption.

Finally, in Fig. 7.8 we show E^{rr} and E^{cc} estimates from the simulated SPAMM data using the different methods (FT, (WFT and MP-WFT) using two grid images for the

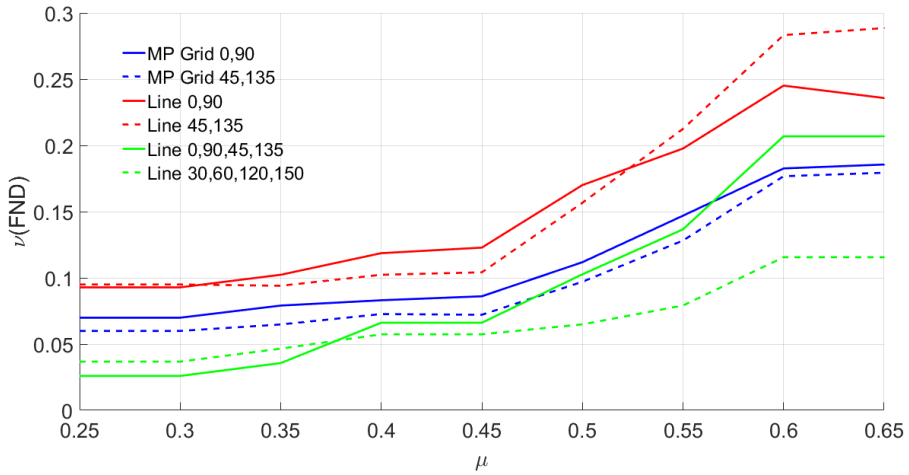

Figure 7.7: Median of the FND obtained with different stripe sets as a function of μ.

FT and WFT approaches, while only one has been employed for the proposed MP-WFT approach (four wave vectors in total).

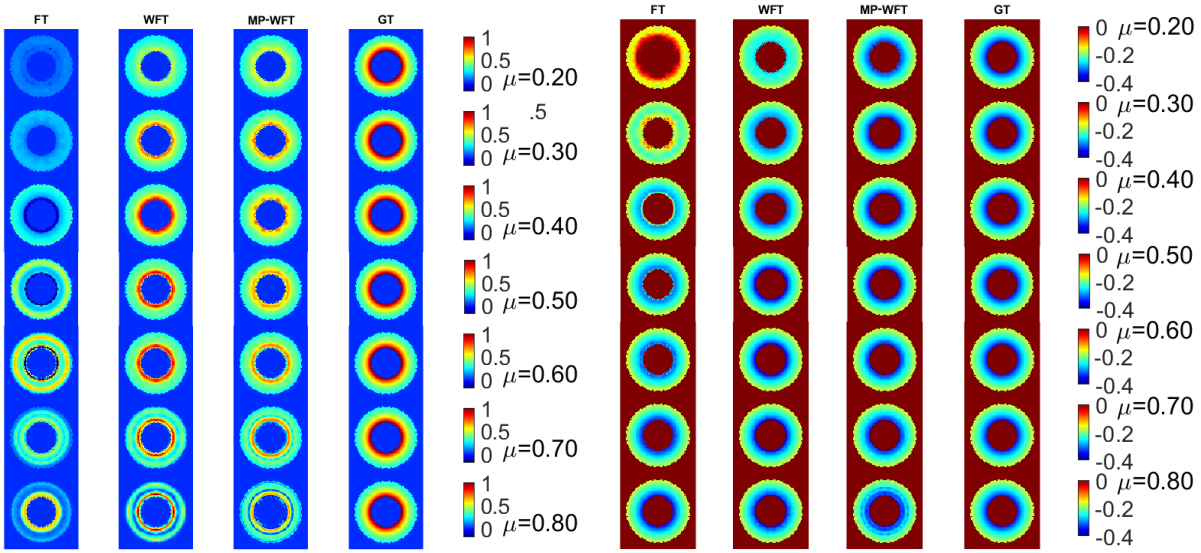

Figure 7.8: E^{rr} (left) and E^{cc} (right) strain components for synthetic data obtained for different bandwidths and methodologies. GT is also shown for the sake of comparison.

Visual results illustrate about the influence of bandwidth; when using smaller ones strain is underestimated whereas when incrementing significant artifacts and interferences arise. Obviously, the emergence of these artifacts would be greatly limited by the use of a larger number of wave vectors, although MP-WFT approach seems less prone to them.

7.5 Conclusions

In this paper we have described a robust alternative to the original HARP method, intended for a single acquisition. To this end, we have observed that information comprised by various peaks of the stripe pattern is useful for achieving robust results despite using a unique acquisition. We have quantified performance of this solution with respect to multi-oriented solutions.

Simulation results indicate that four orientations converge into an orthogonal grid with harmonically related peaks (in a mid to high deformation degree interval) for an optimal performance, so multiple peaks as opposed to multiple stripes is a preferable solution. The proposed pattern has also shown comparable results, for the case of a single acquisition, to those obtained with two different grid acquisitions, while the latter doubles the scan time.

Furthermore, the proposed multi-peaked method has significantly improved both the accuracy and the reproducibility of strain measurements with respect to the standard acquisition in which just two orthogonal orientations are acquired, using same amount of time. With the proposed design, current acquisition protocols can be easily recast to include multiple peaks, which could simultaneously improve the resolution, robustness and precision of motion sensitive MRI and its subsequent analysis.

Acknowledgments.

This work was partially supported by the European Regional Development Fund (ERDF-FEDER) under Research Grants TEC2014-57428-R and TEC2017-82408-R, the Spanish Junta de Castilla y León under Grant VA069U16 and the European Social Fund (ESF-FSE).

Chapter 8

Groupwise Non-Rigid Registration on Multiparametric Abdominal DWI Acquisitions for Robust ADC Estimation: Comparison with Pairwise Approaches and Different Multimodal Metrics

Published as:

Sanz-Estébanez, S.[1], Peña-Nogales, Ó.[1], de-Luis-García, R.[1], Aja-Fernández, S.[1] and Alberola-López, C[1]. Groupwise non-rigid registration on multiparametric abdominal DWI acquisitions for robust ADC estimation: comparison with pairwise approaches and different multimodal metrics. In *Proceedings of the 14th IEEE International Symposium on Biomedical Imaging: From Nano to Macro*, pp:1156-1159, Melbourne, Australia.

[1] Laboratorio de Procesado de Imagen, Department of Teoría de la Señal y Comunicaciones e Ingeniería Telemática, ETSIT, Universidad de Valladolid, Campus Miguel Delibes s.n., 47011, Valladolid, Spain.

Registration of diffusion weighted datasets remains a challenging task in the process of quantifying diffusion indexes. Respiratory and cardiac motion, as well as echo-planar characteristic geometric distortions, may greatly limit accuracy on parameter estimation, specially for the liver. This work proposes a methodology for the non-rigid registration of multiparametric abdominal diffusion weighted imaging by using different well-known metrics under the groupwise paradigm. A three-stage validation of the methodology is carried out on a computational diffusion phantom, a watery solution phantom and a set of voluntary patients. Diffusion estimation accuracy has been directly calculated on the computational phantom and indirectly by means of a residual analysis on the real data. On the other hand, effectiveness in distortion correction has been measured on the phantom. Results have shown statistical significant improvements compared to pairwise registration being able to cope with elastic deformations.

Keywords: Non-rigid registration; Groupwise schemes; Multimodal metric; Diffusion-weighted magnetic resonance imaging; Distortion correction; Motion compensation.

8.1 Introduction

Diffusion is described as the thermally induced behaviour of molecules moving in a microscopic random pattern, often referred to as Brownian motion. DW-MRI is sensitive to this microscopic motion. Common approaches to estimate this motion assume a monoexponential decay in the DWI signal, providing characteristic quantitative parameters of the tissue, such as the well-known ADC. ADC has been shown to be a positive indicator to tumor response (Kim et al., 1999) due to its ability to measure displacement of water molecules, giving evidences about cellular organization and cell permeability of micro-structures (Le Bihan, 2014).

However, in order to thoroughly validate these parameters as biomarkers, a robust parameter estimation methodology is mandatory, which is a complicated task, as an increasingly signal intensity dropout is observed when applying greater strength of the magnetic diffusion gradient values (the so-called *b-values*), as illustrated in Figure 8.1. Currently, simple estimators, such as the linear-LS method (Heiland et al., 2001) are customary for ADC estimation. However, ADC estimation may also be greatly affected by several confounding factors, especially in a visceral organ like the liver, which exhibits considerable movement during imaging caused by respiratory (Mazaheri et al., 2012) and cardiac motion (Liau et al., 2012). In addition, ultrafast sequences typically used for diffusion studies, i.e. EPI, suffer from geometric distortions as well as local signal dropouts caused by static magnetic field inhomogeneities (Bernstein et al., 2004). The resultant distortions are commonly seen near tissue interfaces, where magnetic susceptibility changes rapidly.

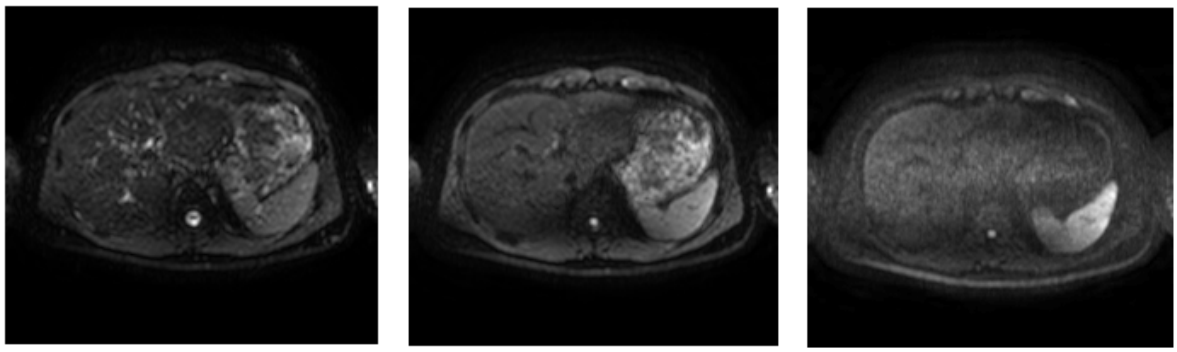

Figure 8.1: Axial slices of DWI acquisition in a healthy patient for *b-values* of 0, 100 and 1000 s/mm^2 (from left to right).

Denoising schemes (Zhang et al., 2014) have been proposed to robustify ADC estimation; in our case, we will focus on multiparametric (multiple *b-values*) abdominal DWI registration schemes to alleviate the effects of these confounding factors. Most approaches pose the registration problem from a PW standpoint (Wu et al., 2008) using an [ideally] undistorted image as reference; this procedure, however, is prone to an undesired bias

towards the a priori chosen template (Wachinger and Navab, 2013), which, depending on its quality, may give rise to multiple outliers in the alignment. On the other hand, GW approaches are based on an image reference that is built out of the whole image set to be registered, so that the template bias disappears.

Methodologies for multiparametric registration towards robust ADC estimation have been designed based on distortion correction methods (Hong et al., 2015) or PW connection metrics (Guyader et al., 2015). GW approaches have been addressed in Veeranghavan et al. (2015) using prior structure segmentations or by minimizing the regression fitting error (Kornapoulos et al., 2016). However, none of them explicitly take into account interaction of liver motion artifacts and EPI geometrical distortions on the deformation field jointly.

In this paper, we address the importance of a registration scheme in the robustness analysis of multiparametric abdominal DWI acquisitions by assessing the adequateness of GW and PW paradigms within an elastic transformation model as well as the suitability of different multimodal voxel-based metrics.

8.2 Materials and Methods

8.2.1 Materials

For the validation of the proposed scheme we have resorted to a three-fold procedure. To begin with, (1) a synthetic experiment has been carried out using a simulation environment based on the 4D XCAT phantom (Segars et al., 2010). The phantom consists of a whole body model that contains high level detailed anatomical labels, which feed a high resolution image synthesis procedure. The 4D XCAT phantom incorporates state-of-the-art respiratory and cardiac mechanics, which provide sufficient flexibility to simulate cardio-torso motion from a user-defined parameter set. Although we assume BH acquisitions, different inspiration levels are simulated for different *b-values*. Residual cardiac artifacts have been neglected. A synthetic deformation field is added in order to simulate typical geometric distortions of EPI acquisitions. Therefore, the phantom provides us not only with the images themselves, but also with a GT ADC map.

Additionally, we have performed two MRI acquisitions, first, (2) on a phantom consisting of a bottle filled with a watery solution and finally (3) with a sample of four healthy volunteers. Axial SENSE DWI and T2W TSE sequences have been acquired on a Philips Achieva 3T scanner in each case of study. The latter will be used to manually delineate the whole liver as ROI on which meaningful measurements will be provided. Acquisition and resolution details for these sequences are shown in Table 8.1.

Params.	XCAT	DWI phant.	DWI volunt.
Δ_p	1	0.7145	1.23-1.85
Δ_l	10	5.5	5.5
N_p	308	480	224-320
N_b	9	12	9-20
N_s	5	12	20-40
T_E	65	31.96	65.65-72.1
N_g	1	3	3
Card.	1	N/a	$\sim$ 1
Resp.	5	N/a	Free

Table 8.1: Details on the image sequences used in the paper. Δ_p : Spatial Resolution (mm). Δ_l : Slice Thickness (mm). N_p: Number of pixels along each direction. N_b: Number of *b-values*. N_s: Number of slices. T_E: Echo Time (ms). N_g: Number of diffusion gradients. Card.: Cardiac Period (s). Resp.: Respiratory Period (s).

8.2.2 Methods

The proposed method has been applied to the GW registration of different *b-value* images in axial abdominal DWI acquisitions and, specifically, for robust estimation of diffusion parameters on both lobes of the liver.

The [ideal] underlying monoexponential decay model applied to the images can be described as follows:

$$S(b) = S_0 e^{-b \cdot \mathrm{ADC}} \tag{8.1}$$

where $S(b)$ and S_0 denote the signal intensity obtained with the diffusion gradient *b-value* of b and null. Sampling of *b-values* is finer for lower *b-values* according to Luna et al. (2012). Nine of this *b-values* are common for every sequence. Those are $b \in \{0, 10, 20, 50, 150, 300, 500, 800, 1000\} s/mm^2$. Finally, ADC has been estimated by the linear LS method.

For the registration scheme, the local transformation T is represented as a combination of B-spline (Rueckert et al., 1999) FFDs. A gradient-descent/ascent optimization scheme is performed for the optimization of the registration metric H.

The developed multimodal metrics for the GW registration approach are the following:

- Entropy of the distribution of intensities (EDI) (Learned-Miller, 2006):

$$H(\mathbf{x}) = S_{\mathcal{T}}(\mathcal{I}(\mathcal{T}(\mathbf{x}))) \simeq \frac{-1}{N} \sum_{n=1}^{N} \log(p(I_n(T_n(\mathbf{x})))), \tag{8.2}$$

  where $p(I_n(T_n(\mathbf{x})))$ is a Parzen window estimation (Wells III et al., 1996) of the

intensity distribution of corresponding pixels. This metric favors those solutions in which pixel intensities are well concentrated in the intensity space.

- Variance of the local entropy (VLE): for the GW approach we will assume that this local entropy is preserved across the image set. Hence, the voxelwise metric will be considered as the SSD of the local entropy images $S_{\mathcal{N}}$ obtained from the transformed image I as described in Wachinger and Navab (2012) as:

$$S_{\mathcal{N}}(\mathbf{I}(\mathcal{N}(\mathbf{x}))) = \frac{-1}{|\mathcal{N}|} \sum_{\mathbf{x}' \in \mathcal{N}(\mathbf{x})} p(I(\mathbf{x}')) \log(p(I(\mathbf{x}'))), \tag{8.3}$$

with $|\mathcal{N}|$ the cardinality of the neighbourhood whose radius has been set empirically to 6 pixels.

- Normalized cross-correlation (NCC):

$$H(\mathbf{x}) = \frac{1}{N} \sum_{n=1}^{N} \frac{< \overline{I_n(T_n(\mathcal{P}(\mathbf{x})))}, \overline{\mu((\mathcal{P}(\mathbf{x}))} >^2}{< \overline{I_n(T_n(\mathcal{P}(\mathbf{x})))} >< \overline{\mu(\mathcal{P}(\mathbf{x}))} >}, \tag{8.4}$$

where $\mu(\mathbf{x}) = \frac{1}{N} \sum_{n=1}^{N} I_n(T_n(\mathbf{x}))$, while $\overline{I_n(T_n(\mathcal{P}(\mathbf{x})))}$ corresponds to the image intensities in a patch $\mathcal{P}$ with its spatial mean subtracted and $<,>$ to the inner product defined in Avants et al. (2008). NCC depends only on estimates of mean and variance from samples of the given patch.

- Modality independent neighbourhood descriptor (MIND): an image descriptor, built from within-patch distances D_p and variance estimates V on a six-neighbourhood search region R, defined as:

$$\text{MIND}(I, \mathbf{x}, r) \propto \exp\left(\frac{D_p(I, \mathbf{x}, \mathbf{x}+r)}{V(I, \mathbf{x})}\right), \tag{8.5}$$

with $r \in R$. Afterwards, sum of simple monomodal similarity measures built from MIND differences is used as a metric, as described in Heinrich et al. (2011).

8.3 Results

In this section, we test the ability of the proposed methods for MC, distortion correction and robust ADC estimation. We have carried out a synthetic experiment with the data provided by the XCAT computational phantom, manually distorted thereafter, on which we have measured the absolute error (over the previously defined ROI) on ADC estimation for the GW multimodal metrics of section 8.2.2 and its counterpart for the PW case. In the latter, the image template is taken from the T2W sequence. Notice that this image is free of EPI distortions, so it is favorable case for PW approaches.

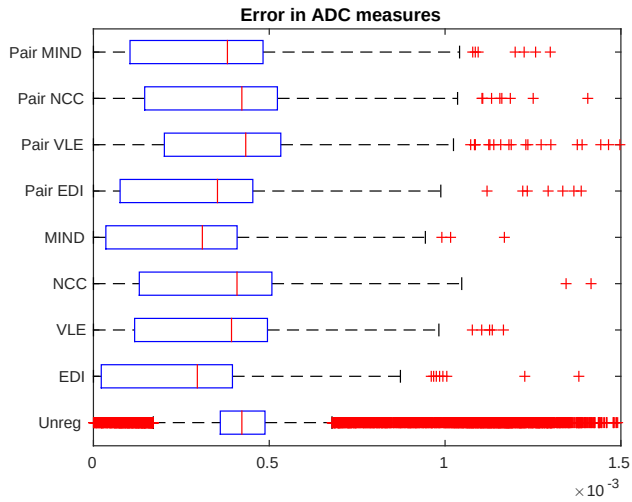

Figure 8.2: Error on ADC estimation for proposed metrics

In Figure 8.2 we show the boxplot diagrams of the absolute error distributions on ADC estimation as a measure of accuracy in MC and distortion correction. Presence of outliers is greatly diminished when performing previous registration.

Mann-Whitney U-tests were performed for each pair of error distributions. Significant differences have been found for EDI, MIND and VLE metrics between its GW and PW approaches (every metric holds $p < 10^{-3}$). Significant differences also exist within GW metrics, with the exception of EDI and MIND metrics ($p = 0.35$), that exhibit best, albeit similar performance in terms of error, specially when compared to the original data ($p < 10^{-9}$ for both).

For the real data, first, we have tested the ability of the aforementioned GW metrics to correct EPI distortions on the MRI phantom described in section 8.2.1. We have performed a quantitative analysis of the overlapping (using the Dice coefficient) between foregrounds obtained from the registered DWI and the undistorted T2W sequences. In Figure 8.3 we show boxplot diagrams of the Dice coefficient for each GW and PW metric and the original data. No significant differences are found for Mann-Whitney U-tests over Dice coefficient distributions of GW metrics compared to its PW counterpart.

Aditionally, Kruskal-Wallis tests were performed, finding significant differences within GW metrics ($p = 0.0027$) and with the original unregistered results ($p < 10^{-6}$). VLE and MIND metrics seem to have better recovered from EPI distortion in this scenario.

In addition, for the volunteer data, as a GT is not available, we have resorted to a goodness-of-fit analysis showing the discrepancy between the data and the diffusion model in equation (8.1). We have measured the Residual Sum of Squares (RSS) obtained in the ADC estimation for each GW and PW metric as a measure of robustness.

After performing U-tests, no differences were found for RSS distributions neither between GW or PW metrics nor with the original data. In this case, apparently, the acquisition protocol parameters and the estimation model have had a greater impact on the RSS than the alignment itself.

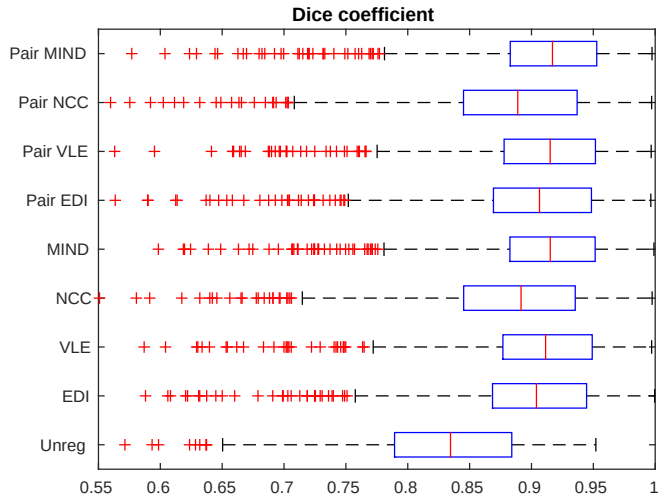

Figure 8.3: Boxplot diagrams of Dice Coefficient of foregrounds obtained from registered DWI and T2W sequences

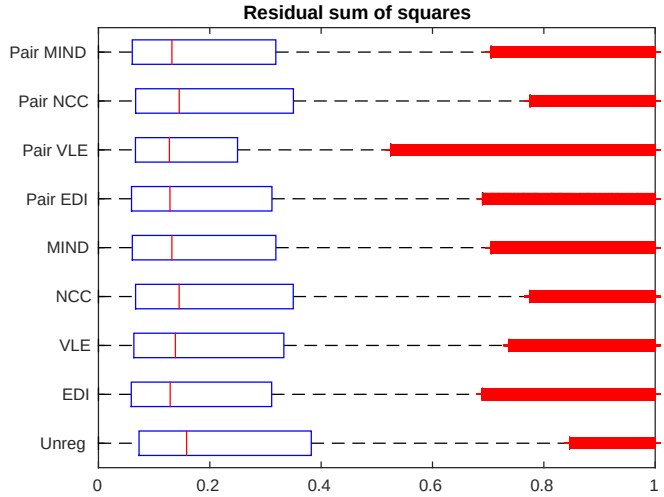

Figure 8.4: Distribution of RSS obtained from the ADC estimation for each registration metric

8.4 Conclusions

In this paper, we have proposed a non-rigid framework for the MC in multiparametric abdominal DWI acquisitions. The GW approach helps to cope with changes in signal intensity and corrects for geometrical distortions. This methodology has been applied to the alignment of DWI sequences in the liver, showing significant improvements in performance compared to PW approaches. The metric choice is also an important issue for avoiding outliers and making the registration process more robust. Thus, although the EDI metric is ranked first in terms of error and RSS, it seems more prone to the presence of outliers than other tested metrics, especially MIND. Consequently, we do not have enough evidence to support one metric over the other for this particular problem.

Chapter 9

ADC-Weighted Joint Registration-Estimation for Cardiac Diffusion Magnetic Resonance Imaging

Published as:

Sanz-Estébanez, S.[1], Royuela-del-Val, J.[1], Broncano-Cabrero, J.[2], Aja-Fernández, S.[1] and Alberola-López, C.[1] (2018). ADC-weighted joint registration-estimation for cardiac diffusion magnetic resonance imaging. In *Proceedings of the XXXV Annual Congress of the Spanish Society of Biomedical Engineering (CASEIB 2017)*, pp:41-44, Bilbao, Spain.

[1] Laboratorio de Procesado de Imagen, Department of Teoría de la Señal y Comunicaciones e Ingeniería Telemática, ETSIT, Universidad de Valladolid, Campus Miguel Delibes s.n., 47011, Valladolid, Spain.

[2] Cardiothoracic Imaging Section , Hospital de la Cruz Roja, RESSALTA, Health Time Group, Córdoba.

The purpose of this work is to develop a method for the group-wise registration of diffusion weighted datasets of the heart which automatically provide smooth Apparent Diffusion Coefficient estimations, by making use of a novel multimodal scheme. To this end, we have introduced a joint methodology that simultaneously performs both the alignment of the images and the ADC estimation. In order to promote diffeomorphic transformations and to avoid undesirable noise amplification, we have included appropriate smoothness constraints for both problems under the same formulation. The implemented multimodal registration metric incorporates the ADC estimation residuals, which are inversely weighted with the b-values to balance the influence of the signal level for each diffusion weighted image. Results show that the joint formulation provides more robust and precise ADC estimations and a significant improvement in the overlap of the contour of manual delineations along the different b-values. The proposed algorithm is able to effectively deal with the presence of both physiological motion and inherent contrast variability for the different b-value images, increasing accuracy and robustness of the estimation of diffusion parameters for cardiac imaging.

9.1 Introduction

DWI is an imaging technique sensitive to water molecule displacement allowing to measure micro-structure density and membrane tortuosity within the tissue. DWI is increasingly employed in clinical practice as it is a relatively quick non-contrast technique that provides quantitative markers, such as the well-known ADC, showing usefulness in early diagnosis of cardiovascular accidents due to its ability to detect early signs of ischemia (Laissy et al., 2009). ADC has been shown to be a positive indicator of tumor response (Kim et al., 1999) due to its ability to measure displacement of water molecules, giving evidence about cellular organization and permeability in the tissue (Le Bihan, 2014).

Nonetheless, in most cases, a previous registration step is performed in order to obtain proper ADC estimations, since images are acquired in different apneas. However, this is not an easy task since a signal intensity dropout is observed when increasing the intensity of the diffusion gradient (hereinafter referred to as b-value), leading to images with very different SNR. This phenomenon, associated to the very nature of the DWI acquisition process, is illustrated in Fig. 9.1.

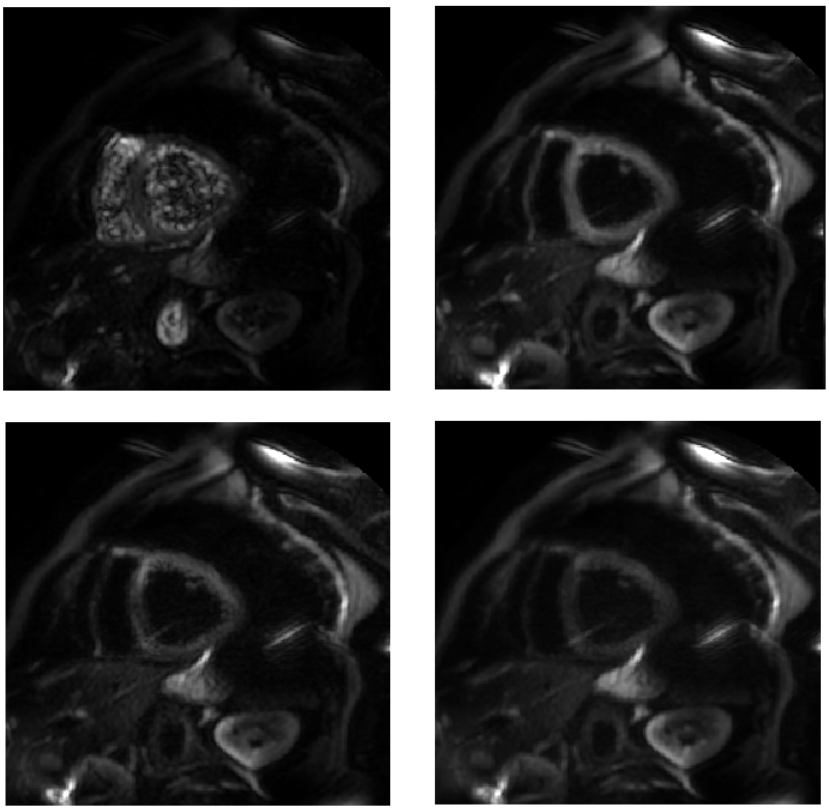

Figure 9.1: Axial slices of DWI acquisition in a healthy patient for b-values of 0, 50, 150 and 300 s/mm^2 (from upper left to bottom right).

Physiological motion is the most dominant confounding factor, specially in cardiac imaging. BH acquisitions are a popular way of avoiding motion artifacts. However, when different images are acquired at different breath holdings and, later, used for ADC estimation, considerable artifacts can arise (McLeish et al., 2002) that stem from the fact that two inspiration levels are never identical. Therefore, the aforementioned registration step is mandatory in order to relate anatomical relevant information from multiparametric acquisitions.

Image registration, to put it short, is concerned with the search of an optimal transformation for the alignment of at least two images. It has many applications in imaging, such as fusion of image information (Cordero-Grande et al., 2012), material point tracking (Ledesma-Carbayo et al., 2006) or atlas construction (Fonseca et al., 2011). As for the GW registration problem, it may be posed as finding a spatial transformation so that every point in each image is matched to a point in a reference image that is built out of the whole image set to be registered.

The cost function (metric) associated to the registration problem is usually designed to measure the image similarity/dissimilarity within the dataset. Examples of common voxel-based metrics are NCC (Avants et al., 2008), MI (Mattes et al., 2001) or SSD, which have proven useful for different image alignment problems.

Different methodologies for multiparametric registration towards robust ADC estimation have been designed for distortion correction (Hong et al., 2015) and MC (Guyader et al., 2015), but from a PW standpoint. GW approaches have also been addressed in Veeranghavan et al. (2015). However, none of them consider explicitly the diffusion process. For these reasons, we hypothesize that a registration metric that takes into account the parameters to be estimated, as proposed in Kornapoulos et al. (2016); Kurugol et al. (2017a), will help diminish the impact of motion artifacts as well as robustify the subsequent ADC estimation.

Therefore, we propose a joint formulation that solves simultaneously the estimation and the registration problems. We aim at finding the optimal transformation over the cardiac DWI dataset which leads to optimal ADC estimates. We have incorporated within the registration metric some weighting parameters that balance the influence of the different images on the registration process according to the DW signal content.

9.2 Materials and Methods

9.2.1 Materials

For the validation of the proposed approach, a synthetic experiment has been carried out using a simulation environment based on the 4D digitalXCAT phantom (Segars et al., 2010). The phantom consists of a whole body model that contains high level detailed anatomical labels, which feed a high resolution image synthesis procedure. The 4D XCAT phantom incorporates state of the art respiratory and cardiac mechanics, which

provide sufficient flexibility to simulate cardio-torso motion from user-defined parameters. Therefore, the phantom provides us not only with the images themselves, but also with a GT displacement field. Diffusion processes are simulated as the molecular displacement, often referred to as Brownian motion. For restricted diffusion, the resulting motion can be modeled as a random walk process (Lewis et al., 2014), where motion presents a non-Gaussian distribution with lower apparent diffusion. Common approaches assume a monoexponential decay in the DW signal (Johansen-Berg and Behrens, 2009).

Additionally, we have performed MRI acquisitions over a healthy volunteer. An axial SENSE DWI sequence has been acquired on a Philips Achieva 3T scanner on free breathing conditions. Cardiac gating has also been activated during the acquisition. The following subset of b-values (N_b=4) has been acquired: $b \in \{0, 50, 150, 300\} s/mm^2$. Acquisition and resolution details for these experiments are shown in Table 9.1.

Parameters	XCAT	DW-MRI
Δ_p	1	1.1719
Δ_l	1	8
N_p	192	256
N_s	70	11
T_R	8000	1052.6
T_E	93	51.74
N_g	1	3

Table 9.1: Details on the image sequences used in the paper. Δ_p : Spatial Resolution (mm). Δ_l : Slice Thickness (mm). N_p: Number of pixels along each direction. N_s: Number of slices. T_R : Repetition Time (ms). T_E: Echo Time (ms). N_s: Number of diffusion gradients.

9.2.2 Methods

The proposed method has been applied to the GW registration of two-dimensional cardiac DWI acquisitions and, specifically, for robust ADC estimation. Bearing in mind this application, local transformation τ has been represented as a combination of B-spline FFDs (Rueckert et al., 2006).

Therefore, we intend to find optimal alignment of DWI dataset $\mathbf{S}$ by solving the following joint registration-estimation problem:

$$[\widehat{\mathrm{ADC}}, \widehat{\tau}] = \arg\min_{\mathrm{ADC},\tau} \int_{\chi} H(\mathbf{S}, \mathrm{ADC}, \tau)) + \beta ||\mathrm{ADC}||_{TV} + \lambda Reg(\tau) d\mathbf{x}, \tag{9.1}$$

where $Reg(\tau(\mathbf{x}))$ is a penalty term which favors the transformation τ to be invertible (Chun and Fessler, 2009) and $||\mathrm{ADC}(\mathbf{x})||_{TV}$ represents the spatial total variation regularization term as defined in Becker et al. (2011). The total variation term has been

introduced so that it contributes to noise removal in the final estimated ADC map dealing with the inhomogeneities derived from the inherent low SNR of each b-value image (Shi et al., 2015). The influence of these two regularization terms is balanced by trade-off parameters λ and β, respectively, which have been set empirically.

As for the metric H, our proposal aims at directly minimizing the residuals in the ADC estimation, so it is defined as:

$$H(\mathbf{S}, \mathrm{ADC}, \tau) = \sum_{j=1}^{N_b} W_j^i (S_j(\tau(\mathbf{x})) - \widehat{S}_j(\mathrm{ADC}^i(\mathbf{x})))^2, \tag{9.2}$$

where S_j represents the acquired image and $\widehat{S}_j = S_0 \exp(-b_j \mathrm{ADC}^i)$ for the current (i-th iteration) ADC estimate. S_0 is the image with no diffusion gradient applied.

The proposed metric extends the one presented in Kornapoulos et al. (2016) by adding proper weighting parameters related to the underlying noise distribution of the magnitude images as a trade-off between the different b-values. Those weights, initially unitary, are redefined along iterations with the predicted DW signals (see Veraart et al. (2013)) as follows:

$$W_j^i = \exp(-2 b_j \mu(\widehat{\mathrm{ADC}^i}), \tag{9.3}$$

where $\mu(ADC)$ represents the median of the current ADC distribution in the myocardium.

We will solve Eq. (9.1) by sequentially solving the estimation and registration problems separately, via *ceteris-paribus* analysis. Hence, we iteratively alternate between estimating model parameters and the optimal transformation until convergence is reached both in transformation τ and metric H. First, the diffusion parameters are estimated by means of the NESTA algorithm (Becker et al., 2011) as described:

$$\widehat{\mathrm{ADC}} = \arg\min_{\mathrm{ADC}} \int_{\chi} [H(\mathbf{S}, \mathrm{ADC}, \tau) + \beta ||\mathrm{ADC}(\mathbf{x})||_{TV}] \, d\mathbf{x}. \tag{9.4}$$

As stated before, the measured images are not spatially aligned and therefore the ADC map cannot be directly computed. Therefore, we have introduced a GW registration framework using the registration metric defined in Eq. (9.2). To constraint the transformation τ to be locally invertible, we have resorted to a simple quadratic regularization scheme described in Chun and Fessler (2009). A GD optimization scheme has been employed (Sanz-Estébanez, 2014) to solve the registration problem posed in Eq. (9.5) as:

$$\widehat{\tau} = \arg\min_{\tau} \int_{\chi} H(\mathbf{S}, \mathrm{ADC}, \tau) + \frac{\lambda}{2} \sum_{l=1}^{L} \sum_{j=1}^{N_b} \sum_{m,n} \left[(\tau_{m+1,n,j}^l - \tau_{m,n,j}^l)^2 + (\tau_{m,n+1,j}^l - \tau_{m,n,j}^l)^2 \right] d\mathbf{x}, \tag{9.5}$$

where $\tau_{m,n,j}^l$ represents each of the (displacements) components of the transformation ($L = 2$ for the 2D case).

9.3 Results

In this section, we test robustness and accuracy of our joint formulation in comparison with other methodologies in the literature. Demons (Pennec et al., 1999) PW registration algorithm has been implemented using a MI based metric. As for GW approaches, apart from our Joint scheme, we have tried EDI (Learned-Miller, 2006), NCC (Avants et al., 2008) and SSD metrics.

With the data provided by the XCAT phantom and for each method mentioned above we have measured the overlap degree —using the Dice coefficient (Dice, 1945)— between the myocardial contours for each b-value and cardiac phase with those at the diastolic instant of the S_0 image.

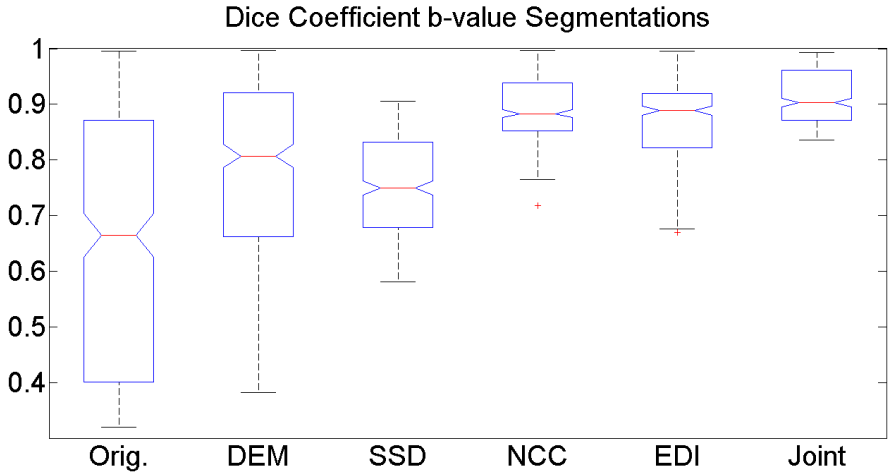

Figure 9.2: Boxplot diagrams of Dice Coefficient distributions between segmentations in different b-values.

In Figure 9.2 we show the boxplot diagrams of the Dice coefficient obtained from the aforementioned registration methods and our joint formulation proposal. The joint formulation shows a considerable improvement in terms of overlapping compared with the other two methods. Mann-Whitney U-tests have been performed on the Dice coefficient distributions, finding significant improvement when introducing any registration step when compared to the non-registered sequence ($p < 10^{-6}$) for all methodologies. The joint formulation presents also significant improvement both over the PW (DEM) and monomodal (SSD) approaches ($p < 10^{-6}$ for both). These results conclusively support the hypothesis that the joint formulation is a better option than sole GW multimodal registration schemes ($p < 10^{-3}$ for both EDI and NCC metrics).

In addition, for the real data we have tested the performance of the aforementioned procedures for the estimation of diffusion parameters. In this experiment, we have measured the mean, variance and coefficient of variation ($CV = std/mean$) of ADC estimates obtained inside the myocardium for each method (see Table 9.2).

$Method$	$Mean(mm^2/s)$	$Variance$	$CV\,\%$
$Orig.$	$1.4863 \cdot 10^{-3}$	$2.5517 \cdot 10^{-7}$	33.99
DEM	$1.4264 \cdot 10^{-3}$	$2.7957 \cdot 10^{-7}$	37.06
SSD	$1.2088 \cdot 10^{-3}$	$4.2366 \cdot 10^{-7}$	53.84
NCC	$1.5348 \cdot 10^{-3}$	$2.5435 \cdot 10^{-7}$	32.86
EDI	$1.5490 \cdot 10^{-3}$	$2.5530 \cdot 10^{-7}$	32.62
$Joint$	$1.7091 \cdot 10^{-3}$	$1.7380 \cdot 10^{-7}$	24.39

Table 9.2: Mean, variance and ADC coefficient of variation over the myocardium of a healthy patient.

As indicated in the table, the CV of the estimated ADC parameters obtained with the joint formulation is significantly lower compared to other methodologies, specially to the monomodal approach. Besides, robustness of ADC estimates was increased and bias in estimation seems greatly diminished, leading to more accurate measures.

Finally, visual inspection of a registered DWI sequence reveals that our approach is able to preserve structure while reducing artifact impact, as it can be seen in Fig. 9.3. Therefore, boundaries will be more clearly identified (as well as tissue heterogeneity or anatomical structure), leading to reconstructed ADC maps with higher quality.

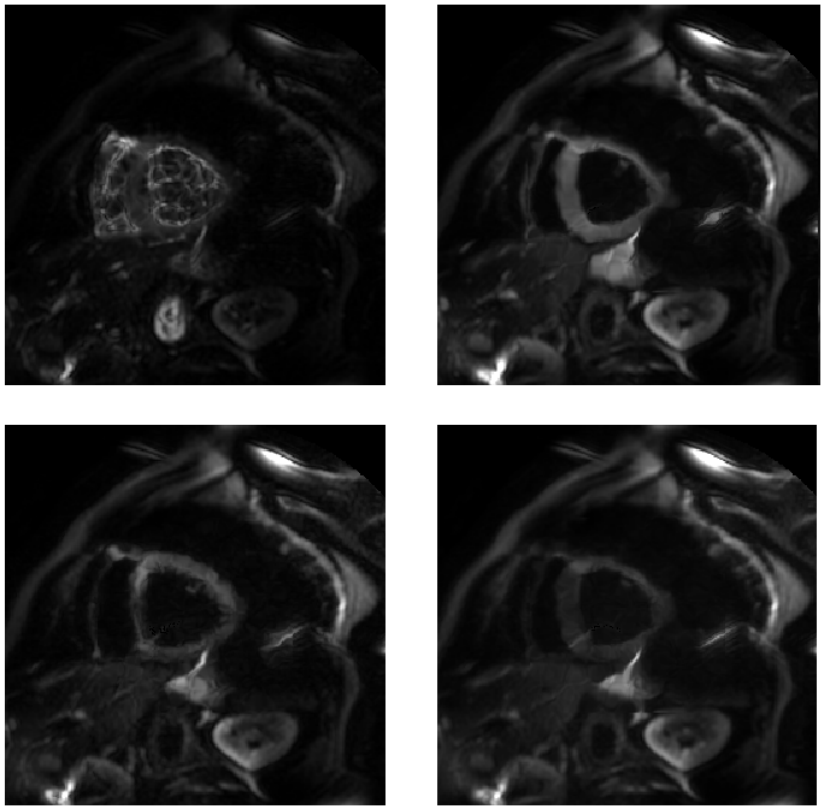

Figure 9.3: Axial slices of registered DWI sequence for b-values of 0, 50, 150 and 300 s/mm^2 (from upper left to bottom right).

9.4 Conclusions and Future Work

We have presented an image processing methodology for the simultaneous ADC estimation and non-rigid registration of cardiac DWI with a novel multimodal metric that weights each b-value by the residuals derived from the estimation. This methodology, under the GW paradigm, has proven to be reliable for misalignment correction and robust in the estimation of diffusion parameters, being able to provide high-quality denoised ADC maps of the heart.

Results have shown that a joint formulation approach is effective in correcting the characteristic boundary smearing of cardiac DW datasets, increasing SNR on the images while preserving myocardial anatomical structure.

9.5 Acknowledgments

This work was partially supported by the Spanish Ministerio de Ciencia e Innovación under Research Grant TEC2013-44194-P, the European Regional Development Fund (ERDF-FEDER) under Research Grant TEC2014-57428-R, the Spanish Junta de Castilla y León under Grant VA069U16 and the European Social Fund (ESF-FSE).

Chapter 10
Conclusions and Future Work

This chapter gathers the main contributions of this thesis, limitations of the described approaches and future research lines.

10.1 Contributions

The Thesis consists of a methodological corpus and a set of results that let us enumerate the following scientific contributions:

1. The estimation of motion based on the WHARP methodology to improve robustness in cardiac MR-T image analysis by using multiple orientations and cardiac planes for 3D ST reconstruction.

2. The proposal of an automatic adaptive approach for the design of both an optimal analysis window and a bandpass filter for the WHARP methodology. The procedure eliminates the need for a manual fine parameter tuning in the local phase estimation pipeline.

3. Optimal tag pattern design by means of the introduction of multiple modulating peaks in k-space intended to improve the robustness of WHARP analysis within a single acquisition.

4. Development a two-stage sequential classification procedure using motion and tensorial features extracted from MR-T image analysis designed for cardiomyopathy screening. The classifier is also capable of discriminating between primary HCM and SLVH.

5. Introduction of vortical patterns descriptors from tensorial magnitudes, based on the curl operator, as myocardial rotation features aimed at improving the differentiation between primary HCM and SLVH.

6. Motion robust ADC calculation from DW-MRI on the liver by means of GW non-rigid registration using different multimodal metrics for elastic alignment and geometric distortion correction.

7. Establishment of a framework for the joint non-rigid registration and ADC estimation in cardiac and liver DWI; we have proposed a novel metric that incorporates an ADC-based weighting vector.

8. Introduction of filtering procedures in the joint framework to account also for the effects of noise in ADC estimation to avoid biases that arise during the interpolation and registration.

10.2 Limitations of the Current Work

The MR field has seen significant developments in recent years. Advances in acquisition techniques have enabled faster scans with superior image quality. However, there are still considerable challenges in MRI that should be carefully addressed before completely relying on image biomarkers, such as physiological motion. This Thesis has tried to emphasize the importance of accounting for patient motion in modern radiology.

One of the most important error sources in the analysis of physiological motion in MR-T is through-plane motion. Through-plane motion occurs when the images are acquired in a 2D plane, while the heart moves in 3D. As the heart moves throughout the image plane, new tissue may enter the image plane; this new tissue is provided with a different HARP phase, which destroys the continuity of the local phase maps, thereby leading to inaccuracies in strain maps. One solution to this problem is to move to 3D HARP techniques (Abd-Elmoniem et al., 2005; Pan et al., 2005; Stoeck et al., 2012).

Another limitation in motion tracking is the presence of artifacts in HARP imaging. Although we have proposed the use of multiple orientations, axis and spectral peaks to diminish their influence, remaining artifacts may obscure the detection of useful features and reduce the clinical usability of the strain maps. The commonly observed zebra artifacts are the manifestations of many sources of error that affect HARP-MRI. This Thesis intends to avoid artifacts that arise from spectral interference and noise; however, artifacts caused by intra-voxel phase dispersion or partial volume effect may still be present.

Regarding phase calculation, it is worth noting that the phase can only be computed between $-\pi$ and π, which means that the measured phase is a wrapped version of the true harmonic phase (Venkatesh et al., 2010). This phase fluctuation may deteriorate the correspondence between the original tag lines and the HARP wrapped lines, thus causing significant artifacts. To alleviate this, artifact reduction methods have been proposed in Wang et al. (2015) using the DC component of the SPAMM MR-T images.

MO methodologies look very promising, although they need to increase the number of acquisitions which, for naive acquisition extensions, will linearly increase acquisition time. The increase in scan time is a major issue; however, it is not the only one since a spatial misalignment between the different acquisitions may also be present. One solution is to develop optimal registration algorithms to align the different MR-T acquisitions, which is not a trivial task due to the presence of different tag patterns in the dataset.

Therefore, multimodal metrics are unavoidable. Another possible solution is performing the alignment over lowpass filtered images although at the price of an important loss in image resolution and, therefore, a coarser alignment.

Furthermore, longer acquisition times would in turn trigger the appearance of other artifacts, such as those caused by the presence of arrhythmias or longer BH periods, which cannot be removed by MO or MP approaches. To avoid multiple acquisitions, we have deepened into optimal k-space pattern designs within a single acquisition as shown in Chapter 7. An optimization procedure has been implemented to search for optimal orientations and between-peaks distance using synthetic data. However, in a more realistic scenario, artifacts coming from the anatomical signal will also influence the estimation. In this regard, extensions of the proposed methodology to diminish the influence of the anatomical signal on the demodulated deformations may also help obtain cleaner estimations in presence of spectral interference.

With respect to the tensorial analysis, classification figures obtained with the rotation and strain features are promising, as the algorithm is able to discriminate between primary HCM and controls. However, differentiation between HCM and secondary cases is much more complicated. Therefore, figures related to the latter problem have been lower. Classification figures of SLVH cases, despite not remarkable, are likely to improve when equalizing the number of subjects in the study. We also hypothesize that the introduction of features that take into account the position of vortical peaks within the myocardium may also be helpful for this task.

As for Diffusion-MRI, we have tried to integrate the diffusion model into the image registration problem. That results in a model-based registration approach, where the DW signal content leverages the influence of each *b-value* image on the ME. Therefore, we do not merely rely on intensity information but on the underlying model. However, accurate and precise ADC mapping is doubtful, even if registration behaves properly. The reason behind this is that the image interpolation included in the image registration step will modify the statistical assumptions of the data. Therefore, deriving the resulting data distribution function is often impossible. For that reason, we have introduced filtering stages within the joint registration-estimation pipeline as stated in Chapter 4. For the proposed approach we rely on accurate noise variance estimates, as described in Section 1.4.2.3.2. However, if proper estimates cannot be achieved, results may be worse than the ones obtained when relying on an inaccurate model. For this reason, noise variance estimation procedure should be chosen carefully.

For the validation procedure, we have used synthetic data generated both with numerical phantoms and from magnitude DICOM images for the initial experiments. Even if the numerical phantom represents realistic geometries of the internal organs, the generated images are much smoother than real MRI data, even in low SNR simulations. This smooth representation is untrue in real scenarios, in which multiple system imperfections such as gradient non-linearities, irregular motion, eddy currents, etc. are present. Despite the presence of these limitations, experiments with real data have shown satisfactory results in terms of ADC reproducibility. Accuracy and precision analysis could not be

performed on real data due to the absence of a GT. For this reason, we cannot make any statement related to the presence of biases in ADC estimation with real data. Clinical validation of estimated ADC maps with a greater cohort would be helpful to completely validate the method.

All the results presented are obtained for 2D images in which several slices are acquired. This means that the procedures have been carried out on a slice basis independently of each other. Typically, lower SNR is obtained from 2D acquisitions given the smaller amount of tissue excited in thin slices. Even though the TV regularization included in the joint formulation can mitigate the effect of noise in the data, slice-by-slice approaches represent a more challenging scenario.Therefore, better alignment and smoother ADC maps can be expected if the whole 3D volume is aligned jointly. Besides, similarly as in MR-T acquisitions, trough-plane motion also takes place, although in this case the effect is more remarked due to the FB conditions. The liver is displaced up and down by the diaphragm during respiration, so the ME technique will never be able to recover the true motion of the imaged structures, just obtaining a partial representation of it.

The proposed joint methodology has considered only TV regularization for the ADC estimation problem, whereas for the registration thin-plate deformation and bending energies have been used as regularization terms. However, multiple regularization terms have been proposed in recent years for different applications with promising results. Examples of that are invertibility constraints (Chun and Fessler, 2009) or volume-preservation regularization for image registration (Tang et al., 2013), while for parameter estimation nonparametric spline or reproducing kernel Hilbert space smoothings (Sima, 2006) have also been proposed.

On the implementation side, the parallel computations capabilities of modern multicore systems have been exploited. All the presented methods have been implemented in MATLAB, which inherently parallelizes the execution of the code when several cores are available. However, the current implementation of the developed tools cannot take advantage of the Graphics Processing Unit (GPU)-based techniques since the CUDA platform is designed to work with programming languages such as C, C++ or Fortran. Therefore, implementation in these languages would help to accelerate the algorithm.

10.3 Future Work

In recent years, MR-T processing and visualization tools have experienced a paradigm shift to allow the fusion of information coming from different techniques and modalities.

WHARP-based procedures perform well at good image qualities but are critically affected by noise and tag fading, especially in myocardial boundaries where a higher tissue contrast is present. Derived errors are unlikely to disappear by using multiple orientations or spectral peaks, neither by redesigning k-space layout or acquisition protocols. Therefore, the here mentioned error sources will introduce a bias in strain estimate which could deteriorate the clinical value of the extracted motion biomarkers.

For example, US is widely used to track heart surface shapes because surface contours are readily extracted and visualized. MR-C tissue tracking could also be useful due to the high between-tissue contrast, which enables the use of intensity-based registration methodologies for material points tracking. On the other hand, HARP analysis may also benefit from other techniques, such as optical flow, which are more tolerant to noise but its performance decreases in the early cardiac phases (before tag fading takes place). One goal in the future could be the fusion of these MRI and US techniques into a single tool for robust and reliable myocardial tracking and a reproducible cardiac study.

Regarding vortical analysis, we have related anomalies on local vortical patterns with the presence of fibrotic tissue. Furthermore, the location of vortical abnormalities may provide important information in hypertrophic diseases to establish a differential diagnosis between primary and secondary cases. Longitudinal studies may help us test the potential clinical utility of this information for cardiomyopathy classification.

Besides, advances in MRI pulse sequences devised to cleverly acquire k-space data by suppressing all other peaks except for the harmonic peak (Epstein and Gilson, 2004) can also help achieve faster scans, thus increasing tagging clinical utility.

Future advances in motion correction should also involve the acquisition. Specifically, the optimal solutions may arise from a combination of prospective and retrospective motion correction methods, although prospective approaches are limited to affine corrections. However, a robust solution could still be achieved relying on prospective corrections to address large displacements, which is fairly an affine model, followed later by a finer retrospective non-rigid correction, such as the proposed in Chapters 3 and 4. Prospective motion problem has been tackled using many different ideas: navigator echoes, self-navigation, image navigators and US measurements. Research and development of these approaches should continue to further improve ME, which may benefit from unsupervised deep learning approaches, that have shown to be useful for registration purposes.

Another key line of future work will be the extension of the proposed joint estimation-registration methodology to work with 3D acquisitions. These acquisitions provide higher SNR value and higher redundancy between adjacent slices, which could help remove possible biases and avoid the problems derived from trough-plane motion. Consequently, smoother and more accurate ADC estimates would be obtained. 3D registration and estimation (with isotropic resolution) could also avoid the planning step, since the slices could be obtained retrospectively from a high resolution ADC volume oriented according to the canonical planes of the MRI system.

It is also worth noting that the proposed joint methodology has shown flexibility towards the *b-value* choice. Delving into this idea, *b-value* independent acquisition protocols could be arranged in which there is no need for a previous *b-value* setting. Furthermore, joint methodologies can also be developed for MR reconstruction from undersampled data as it has been described in other application domains, such as perfusion.

This dissertation has developed novel motion correction approaches for abdominal and cardiac imaging. Nonetheless, these approaches can be extended to any MR application where motion is involved in order to improve the clinical throughput.

Appendix A: Resumen en Castellano

La imagen por resonancia magnética (MRI), hoy en día, representa una potente herramienta para el diagnóstico clínico debido a su flexibilidad y sensibilidad a un amplio rango de propiedades del tejido. Sus principales ventajas son su sobresaliente versatilidad y su capacidad para proporcionar alto contraste entre tejidos blandos. Gracias a esa versatilidad, la MRI se puede emplear para observar diferentes fenómenos físicos dentro del cuerpo humano combinando distintos tipos de pulsos dentro de la secuencia. Esto ha permitido crear distintas modalidades con múltiples aplicaciones tanto biológicas como clínicas. La adquisición de MR es, sin embargo, un proceso lento, lo que conlleva una solución de compromiso entre resolución y tiempo de adquisición (Lima da Cruz, 2016; Royuela-del Val, 2017). Debido a esto, la presencia de movimiento fisiológico durante la adquisición puede conllevar una grave degradación de la calidad de imagen, así como un incremento del tiempo de adquisición, aumentando así también la incomodidad del paciente. Esta limitación práctica representa un gran obstáculo para la viabilidad clínica de la MRI.

En esta Tesis Doctoral se abordan dos problemas de interés en el campo de la MRI en los que el movimiento fisiológico tiene un papel protagonista. Éstos son, por un lado, la estimación robusta de parámetros de rotación y esfuerzo miocárdico a partir de imágenes de MR-*Tagging* dinámica para el diagnóstico y clasificación de cardiomiopatías y, por otro, la reconstrucción de mapas del coeficiente de difusión aparente (ADC) a alta resolución y con alta relación señal a ruido (SNR) a partir de adquisiciones de imagen ponderada en difusión (DWI) multiparamétrica en el hígado.

Sobre el primer problema, la modalidad de MR-*Tagging* es actualmente la primera opción en cuanto a técnicas de imagen para el diagnóstico de numerosas enfermedades cardiovasculares gracias a su sensibilidad a la deformación del tejido miocárdico y su capacidad para detectar indicios precoces de la progresión de la enfermedad, los cuales serían difícilmente discernibles con otras técnicas. Sin embargo, estas imágenes suelen verse afectadas por diversas fuentes de error que menoscaban la precisión del diagnóstico. Éstas son causadas por limitaciones en el *hardware*, el diseño de los pulsos, el tiempo de adquisición o por artefactos en la imagen derivados del movimiento del paciente o el ruido. Además las diferentes etapas del procesado de las imágenes también pueden introducir un gran número de artefactos que pueden degenerar en la presencia de valores atípicos en los mapas de esfuerzo cardiaco, que bien podrían ser confundidos con una patología. Es por ello que el conocimiento de estos artefactos y su origen es de gran importancia para evitar falsos diagnósticos.

Uno de los principales objetivos de esta Tesis Doctoral es proporcionar un esquema de procesado automatizado y robusto para el cálculo de los parámetros de movimiento cardiaco. En particular, en esta Tesis abordamos la estimación del tensor de esfuerzo cardiaco (y tensores relacionados) a partir de MR-*Tagging*, así como la obtención de descriptores de rotación y torsión miocárdica. Mostraremos los resultados obtenidos tanto con simulaciones como con adquisiciones *in-vivo* de voluntarios sanos y pacientes. Además, se han desarrollado herramientas para la clasificación de cardiomiopatías, centrándonos en la cardiomiopatía hipertrófica (HCM), para así, poder comprobar la utilidad clínica de los parámetros cardiacos antes mencionados.

En relación al segundo problema, el desarrollo de biomarcadores clínicos requiere de una metodología de estimación robusta frente a artefactos. Para el caso de la estimación del ADC, el movimiento es especialmente crítico, ya que cuando se adquieren imágenes de distintos *b-valores* en diferentes apneas para ser posteriormente utilizadas para estimar el ADC, pueden aparecer un número considerable de artefactos en los mapas, causados por el hecho que dos apneas distintas nunca pueden ser exactamente iguales.

En esta Tesis Doctoral hemos planteado el problema de registrado de MRI de difusión empleando un enfoque matemático. Normalmente, la baja reproducibilidad en los biomarcadores de difusión se achaca a imprecisiones en el modelado físico del proceso de difusión. Sin embargo, no se han hecho grandes esfuerzos en el diseño de metodologías capaces de lidiar con estas imprecisiones. Debido a esto, gran parte de los errores que provocan el rechazo de los biomarcadores de difusión vienen dados por algoritmos de procesado demasiado simplificados e inadecuados y métodos de registrado subóptimos.

Estas metodologías normalmente proponen una resolución secuencial para la estimación del ADC, donde primero se realiza un alineamiento de las imágenes con el objetivo de robustecer el subsiguiente análisis de los parámetros de difusión. Normalmente, estos dos problemas se tratan por separado utilizando distintas métricas para su resolución, lo que da lugar a una solución subóptima para ambos. Nosotros, por el contrario, hemos hipotetizado que la resolución conjunta de los problemas de estimación y registrado incrementará la reproducibilidad de las medidas, mejorando la capacidad diagnóstica de la adquisición de DWI. Para ello, proponemos introducir información del problema de estimación para la resolución de la estimación de movimiento, para así poder resolver ambos problemas de forma conjunta, usando una métrica común.

En esta Tesis Doctoral se proporcionan algunas de las herramientas necesarias para la estimación de los parámetros de difusión, así como para el registrado no-rígido multimodal, prestando atención a la influencia del ruido en las imágenes de *b-valor* alto.

Ambos problemas, aunque de naturalezas bien distintas, comparten la necesidad de tratar de forma directa el movimiento presente en las imágenes. Esta Tesis Doctoral trata sobre la influencia del movimiento fisiológico, especialmente el movimiento cardiaco y respiratorio, en dos de las distintas modalidades de MRI abdominal empleadas en la práctica clínica. El desarrollo de metodologías robustas para la estimación y compensación del movimiento permitirá avanzar hacia la extracción robusta y reproducible de biomarcadores basados en MR, lo que actualmente representa uno de los mayores desafíos dentro de la

investigación clínica.

Las herramientas desarrolladas hacen uso de las capacidades de cálculo en paralelo presentes en la mayoría de los sistemas de cómputo actuales. Se ha prestado por tanto especial atención al desarrollo de implementaciones eficientes en ambas situaciones, ya que tanto para la estimación de los parámetros de difusión como para la reconstrucción de los mapas de esfuerzo cardiaco deben aplicarse métodos iterativos con un elevado coste computacional.

Este resumen en castellano se complementa con un resumen de los objetivos, la metodología, las principales contribuciones y líneas futuras de la Tesis Doctoral.

A.1 Objetivos

El principal objetivo de esta Tesis Doctoral es el desarrollo e implementación de las herramientas necesarias para la estimación robusta de parámetros funcionales en dos escenarios afectados por el movimiento fisiológico: el cálculo robusto y preciso de parámetros cardiacos de esfuerzo y rotación usando datos de MR-*Tagging* dinámicos y la estimación de mapas de ADC a alta resolución a partir de adquisiciones de DWI multiparamétrica en el hígado. Los objetivos específicos de la tesis son:

1. Proponer un esquema de procesado automático para la estimación robusta del tensor de esfuerzo cardiaco y la extracción de biomarcadores de movimiento basados en MR, permitiendo la utilización de múltiples formas de onda o *tags* en los distintos ejes cardiacos para una reconstrucción 3D suave y libre de artefactos del movimiento. En particular, hemos utilizado secuencias de MR-*Tagging* dinámica, en las que se ha estudiado la deformación del corazón a lo largo del ciclo cardiaco y especialmente en la fase sistólica. Para tal fin se definen los siguientes subobjetivos:

    - Desarrollo de una metodología para la estimación directa del tensor de esfuerzo cardiaco y magnitudes tensoriales relacionadas mediante la extensión del método basado en fase harmónica (HARP). La reconstrucción robusta de la fase local de la imagen está basada en la aplicación de la transformada de Fourier enventanada (WFT) y en la adquisición de un conjunto sobredeterminado de orientaciones de *tag*, lo que permitirá disminuir interferencias de fase provenientes de estructuras fuera del miocardio así como las inestabilidades que surgen de aplicar el operador gradiente.
    - Proponer un procedimiento adaptativo que se ajuste a las propiedades locales del patrón de *tag*, tanto en dominio espacial como espectral, usando un enventanado auto-orientado previo a la WFT y un filtro paso-banda adaptable. Ambos procesos son completamente automáticos y se basan en la información disponible en las cabeceras DICOM o en información adicional estimada directamente de los datos.

- Validación del procedimiento del estimación de esfuerzo cardiaco mediante el análisis de la correlación entre las propiedades mecánicas locales del miocardio con la presencia de tejido fibrótico. Se han encontrado concordancias entre las zonas hiperintensas en imágenes de realce tardío y los valores anormales del tensorde esfuerzo.
- Implementación de una herramienta de clasificación de cardiomiopatías usando descriptores tensoriales para discernir entre grupos heterogéneos de HCM y pacientes sanos. Se ha diseñado un esquema de clasificación en dos etapas usando métodos clásicos de la teoría de aprendizaje estadístico capaz de trabajar con distintas modalidades de MRI. La herramienta desarrollada ha demostrado ser útil en la identificación y diagnóstico de diversos estadíos de HCM.
- Diseño de un patrón de *tag* alternativo basado en el uso de múltiples picos espectrales, en vez de múltiples orientaciones, dentro de una sola adquisición. Para su validación, se ha desarrollado un experimento sintético capaz de simular distintos patrones con el objetivo de encontrar las orientaciones y anchuras óptimas para los *tags* que conforman el patrón que minimice el error en la estimación del tensor.

2. Establecer una metodología capaz de conseguir una estimación del ADC robusta frente al movimiento en todo el hígado, así como en otros órganos abdominales, a partir de adquisiciones DWI multiparamétricas. Se ha prestado especial atención a imágenes con alto *b-valor* donde la presencia de ruido (SNR baja) hace la estimación especialmente sensible. Este objetivo ha sido dividido en los siguientes subobjetivos:

   - Desarrollar un marco de trabajo para el registrado elástico de secuencias de DWI para diferentes paradigmas de registrado (grupal y por pares) que permita utilizar distintas funciones de coste (términos de verosimilitud) y términos de regularización para un análisis preciso del ADC. Debido a la naturaleza no-rígida del esquema propuesto, no sólo se corrige el movimiento cardiaco y respiratorio sino que las distorsiones geométricas también se ven reducidas.
   - Introducción de una formulación conjunta capaz de resolver simultáneamente los problemas de registrado no-rígido y estimación del ADC en aplicaciones para hígado y corazón. La función de coste implementada consiste en los residuos de la estimación del ADC inversamente ponderados de acuerdo a la señal contenida en cada imagen de *b-valor*. Se han incluido además términos de regularización en ambos problemas para evitar transformaciones no realistas y amplificación de ruido.
   - Extensión de la metodología conjunta previamente mencionada para tomar en consideración la naturaleza Rician de los datos, especialmente importante en entornos ruidosos, para la estimación insesgada del ADC. El algoritmo original ha sido mejorado mediante la introducción de etapas de filtrado dedicadas a la corrección de los sesgos producidos durante el registrado o interpolación.

A.2 Metodología

A.2.1 Descriptores de Movimiento Cardiaco

Como se ha descrito anteriormente, uno de los principales objetivos de esta Tesis es la verificación de la hipótesis de que la incorporación de un método robusto de estimación de movimiento cardiaco basado en redundancia puede mejorar la calidad de las estimaciones del esfuerzo miocárdico.

El método utilizado en esta Tesis Doctoral parte del propuesto en Cordero-Grande et al. (2011) en el que se obtiene una estimación local suave de las imágenes de fase, para luego refinar las estimaciones del tensor de esfuerzo con el método de mínimas desviaciones absolutas (LAD), el cual presenta un enfoque más robusto hacia valores atípicos.

En Cordero-Grande et al. (2016) este método fue extendido para permitir el uso de un conjunto sobredeterminado de imágenes de MR-*Tagging* (con diferentes orientaciones del patrón de *tag*), por lo que la presencia de artefactos en las imágenes de fase disminuye considerablemente. El método ha sido comparado con su análogo no enventanado a la hora de estimar el tensor de esfuerzo, mostrando una importante mejoría en términos de precisión y reproducibilidad en ambos casos, con y sin múltiples orientaciones. Se ha adaptado también el método HARP enventanado para extraer las imágenes de fase y se ha extendido la metodología para la computación del tensor gradiente de deformación en 3D usando imágenes de eje corto y eje largo. En caso de no existir intersección de los distintos cortes, se ha procedido a la reconstrucción estándar 2D.

Sin embargo, el esquema de procesamiento presentado requiere de un ajuste fino en algunas partes, especialmente para el diseño de la ventana y el filtro paso-banda. Por ello, se ha extendido el procedimiento de HARP enventanado para que sea completamente automático y adaptable tanto en el dominio espacial como en el espectral. En cuanto a la ventana, se ha diseñado para que se oriente en ángulo con el patrón automáticamente, mientras que el filtro paso-banda se ha diseñado para que sea estrecho en la dirección de modulación y ancho en la ortogonal. Ningún parámetro ha de introducirse manualmente ya que sus valores se basan en la información disponible en las cabeceras DICOM y en información adicional estimada directamente de los datos.

Los diseños de ventanas y filtros han sido descritos y analizados a fondo en el Capítulo 5. El esquema final que contiene todas las mejoras propuestas ha sido explicado detalladamente en la Sección 1.4.1.3.

Por otro lado, también se ha puesto a prueba la capacidad de la metodología propuesta para proporcionar descriptores de movimiento con utilidad clínica. Se ha hecho uso de métodos clásicos de la teoría del aprendizaje estadístico para el desarrollo de una herramienta para el diagnóstico de los distintos estadíos de la HCM, utilizando como características de entrada los descriptores de movimiento obtenidos a partir de imágenes de MR. Se ha propuesto un esquema de clasificación en dos etapas (secuencial) que es capaz de distinguir entre las distintas formas de HCM y pacientes sanos. Los resultados han

demostrado que se pueden rediseñar fácilmente clasificadores comunes para adaptarse al estudio de la HCM, obteniendo un rendimiento aceptable, incluso en conjuntos reducidos y desbalanceados, utilizando como entradas las magnitudes tensoriales extraídas anteriormente. La metodología de clasificación secuencial y el diseño de cada una de sus etapas se han descrito en detalle en el Capítulo 6.

Aunque las medidas de esfuerzo y estrés cardiaco han demostrado ser útiles en la identificación de cardiomiopatías, no son capaces de diferenciar el genotipo subyacente en estas enfermedades. Por lo tanto, no se puede pronosticar con certeza la aparición de fibrosis en el tejido miocárdico a partir de estos descriptores. Por el contrario, las medidas de rotación miocárdica sí han proporcionado información adicional acerca de la mecánica cardiaca que puede complementar a los índices de funcionalidad estándar. Sin embargo, la mayoría de los parámetros de rotación descritos en la literatura requieren implícitamente de una descripción precisa del eje de rotación del corazón. Normalmente, se utiliza el centro de masas del ventrículo, dado por los límites del miocardio (epicardio y endocardio), como tal. Sin embargo, debido a los desplazamientos que experimenta el corazón durante el ciclo cardíaco, es bastante común que exista un desalineamiento del centro entre las distintas imágenes, lo que provocará errores de estimación y, por lo tanto, dificultará enormemente la posterior clasificación.

Como solución, se ha introducido un novedoso descriptor de la rotación local desarrollado a partir de medidas tensoriales que relaciona el incremento local de los valores de vorticidad con la presencia de tejido fibrótico en el corazón. La rotación se estima mediante el operador rotacional sin necesidad de establecer ningún parámetro cardiaco adicional, como el eje de rotación o el radio de la cavidad. Partiendo de este descriptor, se ha llevado a cabo un estudio regional comparativo en pacientes con diferentes etiologías, HCM y formas secundarias de hipertrofia ventricular, así como sujetos sanos. En el Capítulo 2 se ha incluido el estudio que profundiza en la relación entre la aparición local de vórtices en el patrón de deformación cardiaco y la presencia de fibrosis lo que, bajo nuestro punto de vista, representa el primer trabajo que hace uso del operador rotacional para el diagnóstico e identificación de tejido fibrótico y su evolución. El Capítulo 2, que constituye el primer artículo fundamental de esta Tesis Doctoral, se centra en el desarrollo de descriptores de rotación miocárdica derivados de los tensores de estrés y esfuerzo con especial atención al análisis de patrones vorticales en la deformación cardiaca.

Además, también se ha investigado acerca del diseño óptimo de patrones de *tag* explorando la introducción de múltiples picos en el k-espacio, frente al uso de múltiples orientaciones; el objetivo final consiste en comprimir la máxima información posible en una única adquisición. Se ha evaluado, mediante un experimento sintético computacional, las orientaciones y el espaciado óptimos del patrón de *tags* que minimiza la norma de Frobenius del error en la estimación del tensor gradiente de deformación material. Además, se ha evaluado la pérdida en cuanto a rendimiento con respecto a la aproximación con múltiples orientaciones en un experimento con datos reales. Los resultados indican que, para una sola adquisición, la aproximación mediante múltiples picos es preferible al uso de múltiples orientaciones. Estas ideas son desarrolladas más en detalle en el Capítulo 7.

A.2.2 Estimación del ADC y Registrado Conjuntos

La otra contribución importante de esta Tesis Doctoral consiste en el desarrollo de una metodología para la estimación robusta del ADC frente al movimiento del paciente usando secuencias de DWI multiparamétrica, válida para todo el hígado, así como para otros órganos abdominales.

Inicialmente se ha atacado el problema de la estimación robusta del ADC mediante técnicas de registrado no-rígido grupales para la compensación de movimiento en la secuencia DWI, como una etapa de preprocesado previa a la estimación del ADC en el hígado.

En Sanz-Estébanez et al. (2017) se ha presentado un marco de trabajo para evaluar la idoneidad de los paradigmas grupales y por pares para el alineamiento elástico de secuencias de DWI abdominal en respiración libre. También se ha analizado la utilidad de distintas métricas, tales como entropía de las distribuciones de intensidad (EDI), correlación cruzada normalizada (NCC), varianza de entropía local (VLE) y descriptor de vecindad independiente de modalidad (MIND). El procedimiento de alineamiento elástico multimodal es útil no sólo para la corrección de movimiento respiratorio, el cual podría ser corregido en su mayoría recurriendo a transformaciones afines, sino también para tener en cuenta posible distorsiones geométricas. La precisión en la estimación del ADC ha sido evaluada mediante el análisis de los residuos de la estimación (en datos reales), donde el ADC fue estimado con el método de mínimos cuadrados (lineales) en todo caso. Los detalles acerca del procedimiento y el marco de trabajo establecido se proporcionan en el Capítulo 8.

La resolución secuencial del problema de estimación del ADC en presencia de movimiento da lugar, sin embargo, a una solución subóptima debido a la naturaleza no convexa del problema de registrado elástico. Además, los problemas de registrado y estimación se suelen plantear con diferentes formulaciones (distintas funciones de coste); por lo tanto, es muy probable que la solución para ambos problemas difiera y no se consiga llegar al mínimo global en ninguno de los dos problemas. Para solucionar esto, se ha introducido un algoritmo conjunto de registrado y estimación, que presenta una formulación común en donde la métrica de registrado incorpora unos parámetros de ponderación que balancean la influencia de las diferentes imágenes de *b-valor* según el contenido de señal de difusión que presentan. La metodología conjunta resultante proporciona una mejor calidad (tanto cualitativa como cuantitativamente) con respecto a los métodos secuenciales, incluidos aquellos que utilizan métodos de registro grupales alternativos.

El método descrito incorpora en la optimización dos términos de regularización (asociados cada uno a un subproblema) que aseguran estimaciones suaves tanto en los campos de deformación como en los mapas del ADC. Se han simulado dos escenarios diferentes con distintos grados de variación total (TV) en el conjunto de datos para comprobar la idoneidad de estos términos de regularización. La metodología propuesta ha demostrado ser capaz de recuperar con precisión los campos de deformación en ambos escenarios. El Capítulo 3, que constituye el segundo artículo fundamental de esta Tesis Doctoral, explica

en mayor detalle la formulación conjunta desarrollada.

Aunque este esquema ha mostrado ser capaz de lidiar de forma satisfactoria con el movimiento del paciente, no tiene en cuenta ningún modelo de ruido. Como consecuencia, algunas etapas del procesado podrían llegar a introducir un sesgo suficientemente significativo. Este sesgo podría afectar significativamente a la estimación del ADC, sobre todo, en casos con baja SNR, ya que la asunción de Gaussianidad puede dejar de ser válida. Este hecho es crítico en caso de aplicar transformaciones elásticas a los datos. Por lo tanto, para hacer frente tanto a la presencia de ruido como al movimiento fisiológico, hemos incorporado dentro del esquema original una metodología para la corrección del sesgo de interpolación que proviene de la ponderación de datos con una distribución no-Gaussiana y que, en último término, mejorará la estimación del ADC. Se ha demostrado que el algoritmo mejorado produce mapas de ADC de mayor calidad en comparación con la formulación original, especialmente cuando se han adquirido varios *b-valores* altos en la secuencia. Los sesgos introducidos por la presencia de ruido han sido descritos y estudiados de manera detallada en el Capítulo 4, el cual constituye el tercer artículo fundamental de la Tesis Doctoral.

También hemos tenido la oportunidad de validar esta metodología en un entorno más complejo y ruidoso, en concreto, en una adquisición DWI cardiaca. La metodología conjunta ha demostrado ser fiable para la corrección de los desalineamientos (muy presentes), además de robustecer la estimación de los parámetros de difusión. Gracias a esto hemos sido capaces de proporcionar mapas de ADC en el corazón con alta calidad y bajo ruido. Esta metodología también es efectiva en la corrección de la difuminación de las fronteras de las estructuras cardiacas, aumentando la SNR en las imágenes mientras que se preserva la estructura anatómica del miocardio. En el Capítulo 9 se proporcionan más detalles sobre el método aplicado a imágenes de difusión cardiaca.

A.3 Conclusiones

Esta sección recopila las principales contribuciones de esta Tesis y las posibles líneas futuras de trabajo.

A.3.1 Contribuciones

La Tesis Doctoral presentada consiste en un *corpus* metodológico y un conjunto de resultados que nos permite enumerar las siguientes contribuciones científicas:

1. Estimación de movimiento basada en el método HARP enventanado para incrementar la robustez del análisis de la imágenes de MR-*Tagging* cardiacas. El método usa múltiple orientaciones y ejes cardiacos para la reconstrucción del tensor de esfuerzo 3D.

2. Inclusión de un método automático y adaptativo para el diseño óptimo de la ventana de análisis y el filtro paso-banda. El método elimina la necesidad de una sintonización manual de los parámetros relacionados con la estimación de las imágenes de fase harmónica.

3. Diseño de patrones de *tag* óptimos mediante la introducción de múltiples picos espectrales en el k-espacio. El método mejora la robustez del análisis HARP enventanado utilizando una sola adquisición.

4. Desarrollo de un esquema de clasificación secuencial en dos etapas usando características tensoriales y de movimiento obtenidas del procesado de imágenes de MR-*Tagging*. El clasificador está enfocado en el diagnóstico de cardiomiopatías, así como en la identificación de las distintas etiologías conducentes a la hipertrofia ventricular.

5. Empleo de descriptores de patrones vorticales obtenidos a partir de magnitudes tensoriales (usando el operador rotacional) para la caracterización de la rotación miocárdica. Éstos descriptores pretenden ayudar en la diferenciación entre HCM primaria y formas secundarias de hipertrofia ventricular.

6. Cálculo, robusto frente al movimiento, del parámetro de ADC en imágenes de difusión en el hígado mediante registrado grupal elástico. Se han usado diferentes métricas multimodales tanto para la compensación del movimiento respiratorio como para la corrección de distorsiones geométricas.

7. Establecimiento de un marco de trabajo para el registrado elástico y estimación del ADC de forma conjunta en secuencias DWI abdominales en el que se propone una métrica ponderada basada en los residuos de la estimación del ADC.

8. Introducción de metodologías de filtrado en el esquema conjunto para dar cuenta de los efectos de la naturaleza del ruido presente en las imágenes en la estimación del ADC. Con esta metodología se pretende evitar posibles sesgos introducidos durante el registrado y la interpolación de las imágenes.

A.3.2 Líneas Futuras

Los resultados presentados en esta Tesis Doctoral se ciñen a aplicaciones 2D, en las que o bien se excita un único corte o bien se adquieren de forma secuencial un conjunto de éstos, los cuales se procesarían independientemente. Esta aproximación presenta ciertas limitaciones, como la inherente baja SNR, la insensibilidad al movimiento fuera de plano y el no aprovechamiento de la redundancia presente entre cortes consecutivos. Debido a las limitaciones anteriores, se plantea la extensión a 3D de las técnicas presentadas como línea futura de desarrollo. Además, la extensión 3D permitirá el desarrollo de técnicas de adquisición más avanzadas.

En el momento de escribir este documento, se está trabajando activamente en la extensión 3D de los algoritmos de registrado planteados. Una dificultad inmediata al plantear dicha extensión es el drástico incremento en los costes computacionales, por lo que se podrían aplicar técnicas de cálculo en GPU para reducir los costes computacionales resultantes.

En estos últimos años, el procesado y visualización de MR-*Tagging* ha experimentado un cambio de paradigma hacia la fusión de información proveniente de distintas técnicas y modalidades de imagen.

Los procedimientos basados en la técnica de HARP enventanada son de gran utilidad siempre y cuando la imágenes sean de alta calidad; sin embargo, su rendimiento se puede verse afectado de forma crítica por el ruido y el desvanecimiento del *tag*, especialmente en los límites del miocardio donde hay un mayor contraste entre tejidos. Es improbable que los errores derivados desaparezcan al utilizar múltiples orientaciones o picos espectrales, ni tampoco al rediseñar el patrón de *tag* o cambiar los protocolos de adquisición. Por lo tanto, las fuentes de error antes mencionadas pueden llegar a introducir sesgos importantes en la estimación de los tensores que bien podrían poner en jaque el valor clínico de los biomarcadores de movimiento extraídos.

Por poner un ejemplo, la imagen de ultrasonido es comúnmente usada para hacer el seguimiento de las superficies cardiacas, ya que dichos contornos pueden ser fácilmente extraídos y visualizados. La modalidad MR-Cine también podría ser útil para aprovechar el contraste entre tejidos, lo que permitiría recurrir a metodologías de registrado basadas en intensidad para el seguimiento de los puntos materiales, especialmente en los bordes. Por otro lado, el análisis HARP también puede beneficiarse de otras técnicas, como las basadas en flujo óptico, que son más tolerantes frente al ruido, aunque su rendimiento puede disminuir en las fases cardíacas más tempranas (antes de que se produzca el desvanecimiento del *tag*). Una línea de desarrollo futura podría ser la fusión de técnicas de MRI y ultrasonido en una única herramienta para el estudio conjunto de la funcionalidad cardíaca, lo que permitiría aunar múltiples fuentes de información para poder realizar una estimación robusta de los campos de deformación cardiacos y una reconstrucción fiable del tensor de esfuerzo.

Además, recientes avances en el diseño de secuencias de MRI han permitido la adquisición inteligente del k-espacio suprimiendo toda la información sobrante del k-espacio con excepción de los picos espectrales de interés (Epstein and Gilson, 2004), lo que puede ser de gran ayuda para lograr importantes tasas de aceleración y adquisiciones más rápidas, aumentando la presencia de la MR-*Tagging* en los protocolos clínicos.

Los futuros avances en la corrección de movimiento también deberían involucrar directamente la adquisición. Concretamente, la solución óptima para el problema del registrado debería combinar métodos prospectivos y retrospectivos de corrección de movimiento, aunque el enfoque prospectivo esté limitado a correcciones mediante transformaciones afines. Sin embargo, se podría lograr una solución sólida utilizando correcciones prospectivas para afrontar grandes desplazamientos, que pueden aproximarse mediante un modelo afín o rígido incluso, si es convenientemente seguido de una corrección retrospectiva no rígida

a una granularidad más fina, como la propuesta en los Capítulos 3 y 4. Actualmente, la corrección prospectiva de movimiento se ha podido abordar utilizando diferentes ideas, entre ellas, ecos de navegador, auto-navegación, navegadores de imagen y ultrasonidos. La investigación y desarrollo de estos enfoques deberían continuarse para mejorar la precisión y la solidez en la estimación del movimiento.

Conviene señalar también que la metodología conjunta de estimación y registrado ha mostrado cierta flexibilidad hacia la selección de los *b-valores*. Profundizando en esta idea, se podría llegar a diseñar protocolos de adquisición independientes de los *b-valores* en los que no fuese necesaria una selección previa de éstos y se obtuviera como salida directa el mapa de ADC. Además, también se pueden extender la metodología conjunta para la reconstrucción de MR a partir de datos submuestreados como ya se ha descrito para otros dominios de aplicación, como la perfusión.

Esta Tesis Doctoral ha desarrollado técnicas novedosas para la corrección de movimiento en imagen abdominal y cardiaca; sin embargo, la metodología presentada podría ser extendida fácilmente a cualquier aplicación donde el movimiento pueda poner en riesgo el diagnóstico clínico.

Appendix B: B-Spline Free-Form Deformations

In numerical analysis, a B-spline, or basis spline, is a spline function, i.e., a function defined piecewise by polynomials, that has minimal support with respect to a given degree, smoothness and domain partition.

A B-spline function is a combination of polynomials of a given degree that passes through a number of knots and creates smooth curves. We have made use of cardinal B-splines, which have knots that are equidistant from each other. These functions enable the creation and management of complex shapes and surfaces by superimposing a number of displaced B-spline functions as shown in Fig. B.1.

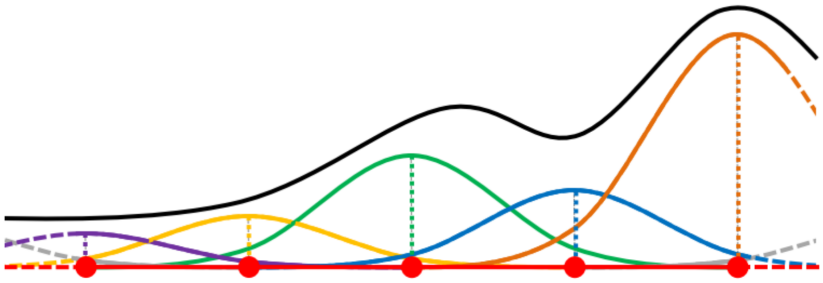

Figure B.1: B-spline representation of a given curve

In this Thesis, we intend to represent nonrigid complex displacements as linear combinations of B-splines with a set of control points. This control points will be defined over the original pixel mesh $\mathbf{x}$, so that the control point mesh encloses the ROI inside the image.

B.1 Control Points Mesh Definition

This mesh will be given by the control points whose coordinates, in the image coordinate space, will be given by $\mathbf{P} = \{\mathbf{p_u}\} = \{\mathbf{p}_{u_1,\ldots,u_L}\}$, where L represents the dimensionality of the mesh. The resolution of the mesh, represented by $\mathbf{\Delta^P}$, is an important parameter since this parameter will control the degree of elasticity of the transformation. For simplicity, we have set this parameter to be constant along a given direction, but it may vary in a different direction. Finer resolutions allow us to obtain very local transformations,

since each control point will only influence inside a small vicinity. This vicinity will be given by a distance

$$r_l^{\mathbf{p}} = \frac{(E+1)\Delta_l^{\mathbf{p}}}{2}. \tag{B.1}$$

along the different directions (l). E indicates the degree of the B-spline curve, i.e., the degree of the polynomials that compose it, whose compact support is given by $E+1$. Therefore, the pixel range, at the direction l, affected by a given control point will be:

$$\left[\max(p_{\mathbf{u}_l} - r_l^{\mathbf{p}}, x_{1,l}), \min(p_{\mathbf{u}_l} + r_l^{\mathbf{p}}, x_{2,l})\right], \tag{B.2}$$

where $x_{1,l}$ and $x_{2,l}$ represent the minimal and maximal pixel coordinate.

Now, we will assume a ROI whose bounding box can be defined by its limits $X_{1,l}$ and $X_{2,l}$ in the image coordinate space. Our goal is to define a mesh with the minimal number of control points so that the bounding box of the ROI is fully covered. We have extended these limits by leaving a certain margin in each direction to avoid boundary effects. This criterion means that a control point located out these limits will not have any influence over the ROI. Therefore, we can define a matrix given by $\mathbf{C}$ which indexes the lower and upper bounds of the control point mesh at each direction l. This indexes will be defined as:

$$\begin{aligned} C_{1,l} &= -\text{floor}\left(\frac{c_l - X_{1,l} + r_l^{\mathbf{p}}}{\Delta_l^{\mathbf{p}}}\right) \\ C_{2,l} &= \text{floor}\left(\frac{X_{2,l} - c_l + r_l^{\mathbf{p}}}{\Delta_l^{\mathbf{p}}}\right), \end{aligned} \tag{B.3}$$

where $\mathbf{c}$ represents the center of the ROI. Hence, the number of control points within the mesh will be $\prod_{l=1}^{L}(C_{2,l} - C_{1,l} + 1)$. Both the total number and control points and its radius of influence $r_l^{\mathbf{p}}$ are key parameters that will not only establish the complexity of the compensating transformation but also the computational costs of the procedure.

All the elements involved in the construction of the control point mesh have been graphically represented in Fig. B.2 for a better comprehension.

B.2 Groupwise Transformations

B.2.1 Forward Transformation

Once the control point mesh has been defined, we can obtain a dense (forward) transformation $\mathbf{T}_{\boldsymbol{\theta}}$ by applying Eq. (1.41) which maps the original pixel mesh grid $\mathbf{x}$ into non-gridded locations $\mathbf{x}'$ according to $\boldsymbol{\theta}$. This control points displacements $\boldsymbol{\theta}$ can be obtained by means of any of the gradient-based optimization methodologies explained in Section 1.4.2.3.1 and in Appendix C.

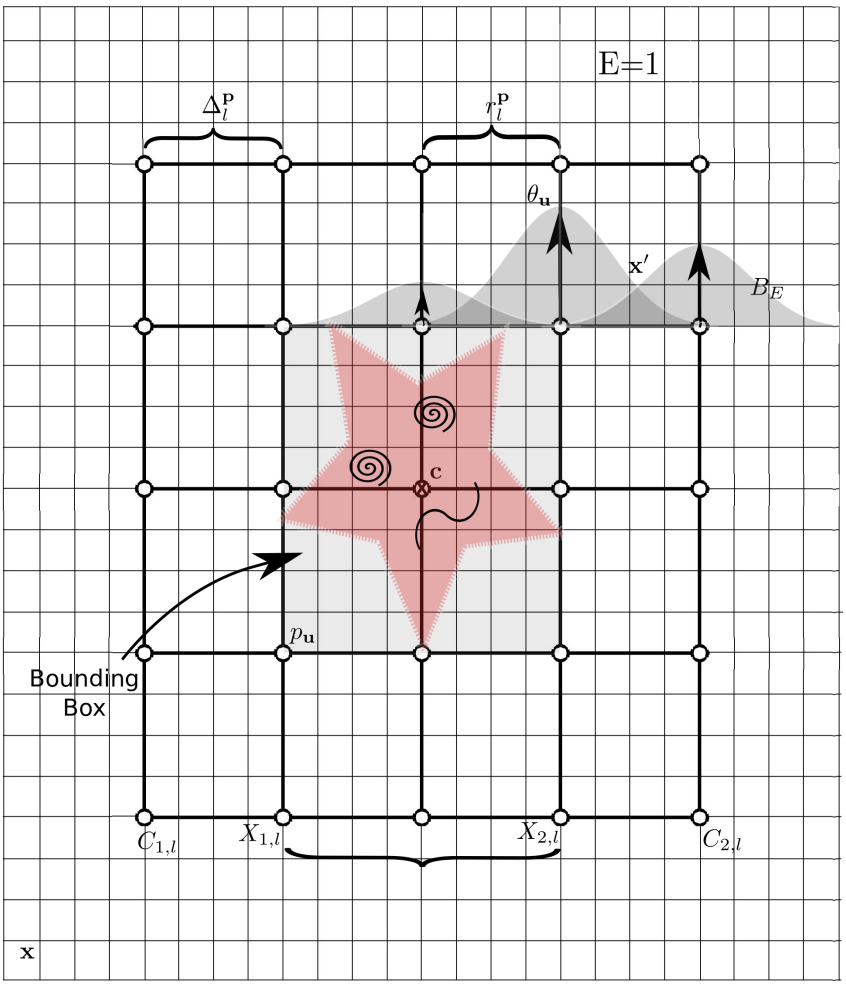

Figure B.2: Design of the control point mesh for the nonrigid transformation of a given object

In this Thesis, we have resorted to GW methodologies so additional constraints have to be considered (no further considerations are necessary when working under the PW paradigm). As aforementioned, the GW formulation makes no assumption about the selection of the reference frame. This results in an underconstrained optimization problem, since multiple solutions exist for the minimization of the metric. We therefore have to restrict the average deformation to be the identity transform (Cordero-Grande et al., 2013a):

$$\frac{1}{N_b}\sum_{n=1}^{N_b} T_n(\mathbf{x}) = \mathbf{x}, \tag{B.4}$$

with N_b the number of images.

This constraint can be enforced in the optimization procedure just by projecting the

gradient, i.e., subtracting its mean, before updating the parameters $\boldsymbol{\theta}$ in Eq. (1.45) as:

$$\widehat{\frac{\partial H}{\partial \theta_{k,n}}} = \frac{\partial H}{\partial \theta_{k,n}} - \frac{1}{N_b}\sum_{n=1}^{N_b}\frac{\partial H}{\partial \theta_{k,n}}. \tag{B.5}$$

The zero average displacement constraint in the GW paradigm implicitly defines a reference frame that lies in the center of the dynamics described by the image. After registration all images are aligned to this reference frame when applying the forward transformation $\mathbf{T}_{\boldsymbol{\theta}}$ (Eq. (1.41)). Depending on the type of application the registration procedure is used for, it might be useful to know transformation maps coordinates from an image to another $T^{n\to m}$. To be able to define this transformation, the inverse mapping or backward transformation, which maps coordinates from the reference frame to the input image coordinate frame, is needed.

B.2.2 Backward Transformation

The inverse of a B-spline transformation cannot be obtained from a in closed-form. Therefore, additional optimization procedures need to be applied. First, we obtain the (non-parametric) inverse transformation $\mathbf{T}_{\boldsymbol{\epsilon}}^{-1}$ in a similar fashion as in the registration procedure. Note that this transformation $\mathbf{T}_{\boldsymbol{\epsilon}}^{-1}$ represents an approximation to the true inverse $\mathbf{T}^{-1}$. The approximation to the inverse transformation can be obtained as the transformation that cancels $\mathbf{T}_{\boldsymbol{\theta}}$ by minimizing the following cost function:

$$V(\boldsymbol{\epsilon}) = \sum_{\mathbf{x}\in\chi} ||\mathbf{T}_{\boldsymbol{\epsilon}}^{-1}(\mathbf{T}_{\boldsymbol{\theta}}(\mathbf{x})) - \mathbf{x}||^2, \tag{B.6}$$

where χ determines the ROI. We have used a CG methodology (Metz et al., 2011) to solve the inversion problem. Although in this Thesis we have not made direct use of this inverse transformation, this approximation is extremely useful in motion robust reconstruction methodologies where encoding and decoding operators must be iteratively applied.

However, the inverse transformation $\mathbf{T}_{\boldsymbol{\epsilon}}^{-1}$ cannot be modeled exactly with another B-spline transformation. To make sure a smooth inverse, we should prevent possible foldings in the inverse transformation. One possibility could be adding a penalty term which incorporates constraints on the Jacobian of the transformation, but we have recycled the previous optimizer to fit the inverse deformation field into a pure B-spline transformation.

Consequently, the cost function will be as follows:

$$V(\boldsymbol{\theta}) = \sum_{\mathbf{x}\in\chi} ||\mathbf{T}_{\boldsymbol{\epsilon}}^{-1}(\mathbf{x}) - \mathbf{T}_{\boldsymbol{\theta}}^{-1}(\boldsymbol{\theta}, \mathbf{x})||^2. \tag{B.7}$$

For the gradient direction calculation we only need to multiply the residuals of Eq. (B.7) and the $\frac{\partial x_{n,l}}{\partial \theta_{k,n}}$ term, which represents the gradient of the transformation given by Eq. (1.41)

(see Eq. (C.5) in Appendix C). This approach may also be useful when fitting any other transformation to a pure B-spline transformation, which may be more suitable for initialization purposes than a pixelwise defined deformation field.

With the inverse B-spline transformation $\mathbf{T}_{\boldsymbol{\theta}}^{-1}$ we can easily map any point in a given image n to its corresponding in image m just by combining forward and backward transformations as:

$$T_{\boldsymbol{\theta}}^{n\to m} = T_{\boldsymbol{\theta}}^{-1}(\boldsymbol{\theta}_m) \circ T_{\boldsymbol{\theta}}(\boldsymbol{\theta}_n) = T_{\boldsymbol{\theta}}(\boldsymbol{\theta}_n + \overline{\boldsymbol{\theta}_m}). \tag{B.8}$$

For clarification, $\overline{\boldsymbol{\theta}_m}$ represents the control point displacements obtained by minimizing Eq. (B.7) at the image m (backward transformation), whereas $\boldsymbol{\theta}_n$ are obtained by solving the GW registration problem posed in Eq. (1.43) (forward transformation). Note that $\mathbf{T}_{\boldsymbol{\epsilon}}^{-1}$ could be used instead of $\mathbf{T}_{\boldsymbol{\theta}}^{-1}$. However, we have preferred the latter since simplifies the manipulation of the transformations by operating only with the control points displacements set.

B.3 Interpolation

Once calculated the forward and backward transformation, we can obtain each of the possible elastic transformations between any of the images within our dataset, just by appropriately combining them. By applying the forward transformation, we can map the original grid locations $\mathbf{x}$ of the input image into non-gridded locations $\mathbf{x}'$ corresponding to the reference frame. On the other hand, for the backward transformation, we start from the grid locations in the reference image and transform back this location in order to fall at a location between the gridded locations of the original image.

But the definition of the elastic transformation to be applied is not enough, an additional step is mandatory; an interpolation over the source images must be performed to obtain the intensities of the images associated with the updated mesh given either by the forward or backward transformation.

The most commonly used interpolation methods are:

- Nearest neighbor: the intensity of the pixel in the source image that is nearest to x' is associated with the target point.
- Linear: in this case, the intensity associated with the target point x' is obtained by linearly weighting the intensity values on the adjacent points (neighborhood) around x' in the source image.
- Cubic: similar to the linear approach but applying a cubic polynomial kernel instead of linear interpolations along each axis.

In this Thesis, we have resorted to the linear interpolation is used to obtain the intensity of the deformed images on the updated grid $\mathbf{x}'$ since it is also supported on GPU.

Appendix C: Regularization and Likelihood Term Gradients Calculus

To begin with, we will show how to get to the gradient of any given likelihood term $V((\theta))$, but first, let us redefine our cost function as:

$$V(\boldsymbol{\theta}) = V(\mathbf{I}(\mathbf{x}(\boldsymbol{\theta}))), \tag{C.1}$$

where $\mathbf{I} = \{I_1, \ldots, I_N\}$ represents the image set, $\mathbf{x} = \{\mathbf{x}_1, \ldots, \mathbf{x}_n\} = \{x_{1,1}, \ldots, x_{N,1}, \ldots, x_{N,L}\}$ the spatial coordinates and $\boldsymbol{\theta} = \{\boldsymbol{\theta}_1, \ldots, \boldsymbol{\theta}_N\} = \{\theta_{1,1}, \ldots, \theta_{K,1}, \ldots, \theta_{1,N}, \ldots, \theta_{K,N}\}$ the parameters, with K the number of control points over an image and L the dimensionality of the image (2D or 3D). By applying the chain rule, we can get to:

$$\frac{\partial V}{\partial \theta_{k,n}} = \sum_{n'=1}^{N} \frac{\partial V}{\partial I_{n'}} \sum_{n''=1}^{N} \sum_{l=1}^{L} \frac{\partial I_{n'}}{\partial x_{n'',l}} \frac{\partial x_{n'',l}}{\partial \theta_{k,n}}. \tag{C.2}$$

Taking into account that image coordinates $\mathbf{x}_n$ will only be affected by the parameters defined only over this images $\boldsymbol{\theta}_n$ only derivatives $\dfrac{\partial x_{n'',l}}{\partial \theta_{k,n}}$ be non null if $n'' = n$, thus leading to:

$$\frac{\partial V}{\partial \theta_{k,n}} = \sum_{n'=1}^{N} \frac{\partial V}{\partial I_{n'}} \sum_{n''=1}^{N} \sum_{l=1}^{L} \frac{\partial I_{n'}}{\partial x_{n'',l}} \frac{\partial x_{n'',l}}{\partial \theta_{k,n}} \delta(n'', n) = \sum_{n'=1}^{N} \frac{\partial V}{\partial I_{n'}} \sum_{l=1}^{L} \frac{\partial I_{n'}}{\partial x_{n,l}} \frac{\partial x_{n,l}}{\partial \theta_{k,n}}. \tag{C.3}$$

Besides, image intensities I_n are defined only over image coordinates $\mathbf{x}_n$, so if same reasoning is applied over $\dfrac{\partial I_{n'}}{\partial x_{n,l}}$, we obtain:

$$\frac{\partial V}{\partial \theta_{k,n}} = \sum_{n'=1}^{N} \frac{\partial V}{\partial I_{n'}} \sum_{l=1}^{L} \frac{\partial I_{n'}}{\partial x_{n,l}} \frac{\partial x_{n,l}}{\partial \theta_{k,n}} \delta(n', n) = \frac{\partial V}{\partial I_n} \sum_{l=1}^{L} \frac{\partial I_n}{\partial x_{n,l}} \frac{\partial x_{n,l}}{\partial \theta_{k,n}}, \tag{C.4}$$

which is the same expression as in Eq. 1.46.

With respect to each of the terms in the equations, $\dfrac{\partial I_n}{\partial x_{n,l}}$ term can be easily obtained since it is the spatial gradient of the image n, while the derivative of the B-spline transformation with respect to the control point $\theta_{k,n}$ is:

$$\frac{\partial x_{n,l}}{\partial \theta_{k,n}} = \left(\prod_{l''=1}^{L} B_E(v_{l''}(x_{l''} - p_{\mathbf{u}_{l''}})) \right) \delta(l, l'). \tag{C.5}$$

Regarding the regularization terms, we have resorted to first and second order spatial derivatives of the B-spline transformation $\mathbf{T}$ defined in Eq. 1.41. First order derivatives are written as follows:

$$\begin{aligned}
\frac{\partial \mathbf{T}_l(\mathbf{x},t_n)}{\partial x_1} &= \sum_{u_1=C_{1,1}}^{C_{2,1}} \sum_{u_2=C_{1,2}}^{C_{2,2}} \sum_{u_3=C_{1,3}}^{C_{2,3}} \Delta_1^{\mathbf{P}} B'_E(v_1(x_1-p_{\mathbf{u}_1}))B_E(v_2(x_2-p_{\mathbf{u}_2}))B_E(v_3(x_3-p_{\mathbf{u}_3}))\theta_{\mathbf{u}_l,n} \\
\frac{\partial \mathbf{T}_l(\mathbf{x},t_n)}{\partial x_2} &= \sum_{u_1=C_{1,1}}^{C_{2,1}} \sum_{u_2=C_{1,2}}^{C_{2,2}} \sum_{u_3=C_{1,3}}^{C_{2,3}} \Delta_2^{\mathbf{P}} B_E(v_1(x_1-p_{\mathbf{u}_1}))B'_E(v_2(x_2-p_{\mathbf{u}_2}))B_E(v_3(x_3-p_{\mathbf{u}_3}))\theta_{\mathbf{u}_l,n} \\
\frac{\partial \mathbf{T}_l(\mathbf{x},t_n)}{\partial x_3} &= \sum_{u_1=C_{1,1}}^{C_{2,1}} \sum_{u_2=C_{1,2}}^{C_{2,2}} \sum_{u_3=C_{1,3}}^{C_{2,3}} \Delta_1^{\mathbf{P}} B_E(v_1(x_1-p_{\mathbf{u}_1}))B_E(v_2(x_2-p_{\mathbf{u}_2}))B'_E(v_3(x_3-p_{\mathbf{u}_3}))\theta_{\mathbf{u}_l,n},
\end{aligned} \tag{C.6}$$

where B'_E and B''_E are the first and second derivatives of the 1D B-spline function of E-th order. On the other hand, second order derivatives will be[1]:

$$\begin{aligned}
\frac{\partial^2 \mathbf{T}_l(\mathbf{x},t_n)}{\partial x_1^2} &= \sum_{u_1=C_{1,1}}^{C_{2,1}} \sum_{u_2=C_{1,2}}^{C_{2,2}} \sum_{u_3=C_{1,3}}^{C_{2,3}} (\Delta_1^{\mathbf{P}})^2 B''_E(v_1(x_1-p_{\mathbf{u}_1}))B_E(v_2(x_2-p_{\mathbf{u}_2}))B_E(v_3(x_3-p_{\mathbf{u}_3}))\theta_{\mathbf{u}_l,n} \\
\frac{\partial^2 \mathbf{T}_l(\mathbf{x},t_n)}{\partial x_2^2} &= \sum_{u_1=C_{1,1}}^{C_{2,1}} \sum_{u_2=C_{1,2}}^{C_{2,2}} \sum_{u_3=C_{1,3}}^{C_{2,3}} (\Delta_2^{\mathbf{P}})^2 B_E(v_1(x_1-p_{\mathbf{u}_1}))B''_E(v_2(x_2-p_{\mathbf{u}_2}))B_E(v_3(x_3-p_{\mathbf{u}_3}))\theta_{\mathbf{u}_l,n} \\
\frac{\partial^2 \mathbf{T}_l(\mathbf{x},t_n)}{\partial x_3^2} &= \sum_{u_1=C_{1,1}}^{C_{2,1}} \sum_{u_2=C_{1,2}}^{C_{2,2}} \sum_{u_3=C_{1,3}}^{C_{2,3}} (\Delta_1^{\mathbf{P}})^2 B_E(v_1(x_1-p_{\mathbf{u}_1}))B_E(v_2(x_2-p_{\mathbf{u}_2}))B''_E(v_3(x_3-p_{\mathbf{u}_3}))\theta_{\mathbf{u}_l,n} \\
\frac{\partial^2 \mathbf{T}_l(\mathbf{x},t_n)}{\partial x_1 \partial x_2} &= \sum_{u_1=C_{1,1}}^{C_{2,1}} \sum_{u_2=C_{1,2}}^{C_{2,2}} \sum_{u_3=C_{1,3}}^{C_{2,3}} \Delta_1^{\mathbf{P}}\Delta_2^{\mathbf{P}} B'_E(v_1(x_1-p_{\mathbf{u}_1}))B'_E(v_2(x_2-p_{\mathbf{u}_2}))B_E(v_3(x_3-p_{\mathbf{u}_3}))\theta_{\mathbf{u}_l,n}.
\end{aligned} \tag{C.7}$$

For the sake of completeness, we also show temporal derivatives in case of dynamic sequences. The first order:

$$\begin{aligned}
&\frac{\partial \mathbf{T}_l(\mathbf{x},t_n)}{\partial t}\Big|_{t=\frac{t_{n+1}+t_n}{2}} \simeq \tfrac{\mathbf{T}_l(\mathbf{x},t_{n+1})-\mathbf{T}_l(\mathbf{x},t_n)}{\Delta_t} = \\
&= \tfrac{1}{\Delta_t} \sum_{u_1=C_{1,1}}^{C_{2,1}} \sum_{u_2=C_{1,2}}^{C_{2,2}} \sum_{u_3=C_{1,3}}^{C_{2,3}} B_E(v_1(x_1-p_{\mathbf{u}_1}))B_E(v_2(x_2-p_{\mathbf{u}_2}))B_E(v_3(x_3-p_{\mathbf{u}_3}))(\theta_{\mathbf{u}_l,n+1}-\theta_{\mathbf{u}_l,n})
\end{aligned} \tag{C.8}$$

and second order:

$$\begin{aligned}
&\frac{\partial^2 \mathbf{T}_l(\mathbf{x},t)}{\partial t^2}\Big|_{t=t_n} \simeq \tfrac{\mathbf{T}_l(\mathbf{x},t_{n+1})-2\mathbf{T}_l(\mathbf{x},t_n)+\mathbf{T}_l(\mathbf{x},t_{n-1})}{\Delta_t^2} = \\
&= \tfrac{1}{\Delta_t^2} \sum_{u_1=C_{1,1}}^{C_{2,1}} \sum_{u_2=C_{1,2}}^{C_{2,2}} \sum_{u_3=C_{1,3}}^{C_{2,3}} [B_E(v_1(x_1-p_{\mathbf{u}_1}))B_E(v_2(x_2-p_{\mathbf{u}_2}))B_E(v_3(x_3-p_{\mathbf{u}_3})) \\
&\qquad (\theta_{\mathbf{u}_l,n+1}-2\theta_{\mathbf{u}_l,n}+\theta_{\mathbf{u}_l,n-1})].
\end{aligned} \tag{C.9}$$

Furthermore, gradients of these regularization terms with respect to the parameters $\boldsymbol{\theta}$

[1] For the sake of conciseness, not all second order derivatives are shown.

need also to be calculated. First order spatial regularization gradient can be written as:

$$\frac{\partial}{\partial\theta_{\mathbf{u}_l,n}}\left(\frac{\partial\mathbf{T}_l(\mathbf{x},t=t_n)}{\partial x_1}\right)^2 = 2\left(\frac{\partial\mathbf{T}_l(\mathbf{x},t=t_n)}{\partial x_1}\right)\Delta_1^{\mathbf{P}}B'_E(v_1(x_1-p_{\mathbf{u}_1}))B_E(v_2(x_2-p_{\mathbf{u}_2}))$$
$$B_E(v_3(x_3-p_{\mathbf{u}_3}))$$
$$\frac{\partial}{\partial\theta_{\mathbf{u}_l,n}}\left(\frac{\partial\mathbf{T}_l(\mathbf{x},t=t_n)}{\partial x_2}\right)^2 = 2\left(\frac{\partial\mathbf{T}_l(\mathbf{x},t=t_n)}{\partial x_2}\right)\Delta_2^{\mathbf{P}}B_E(v_1(x_1-p_{\mathbf{u}_1}))B'_E(v_2(x_2-p_{\mathbf{u}_2}))$$
$$B_E(v_3(x_3-p_{\mathbf{u}_3}))$$
$$\frac{\partial}{\partial\theta_{\mathbf{u}_l,n}}\left(\frac{\partial\mathbf{T}_l(\mathbf{x},t=t_n)}{\partial x_3}\right)^2 = 2\left(\frac{\partial\mathbf{T}_l(\mathbf{x},t=t_n)}{\partial x_3}\right)\Delta_3^{\mathbf{P}}B_E(v_1(x_1-p_{\mathbf{u}_1}))B_E(v_2(x_2-p_{\mathbf{u}_2}))$$
$$B'_E(v_3(x_3-p_{\mathbf{u}_3})), \tag{C.10}$$

whereas for the second order:

$$\frac{\partial}{\partial\theta_{\mathbf{u}_l,n}}\left(\frac{\partial^2\mathbf{T}_l(\mathbf{x},t=t_n)}{\partial x_1^2}\right)^2 = 2\left(\frac{\partial^2\mathbf{T}_l(\mathbf{x},t=t_n)}{\partial x_1^2}\right)(\Delta_1^{\mathbf{P}})^2B''_E(v_1(x_1-p_{\mathbf{u}_1}))B_E(v_2(x_2-p_{\mathbf{u}_2}))$$
$$B_E(v_3(x_3-p_{\mathbf{u}_3}))$$
$$\frac{\partial}{\partial\theta_{\mathbf{u}_l,n}}\left(\frac{\partial^2\mathbf{T}_l(\mathbf{x},t=t_n)}{\partial x_2^2}\right)^2 = 2\left(\frac{\partial^2\mathbf{T}_l(\mathbf{x},t=t_n)}{\partial x_2^2}\right)(\Delta_2^{\mathbf{P}})^2B_E(v_1(x_1-p_{\mathbf{u}_1}))B''_E(v_2(x_2-p_{\mathbf{u}_2}))$$
$$B_E(v_3(x_3-p_{\mathbf{u}_3}))$$
$$\frac{\partial}{\partial\theta_{\mathbf{u}_l,n}}\left(\frac{\partial^2\mathbf{T}_l(\mathbf{x},t=t_n)}{\partial x_3^2}\right)^2 = 2\left(\frac{\partial^2\mathbf{T}_l(\mathbf{x},t=t_n)}{\partial x_3^2}\right)(\Delta_3^{\mathbf{P}})^2B_E(v_1(x_1-p_{\mathbf{u}_1}))B_E(v_2(x_2-p_{\mathbf{u}_2}))$$
$$B''_E(v_3(x_3-p_{\mathbf{u}_3}))$$
$$\frac{\partial}{\partial\theta_{\mathbf{u}_l,n}}\left(\frac{\partial^2\mathbf{T}_l(\mathbf{x},t=t_n)}{\partial x_1\partial x_2}\right)^2 = 2\left(\frac{\partial^2\mathbf{T}_l(\mathbf{x},t=t_n)}{\partial x_1\partial x_2}\right)\Delta_1^{\mathbf{P}}\Delta_2^{\mathbf{P}}B'_E(v_1(x_1-p_{\mathbf{u}_1}))B'_E(v_2(x_2-p_{\mathbf{u}_2}))$$
$$B_E(v_3(x_3-p_{\mathbf{u}_3})). \tag{C.11}$$

First order temporal regularization gradient is also included:

$$\frac{\partial}{\partial\theta_{\mathbf{u}_l,n}}\left(\frac{\partial\mathbf{T}_l(\mathbf{x},t)}{\partial t}\right)^2\Big|_{t=t_n} \simeq \tfrac{2}{\Delta_t}\left(\frac{\partial\mathbf{T}_l(\mathbf{x},t)}{\partial t}\Big|_{t=\frac{t_n+t_{n-1}}{2}} - \frac{\partial\mathbf{T}_l(\mathbf{x},t)}{\partial t}\Big|_{t=\frac{t_n+t_{n+1}}{2}}\right)[B_E(v_1(x_1-p_{\mathbf{u}_1}))$$
$$B_E(v_2(x_2-p_{\mathbf{u}_2}))B_E(v_3(x_3-p_{\mathbf{u}_3}))] \simeq \tfrac{2}{\Delta_t}\left(\frac{2\mathbf{T}_l(\mathbf{x},t_n)-\mathbf{T}_l(\mathbf{x},t_{n+1})-\mathbf{T}_l(\mathbf{x},t_{n-1})}{\Delta_t}\right)$$
$$B_E(v_1(x_1-p_{\mathbf{u}_1}))B_E(v_2(x_2-p_{\mathbf{u}_2}))B_E(v_3(x_3-p_{\mathbf{u}_3})), \tag{C.12}$$

as well as the second order:

$$\frac{\partial}{\partial\theta_{\mathbf{u}_l,n}}\left(\frac{\partial^2\mathbf{T}_l(\mathbf{x},t)}{\partial t^2}\right)^2\Big|_{t=t_n} \simeq \tfrac{2}{\Delta_t^2}\left(\frac{\partial^2\mathbf{T}_l(\mathbf{x},t)}{\partial t^2}\Big|_{t=t_{n-1}} - 2\frac{\partial^2\mathbf{T}_l(\mathbf{x},t)}{\partial t^2}\Big|_{t=t_n} + \frac{\partial^2\mathbf{T}_l(\mathbf{x},t)}{\partial t^2}\Big|_{t=t_{n+1}}\right)$$
$$B_E(v_1(x_1-p_{\mathbf{u}_1}))B_E(v_2(x_2-p_{\mathbf{u}_2}))B_E(v_3(x_3-p_{\mathbf{u}_3})) \simeq$$
$$\simeq \tfrac{2}{\Delta_t}\left(\frac{6\mathbf{T}_l(\mathbf{x},t_n)-4\mathbf{T}_l(\mathbf{x},t_{n-1})-4\mathbf{T}_l(\mathbf{x},t_{n+1})+\mathbf{T}_l(\mathbf{x},t_{n+2})+\mathbf{T}_l(\mathbf{x},t_{n-2})}{\Delta_t}\right)$$
$$B_E(v_1(x_1-p_{\mathbf{u}_1}))B_E(v_2(x_2-p_{\mathbf{u}_2}))B_E(v_3(x_3-p_{\mathbf{u}_3})). \tag{C.13}$$

Bibliography

Abd-Elmoniem, K., Parthasarathy, V., Prince, J., 2006. Artifact reduction in HARP strain maps using anisotropic smoothing. In: SPIE. Vol. 6143. pp. 6143–6152.

Abd-Elmoniem, K., Stuber, M., Osman, N., Prince, J., 2005. Zharp: three-dimensional motion tracking from a single image plane. Inf Processs Med Imaging 19, 639–651.

Abhinav, J., Rodríguez, J., Stopeck, A., 2016. A maximum-likelihood method to estimate a single ADC value of lesions using diffusion MRI. Magn Reson Med 76 (6), 1919–1931.

Aelen, F., Arts, T., Sanders, D., Thelissen, G., Muijtjens, A., Prinzen, F., Reneman, R., 1997. Relation between torsion and cross-sectional area change in the human left ventricle. J Biomech 30, 207–212.

Agarwal, H., Prince, J., Abd-Elmoniem, K., 2010. Total removal of unwanted harmonic peaks (TruHARP) MRI for single breath-hold high-resolution myocardial motion and strain quantification. Magn Reson Med 64 (2), 574–585.

Aja-Fernández, S., Alberola-López, C., Westin, C., 2008. Noise and signal estimation in magnitude MRI and Rician distributed images: a LMMSE approach. IEEE Trans Image Process 17 (8), 1383–1398.

Aja-Fernández, S., de Luis Garcia, R., Alberola-Lopez, C., Hernando, D., 2013. Quantitative diffusion MRI in the presence of noise: effects of filtering and fitting technique. In: Quantitative Medical Imaging. Optical Society of America, pp. QTu2G–2.

Aja-Fernández, S., Krissian, K., 2008. An unbiased non-local means scheme for DWI filtering. In: MICCAI: Workshop on Computational Diffusion MRI. Lecture Notes in Computer Science. Springer, pp. 277–284.

Aja-Fernández, S., Niethammer, M., Kubicki, M., Shenton, M., Westin, C., 2008. Restoration of DWI data using a Rician LMMSE estimator. IEEE Trans Med Imag 27 (10), 1389–1403.

Aja-Fernández, S., Pieçiak, T., Vegas-Sánchez-Ferrero, G., 2014. Spatially variant noise estimation in MRI: a homomorphic approach. Med Image Anal 20, 184–197.

Aja-Fernández, S., Vegas-Sánchez-Ferrero, G., 2016. Statistical analysis of noise in MRI. 1sted. Springer Publishing Company, Incorporated.

Al-Kwifi, O., Stainsby, J., Foltz, W., Sussman, M., Huang, Y., Wright, G., 2006. Characterizing coronary motion and its effect on mr coronary angiographyinitial experience. J Magn Res Imag 24 (4), 842–850.

Arts, T., Prinzen, F., Delhaas, T., Milles, J., Rossi, A., Clarysse, P., 2010. Mapping displacement and deformation of the heart with local sine-wave modeling. IEEE Trans Med Imag 29 (5), 1114–1123.

Aster, R., Borchers, B., Thurber, C., 2012. Magnetic resonance imaging: physical principles and applications. 1st ed. San Diego, CA, USA: Academic Press.

Atalar, E., McVeigh, E., 1994. Optimization of tag thickness for measuring position with magnetic resonance imaging. IEEE Trans Med Imag 13 (1), 152–160.

Avants, B. B., Epstein, C. L., Grossman, M., Geel, J. C., 2008. Symmetric diffeomorphic image registration with cross-correlation: evaluating automated labeling of elderly and neurodegenerative brain. Med Image Anal 12, 26–41.

Axel, L., Dougherty, L., 1989. MR imaging of motion with spatial modulation of magnetization. Radiology 171 (3), 841–845.

Axel, L., Montillo, A., Kim, D., 2005. Tagged magnetic resonance imaging of the heart: a survey. Med Imag Anal 9, 376–393.

Bai, W., Peressutti, D., Parisot, S., Oktay, O., Rajchl, M., O'Regan, D., Cook, S., King, A., Rueckert, D., 2016. Beyond the AHA 17-segment model: motion-driven parcellation of the left ventricle. Springer, Lecture Notes Bioinformatics 9354, 13–20.

Balakrishnan, G., Zhao, A., Sabuncu, M., Guttag, J., Dalca, A., 2019. VoxelMorph: A learning framework for deformable medical image registration. IEEE Trans Med Imag, in press.

Bansala, M., Kasliwalb, P., 2013. How do I do it? Speckle-Tracking echocardiography. Indian Heart J 65 (1), 117–123.

Baron, B., 2008. The 2006 american heart association classification of cardiomyopathies is the gold standard. Circ Heart Fail 1, 72–76.

Bartlett, M., 1947. The use of transformations. Biometrics 3 (1), 39–52.

Basser, P., Pierpaoli, C., 1996. Microstructural and physiological features of tissues elucidated by quantitative–diffusion–tensor MRI. J Magn Reson 111 (3), 209–219.

Becker, S., Bobin, J., Candés, E., 2011. NESTA: A fast and accurate first-order method for sparse recovery. SIAM J Imaging Sci 4, 1–39.

Bernstein, M., King, K., Zhou, X., 2004. Handbook of MRI pulse sequences. 1st ed. Burlington, MA, USA; Elsevier.

Bezdec, J., 1981. Pattern recognition with fuzzy objective function algorithms. Advanced Applications in Pattern Recognition. Plenum Press, New York.

Bloch, F., 1946. Nuclear induction. Physical Review 70, 460–474.

Bogaert, J., Dymarkowski, S., Taylor, A., Muthurangu, V., 2012. Clinical cardiac MRI. Medical Radiology. 2nd ed. Springer-Verlag, Berlin, Germany.

Bogren, H., Lantz, B., Miller, R., Mason, D., 1977. Effects of respiration on cardiac motion determined by cineangiography: implications concerning three-dimensional heart reconstruction using computer tomography. Radiological record: diagnosis 18 (6), 609–620.

Braunwald, E., Seidman, C. E., Sigwart, U., 2002. Contemporary evaluation and management of hypertrophic cardiomyopathy. Circulation 106, 1312–1316.

Buades, A., Coll, B., Morell, J., 2005. A non local algorithm for image denoising. In: IEEE Computer Society CVPR 2005. San Diego, USA, pp. 60–65.

Buchalter, M., Weiss, J., Rogers, W., Zerhouni, E., Weisfeldt, M., Beyar, R., Shapiro, E., 1990. Noninvasive quantification of left ventricular rotational deformation in normal humans using magnetic resonance imaging myocardial tagging. Circulation 81 (4), 1236–1244.

Budinger, T., Berson, A., McVeigh, E., Pettigrew, R., Pohost, G., Watson, J., Wickline, S., 1998. Cardiac MR imaging: report of a working group sponsored by the national heart, lung, and blood institute. Radiology 208 (3), 573–576.

Cattaneo, C., Larcher, L., Ruggeri, A., Herrera, A., Biasoni, E., 2011. Métodos de umbralización de imágenes digitales basados en entropía de Shannon y otros. Mec Comput 30, 2785–2805.

Cerqueira, M., 2002. Standardized myocardial segmentation and nomenclature for tomographic imaging of the heart: a statement for healthcare professionals from the cardiac imaging committee of the council on clinical cardiology of the american heart association. Circulation 105 (4), 539–542.

Chandarana, H., Block, T., Rosenkrantz, A., Lim, R., Kim, D., Mossa, D., Babb, J., Kiefer, B., Lee, V., 2011. Free-Breathing radial 3D fat-suppressed T1-weighted gradient echo sequence: a viable alternative for contrast-enhanced liver imaging in patients unable to suspend respiration. Radiology 46 (10), 648–653.

Che, T., Zheng, Y., Cong, J., Jiang, Y., Niu, Y., Jiao, W., Xhao, B., Ding, Y., 2019. Deep group-wise registration for multi-spectral images from fundus images. IEEE Access 7, 27650–27661.

Chun, S., Fessler, J., 2009. A simple regularizer for B-spline nonrigid image registration that encourages local invertibility. IEEE J Sel Top Sign Process 3 (1), 159–169.

Cordero-Grande, L., Alberola-López, C., May 2012. Extending HARP imaging by acquiring an overdetermined set of stripes. In: 20th Proceedings of the International Society on Magnetic Resonance in Medicine. Melbourne, Australia, p. 4158.

Cordero-Grande, L., Merino-Caviedes, S., Aja-Fernández, S., Alberola-López, C., 2013a. Groupwise elastic registration by a new sparsity-promoting metric: application to the alignment of cardiac magnetic resonance perfusion images. IEEE Trans Pattern Anal Mach Intell 35, 2638–2650.

Cordero-Grande, L., Merino-Caviedes, S., Albà, X., Figueras i Ventura, R., Frangi, A., Alberola-López, C., 2012. 3D fusion of cine and late-enhanced cardiac magnetic resonance images. In: 9th IEEE International Symposium on Biomedical Imaging (ISBI). Barcelona, Spain, pp. 286–289.

Cordero-Grande, L., Royuela-del-Val, J., Martín-Fernández, M., Alberola-López, C., May 2014. MOWHARP: Multi-oriented windowed HARP reconstruction for robust strain imaging. In: 22nd Proc Intl Soc Magn Reson Med. Milan, Italy, p. 7540.

Cordero-Grande, L., Royuela-del-Val, J., Sanz-Estébanez, S., Martín-Fernández, M., Alberola-López, C., 2016. Multi-Oriented windowed harmonic phase reconstruction for robust cardiac strain imaging. Med Image Anal 29, 1–11.

Cordero-Grande, L., Sevilla, T., Revilla, A., Martín-Fernández, M., Alberola-López, C., 2013b. Assessment of the fibrotic myocardial tissue mechanics by image processing. IEEE CinC Conf, 635–638.

Cordero-Grande, L., Vegas-Sánchez-Ferrero, G., Casaseca-de-la-Higuera, P., Alberola-López, C., March-April 2011. Improving harmonic phase imaging by the windowed fourier transform. In: 8th IEEE International Symposium on Biomedical Imaging: From Nano to Macro. Chicago, USA, pp. 520–523.

Cortes, C., Vapnik, V., 1995. Support-Vector networks. Mach Learn 20, 273–297.

De Boor, C., 1978. A practical guide to splines. Mathematics of Computation. Springer-Verlag, New York.

Delmon, V., Rit, S., Pinho, R., Sarrut, D., 2013. Registration of sliding objects using direction dependent B-splines decomposition. Phys Med Biol 58 (5), 1303–1314.

Denney, T., McVeigh, E., 1997. Model-free reconstruction of three dimensional myocardial strain from planar tagged MR images. J Magn Res Imag 7, 799–810.

Dhillon, A., Sweet, W., Popovic, Z., Smedira, N., Thamilarasan, M., Lytle, B., Tan, C., Starling, R., Lever, H., Moravec, C., Desai, M., 2014. Association of noninvasively measured left ventricular mechanics with in vitro muscle contractile performance: a prospective study in hypertrophic cardiomyopathy patients. J Am Heart Assoc 3 (6), 1–11.

Dice, L. R., 1945. Measures of the amount of ecologic association between species. Ecology 26, 297–302.

Dikaios, N., Punwani, S., Hamy, V., Purpura, P., Rice, S., Forster, M., Mendes, R., Taylor, S., Atkinson, D., 2014. Noise estimation from averaged diffusion weighted images: can unbiased quantitative decay parameters assist cancer evaluation? Magn Reson Med 71 (6), 2105–2117.

Dong, S., MacGregor, J., Crawley, A., McVeigh, E., Belenkie, I., Smith, E., Tyberg, J., Beyar, R., 1994. Left ventricular wall thickness and regional systolic function in patients with hypertrophic cardiomyopathy. A three-dimensional tagged magnetic resonance imaging study. Ciculation 90 (3), 1200–1209.

Du, H., Wang, L., Liu, W., Yang, F., Li, Z., Zhu, Y., 2016. Diffusion MRI simulation for human brain based on the atlas. In: 13th IEEE International Symposium on Biomedical Imaging (ISBI). Prague, Czech Republic, pp. 898–902.

Edvardsen, T., Rosen, B., Pan, L., Jerosch-Herold, M., Lai, S., Hundley, W., Sinha, S., Kronmal, R., Bluemke, D., Lima, J., 2006. Regional diastolic dysfunction in individuals with left ventricular hypertrophy measured by tagged magnetic resonance imagingthe multi-ethnic study of atherosclerosis (MESA). Am Heart J 151 (1), 109–114.

Epstein, F., Gilson, W., 2004. Displacement-Encoded cardiac MRI using cosine and sine-modulation to eliminate (cansel) artifact-generating echoes. Magn Reson Med 52 (4), 774–781.

Fieremans, E., 2008. Validation methods for fiffusion weighted magnetic resonance imaging in brain white matter. Ph.D. thesis, Doctoral dissertation, Ghent University.

Fischer, S., McKinnon, G., Maier, S., Boesiger, P., 1993. Improved myocardial tagging contrast. Magn Res Med 30, 191–200.

Foi, A., 2011. Noise estimation and removal in MR imaging: the variance-stabilization approach. In: 8th IEEE International Symposium on Biomedical Imaging (ISBI). Chicago, IL, USA, pp. 1809–1814.

Fonseca, G., Backhaus, M., Bluemke, D., Britten, R., Chun, J., Cowan, B., Dinov, I., Finn, J., Hunter, P., Kadish, A., Lee, D., Lima, J., Medrano-Gracia, P., Shivkumar, K., Suinesiaputra, A., Young, A., 2011. The cardiac atlas project: an imaging database for computational modeling and statistical atlases of the heart. Bioinformatics 27 (16), 2288–2295.

Fu, Y., Chui, C., Teo, C., 2013. Accurate two-dimensional cardiac strain calculation using adaptive windowed Fourier transform and Gabor wavelet transform. Int J Comput Assist Radiol Surg 8 (1), 135–144.

Fung, Y., 1965. Foundations of solid mechanics. Prentice-Hall, Englewood Cliffs, NJ.

Gilles, J., Heal, K., 2014. A parameterless scale-space approach to find meaningful modes in histograms - application to image and spectrum segmentation. CoRR 1401, 2686.

Glocker, B., Sotiras, A., Komodakis, N., Paragios, N., 2011. Deformable medical image registration: setting the state of the art with discrete methods. Annual Rev of Biomed Engineering 46, 219–244.

Gopalakrishnan, V., Menon, P., Madan, S., 2014. cMRI-BED: a novel informatics framework for cardiac MRI biomarker extraction and discovery applied to pediatric cardiomyopathy classification. In: 2nd International Work-Conference on Bioinformatics and Biomedical Engineering. Granada, Spain, p. 14(Suppl 2): S7.

Gupta, S., Prince, J., Androutsellis-Theotokis, S., August 1997. Bandpass optical flow for tagged mr imaging. In: 14th IEEE International Conference on Image Processing. Santa Barbara, CA, USA, pp. 364–527.

Guttman, M., Prince, J., McVeigh, E., 1994. Tag and contour detection in tagged MR images of the left ventricle. IEEE Trans Med Imag 13, 74–88.

Guyader, J., Bernandin, L., Douglas, N., Poot, D., Niessen, W., Klein, S., 2015. Influence of image registration on apparent diffusion coefficient images computed from free-breathing diffusion MR images of the abdomen. J Magn Reson Imaging 42 (2), 315–330.

Haber, E., Modersitzki, J., 2007. Intensity gradient based registration and fusion of multi-modal images. Methods Inf Med 46 (3), 292–299.

Hanh, R., 1950. Spin echoes. Physical Review 80, 545–554.

Hansen, P., 2010. Discrete inverse problems: insight and algorithms. Fundamentals of Algorithms. Society for Industrial and Applied Mathematics.

Heermann, P., Hedderich, D., Paul, M., Schulke, C., Kroeger, J., Baessler, B., Wichter, T., Maintz, D., Waltenberger, J., Heindel, W., Bunck, A., 2014. Biventricular myocardial strain analysis in patients with arrhythmogenic right ventricular cardiomyopathy

(ARVC) using cardiovascular magnetic resonance feature tracking. J Cardiovasc Magn Reson 16 (1), 75–87.

Heiland, S., Dietrich, O., Sartor, K., 2001. Diffusion-Weighted imaging of the brain: comparison of stimulated- and spin-echo echo-planar sequences. Neurorad 43 (6), 442–447.

Heinrich, M., Jenkinson, M., Bhushan, M., Matin, T., Gleeson, F., Brady, J., Schnabel, J., 2011. Non-local shape descriptor: a new similarity metric for deformable multi-modal registration. MICCAI 2011. Lecture Notes in Computer Science 6892 (2), 541–548.

Helle-Valle, T., Crosby, P., Edvardsen, T., Lyseggen, E., Amundsen, B., Smith, H., Rosen, B., Lima, J., Torp, H., Ihlen, H., Smiseth, O., 2005. New noninvasive method for assessment of left ventricular rotation: speckle tracking echocardiography. Circulation 112, 3149–3158.

Hestenes, M., Stiefel, E., 1952. Methods of conjugate gradients for solving linear systems. Journal of Research of the National Bureau of Standards 49 (6), 409–436.

Hong, X., Vinh, X., Teh, I., Soh, J., Chuang, K., 2015. Evaluation of EPI distortion correction methods for quantitative MRI of the brain at high magnetic field. Magn Reson Med 33, 1098–1105.

Horn, B., Schunck, B., 1981. Determining optical flow. Artificial Intel 17 (185), 185–203.

Huisman, T., 2003. Diffusion-Weighted imaging: basic concepts and application in cerebral stroke and head trauma. Eur Radiol 13 (10), 2283–2297.

Huizinga, W., Poot, D., Guyader, J., Klaasen, R., Coolen, B., van Kranenburg, M., van Geunsl, R., Uitterdijk, A., Polfliet, M., Vandemeulebrouckel, J., Leemans, A., Niessen, W., Klein, S., 2016. PCA-based groupwise image registration for quantitative MRI. Med Imag Anal 29, 65–78.

Ibrahim, E., 2011. Myocardial tagging by cardiovascular magnetic resonance: evolution of techniques pulse sequences, analysis, algorithms and applications. J Cardiovasc Magn Reson 13, 36.

Ibrahim, E., Swanson, S., J., S., Duvernoy, C., Pop-Busui, R., April 2016. Harmonic phase versus sine-wave modulation for measuring regional heart function from tagged MRI images. In: 2016 IEEE 13th International Symposium on Biomedical Imaging (ISBI). pp. 444–447.

Jain, A., 1988. Fundamentals of digital image processing. United States Edition: Prentice Hall Information and System Sciences Series.

Jeung, M., Germain, P., Croisille, P., El ghannudi, S., Roy, C., Gangi, A., 2012. Myocardial tagging with MR Imaging: overview of normal and pathologic findings. RadioGraphics 32, 1381–1398.

Jha, A., Rodríguez, J., 2012. A maximum-likelihood spproach for ADC estimation of lesions in visceral organs. In: Image Analysis and Interpretation (SSIAI), 2012 IEEE Southwest Symposium on. IEEE, pp. 21–24.

Johansen-Berg, H., Behrens, T., 2009. Diffusion MRI: from quantitative measurement to in vivo neuroanatomy. 1st ed. Academic Press New York: Elsevier.

Jonasson, L., 2005. Segmentation of diffusion weighted MRI using the level set framework. Ph.D. thesis, Doctoral dissertation, Ecole Polytechnique Federale de Lausanne.

Jones, D., 2010. Diffusion MRI: theory, methods, and applications. Oxford University Press.

Jung, B., Föll, D., Böttler, S., Hennig, J., Markl, M., 2006. Detailed analysis of myocardial motion in volunteers and patients using high-temporal resolution MR tissue phase mapping. J Magn Res Imag 24 (5), 1033–1039.

Karamitsos, T., Neubauer, S., 2011. The interplay between cardiac strain and fibrosis in non-ischaemic cardiomyopathies: insights from cardiovascular magnetic resonance. Eur J Heart Fail 13, 927–928.

Kay, S., 1993. Fundamentals of statistical signal processing: estimation theory. Prentice-Hall, Englewood Cliffs, NJ.

Kerwin, W., Osman, N., Prince, J., 2000. Image processing and analysis in tagged cardiac MRI. Handbook of Medical Image Processing, 375–392.

Kerwin, W., Prince, J., 2002. Kriging filter for space-time interpolation. Advances in Imaging and Electron Physics 124, 139–193.

Kim, T., Murakami, T., Takahashi, S., Hori, M., Tsuda, K., Nakamura, H., 1999. Diffusion-Weighted single-shot echoplanar MR imaging for liver disease. AJR Am J Roentgenol 173, 393–398.

King, K., Moran, P., 1984. A unified description of NMR imaging, data collection strategies and reconstruction. Medical Physics 11 (1), 1–14.

Köhler, B., Gasteiger, R., Preim, U., Theisel, S., Maintz, D., Preim, B., 2013. Semi-Automatic vortex extraction in 4D PC-MRI cardiac blood flow data using line predicates. IEEE Trans Vis Comp Graph 19 (12), 2773–2782.

Komodakis, N., Tziritas, G., Paragios, N., 2007. Fast, approximately optimal solutions for single and dynamic MRFs. In: Comp Vis and Patt Recogn, 2007. CVPR '07. IEEE Conference. Minnesota, United States, pp. 1–8.

Kornapoulos, E., Zacharaki, E., Zerbib, P., Lin, C., Rahmouni, A., Paragios, N., 2016. Deformable groupwise registration using a physiological model: application to diffusion-weighted MRI. In: IEEE International Conference on Image Processing (ICIP). Arizona, United States, pp. 2345–2349.

Kuperman, V., 2000. Magnetic resonance imaging: physical principles and applications. 1st ed. San Diego, CA, USA: Academic Press.

Kurugol, S., Freiman, M., Afacan, O., Domachevsky, L., Perez-Rossello, J., Callahan, M., Warfield, S., 2017a. Motion compensated abdominal diffusion weighted MRI by simultaneous image registration and model estimation (SIR-ME). Med Imag Anal 17, 64–6.

Kurugol, S., Freiman, M., Afacan, O., Domachevsky, L., Perez-Rossello, J., Callahan, M., Warfield, S., 2017b. Motion-Robust parameter estimation in abdominal diffusion-weighted MRI by simultaneous image registration and model estimation. Med Imag Anal 39, 124–132.

Kybic, J., Unser, M., 2003. Fast parametric elastic image registration. IEEE Trans Imag Process 12 (11), 1427–1442.

Laissy, J., Serfaty, J., Messika-Zeitoun, D., Ribet, A., Chillon, S., Steg, P., Klein, I., 2009. Cardiac diffusion MRI of acute and chronic myocardial infarction: preliminary results. J Radiol 90, 481–4.

Landman, B., Bazin, P.-L., Prince, J., 2007. Diffusion tensor estimation by maximizing Rician likelihood. In: Computer Vision, 2007. ICCV 2007. IEEE 11th International Conference on. IEEE, pp. 1–8.

Larkman, D., Nunes, R., 2007. Parallel magnetic resonance imaging. Medical Biology 52, 15–55.

Lauterbur, P., 1973. Image formation by induced local interactions: Examples employing nuclear magnetic resonance. Nature 242, 190–191.

Le Bihan, D., 2014. Diffusion MRI: What water tells us about the brain. EMBO Mol Med 6 (5), 569–573.

Le Bihan, D., Breton, E., 1985. Imagerie de diffusion in-vivo par résonance magnétique nucléaire. Comptes-Rendus de l'Académie des Sciences 301 (15), 1109–1112.

Le Bihan, D., Breton, E., Lallemand, D., Aubin, M., Vignaud, J., Laval-Jeantet, M., 1988. Separation of diffusion and perfusion in intravoxel incoherent motion MR imaging. Radiology 168 (2), 497–505.

Le Bihan, D., Breton, E., Lallemand, D., Grenier, P., Cabanis, E., Laval-Jeantet, M., 1986. MR imaging of intravoxel incoherent motions: application to diffusion and perfusion in neurologic disorders. Radiology 161 (2), 401–407.

Learned-Miller, E., 2006. Data driven image models through continuous joint alignment. IEEE Trans Pattern Anal Mach Intel 28, 236–250.

Ledesma-Carbayo, M., Bajo, A., Santa-Marta, C., Perez-David, E., Caso, I., Garcia-Fernandez, M., Santos, A., Desco, M., 2006. Cardiac motion analysis from cine MR sequences using non-rigid registration tecniques. In: Computers in Cardiology. Valencia, Spain, pp. 520–523.

Lee, S., Wolberg, G., Shin, S., 1997. Scattered data interpolation with multilevel B-splines. IEEE Trans Visualization Comput 3, 228–244.

Lewis, S., Dyvorne, H., Cui, Y., Taouli, B., 2014. Diffusion-Weighted imaging of the liver: techniques and applications. Magn Reson Imaging Clin N Am 22 (3), 373–395.

Liang, X., Garnavi, R., Wail, S., Liang, S., Prassanna, P., 2015. Automatic segmentation of the left ventricle into 17 anatomical regions in cardiac MR imaging. In: 37th Conf Proc IEEE Eng Med Biol Soc. Milan, Italy, pp. 6531–5.

Liang, Z., Lauterbur, C., 2000. Principles of magnetic resonance imaging: a signal processing perspective. 1st ed. Washington, USA: SPIE Optical Engineering Press.

Liau, J., Lee, J., Schroeder, M., Sirlin, C., Bydder, M., 2012. Cardiac motion in diffusion weighted MRI of the liver: artifact and a method of correction. J Magn Reson Imaging 35 (2), 318–327.

Lima da Cruz, G., 2016. Advanced motion corrected reconstruction techniques for magnetic resonance imaging. Ph.D. thesis, Doctoral dissertation, King's College London.

Lorenz, C., Pastorek, S., Bundy, J., 2000. Delineation of normal human left ventricular twist throughout systole by tagged cine magnetic resonance imaging. J Cardiovasc Magn Reson 2 (2), 97–108.

Luna, A., Ribes, R., Soto, J., 2012. Diffusion MRI outside the brain: a case-based review and clinical applications. Springer-Verlag.

Maes, F., Collignon, A., Vandermeulen, D., Marchal, D., Suetens, P., 1997. Multimodality image registration by maximization of mutual information. Trans Med Imaging 16, 187–198.

Maggioni, M., Katkovnik, V., Egiazarian, K., Foi, A., 2013. Nonlocal transform-domain filter for volumetric data denoising and reconstruction. IEEE Trans Image Process 22 (1), 119–133.

Makram, A., Khalifa, A., El-Rewaidy, H., Fahmy, A., Ibrahim, E., 2015. Assessment of global cardiac function from tagged magnetic resonance images. Comparison with cine MRI. In: 23rd Proc Intl Soc Mag Reson Med. Vol. 23. Toronto, Canada, p. 4472.

Makram, A., Khalifa, A., El-Rewaidy, H., Fahmy, A., Ibrahim, E., 2016. Assessment of cardiac mass from tagged magnetic resonance images. Jpn J Radiol 34 (2), 158–165.

Manjón, José V and Coupé, Pierrick and Concha, Luis and Buades, Antonio and Collins, D Louis and Robles, Montserrat, 2013. Diffusion weighted image denoising using overcomplete local PCA. PloS one 8 (9), e73021.

Mansfield, P., Grannel, P., 1973. NMR diffraction in solids. Journal of Physical Chemics 6, 422–426.

Markl, M., Kilner, P., Ebbers, T., 2011. Comprehensive 4D velocity mapping of the heart and great vessels by cardiovascular magnetic resonance. J Cardiovac Magn Reson 13 (7), 13–17.

Maron, B., Ommen, S., Semsariam, C., Spirito, P., Olivotto, I., Maron, M., 2014. Hypertrophic cardiomyopathy: present and future, with translation into contemporary cardiovascular medicine. JACC Cardiovasc Imaging 64, 83–990.

Maron, B., Towbin, J., Thiene, G., Antzelevitch, C., Corrado, D., Arnett, D., Moss, A., Seidman, C., Young, J., 2006. Contemporary definitions and classification of the cardiomyopathies. Circulation 113, 1807–1816.

Maron, B., Wolfson, J., Roberts, W., 1992. Relation between extent of cardiac muscle cell disorganization and left ventricular wall thickness in hypertrophic cardiomyopathy. Amer J Cardiol 70, 785–790.

Mattes, D., Haynor, D., Vesselle, H., Lewellen, T., Eubank, W., 2001. Non-Rigid multimodality image registration. Med Imag 2001: Image Proc 4322, 1609–1620.

Mazaheri, Y., Do, R., Shukla-Dave, A., Deasy, J., Lu, Y., Akin, O., 2012. Motion correction of multi-b-value diffusion-weighted imaging in the liver. Acad Radiol 19 (12), 1573–1580.

McCulloch, A., Mazhari, R., 2001. Regional myocardial mechanics: integrative computational models of flow-function relations. J Nuclear Cardiology 8 (4), 506–519.

McFadden, D., 2000. Statistical tools. University of California, Berkeley, CA, USA.

McLeish, K., Hill, D., Atkinson, D., Blackall, J., Razavi, R., 2002. A study of the motion and deformation of the heart due to respiration. IEEE Trans Med Imag 21 (9), 1142–1150.

McVeigh, E., Prinzen, F., Wyman, B., Tsitlik, J., Halperin, H., Hunter, W., 1998. Imaging asynchronousmechanical activation of the paced heart with tagged MRI. Magn Res Med 39, 507–513.

Metz, C., Klein, S., Schaap, M., van Walsum, T., Niessen, W., 2011. Nonrigid registration of dynamic medical imaging data using nD + t B-splines and a groupwise optimization approach. Med Imag Anal 15, 238–249.

Miao, S., Wang, Z., Laio, R., 2016. A CNN regression approach for real-time 2D/3D registration. IEEE Trans Med Imag 35 (5), 1352–1363.

Moser, T., Smith, M., 1990. A dante tagging sequence for the evaluation of translation sample motion. Magn Res Med 2, 334–339.

Nelder, J., Mead, R., 1965. A simplex method for function minimization. Computer Journ 7, 308–313.

Osman, N., Kerwin, W., McVeigh, E., Prince, J., 1999. Cardiac motion tracking using CINE harmonic phase (HARP) magnetic resonance imaging. Magn Res Med 42, 1048–1060.

Osman, N., McVeigh, E., Prince, J., 2000. Imaging heart motion using harmonic phase MRI. IEEE Trans Med Imaging 19 (3), 186–02.

Osman, N., Prince, J., 2004. Regenerating MR tagged images using harmonic phase (HARP) methods. IEEE Trans Biomed Eng 51 (8), 1428–1433.

Otsu, N., Sonoda, L., Hayes, C., Hill, D., Leach, M., Hawkes, D., 1979. A threshold selection method from gray-level histograms. IEEE Trans Syst, Man & Cybern SMC-9.

Ozturk, C., McVeigh, E., 2000. Four-dimensional B-spline based motion analysis of tagged MR images: introduction and in vivo validation. Physics in Medicine and Biology 45, 1683–1702.

Padhani, A., Liu, G., Mu-Koh, D., Chenevert, T., Thoeny, H., Takahara, T., Dzik-Jurasz, A., Ross, B., Van Cauteren, M., Collins, D., Hammoud, D., Rustin, G., Taouli, B., Choyke, P., 2009. Diffusion-Weighted magnetic resonance imaging as a cancer biomarker: consensus and recommendations. Neoplasia 11 (2), 102–125.

Pan, L., Prince, J., Lima, J., Osman, N., 2005. Fast tracking of cardiac motion using 3D-HARP. IEEE Trans Biomed Eng 52 (8), 1425–1435.

Park, J., Metaxas, D., Young, A., Axel, L., 1996. Deformable models with parameter functions for cardiac motion analysis from tagged MRI data. IEEE Trans Med Imag 15 (3), 278–289.

Parthasarathy, V., 2006. Characterization of harmonic phase MRI: theory, simulations and applications. Ph.D. thesis, Doctoral dissertation, The Johns Hopkins University, Maryland, USA.

Parthasarathy, V., Prince, J., 2003. On the resolution of HARP-MRI. In: 11th Proc Intl Soc Mag Reson Med. Vol. 11. Toronto, Canada, p. 949.

Parthasarathy, V., Prince, J., 2004. Strain resolution from HARP-MRI. In: 12th Proc Intl Soc Mag Reson Med. Vol. 11. Kyoto, Japan, p. 1797.

Pennec, X., Cachier, P., Ayache, N., 1999. Non-Local understanding the "Demon's Algorithm": 3D non-rigid registration by gradient descent shape descriptor: a new similarity metric for deformable multi-modal registration. MICCAI 1999. Lecture Notes in Computer Science 1679, 597–606.

Petersen, S., Jung, B., Wiesmann, F., Selvanayagam, J., Francis, J., Hennig, J., Neubauer, S., Robson, M., 2006. Myocardial tissue phase mapping with cine phase-contrast MR imaging: regional wall motion analysis in healthy volunteers. Radiology 238 (3), 816–826.

Petitjean, C., Rougon, N., Cluzel, P., 2005. Assessment of myocardial function: a review of quantification methods and results using tagged MRI. J Cardiovasc Magn Res 7 (2), 601–516.

Pieciak, T., Aja-Fernández, S., Vegas-Sánchez-Ferrero, G., 2017. Non-stationary Rician noise estimation in parallel MRI using a single image: a variance-stabilizing approach. IEEE Trans Pattern Anal Mach Intell 39 (10), 2015–2029.

Piella, G., De Craene, M., Bijnens, B., Tobon-Gómez, C., Huguet, M., Avegliano, G., Frangi, A., 2010. Characterizing myocardial deformation in patients with left ventricular hypertrophy of different etiologies using the strain distribution obtained by magnetic resonance imaging. Rev Esp Cardiol 63, 1281–1291.

Pipe, J., 1999. Motion correction with PROPELLER MRI: application to head motion and free-breathing cardiac imaging. Magn Reson Med 42 (5), 963–969.

Poupon, C., Roche, A., Dubois, J., Mangin, J., Poupon, F., 2008. Real-Time MR diffusion tensor and Q-Ball imaging using Kalman filtering. Med Image Anal 12, 527–534.

Prasad, M., Ramesh, A., Kavanagh, P., Tamarappoo, B., Nakazato, R., Gerlach, J., Cheng, V., Thomson, L., Berman, D., Germano, G., Slomka, P., 2010. Quantification of 3D regional myocardial wall thickening from gated magnetic resonance images. J Magn Reson Imag 31, 317–327.

Pruessmann, K., Weiger, M., Scheidegger, M., Boesiger, P., 1999. SENSE: sensitivity encoding for fast MRI. Magn Reson Med 42 (5), 952–962.

Purcell, E., Torrey, H., 1946. Resonance absorption by nuclear magnetic moments in a solid. Physical Review 69, 37.

Puyol-Antón, E., Sinclair, M., Gerber, B., Amzulescu, M., Langet, H., De Craene, M., Aljabar, P., Schnabel, J., Piro, P., King, A., 2017. Multiview machine learning using an atlas of cardiac cycle motion. In: 8th MICCAI/STACOM. Lecture Notes in Computer Science. Vol. 001. pp. 3–11.

Radeva, P., Amini, A., Huang, J., 1997. Deformable B-solids and implicit snakes for 3D localization and tracking of MRI-SPAMM data. Comp Vis and Imag Understanding 66 (2), 163–178.

Rahman, Q. A., Tereshchenko, L. G., Kongkatong, M., Abraham, T., Abraham, M. R., Shatkay, H., 2015. Utilizing ECG-based heartbeat classification for hypertrophic cardiomyopathy identification. IEEE Trans Nanobioscience 14, 505–512.

Reischauer, C., Gutzeit, A., 2017. Image denoising substantially improves accuracy and precision of intravoxel incoherent motion parameter estimates. PloS one 12 (4), e0175106.

Richard, P., Charron, P., Carrier, L., Ledeuil, C., Cheav, T., Pichereau, C., Benaiche, A., Isnard, R., Dubourg, O., Burban, M., Gueffet, J. P., Millaire, A., Desnos, M., Schwartz, K., Hainque, B., Komajda, M., 2003. Hypertrophic cardiomyopathy: distribution of disease genes, spectrum of mutations and implications for a molecular diagnosis strategy. Circulation 107, 2227–2232.

Royuela-del Val, J., 2017. Software solutions for two computationally intensive problems: reconstruction of dynamic MR and handling of alpha-stable distributions. Ph.D. thesis, Doctoral dissertation, Universidad de Valladolid.

Royuela-del-Val, J., Cordero-Grande, L., Simmross-Wattenberg, F., Martín-Fernández, M., Alberola-López, C., 2017. Jacobian weighted temporal total variation for motion compensated compressed sensing reconstruction of dynamic MRI. Magn Reson Med 77, 1208–1215.

Rueckert, D., Aljabar, P., Heckemann, R., Hajnal, J., Hammers, A., 2006. Diffeomorphic registration using B-splines. MICCAI 2006. Lecture Notes in Computer Science 4191, 702–709.

Rueckert, D., Sonoda, L., Hayes, C., Hill, D., Leach, M., Hawkes, D., 1999. Nonrigid registration using free-form deformations: application to breast MR images. IEEE Trans Med Imag 18, 712–721.

Rüssel, I., Götte, M., Bronzwaer, J., Knaapen, P., Paulues, W., van Rossum, A., 2009a. Left ventricular torsion: an expanding role in the analysis of myocardial dysfunction. JACC Cardiovasc Imaging 2 (5), 648–655.

Rüssel, I., Tecelao, S., Kuijer, J., Heethaar, R., Marcus, J., 2009b. Comparison of 2D and 3D calculation of left ventricular torsion as circumferential-longitudinal shear angle using cardiovascular magnetic resonance tagging. J Cardiovasc Magn Reson 11 (8), 648–655.

Rutz, A., Ryf, S., Plein, S., Boesiger, P., Kozerke, S., 2008. Accelerated whole-heart 3D CSPAMM for myocardial motion quantification. Magn Reson Med 59, 755–763.

Saltijeral, A., Perez-de-Isla, L., Veras, K., Fernández, M., Gorissen, W., Rementeria, J., Almeria, C., Rodrigo, J., Fernández-Golfin, C., Marcos-Alberca, C., Macaya, C., Zamorano, J., 2010. Myocardial strain characterization in different left ventricular adaptative responses to high blood pressure: a study based on 3D-wall motion tracking analysis. Echocardiography 27, 1238–1246.

Sandrasegaran, K., Akisik, F., Lin, C., Tahir, B., Rajan, J., Saxena, R., Aisen, A., 2009. Value of diffusion-weighted MRI for assessing liver fibrosis and cirrhosis. AJR Am J Roentgenol 193 (6), 1556–1560.

Sanz-Estébanez, S., 2014. Esquema de compensación de movimiento mediante registrado grupal aplicado a imagen cardiaca dinámica. Master's thesis, Universidad de Valladolid, Spain.

Sanz-Estébanez, S., Cordero-Grande, L., Martín-Fernández, M., Aja-Fernández, S., Alberola-López, C., 2016a. Spatial and spectral anisotropy in HARP images: an automated approach. In: 13th IEEE International Symposium on Biomedical Imaging (ISBI). Prague, Czech Republic, pp. 1156–1159.

Sanz-Estébanez, S., Merino-Caviedes, S., Sevilla, T., Revilla-Orodea, A., Martín-Fernández, M., Alberola-López, C., 2015. Cardiac strain assessment for fibrotic myocardial tissue detection in left ventricular hypertrophic cardiomyopathy. In: Congreso Anual de la Sociedad Española de Ingeniería Biomédica. Madrid, Spain, pp. 10–13.

Sanz-Estébanez, S., Peña-Nogales, O., de-Luis-García, R., Aja-Fernández, S., Alberola-López, C., 2017. Groupwise non-rigid registration on multiparametric abdominal DWI acquisitions for robust ADC estimation: comparison with pairwise approaches and different multimodal metrics. In: 14th IEEE International Symposium on Biomedical Imaging (ISBI). Melbourne, Australia, pp. 1156–1159.

Sanz-Estébanez, S., Rabanillo-Viloria, I., Royuela-del-Val, J., Aja-Fernández, S., Alberola-López, C., 2018. Joint groupwise registration and ADC wstimation in the liver using a b-value weighted metric. Magn Reson Imaging 46, 1–9.

Sanz-Estébanez, S., Royuela-del-Val, J., Merino-Caviedes, S., Revilla-Orodea, A., Sevilla, T., Cordero-Grande, L., Martín-Fernández, S., Alberola-López, C., 2016b. An automated tensorial classification procedure for left ventricular hypertrophic cardiomyopathy.

In: 4th International Conference on Bioinformatics and Biomedical Engineering (IWBBIO). Vol. 9656. Granada, Spain, pp. 184–195.

Schneider, N., Piewak, F., Stiller, C., Franke, U., 2017. RegNet: Multimodal sensor registration using deep neural networks. In: IEEE Intelligent Vehicles Symposium. Redondo Beach, CA, USA, pp. 1803–1810.

Segars, W., Sturgeon, G., Mendonca, S., Grimes, J., Tsui, B., 2010. 4D XCAT phantom for multimodality imaging research. Med Phys 37, 4902–4915.

Sengupta, P., Tajik, A., Chandrasekaran, K., Khandheria, B., 2008. Twist mechanics of the left ventricle: principles and application. JACC Cardiovascular Imaging 1 (3), 366–1376.

Shehata, M., Cheng, S., Osman, N., Bluemke, D., Lima, J., 2009. Myocardial tissue tagging with cardiovascular magnetic resonance. J Cardiovasc Magn Reson 11 (1), 55.

Shi, F., Cheng, J., Wang, L., Yap, P., Shen, D., 2015. Super-Resolution reconstruction of diffusion-weighted images using 4D low-rank and total variation. Comput Diffus MRI, 15–25.

Shimon, A., Reisner, M., Lysyansky, P., Agmon, Y., Mutlak, D., Lessick, J., Friedman, Z., 2000. Global longitudinal strain: a novel index of left ventricular systolic function. J Am Soc Echocardiogr 17, 630–633.

Sijbers, J., den Dekker, A., Scheunders, P., Van Dyck, D., 1998. Maximum-likelihood estimation of Rician distribution parameters. IEEE Trans Med Imag 17, 357–361.

Sima, D., 2006. Regularization techniques in model fitting and parameter estimation. Ph.D. thesis, Doctoral dissertation, Katholieke Universitet Leuven.

Simpson, R., Keegan, J., Firmin, D., 2013. MR assessment of regional myocardial mechanics. J Cardiovasc Magn Reson 37, 576–599.

Smiseth, O., Torp, H., Opdahl, A., Haugaa, K., Urheim, S., 2016. Myocardial strain imaging: how useful is it in clincical decision making? Eur Heart Journal 37 (15), 1196–1207.

Soderman, O., Jonsson, B., 1995. Restricted diffusion in cylindrical geometry. J Magn Res 117, 94–97.

Stalder, A., Frydrychowicz, A., Harloff, A., Yang, Q., Bock, J., Henning, J., 2010. Vortex core detection and visualization using 4D flow-sensitive MRI. In: 18th Proc Intl Soc Mag Reson Med. Stockholm, Sweden, p. 3708.

Stejskal, E., Tanner, J., 1965. Spin diffusion measurements: spin echoes in the presence of a time-dependent field gradient. Journal of Chemical Physics 42, 288–292.

Stephen, R., Jha, A., Roe, D., Trouard, T., Galons, J., Kupinski, M., Frey, G., Cui, H., Squire, S., Pagel, M., Rodriguez, J., Gillies, R., Stopeck, A., 2015. Diffusion MRI with semi-automated segmentation can serve as a restricted predictive biomarker of the therapeutic response of liver metastasis. Magn Reson Imaging 33 (10), 1267–1273.

Steven, A., Zhuo, J., Melhem, E., 2014. Diffusion kurtosis imaging: an emerging technique for evaluating the microstructural environment of the brain. Amer Jour Roentgenology 202 (1), W26–W33.

Stoeck, C., Manka, R., Boesiger, P., Kozerke, S., 2012. Undersampled cine 3D tagging for rapid assessment of cardiac motion. J Cardiovasc Magn Reson 14 (1), 60.

Swoboda, P., Larghat, A., Zaman, A., Fairbairn, T., Motwani, M., Greenwood, J., Plein, S., 2014. Reproducibility of myocardial strain and left ventricular twist measured using complementary spatial modulation of magnetization. J Magn Reson 39, 887–894.

Taimouri, V., Afacan, O., Perez-Rossello, J., Callahan, M., Mulkern, R., Warfield, S., Freiman, M., 2015. Spatially constrained incoherent motion method improves diffusion-weighted MRI signal decay analysis in the liver and spleen. Med Phys 42 (4), 1895–1903.

Tang, L., Hamarneh, G., Iniewski, K., 2013. Medical image registration: a review. Medical imaging: technology and applications, 619–660.

Theilmann, R., Borders, R., Trouard, T., Xia, G., Outwater, E., Ranger-Moore, J., Gillies, R., Stopeck, A., 2004. Changes in water mobility measured by diffusion MRI predict response of metastatic breast cancer to chemotherapy. Neoplasia 6, 831–837.

Theodoridis, S., Koutroumbas, K., 1999. Pattern recognition. Academic Press, San Diego: ELsevier.

Thoeny, H., Ross, B., 2010. Predicting and monitoring cancer treatment tesponse with diffusion-weighted MRI. J Mag Res Imag 32 (1), 2–16.

Thunberg, P., Zetterberg, P., 2007. Noise distribution in SENSE- and GRAPPA- reconstructed images: a computer simulation study. Magn Reson Imaging 25, 1089–1094.

Tobon-Gomez, C., De Craene, M., McLeod, K., Tautz, L., Shi, W., Hennemuth, A., Prakosa, A., Wang, H., Carr-White, G., Kapetanakis, S., Lutz, A., Rasche, V., Schaeffter, T., Butakoff, C., Friman, O., Mansi, T., Sermesant, M., Zhuang, X., Ourselin, S., Peitgen, H., Pennec, X., Razavi, R., Rueckert, D., Frangi, A., Rhode, K., 2013. Benchmarking framework for myocardial tracking and deformation algorithms: an open access database. Med Imag Anal 17 (6), 632 – 648.

Tofts, P., 2004. Quantitative MRI of the brain: measuring changes caused by disease. Chichester, England: John Wiley & Sons.

Tomasi, C., Manduchi, R., 1998. Bilateral filtering for gray and color images. In: 6th IEEE International Conference on Computer Vision (ICCV). Venice, Italy, pp. 839–846.

Tristán-Vega, A., 2009. A novel framework for the study of neural architectures in the human brain with diffusion MRI. Ph.D. thesis, Doctoral dissertation, Universidad de Valladolid.

Tristán-Vega, A., García -Pérez, V., Aja-Fernández, S., Westin, C., 2012. Efficient and robust non-local means denoising of MR data based on salient features matching. Comput Methods Programs Biomed 105, 131–144.

Urbano-Moral, J., Rowin, E., Maron, M., Crean, A., Pandian, N., 2014. Investigation of global and regional myocardial mechanics with three-dimensional speckle tracking echocardiography and relations to hypertrophy and fibrosis in hypertrophic cardiomyopathy. Circ Cardiovasc Imaging 7, 11–19.

Veeranghavan, H., Do, R., Reidy, D., Deasy, J., 2015. Simultaneous segmentation and iterative registration method for computing ADC with reduced artifacts from DW-MRI. Med Phys 42 (5), 2249–2260.

Venkatesh, B., Gupta, H., Lloyd, S., Italia, L., Denney, T., 2010. 3D left ventricular strain from unwrapped harmonic phase measurements. J Magn Reson Imag 31, 854–862.

Veraart, J., Sijbers, J., Sunaert, S., Leemans, A., Jeurissen, B., 2013. Weighted linear least squares estimation of diffusion MRI parameters: strengths, limitations, and pitfalls. Neuroimage 81, 335–346.

Vercauteren, T., Pennec, X., Perchant, A., Ayache, N., 2009. Diffeomorphic demons: efficient non-parametric image registration. Neuroimage 45 (1), 61–72.

Vert, J., Tsuda, K., Schölkopf, B., 2004. A primer on kernel methods. Kernel Meth Comput Biology, 35–70.

von Spiczak, J., Crelier, G., Giese, D., Kozerke, S., Maintz, D., Bunck, A., 2015. Quantitative analysis of vortical blood flow in the thoracic aorta using 4D phase contrast MRI. PLoS One 10 (9), e0139025.

Wachinger, C., Navab, N., 2012. Entropy and laplacian images: structural representations for multi-modal registration. Med Image Anal 16, 1–17.

Wachinger, C., Navab, N., 2013. Simultaneous registration of multiple images: similarity metrics and efficient optimization. IEEE Trans Pattern Anal Mach Intell 35 (5), 1221–1233.

Walker-Samuel, S., Orton, M., McPhail, L., Robinson, S., 2009. Robust estimation of the apparent diffusion coefficient (ADC) in heterogeneous solid tumors. Magn Reson Med 62, 420–429.

Wang, D., Fu, Y., Ashraf, M., 2015. Artifacts reduction in strain maps of tagged magnetic resonance imaging using harmonic phase. Open Med 10 (1), 425–433.

Wang, L., Zhu, Y., Li, H., Liu, W., Magnin, I., 2012. Multiscale modeling and simulation of the cardiac fiber architecture for DMRI. IEEE Trans Biomed Eng 59 (1), 16–19.

Wang, Y., Riederer, S., Ehman, R., 1995. Respiratory motion of the heart: kinematics and the implications for the spatial resolution in coronary imaging. Magn Reson Med 33 (5), 713–719.

Weis, J., Budinsky, E., 1990. Simulation of the influence of magnetic field inhomogeneity and distortion correction in MR imaging. Magn Reson Med 8, 483–489.

Weisskoff, R., Baker, J., Belliveau, J., Davis, T., Kwong, K., Cohen, M., Rosen, B., 1993. Power spectrum analysis of functionally-weighted MR data: what's in the noise. In: Proc Soc Magn Reson Med. Vol. 1. p. 7.

Weissler, A., Harris, W., Schoenfeld, C., 1968. Systolic time intervals in heart failure in man. Circulation 37 (2), 149–159.

Wells III, W., Viola, P., Atsumi, H., Nakajima, S., Kikinis, R., 1996. Multi-Modal volume registration by maximization of mutual information. Med Image Anal 1, 35–51.

Wu, M., Chang, L., Walker, L., Lemaitre, H., Barnett, A., Marenco, S., Pierpaoli, C., 2008. Comparison of EPI distortion correction methods in diffusion tensor MRI using a novel framework. MICCAI 2008. Lecture Notes in Computer Science 5242 (2), 321–329.

Yang, X., Kwitt, R., Styner, M., Niethammer, M., 2017. Quicksilver: Fast predictive image registration – A deep learning approach. Neuroimage 158, 378–396.

Young, A., Axel, L., 1992. Three-Dimensional motion and deformation of the heart wall: estimation with spatial modulation of magnetization, a model-based approach. Radiology 185 (1), 241–247.

Young, A., Cowan, B., 2012. Evaluation of left ventricular torsion by cardiovascular magnetic resonance. J Cardiovasc Magn Reson 14 (49), 1–10.

Young, A., Kraitchman, D., Dougherty, L., Axel, L., 1995. Tracking and finite element analysis of stripe deformation in magnetic resonance tagging. IEEE Trans Med Imag 14, 413–421.

Young, A., Kramer, C., Ferrari, V., Axel, L., Reichek, N., 1994. Three-Dimensional left ventricular deformation in hypertrophic cardiomyopathy. Circulation 90, 854–867.

Zaitsev, M., Maclaren, J., Herbst, M., 2015. Motion artifacts in MRI: a complex problem with many partial solutions. J Magn Reson Imaging 42 (4), 887–901.

Zerhouni, E., Parish, D., Rogers, W., Yangand, A., Shapiro, E., 1988. Human heart: tagging with MR imaging – a method for noninvasive assessment of myocardial motion. Radiology 169, 59–63.

Zhang, X., Hou, G., Ma, J., Yang, W., Lin, B., Xu, Y., 2014. Denoising MR images using non-local means filter with combined patch and pixel similarity. PLoS ONE 9 (6), 1–12.

Zhong, X., Spottiswoode, B., Meyer, C., Kramer, C., Epstein, F., 2010. Imaging three-dimensional myocardial mechanics using navigator-gated volumetric spiral cine DENSE MRI. Magn Reson Med 64 (4), 1089–97.